The Investigation of Phosphorescent Dopants and Novel Blue Fluorescent Polymer Hosts for PLED Devices

JAVAN HAROLD COOK

THE INVESTIGATION OF PHOSPHORESCENT DOPANTS AND NOVEL BLUE FLUORESCENT POLYMER HOSTS FOR PLED DEVICES

Javan Harold Cook

Abstract

This thesis has focused on using experimental and simulation based techniques in an attempt to understand the interactions between polymer hosts and phosphorescent dopants in Organic Light Emitting Devices (OLEDs).

The viability of the SEmiconducting Thin Film Optics Simulation (SETFOS) software as a modelling tool has been established using the well documented material poly(3,4-ethylenedioxythiophene) (PEDOT). Parameters including resistivity and work function were extracted using SETFOS and the trends observed compared favourably to the commercially provided values, despite some limitations.

SETFOS was then used, along with steady state and transient electroluminescence characterisation, to investigate the effects of both phosphorescent dopant colour and concentration on device performance and extract important device parameters, such as the density of states and carrier mobilities. Different device behaviours were observed depending upon the dopant colour and concentration, highlighting the importance of both to device performance. SETFOS was again found to be able to produce quantitative values for a number of device parameters, but several more limitations within the models were identified, which makes further analysis and investigation necessary.

Having gained an understanding of host and dopant interactions in OLED devices, the information gathered was used in the characterization of novel high triplet host polymers for OLED applications. Seven polyfluorene based copolymers were investigated in devices with a range of different coloured phosphorescent dopants and charge transport molecules. Unfortunately, they were found to be unsuitable for use as host materials in OLEDs, acting instead as charge traps.

These polymers, along with four others, were alternatively assessed on their ability to perform as deep blue, or violet, fluorescent materials in undoped Polymer LED (PLED) devices. These devices were found to have some of the highest device characteristics currently detailed in the literature, and represent a variety of new ways of achieving efficient deep blue emission using PLED devices.

THE INVESTIGATION OF PHOSPHORESCENT DOPANTS AND NOVEL BLUE FLUORESCENT POLYMER HOSTS FOR PLED DEVICES

Javan Harold Cook

A thesis submitted to the Faculty of Science, Durham University,
for the degree of Doctor of Philosophy

Organic Electroactive Materials Group
Department of Physics
University of Durham
March 2015

Contents

List of Figures

List of Tables

Index of Abbreviations

Declaration

All material contained in this thesis is original and is the result of my own work except where explicit reference is made to the work of others.

This thesis has not been submitted in whole or part for the award of a degree at this or any other university.

Acknowledgements

Many people have helped and supported me during the course of my PhD. I would first like to thank my supervisor Professor Andy Monkman for the vital advice and guidance he has provided me throughout my studies. I would also like to thank my second supervisor Dr. Marek Szablewski for always being happy to help whenever I needed it. I've been extremely fortunate to have been funded by the Durham Energy Institute's Centre for Doctoral Training for the duration of my PhD. This has provided me with a number of opportunities that I would not have otherwise had access to, and I would like to thank Dr. Douglas Halliday and the DEI for making them possible. I would also like to thank Dr. José Santos and Professor Martin Bryce for providing a number of the polymers featured in this thesis and for being a valuable source of discussion. I have also been fortunate enough to work with a number of talented researchers within the OEM group and I would like to thank them all for their suggestions and help.

I would like to thank my brother, my parents and my parents-in-law for all of their support and encouragement. Finally, and perhaps most importantly, I would like to thank my wife Emily for everything, especially her love, patience and understanding when things took longer than anticipated.

To Emily,

For all of your love and support.

Chapter 1 Introduction:

1.1). Introduction:

The term Organic Light Emitting Device, abbreviated to the acronym OLED, refers to a light emitting diode (LED) that utilises an electroluminescent organic layer to generate the light emitted. The organic layer typically comprises of either a polymer or a small organic molecule and can include mixtures of the two along with organo-metallic compounds. A very basic OLED structure can be seen in Figure 1.1.

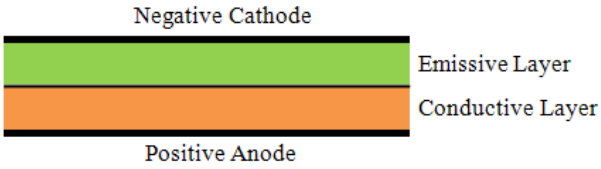

Figure 1.1: *This figure shows some of the layers often featured in an OLED device.*

OLEDs have been the focus of intense study for almost thirty years. The process was started by the original discovery of electroluminescence in organic materials in the 1950s by A. Bernanose [1] and moved on to Pope's work on organic crystals in the 1960s [2]. Pope identified that electroluminescence in organics was due to the recombination of holes and electrons; he then described what would be necessary to produce OLED devices that would function. Unfortunately, due to limitations in the conductivity of the materials available, exceptionally high voltages of over 400 V were required to produce electroluminescence.

Work continued in the field with the development of new polymers and organic compounds that were more conductive, and so could be operated at reasonable voltages, until the first true OLED was achieved in 1987 at Eastman Kodak by C. W. Tang and S. A. Van Slyke [3]. They produced an OLED that utilised a bilayer structure of monopolar materials to produce a heterojunction of an electron transporting aluminium based organic molecule, tris(8-hydroxyquinoline) aluminium (Alq_3), and a hole transporting aromatic diamine. The

production of these small molecule based devices using bilayers marked the beginning of the current period of investigation into OLED devices. This was followed in 1990 by the first polymer based OLED device, also known as a PLED, which was produced in Cambridge by J. H. Burroughes, D. D. C. Bradley, A. R. Brown, R. N. Marks, K. Mackay, R. H. Friend, P. L. Burn and A. B. Holmes [4]. This device used the polymer poly(p-phenylene vinylene) (PPV), and was a highly efficient emitter of green-yellow light.

The reason that OLEDs have been subjected to such intense scrutiny is that they offer numerous potential benefits over commercial liquid crystal displays (LCDs) and other sources of lighting. In the future OLEDs have the potential to be cheaper, both to manufacture and to power, than inorganic light sources of equivalent area or luminous intensity. This is primarily because OLEDs produce their own light and therefore have no need for supplementary backlighting. This is in direct contrast to the LCD displays currently available, which primarily incorporate an LED backlight. If an area of the OLED display is not being used it is switched off and will therefore not be expending power, making the display more efficient.

An additional beneficial side effect of the absence of backlighting is the ability of OLED displays to express true black, where an individual pixel is simply switched on or off as required. LCD displays rely on shutters or filters to remove the majority of light produced by the backlight, which can negatively impact the contrast ratios achieved. This can be alleviated somewhat by the use of dynamic backlighting, where areas of an LED backlight can be switched off when not in use. The removal of the backlight from a display also allows for much thinner displays, for example the world's first OLED television is a mere 3mm thick at its thinnest point [6]. OLED devices do still require the use of circular polarisers in order to remove reflected ambient light, which can otherwise severely inhibit the ability to view a display in bright light.

OLED displays potentially possess several other significant advantages over their competitors, which include: faster response times, larger colour and contrast ranges, and wider viewing angles [7-10]. These abilities are another direct positive effect of OLEDs producing their own light and not being required to use LCD filters. In current LCD displays the response time is limited to the order of milliseconds [11] by the turn on time of the liquid crystals changing orientation, whereas the response time of OLED displays are currently in the microsecond range and limited by the time taken to turn a pixel on or off. Finally it is possible to print OLEDs [12, 13] onto different surfaces which allows for not just the inexpensive, rapid and efficient manufacture of OLED devices but it also provides the ability to produce flexible displays [14]. Using flexible polymers like poly(ethylene terephthalate) (PET) it may even be possible to print fold-able or roll-able OLEDs onto fabrics, such as on t-shirts, or onto paper and other flexible media.

Figure 1.2: *This figure shows the first OLED television made by Sony, the XEL-1, with a thickness of 3mm at its thinnest point. Also featured is the Samsung Galaxy S5, the Sony PlayStation Vita and the LG 55EC930V, all of which use OLED technology. [15-18]*

There are, however, a number of disadvantages also currently associated with OLEDs when they are compared to other commercially available LCD displays. Currently OLEDs suffer from lifetimes that are limited by the organic constituents of the active layers. These lifetimes are usually lower than those made with LCD components and can sometimes be

significantly shorter. This is because OLED devices are current driven, as opposed to voltage driven like LCD displays, which allows for the disassociation of charge to occur within the layers creating non-emissive trap states. Upon exposure to light or when contaminated by air or water, the device layers that incorporate organic components can also be oxidised and break down. This can be extremely harmful to the OLED device performance, therefore improved encapsulation techniques or organic chemicals with enhanced stability are required to make them comparable and viable alternatives to inorganic devices.

These issues can be particularly problematic for flexible displays. Due to the nature of their operation they are often more challenging to encapsulate successfully and as such can have severely limited lifetimes. The materials used as cathodes for OLED devices, such as barium or lithium fluoride, can also present potential problems to device capabilities, as they are very readily oxidised if left exposed to ambient conditions. Despite these challenges, much progress has been made in recent years that should see OLEDs being fully competitive with their inorganic rivals [19, 20].

OLEDs have several possible applications because of their numerous advantages over current technologies; these primarily encompass lighting and display technologies. A number of OLED televisions have been produced to date; these include the Sony XEL-1 [6] and the LG 15EL9500 [21], which were regularly presented at technology shows, along with more recently produced displays which are now commercially available including the LG 55EC930V. As OLED displays are energy efficient they have been used in a number of smaller devices, such as in screens for mobile phones or mp3 players, resulting in prolonged battery life. These types of product typically have a short life as they tend to be upgraded fairly often, so their transitory nature alleviates the limitations usually associated with OLED lifetime. This includes the massively successful Galaxy S range produced by Samsung which

has sold a combined total of 216 million units in the last five years [22]. Several devices using OLED screens can be found in Figure 1.2.

In addition to displays, because OLEDs have the potential to be extremely efficient they could also be used as large area lighting sources or signs and backlights for future LCD displays [23]. OLEDs remain a comparatively novel form of technology, and as such there should be many more applications in the future ranging from virtual reality headsets [24] to transparent displays [25] and beyond.

1.2). Thesis Motivation:

This thesis investigates the role of simulation software in developing OLED technologies and understanding the trends exhibited by experimental results. Novel methods of producing deep blue OLEDs are also investigated, including new high triplet host materials for use with blue phosphorescent dopants and deep blue fluorescent polymers. Efficient blue emission is of extreme importance to OLED devices as it is not only essential for good colour rendering but it is also the limiting factor in device lifetime, with current blue OLED lifetimes being approximately 50,000 hours [26]. At present displays utilise fluorescent blue emitters which currently have longer lifetimes than their phosphorescent alternatives [27], but the latter have the potential for far superior efficiencies, obtained by making use of the otherwise spin forbidden triplet states.

Following on from this introductory chapter, Chapter 2 and Chapter 3 provide the background theory and the experimental procedures for this thesis respectively. This includes a basic overview of the operating principles behind OLED devices and progresses to an in-depth discussion of the fundamental and material concepts involved in the later chapters. The experimental techniques involved in both producing and characterising OLED devices are detailed in Chapter 3, along with instructions for additional photophysical measurements.

Chapter 4 introduces the OLED simulation software Semiconducting Thin Film Optics Simulation (SETFOS). An in depth discussion of the fundamental models and equations used by the SETFOS software is presented, and its ability to accurately reproduce experimental results and extract physical device parameters is assessed. This was achieved using experimentally observed device data based on three different versions of commercially produced poly(3,4-ethylenedioxythiophene) (PEDOT). It was determined that whilst the general trends expected based on the experimental data were correct, the magnitude of the physical values were not within the expected ranges. This was attributed to a combination of flaws within the SETFOS model but it was concluded that SETFOS was able to successfully model device data, producing quantitative values for device parameters that fit with the experimentally observed trends.

Chapter 5 attempts to further the work of Chapter 4 by increasing the complexity of the data to fit using an updated version of SETFOS. In addition to this, the effects of phosphorescent dopant colour and concentration on device performance were investigated. These investigations yielded important results relating the energy levels of both the dopant and the host to device behaviour; in addition to this optimum dopant concentrations for device performance were obtained. As in Chapter 4, SETFOS was found to have a number of limitations preventing it from accurately reproducing experimentally determined results. It was, however, still possible to obtain qualitative values and trends that reinforced the observed data.

Chapter 6 aims to use the lessons learnt about the relationships between polymer hosts and phosphorescent dopants in Chapter 5 to develop a series of new high triplet polymer hosts for deep blue OLED applications. Seven polyfluorene based copolymers, which made use of restricted conjugation to increase the triplet levels, were investigated and found to be unsuitable hosts for a variety of different phosphorescent dopants. This was attributed to a

severe offset between the highest occupied molecular orbital (HOMO) and lowest unoccupied molecular orbital (LUMO) levels of the hosts and the dopants, the highly charge trapping nature of the polymers, and poor charge transport properties for the least conjugated polymers. However, it was discovered that the polymers were promising deep blue fluorescent emitters that warranted further investigation.

Chapter 7 investigates the seven polymers from Chapter 6, in addition to four new polyfluorene-carbazole based copolymers, to determine their suitability for use in deep blue, or violet, fluorescent polymer LEDs (PLEDs). Different chemical engineering techniques were used to produce deep blue or violet devices, including changing bonding positions to reduce conjugation length or incorporating large pendant groups, with various degrees of success. No dopants for charge transport, or emission, were used in the polymer layers but an electron injecting layer of 1,3,5-tris(N-phenylbenzimidazole-2-yl)benzene (TPBi) evaporated on top of the polymer layer was found to drastically boost performance. The devices produced are amongst the highest of their type currently reported in the literature in terms of both brightness and efficiency, and feature extremely good turn on voltages.

References:

1. A. Bernanose, *Electroluminescence of Organic Compounds.* British Journal of Applied Physics, 1955: p. S54-S56.
2. M. Pope, P. Magnante, and H.P. Kallmann, *Electroluminescence in Organic Crystals.* Journal of Chemical Physics, 1963. **38**(8): p. 2042-&.
3. C.W. Tang and S.A. Vanslyke, *Organic Electroluminescent Diodes.* Applied Physics Letters, 1987. **51**(12): p. 913-915.
4. J.H. Burroughes, et al., *Light-Emitting-Diodes Based on Conjugated Polymers.* Nature, 1990. **347**(6293): p. 539-541.
5. L.S. Hung and C.H. Chen, *Recent progress of molecular organic electroluminescent materials and devices.* Materials Science & Engineering R-Reports, 2002. **39**(5-6): p. 143-222.
6. Sony, *Sony Launches World's First OLED TV*. 2007 [cited 20/06/11]; Available from: http://www.sony.net/SonyInfo/News/Press/200710/07-1001E/index.html.

7. R. Friend, J. Burroughes, and T. Shimoda, *Polymer diodes.* Physics World, 1999. **12**(6): p. 35-40.

8. S.C. Stinson, *Fine chemicals strive to expand.* Chemical & Engineering News, 2000. **78**(26): p. 22-23.

9. W.E. Howard, *Better displays with organic films.* Scientific American, 2004. **290**(2): p. 76-81.

10. W.Y. Wong and C.L. Ho, *Functional metallophosphors for effective charge carrier injection/transport: new robust OLED materials with emerging applications.* Journal of Materials Chemistry, 2009. **19**(26): p. 4457-4482.

11. V. Borshch, S.V. Shiyanovskii, and O.D. Lavrentovich, *Nanosecond Electro-Optic Switching of a Liquid Crystal.* Physical Review Letters, 2013. **111**(10): p. 107802.

12. T.R. Hebner, et al., *Ink-jet printing of doped polymers for organic light emitting devices.* Applied Physics Letters, 1998. **72**(5): p. 519-521.

13. J. Bharathan and Y. Yang, *Polymer electroluminescent devices processed by inkjet printing: I. Polymer light-emitting logo.* Applied Physics Letters, 1998. **72**(21): p. 2660-2662.

14. C.S. Ha, M.C. Choi, and Y. Kim, *Polymers for flexible displays: From material selection to device applications.* Progress in Polymer Science, 2008. **33**(6): p. 581-630.

15. TechyTalk, *Sony's XEL-1*. 2011 [cited 12/01/15]; Available from: http://techytk.blogspot.co.uk/2012/04/sonys-xel-1.html.

16. GSMArena, *Samsung Galaxy S5 Pictures*. 2014 [cited 12/01/15]; Available from: http://www.gsmarena.com/samsung_galaxy_s5-pictures-6033.php.

17. GamesBeat, *Sony will refund consumers over 'deceiving' PlayStation Vita ads*. 2014 [cited 12/01/15]; Available from: http://venturebeat.com/2014/11/25/sony-will-refund-consumers-over-deceiving-playstation-vita-ads/.

18. J. Lewis, *LG 55EC930V Curved OLED Full HD 3D Smart TV, 55" with Freeview HD and 1x 3D Glasses*. 2014 [cited 12/01/15]; Available from: http://www.johnlewis.com/lg-55ec930v-curved-oled-full-hd-3d-smart-tv-55-with-freeview-hd-and-1x-3d-glasses/p1719631.

19. A.C. Grimsdale, et al., *Synthesis of Light-Emitting Conjugated Polymers for Applications in Electroluminescent Devices*. Chemical Reviews, 2009. **109**(3): p. 897-1091.

20. OLED-Info, *DisplayMate: the GS5 display is the best mobile display ever, outperforming all previous OLED and LCD panels*. 2014 [cited 08/01/15]; Available from: http://www.oled-info.com/displaymate-gs5-display-best-mobile-display-ever-outperforming-all-previous-oled-and-lcd-panels.

21. AVR, *LG 15EL9500 OLED TV*. 2010 [cited 20/06/11]; Available from: http://www.avreview.co.uk/news/article/mps/uan/3345.

22. Wikipedia, *List of best-selling mobile phones*. 2014 [cited 12/01/125]; Available from: http://en.wikipedia.org/wiki/List_of_best-selling_mobile_phones.

23. K. Meerholz, et al., *Highly color-stable solution-processed multilayer WOLEDs for lighting application.* Journal of Materials Chemistry, 2010. **20**(16): p. 3301-3306.

24. Sony, *Head-Mounted Display*. 2013 [cited 12/01/15]; Available from: http://www.sony.co.uk/electronics/head-mounted-display/t/head-mounted-display.

25. EXTREMETECH, *LG's flexible and transparent OLED displays are the beginning of the e-paper revolution*. 2014 [cited 08/01/15]; Available from: http://www.extremetech.com/computing/186241-lgs-flexible-and-transparent-oled-displays-are-the-beginning-of-the-e-paper-revolution.

26. OLED-Info, *Kaneka developed a 50,000 hours OLED lighting panel, plans to increase production capacity*. 2014 [cited 08/01/15]; Available from: http://www.oled-info.com/kaneka-developed-50000-hours-oled-lighting-panel-plans-increase-production-capacity.

27. OLED-Info, *Blue PHOLED breakthrough: researchers manage to extend the lifetime tenfold*. 2014 [cited 08/01/15]; Available from: http://www.oled-info.com/blue-pholed-breakthrough-researchers-manage-extend-lifetime-tenfold.

Chapter 2 Theory:

2.1). Basic Principles:

This section provides a brief overview of how organic light emitting devices (OLEDs) work and produce light. A more in depth look at the theory behind the topics covered in this section can be found further on in this chapter and in the subsequent chapters.

OLEDs produce light using electroluminescence, and are classed as diodes because of the change in conductivity amongst the constituent layers when driven by a current. The most rudimentary OLED devices characteristically comprise of four key layers, an anode, a cathode, a conducting layer and finally an emissive layer [1]. Typically, the device would possess an anode, made up of a transparent conducting metal oxide; a metal cathode, such as barium; and conducting and emissive layers, either polymer or small molecule based. This thesis will focus on polymer based devices.

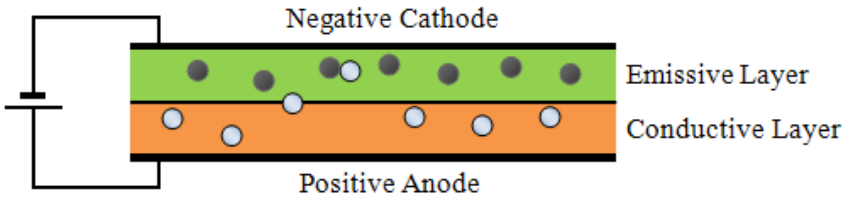

Figure 2.1: *A simple example of an OLED device. The electrons, represented by dark circles, recombine with the holes, represented by light circles, to form excitons. These excitons then decay to emit light.*

A potential difference is generated between the two electrodes, inducing a current in the organic layers, as seen in Figure 2.1. Electrons from the metal cathode are injected in to the Lowest Unoccupied Molecular Orbital (LUMO) of the emissive material. Simultaneously, holes from the anode are first injected into the valence band of the conductive layer, and then injected into the Highest Occupied Molecular Orbital (HOMO) of the emissive material. Electron holes, also called holes, are the absence of the normally present electrons when a bias voltage is applied. The positive holes and negative electrons are drawn together along

the polymer chains by both the applied field and electrostatic interactions, where they eventually meet and recombine to form an exciton. This recombination typically occurs in the emissive layer, as the holes are usually the more mobile of the two charge carriers [2]. The recombination results in an electron being in a higher energy state than it ordinarily would be in; from there it may experience a radiative decay, emitting light, in order to return to the lower energy ground state. The wavelength of the photon emitted due to the radiative decay is determined by the band gap between the HOMO and the LUMO of the emitter. This process is discussed in more detail in 2.4).

It is possible to produce more sophisticated OLED devices, which have more layers than just the emissive and conductive ones mentioned earlier. The motivation behind this is to confer benefits, such as increased efficiency, brightness or stability, upon the device depending upon the layers and properties selected. The electronic profile of the device can be smoothed by inserting extra layers, with intermediate work functions, between layers with a big energy step, thus increasing carrier injection or transport. The opposite is also true, and extra layers can be inserted to block either electrons or holes from being wasted by reaching their opposing electrode [3, 4]. This can be achieved by using the conductive properties of different materials, or their work functions, to create unfavourable boundaries that the carriers would struggle to penetrate. This can potentially make the OLED devices more efficient and even make them more stable during operation.

There are several techniques that can be used to deposit the organic layers and these usually depend on the type of compound used. Evaporation techniques are generally preferred for small molecules [5], whilst solution processing, such as spin coating techniques [6] or inkjet printing [7], is preferred for polymers. The primary challenge associated with solution processing is to produce multilayer devices whilst still preserving the discrete layers necessary for the devices to work properly. Depositing sequential layers can disturb or

partially dissolve the layer underneath, which can damage their interfaces and impact upon device performance. This is less of an issue for evaporated devices due to the low rate of deposition involved. This thesis is primarily concerned with solution processed OLEDs.

2.2). Bonding and Conjugation:

2.2.1). Chemical Bonding:

The term chemical bond encompasses the different degrees of attraction between two atoms that can result in the formation of a new chemical species [8]. There are two main categories for chemical bonds, strong bonds and weak bonds. The strong bond category includes ionic bonding, covalent bonding and metallic bonding and is usually the result of the sharing of, or exchange of, electrons between two atoms. These strong bonds are the intramolecular forces responsible for holding together the atoms in molecules.

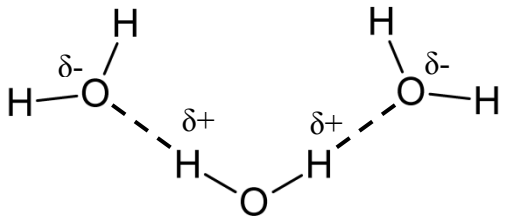

Figure 2.2: *An example of strong and weak chemical bonds. The solid lines represent the covalent bonds between the hydrogen and oxygen atoms. The dashed lines represent the hydrogen bonds between the water molecules.*

The weak bond category includes dipole-dipole interactions, hydrogen bonding, London dispersion forces and cation-pi interactions, and is usually the result of electrostatic interactions between molecules. These weak bonds are the intermolecular forces between molecules and often affect the properties of a substance, such as the melting point. An example of this can be seen in Figure 2.2 where the solid lines represent the covalent bonds between the hydrogen and oxygen atoms making a H_2O molecule, whilst the dashed line represents the hydrogen bonding between two H_2O molecules.

For OLEDs we are primarily interested in covalent bonding and the chemistry of organic, carbon based, molecules and compounds. Covalent bonds are formed between atoms that share a pair of electrons between them. Dative, or coordinate, covalent bonds are formed when one of the atoms donates both of the electrons incorporated into the bond. This type of covalent bond is also known as a non-polar covalent bond as the electrons are shared almost equally between the two atoms. It is also possible to form polar covalent bonds, or covalent bonds with ionic character, where a difference in electronegativity between the two atoms leads to an imbalance of charge and can cause dipole-dipole interactions as seen in Figure 2.2.

When considering chemical bonds, it is necessary to have some understanding of electrons in atomic orbitals and their associated nomenclature. For the considerations of this thesis, the electron can behave both as a wave and as a particle. As such an electron orbiting an atom has a wavefunction, ψ, associated with it, which describes its quantum state. These wavefunctions correspond to spherical harmonic standing waves for each of the quantum states available. The modulus squared, $|\psi|^2$, gives the probability of finding the electron in a given position. For the electron wavefunction, there are five quantum numbers that are of interest and these are n, ℓ, m_ℓ, s and m_s.

The principal quantum number, n, represents the energy level, or electron shell, in which the electron resides. Within each energy level there are a number of allowed states that the electron can occupy. The azimuthal quantum number, ℓ, describes the orbital angular momentum of the electron; in effect this represents the sub-shells within the energy level and can take values ranging from 0 to (n-1). Associated with ℓ is m_ℓ, which is the projection of the angular momentum onto the quantisation axis, conventionally termed the z-axis, and has integer values in the range $-\ell$ to ℓ. This represents the degenerate states that an electron can occupy within a specific sub-shell. The s quantum number is the spin quantum number,

which for electrons is equal to ½. This is because electrons are fermions and all fermions have a spin quantum number of ½. The m_s quantum number is the projection of the spin upon the z-axis and for electrons can either be +½ or -½, corresponding to the electrons being spin up or spin down.

Table 2.1: *A table showing how many electrons can occupy a quantum state defined by the quantum numbers n, ℓ and m_ℓ. There can be two electrons in each possible state due to electrons pairing up into spin up and spin down configurations. The total number of electrons per shell is also given.*

Quantum Number	ℓ = 0	ℓ = 1			ℓ = 2					Total
	m_ℓ = 0	m_ℓ = -1	m_ℓ = 0	m_ℓ = 1	m_ℓ = -2	m_ℓ = -1	m_ℓ = 0	m_ℓ = 1	m_ℓ = 2	
n = 1	2									2
n = 2	2	2	2	2						8
n = 3	2	2	2	2	2	2	2	2	2	18

Using these quantum numbers and the Pauli Exclusion Principle, which states that no two electrons can have the same value for these quantum numbers within an atom or molecule, it is possible to fill the states with electrons. Table 2.1 shows how the different energy levels can be filled with electrons as well as the total number of electron possible in

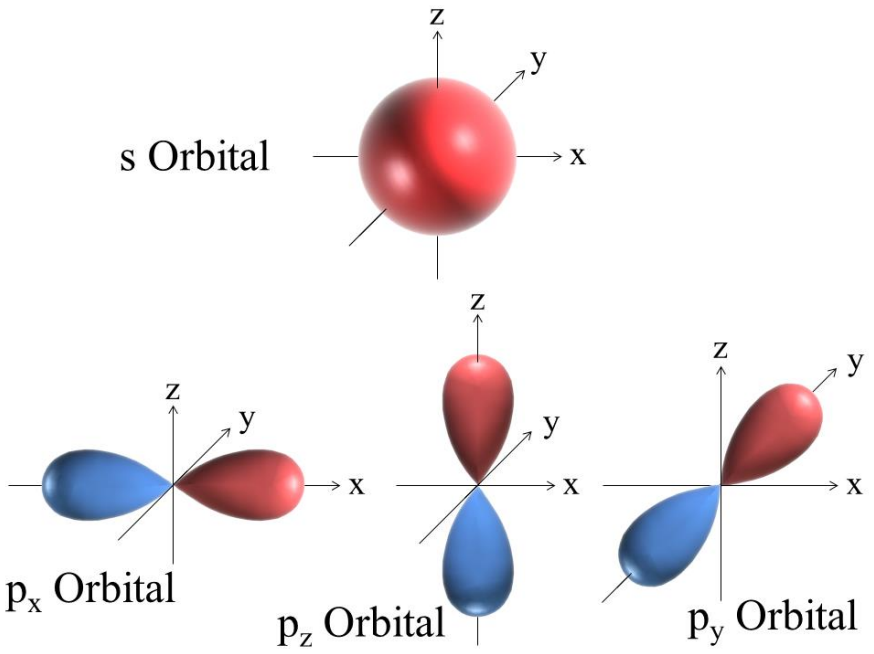

Figure 2.3: *A pictorial representation of the s (ℓ = 0) orbital and the three degenerate p (ℓ = 1) orbitals. For the p orbitals, the node at the origin results in a change from positive wavefunction to negative wavefunction, represented by the difference in colour between the two lobes.*

each shell. The spectroscopic notation for $\ell = 0$ is "s", $\ell = 1$ is "p" and $\ell = 2$ is "d". For conjugated polymers, we only really need to be concerned with the s and p orbitals, of which a pictorial representation of the wavefunctions can be seen in Figure 2.3. The p orbital has three degenerate levels and these can be considered to point along the three axes in Cartesian coordinates.

The covalent bond can be explored further by considering the bond present between the diatom H_2 [9]. Hydrogen has one negatively charged electron and the electronic structure $1s^1$ (one electron in the 1s level), and one positively charged proton in its nucleus. When two hydrogen atoms come into close proximity with each other, the electron orbitals overlap and ultimately produce two new molecular orbitals with their own energies. This is due to the electrostatic interactions between electrons and protons resulting in the blurring and eventual merging of the individual electron orbitals as seen in Figure 2.4.

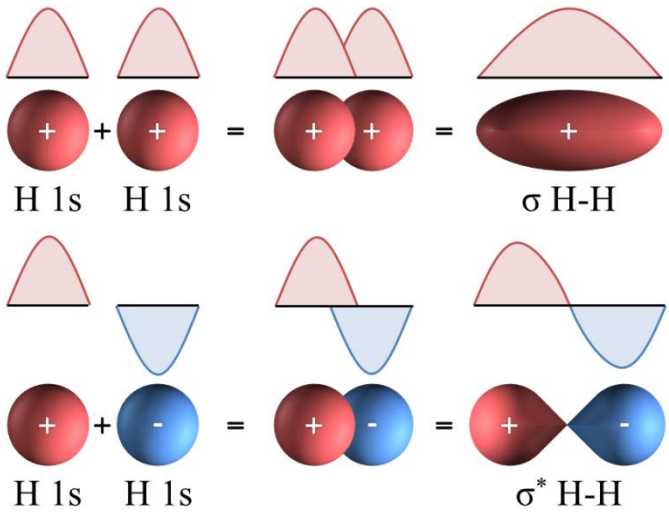

Figure 2.4: *A representation of the formation of a bond between two hydrogen atoms to form diatomic hydrogen. When the two atomic orbitals are in phase and interfere constructively the bonding orbital (σ orbital) is formed, whereas when they are out of phase and interfere destructively the anti-bonding orbital (σ^* orbital) is formed.*

The formation of molecular orbitals is symmetry dependent and the number of molecular orbitals formed must be equal to the number of atomic orbitals for the atoms combined. For diatomic hydrogen, this is two due to the combination of two 1s atomic

orbitals from the two hydrogen atoms. There are three possible types of molecular orbitals that can be formed when atomic orbitals are combined. The first of these is the bonding orbital, which is lower in energy than the atomic orbitals, and corresponds to constructive interactions between them. The second of these is the anti-bonding orbital, which is higher in energy than the atomic orbitals, and corresponds to the destructive interactions between them; there is also a nodal plane between the atoms. Finally, there are the non-bonding orbitals, which have the same energy as the atomic orbitals, and correspond to no interaction between them; this is the result of incompatible symmetries. For hydrogen the two new molecular orbitals are the bonding, or σ, orbital and the anti-bonding, or σ*, orbital respectively.

For the bonding orbital, the electrons have a high probability of being between the hydrogen nuclei, which increases the electrostatic attractions between them and lowers the energy of the system. For the anti-bonding orbital, there is a node between the two nuclei where the probability of finding an electron is zero; this increases the energy of the system as the electrons are more tightly bound than before. This means that when electrons are added to

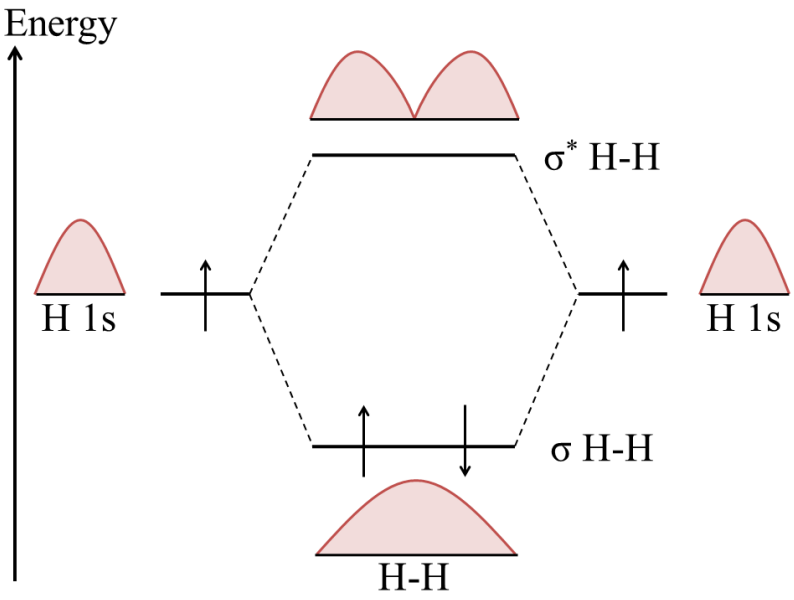

Figure 2.5: *A molecular orbital diagram for diatomic hydrogen. The electrons from each hydrogen atom occupy the bonding orbital forming a covalent bond. Also shown is a representation of the probability distribution ($|\psi|^2$) of the molecular orbitals, highlighting the zero probability of finding electrons in the middle of the anti-bonding orbital.*

the bonding orbital the energy of the system stabilised, whilst adding electrons to the anti-bonding orbital destabilises the system. The molecular orbitals are filled from lowest energy to highest energy, so that the system has the lowest total energy possible. This is carried out in accordance with the Pauli Exclusion Principle, so each level can have a spin up and a spin down electron. The electrons would prefer not to be paired up if there were more degenerate bonding states available, but they will readily pair up to minimise energy and avoid occupying an anti-bonding orbital. For diatomic hydrogen this means that both electrons go into the bonding orbital as seen in Figure 2.5. In this case the bonding orbital is the HOMO of the molecule whilst the anti-bonding orbital is the LUMO.

2.2.2). Hybridisation:

Carbon has an atomic number of six and so has the electron configuration $1s^2 2s^2 2p^2$. This would usually only allow carbon to bond covalently to just two other atoms, such as hydrogen, due to the two unpaired electrons in the 2p level. However, it is possible to excite one of the electrons from the filled 2s state to a 2p state resulting in four unpaired electrons that can now form covalent bonds. This is energetically favourable as the excitation energy required is more than offset by the formation of two new bonds. It is also this ability that leads us to the property of hybridisation.

Typically, in order to minimise the energy of the bonded system, the 2s and 2p states should have the same energy and be degenerate. This gives rise to the three types of hybridisation. The first of these is sp^3 hybridisation, which occurs when the 2s orbital mixes character with the three 2p orbitals to form four new hybrid orbitals. These new orbitals are in a tetrahedral formation, with an angle of 109.5° between them, and allow for the formation of four identical sigma bonds.

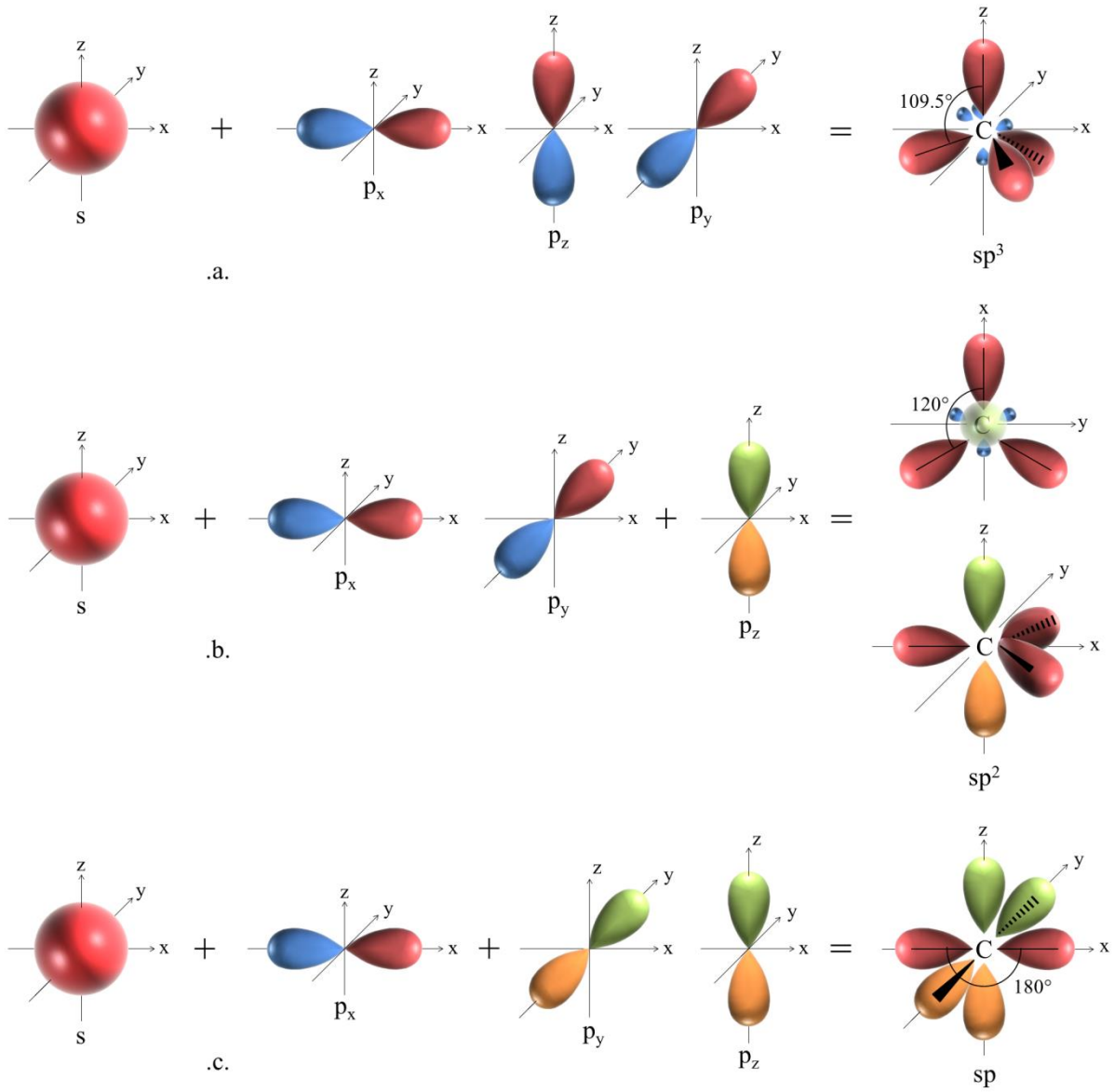

Figure 2.6: *A graphical representation of the formation of three types of hybridisation. Red and green areas represent positive wavefunctions whilst blue and orange areas represent negative wavefunctions. Part .a. shows the formation of four sp^3 hybrid orbitals. These adopt a tetrahedral formation where the bonds are 109.5° apart. Part .b. shows the formation of three sp^2 hybrid orbitals. These orbitals form in a plane 120° apart with the remaining 2p orbital perpendicular to them. Part .c. shows the formation of two sp orbitals. These orbitals form in a plane 180° apart with the two remaining 2p orbitals perpendicular to them.*

The second of these is sp^2 hybridisation; here two of the 2p orbitals combine with the 2s orbital to form three new hybrid orbitals in a plane 120° apart. This allows for the formation of three sigma bonds whilst the remaining 2p orbital is used to form a pi bond, or double bond, with an adjacent sp^2 hybridised carbon atom. The pi bond will be discussed in more detail in 2.2.3). Finally, there is sp hybridisation; this is where just one of the 2p orbitals combines with a 2s orbital to form two new hybrid orbitals in a plane 180° apart. This allows for the formation of just two linear sigma bonds whilst the two remaining 2p orbital are used

to form two pi bonds, or a triple bond, with an adjacent sp hybridised carbon atom. A graphic representation of the three hybridisations can be seen in Figure 2.6.

2.2.3). Conjugation:

Conjugation is a property that occurs in polymers and other organic molecules where there is a sequence of alternating double and single bonds along the primary chain. Conjugation is primarily a result of the electronic configuration of the carbon atom, which allows hybridisation to occur between orbitals. The hybridisation of interest for these conjugated structures is sp2 hybridisation. As discussed in 2.2.2), sp2 hybridisation occurs when a 2s orbital mixes with two 2p orbitals in order to form three new hybrid orbitals. These three new hybrid orbitals occur all in the same plane and are separated by 120°, whilst the last of the 2p orbitals remains perpendicular to the plane.

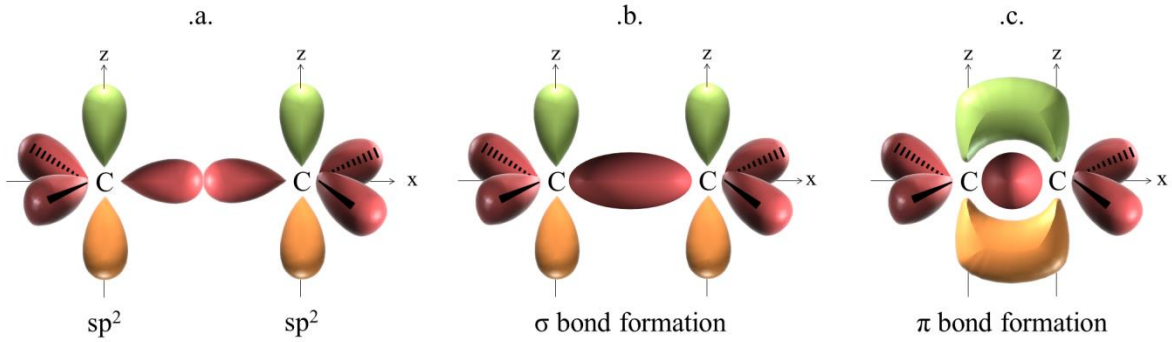

Figure 2.7: *Formation of a σ bond and a π bond between two sp^2 hybridised carbon atoms. Part a. shows two of the orbitals coming into close proximity. Part .b. shows the formation of a σ bond as the two orbitals overlap. Part .c. shows the formation of the π bond as the remaining p orbitals perpendicular to the sp^2 plane overlap.*

Sigma bonds form between carbon atoms when two of these sp2 hybridised orbitals overlap. A pi bond is then formed between neighbouring carbon atoms by overlapping the remaining 2p orbitals. This can be seen in Figure 2.7. Pi bonds are not as strong as sigma bonds as there is a smaller degree of overlap between the orbitals. Another property of pi bonds is that they cannot be rotated about the bond without breaking it, as any rotation removes the overlap between orbitals. This is in direct contrast to sigma bonds, which can rotate freely about the bond. Finally, as can be seen in Figure 2.7, there is one nodal plane

between the wavefunctions for the bonding orbital; for the π* orbital, however, there is an additional nodal plane, taking the total to two nodal planes.

Conjugated structures are formed when there is an alternating chain of double and single bonds, as shown in Figure 2.8. This allows a delocalised region of electron density to form along the alternating chain. This delocalised region of electron density forms the HOMO of the compound. The π* anti-bonding orbitals also overlap creating an absence of electron density which forms the LUMO of the compound. This means that for conjugated polymers, the core transition is the π-π*, as an electron is excited from the HOMO to the LUMO. Unfortunately, even if a perfectly conjugated system were assembled, charge would not be freely conducted along the chain like a metallic state. Instead, due to Peirels distortion [10], conjugated polymers are insulators in their pure form and require interstitial doping with oxidising or reducing agents to make them conducting [11].

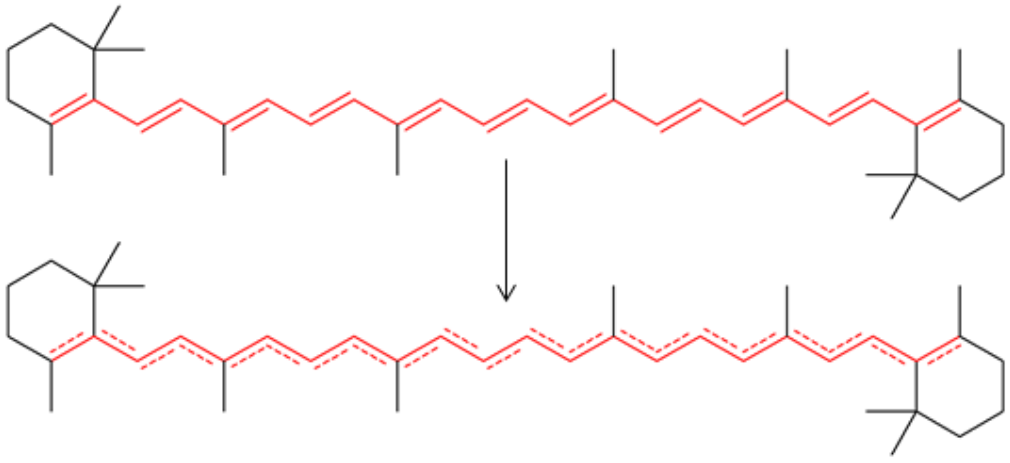

Figure 2.8: *The chemical structure of β-carotene. This molecule has a backbone featuring alternate single and double bonds, highlighted in red, and is considered a conjugated molecule. This is denoted by the use of a solid and dotted line, replacing the single and double bonds, representing the delocalisation of electrons along the backbone.*

An important factor for OLEDs concerning conjugation is the energy gap between the HOMO and the LUMO, which determines the wavelength of light emitted. This energy difference is directly related to the number of atoms, and their electrons, that are involved in the delocalised region of electron density. This factor is known as the conjugation length

[12]. For molecules or polymers with a longer conjugation length there are more units involved in conjugation, which has the effect of reducing the energy gap by stabilising the bonding region involved.

Unfortunately, unlike other semiconductor materials which are typically highly ordered, polymers typically experience a significant degree of disorder. This is caused by imperfections both within the chains themselves and by interactions between adjacent chains, which result in bends and twists causing the conjugation to be broken when the p-orbital overlap is removed. This results in the polymer chain being broken up into conjugated sections of different lengths called chromophores. When averaged over all the polymer chains, the distribution of chromophore conjugation length can be thought of as being Gaussian. The methods of charge transfer between and within chromophores is discussed further in 2.5.2) and 2.5.3). This means that by tuning the degree of conjugation, or disrupting the conjugation, of a polymer it is possible to affect both the colour of light emitted and the transport properties of the device, making conjugation an important consideration in OLED design.

2.3). Excited States in Conjugated Polymers:

2.3.1). Excitons:

An exciton is an excited state of the system [12]. In its simplest form it is a neutrally charged, quasi-particle state that can exist between an electron and a hole, and can transport energy through a system without affecting the net charge. They can be formed following the excitation of an electron from the HOMO to the LUMO of a compound, where it remains coupled to the hole left behind in the HOMO due to a Coulomb force. This Coulomb force combined with the typically low Coulomb screening for conjugated polymers provides

enough of a stabilizing effect that the resultant exciton has a lower energy, and is thus more favourable, than an unbound electron and hole.

The formation of an exciton can have a substantial effect on a conjugated polymer, causing it to rearrange itself around the exciton in order to minimise the change in energy. This is a result of the strong electron-phonon coupling in conjugated polymers and the exciton is enclosed in a cloud of phonons, which lowers its energy. The rearrangement of the polymer typically takes the form of an attempt at planarization, and will follow the exciton as it migrates through the conjugated system. It is this rearrangement, together with the bound charged pair, that makes it a quasi-particle state.

Excitons can be sorted into two groups depending upon their binding energy. Tightly bound, usually intrachain, excitons common to materials with a low dielectric constant are called Frenkel excitons. Frenkel excitons are typically small in size, are often confined to the same molecular unit, and usually have binding energies in the range of 0.1-1 eV [13]. Less tightly bound, usually interchain, excitons common to materials with a high dielectric constant are called Wannier-Mott excitons. These excitons are larger in size, can exist between separate conjugated polymer chains, and typically have binding energies around 0.1-0.01 eV [14]. For conjugated polymers, because of their typically low dielectric constant, Frenkel type excitons with binding energies of approximately 0.5 eV are the ones most commonly formed by photoexcitation.

It is possible for excitons to be formed in one of four different configurations, each with equal probability. Holes and electrons behave as spin ½ particles, and as such they obey the exclusion rules that apply for fermions. Fermions are either spin up,$|\uparrow\rangle$, or spin down, $|\downarrow\rangle$. Therefore when an exciton is formed which involves the equivalent of two spin ½ particles, there are four different ways to combine the two spins. The particles are uncorrelated, and as

such they only know each other at the point of recombination, making this a spin independent, random, process. The four possible combinations, along with the relevant quantum numbers for the different states discussed in 2.2.1), are given in Equations 2.1 and 2.2.

$$S = 1, \quad \begin{cases} |\uparrow_1\uparrow_2\rangle, & m_s = 1 \\ \frac{1}{\sqrt{2}}(|\uparrow_1\downarrow_2\rangle + |\downarrow_1\uparrow_2\rangle), & m_s = 0 \\ |\downarrow_1\downarrow_2\rangle, & m_s = -1 \end{cases} \tag{2.1}$$

$$S = 0, \quad \frac{1}{\sqrt{2}}(|\uparrow_1\downarrow_2\rangle - |\downarrow_1\uparrow_2\rangle), \qquad m_s = 0 \tag{2.2}$$

The $|\uparrow_1\uparrow_2\rangle$ and $|\downarrow_1\downarrow_2\rangle$ states correspond to when the spins are both aligned in the same direction; either when both are spin up or both are spin down. The $\frac{1}{\sqrt{2}}(|\uparrow_1\downarrow_2\rangle + |\uparrow_1\downarrow_2\rangle)$ and $\frac{1}{\sqrt{2}}(|\uparrow_1\downarrow_2\rangle - |\uparrow_1\downarrow_2\rangle)$ states correspond to the spins being aligned in opposite directions. After the total spin of the states is calculated the $|\uparrow\uparrow\rangle$, $|\downarrow\downarrow\rangle$ and $\frac{1}{\sqrt{2}}(|\uparrow\downarrow\rangle + |\uparrow\downarrow\rangle)$ states from Equation 2.1 each have a spin value of 1 making them triplet, or T, states. The remaining $\frac{1}{\sqrt{2}}(|\uparrow\downarrow\rangle - |\uparrow\downarrow\rangle)$ state from Equation 2.2 has a total spin value of 0, making it the singlet, or S, state. A pictorial representation of the singlet and triplet states can be seen in Figure 2.9, which shows that $\frac{1}{\sqrt{2}}(|\uparrow\downarrow\rangle - |\uparrow\downarrow\rangle)$ precesses out of phase and $\frac{1}{\sqrt{2}}(|\uparrow\downarrow\rangle + |\uparrow\downarrow\rangle)$ precesses in phase. The importance of the difference between singlet and triplet states will be discussed further in 2.4.3).

As stated earlier in 2.1), excitons can also be formed when mobile charge carriers recombine. Several different excited states, or types of excitons, can instead be formed when recombination occurs. Excited states called excimers, named from excited dimers, are formed

when two separate charge carrying molecules that are both the same compound recombine. However if the recombination occurs between two separate charge carriers of different compounds the resulting excited state is called an exciplex, also known as an excited complex [15, 16]. These two states are basically different versions of the Wannier-Mott type excitons.

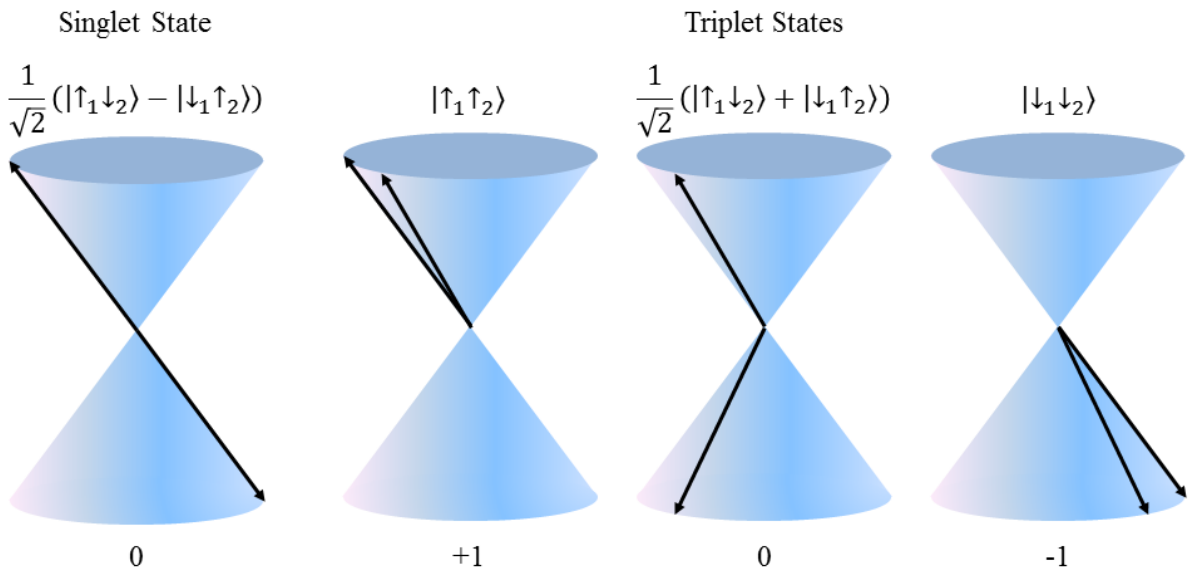

Figure 2.9: *A pictorial representation of the four different combinations of spin ½ particles. There is one singlet state where the spins are in opposite directions and precess out of phase and three triplet states; one with both spins up, one with both spins down and another where the spins are in opposite directions and they precess in phase.*

2.3.2). Polarons:

Polarons are quasi-particle states existing between a charge, such as a hole or an electron, and the distortion to the polymer bonding geometry caused by the charged particle; this is similar to the excitons discussed in 2.3.1). When a voltage is applied across the system polarons are free to move and transport charge between chromophores, forming an electric current. An electric field is necessary for polarons to be able to migrate as the polaron binding energy needs to be overcome. This is the energy required to reorganise the system around the charge, and the process can be thought of as self-trapping when the energy required is too high.

Crystalline inorganic structures have lower reorganisation energies due to the rigid crystal lattice preventing significant rearrangements, whilst polymers have much higher reorganisation energies as the charged particle can cause a molecule wide deformation. This accounts for the large difference in conductivity between organic and inorganic semiconductors. Inorganic semiconductors typically have conductivities of the order $1x10^{3}$ to $1x10^{6}$ $cm^{2}.V^{-1}.s^{-1}$, whilst organic semiconductors have been recorded in the range of $1x10^{-6}$ to 1 $cm^{2}.V^{-1}.s^{-1}$ [17]. This range of values for organic semiconductors highlights how much the carrier mobility of a system can be affected by the polaron binding energy of the system.

There are three main types of polaron, the free electron polaron, the free hole polaron and the electron-hole polaron pair. For OLEDs the first two of these are of primary interest, as the polaron pair is usually the intermediate step between excitons and free polarons, and are more important for photovoltaics. Free polarons can be formed directly, either by charge injection from an electrode by an electric field, or by chemical means, using a dopant to perform redox reactions. Polarons have energy levels between the HOMO and LUMO levels of the polymer due to the interaction of the charge and the geometric distortion [18]. The free electron polaron is formed following the addition of an electron to the LUMO of the polymer whilst free hole polarons are formed following the removal of an electron from the HOMO.

2.4). Absorption and Luminescence:

2.4.1). Processes and Selection Rules for Excited States:

There are many properties and processes associated with excited states and the majority of them can be summarised in a Jablonski Diagram [19] such as Figure 2.10. The vertical axis corresponds to energy and shows the relative positions of the different levels along with their vibrational manifolds. This means that vertical transitions correspond to changes in energy whilst horizontal transitions represent a change in the electronic state. The

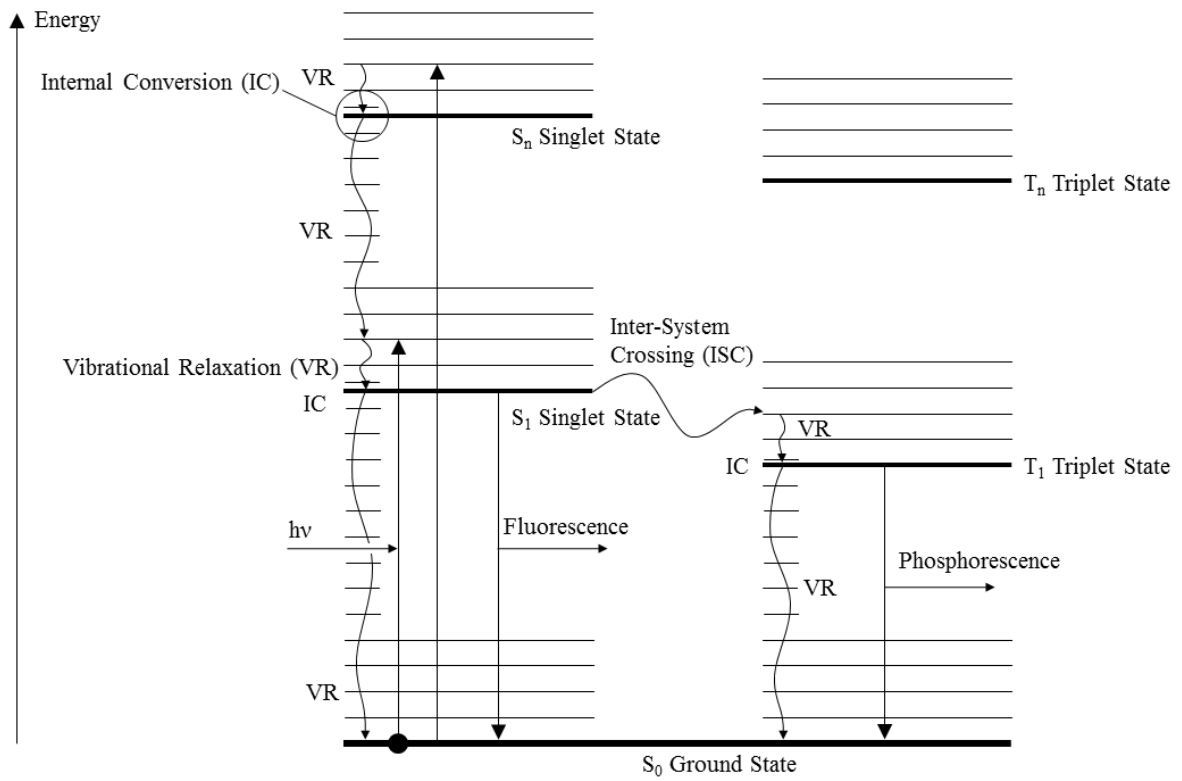

Figure 2.10: *This Jablonski diagram shows the processes that can take place in a system after an electron is excited in some way. The bold horizontal lines are the excited states whilst the normal horizontal lines represent the different vibrational manifolds for each state.*

radiative processes associated with excited states, namely absorption and emission, are characterised by straight lines whilst non-radiative processes, such as Inter-System Crossing (ISC), are represented by wavy lines. Also included is the Vibrational Relaxation (VR) and Internal Conversion (IC) within the associated manifold, represented by a vertical wavy line. Some of these processes will be discussed in more detail later.

These processes all have selection rules associated with them. The most basic of these is absorption, where the excited state is produced after the absorption of electromagnetic radiation. For absorption to occur it is necessary for $h\nu \geq \Delta E$. This usually corresponds to light in the region of 200-900 nm as longer wavelengths do not have enough energy, and shorter wavelengths may ionise the sample removing the electron completely. The probability of absorbing energy in this case is proportional to the transition dipole moment squared [20]. For the selection rules that are relevant here, the Born-Oppenheimer approximation is used to simplify the expression for the transition dipole moment.

The Born-Oppenheimer approximation assumes that as the motion of the nucleus is slow, when compared to the motion of the electron it is effectively motionless. This allows us to separate out the nuclear and electronic components from the total wavefunction; the electronic term is then further separated into the spin and electronic transition moment (TM) functions for the promoted electron. This gives a simplified equation [20, 21] for the transition dipole moment of the form:

$$TM = \int \theta_i \,.\, \theta_f . d\tau_N . \int S_i . S_f . d\tau_s . \int \varphi_i . \varphi_f . d\tau_e \qquad (2.3)$$

The first integral refers to the overlap of the initial and final nuclear configurations, also known as the Franck-Condon factor, a visual representation of this can be seen in Figure 2.11. The second integral refers to spin overlap between the initial and final states and is one when there is no change in multiplicity and zero otherwise. This means that whilst S←S transitions are allowed transitions, the S←T transitions, for example, are not. The third integral refers to the electronic transition moment, which is related to the symmetry of the molecular orbitals of the initial and final states. Also intrinsic in this equation is the requirement for spatial overlap between the initial and final states.

If any of the integrals above are equal to zero for a system then the transition is forbidden. However, due to the approximations used, it is possible that the transition is not completely forbidden, but occurs with a much lower probability. For example, transitions between different multiplicities can still occur, as it is the total angular momentum that must be conserved, not just the spin. This is especially pertinent for heavy atoms like transition metals and will be discussed further in 2.4.4). It should also be noted that symmetry forbidden transitions can also occur due to vibronic coupling.

2.4.2). Absorption:

This is the excitation of an electron into a higher energy state in response to incident photons. As discussed earlier in 2.4.1), if all of the selection rules are met, and light of the correct energy is incident upon a sample, an electron can be excited to a higher energy level, where the energy difference of the transition will be equal to that of the absorbed photon. Absorption follows the Beer-Lambert Law which relates the intensity of the light before, and after, absorption occurs to both the thickness and concentration of the absorbing sample [22]:

$$I = I_0 . 10^{\varepsilon l c} \tag{2.4}$$

Where I is the light intensity after absorption, I_0 is the initial light intensity, ε is the molar absorption coefficient, l is the sample thickness and c is the concentration of the sample. The absorbance of a sample, also referred to as the optical density can be calculated using Equation 2.5:

$$A = -\log_{10}\left(\frac{I}{I_0}\right) \tag{2.5}$$

Where again, I is light intensity after absorption and I_0 is the initial light intensity. Inspecting Equations 2.4 and 2.5 shows that the absorption of a material varies linearly with both concentration and path length.

2.4.3). Luminescence:

Photoluminescence occurs when excitation is caused by a photon being absorbed by the material. An electron is excited from the HOMO to the LUMO, it then decays back again by emitting a photon. Electroluminescence is when a material emits light in response to an electric current; this is the primary process by which both OLEDs and LEDs produce light. There are two possible pathways for this decay, fluorescence and phosphorescence. When an

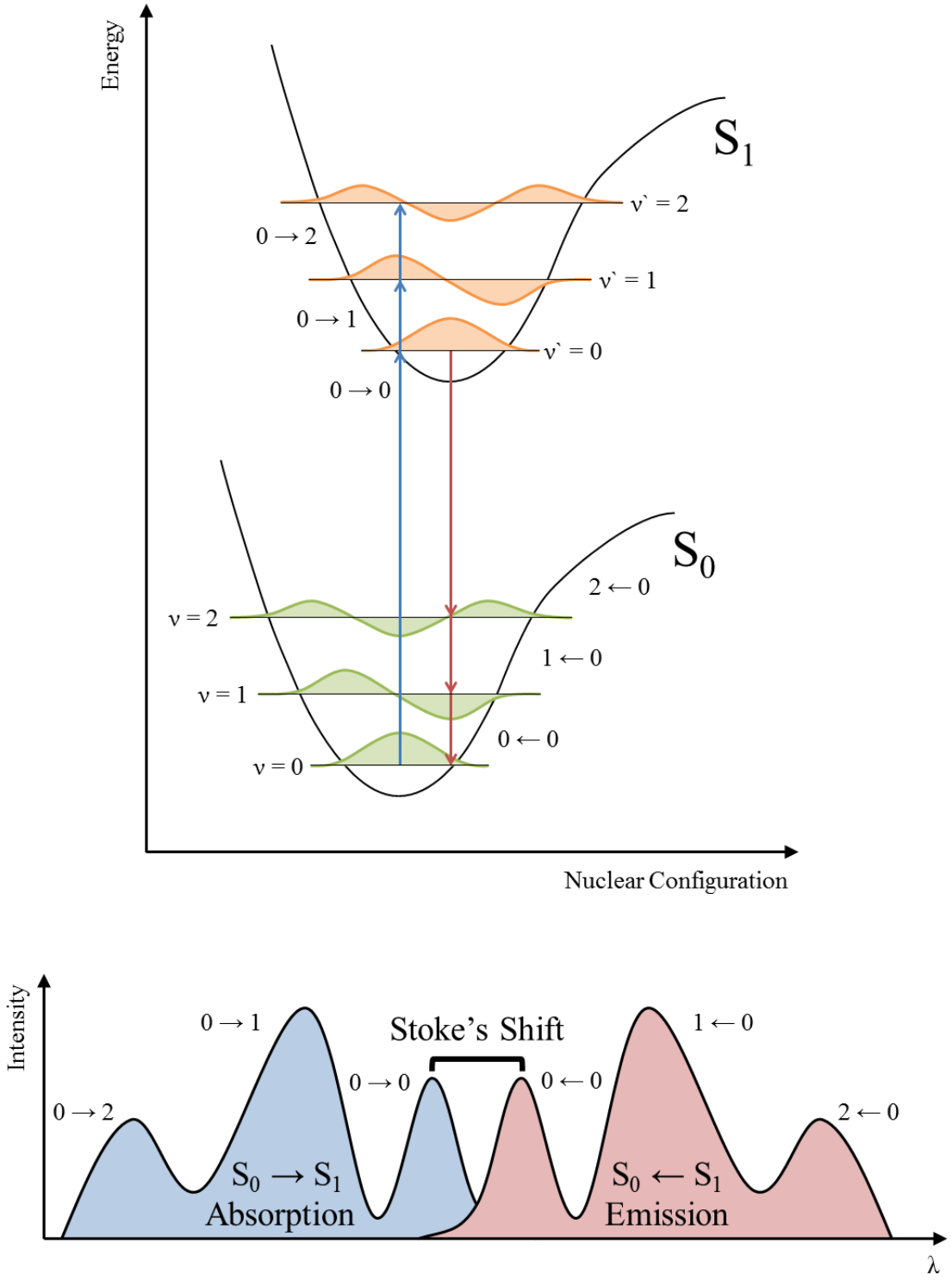

Figure 2.11: *A visual representation of the Frank-Condon Factor for the radiative transitions between the ground state (S_0) and the first excited state (S_1) of a conjugated polymer. It can be seen that for these transitions there is a significant overlap between the two nuclear configurations. The blue arrows represent the absorption of a photon from the zero phonon, or ground vibration, level (v = 0) of the ground state to the different vibrational levels (v` = 0, 1, 2) of the excited state. After the photon is absorbed it relaxes to the v` = 0 level of the excited state, in accordance with Kasha's Rule, where emission to the vibrational levels of the ground state occurs, represented by the red arrow. This produces an emission spectrum (red plot) that is a mirror image of the absorption spectra (blue plot) which is offset by the Stoke's shift between the 0→0 and 0←0 peaks, which is the result of Kasha's Rule. The intensities of the different peaks are governed by the overlap of the wavefunctions of the S_0 and S_1 states, represented here as the green (S_0) and orange (S_1) plots. As can be seen above, the 0→1 and 1←0 transitions have the largest overlap, followed by the 0→0 and 0←0 and finally the 0→2 and 2←0. This overlap depends both on the nuclear configurations and the different wavefunctions in question, as discussed in Equation 2.3.*

electron is promoted into a higher electronic state, e.g. S_2, or a higher vibrational mode of an excited state, it relaxes back to the lowest mode of the first excited state again through internal conversion and vibrational relaxation. The electron can then decay from the first excited state to the manifolds of the ground state by emitting a photon. This is the fluorescence pathway. The relaxation and conversion processes usually have a much lower lifetime than the fluorescence process and so all emissions originate from the lowest excited state. This is called Kasha's Rule [23]. Internal conversion involves the loss of energy in the form of heat. This means that the photon that is emitted has less energy than the photon that was originally absorbed. This results in the emission peak being shifted with respect to the absorbance peak for a fluorescence spectrum. The difference in wavelength between the peaks is called the Stokes Shift [24] and it is proportional to the number of vibrational quanta lost, or how much geometric relaxation occurs upon excitation.

The electron can instead undergo inter-system crossing, and be transferred to the triplet state where phosphorescence takes place. For a transition from the excited triplet state back down to the ground singlet to occur there would need to be a change in the total spin of the system, which is forbidden as discussed in 2.4.1). This process, therefore, has a substantially longer lifetime than fluorescence as the triplets rarely decay radiatively. This means that phosphorescent materials can still emit light even after the initial source of excitation is removed, sometimes for seconds, minutes or even hours, unlike fluorescent materials which typically last for just nanoseconds [25].

The triplet level is lower in energy than the singlet level due to the exchange energy between the hole and electron in the formed exciton. As these two fermions are in close proximity to each other, with their wavefunctions overlapping, a new exchange interaction term is introduced. This term is related to the Pauli Exclusion Principle and the result is that singlet excitons must have symmetric spatial wavefunctions whilst triplet excitons must have

anti-symmetric wavefunctions. This means the triplet state is lower in energy because the repulsion between the fermions is reduced. In practical terms this results in the triplet state being lower in energy than the singlet by approximately 0.7 eV [26], as well as the triplet state having a substantially longer lifetime than the singlet state.

2.4.4). Enabling Phosphorescent Emission:

When forming the four excited states by charge recombination, as discussed in 2.3.1), each of them has an equal probability of being formed. There is a 25% chance of forming a singlet state and a 75% chance of forming a triplet state. Due to the selection rules mentioned earlier, it is predicted that only the singlets would emit light, resulting in the loss of 75% of the formed excitons. This limits the internal quantum efficiency to 25% and further restricts the maximum external quantum efficiency (E.Q.E.) to just 5% [27] when only singlet states are used. It is, however, possible to dope the material with a phosphorescent emitter. This dopant can harvest all of the four possible excitons via energy transfer, meaning that both the singlets and the triplets can now emit radiatively [28].

This dopant often takes the form of an organometallic complex with a heavy metal ion centre, such as iridium. These complexes possess a high angular momentum, causing a strong spin-orbit coupling which in turn mixes the characters of the triplet and singlet states. This allows inter-system crossing to occur between the two more readily [29, 30]. The assumptions made in 2.4.1), from the Born-Oppenheimer approximation, to determine the selection rules, did not account for the total angular momentum of the system, so the previously forbidden transitions are actually more probable.

It is also possible for the organometallic compounds to form their own excited states when the ligands and metal atoms exchange charge carriers. These are metal to ligand charge transfer (MLCT) and ligand to metal charge transfer (LMCT) states [31]. Emissions from

these complexes are frequently due to mixtures of these two states. It is also possible to increase the dopant efficiency by producing stronger MLCT states. This has the effect of increasing the overlap between the singlet and triplet states making transitions more probable. Using these dopants to produce electrophosphorescent OLEDs, it is theoretically possible to attain internal quantum efficiencies of 100% [28, 32, 33].

These theoretical values of 100% do not transfer over to the E.Q.E. of the OLED device. There are several factors, such as internal reflection and reabsorption, which result in the E.Q.E. being considerably lower than 100%. It is also possible for quenching of the triplet states to occur in the presence of other molecules, such as oxygen, or even for them to be self-quenched. The mechanisms of quenching and energy transfer will be discussed in more detail in the next section 2.5).

2.5). Energy Transfer:

2.5.1). Quenching:

There are a number of different mechanisms by which quenching can occur within a sample. These mechanisms involve the radiative or non-radiative transfer of energy or an electron from a donor (a molecule in an excited state) to an acceptor (usually a molecule in the ground state). The simplest of these mechanisms is probably the reabsorption of a photon, produced by an excited donor, by an acceptor. It is possible for this to occur over infinite distances [20].

Another relatively simple quenching mechanism is singlet-singlet annihilation. This is only relevant when significant populations of excited singlets have been generated, such as at high voltages or when subjected to intense laser excitation. This occurs when two excited singlet states collide, and results in the creation of a ground state singlet and a higher energy

excited singlet. This is an example of dynamic quenching where the lifetime and the intensity of the emission is reduced due to a depopulation of the excited state. There is also static quenching, where the lifetime of emission is unaffected. This is because static quenching occurs when ground state molecules form complexes that can no longer be excited, therefore only the intensity of light produced is quenched [25].

There is also triplet-triplet annihilation (TTA) to consider, which is more complex than singlet-singlet annihilation. As mentioned earlier in 2.3.1), there are three different triplet states. This leads to three different possible outcomes when annihilation occurs. The first case results in the conversion of two triplets to one triplet and a ground state singlet, removing a potential emitter. The second case results in the formation of a quintet, however this is still unobserved so far. The third case results in either the formation of two ground state singlets or a ground state singlet and an excited singlet. It is this case, also known as triplet fusion, which results in the observation of p-typed delayed fluorescence. The types of delayed fluorescence are discussed in more detail below. This increases the maximum E.Q.E. from the 5% mentioned in 2.4.4) to 12.5% after the different losses and gains from TTA are all accounted for [34].

There is another type of delayed fluorescence that can occur, namely e-type; this is observed when the triplet state converts back to the S_1 state by reverse intersystem crossing caused by absorbed thermal energy. This is also known as thermally activated delayed fluorescence (TADF) and has recently been used to increase OLED performance [35-37]. The exact mechanisms involved in using TADF in OLED devices are currently not clearly defined but E.Q.E.'s of greater than 14% have been achieved [38]. It is possible to tell the two types of delayed fluorescence apart by their lifetimes. E-type has a lifetime on the order of the phosphorescent lifetime, whereas p-type has a lifetime of approximately half the phosphorescent lifetime. The names p-type and e-type have their origins in the chemicals for

which these effects were first observed. The chemical pyrene gives its name to p-type delayed fluorescence, whilst e-type gets its name from the chemical eosin.

2.5.2). Förster Resonant Energy Transfer:

Förster Resonant Energy Transfer [25, 39] (FRET) is the result of dipole-dipole interactions between the donor and acceptor molecules. The motion of the electrons on the donor can cause perturbations in the motion of the electrons on the acceptor, and if these electron oscillations reach resonance then energy transfer can occur. For FRET to occur a number of conditions must first be satisfied. These conditions include no change of spin between donor and acceptor, and that their dipoles must have a significant parallel component with respect to one another. The other major requirement for FRET is that there must be an overlap between the absorption spectrum of the acceptor and the emission spectrum of the donor. This overlap is described in Equation 2.6 by the overlap integral, J, where F_D is the emission spectrum of the donor, or how much light is emitted by the donor at a particular wavelength, and ε_A represents the acceptor's molar absorptivity, the measure of how much light of a particular wavelength is absorbed:

$$J(\lambda) = \frac{\int_0^\infty F_D(\lambda)\varepsilon_A(\lambda)\lambda^4 d\lambda}{\int_0^\infty F_D d\lambda} \tag{2.6}$$

Equations 2.7 and 2.8 then relate the overlap integral to the lifetime of the donor, τ_D, the rate of FRET, k_{FRET}, and the Förster radius, R_0:

$$R_0 = 0.211[\kappa^2 n^{-4} \Phi_D J(\lambda)]^{\frac{1}{6}} \tag{2.7}$$

Where κ is the orientation factor, n is the refractive index and Φ_D is the quantum yield of the donor.

$$k_{FRET} = \frac{1}{\tau_D}\left(\frac{R_0}{R}\right)^6 \quad (2.8)$$

Where R is the distance between the donor and acceptor, this can be a reasonably large length scale. If the rate of FRET is similar to, or larger than, the rate of decay of the donor then FRET can be a major source of quenching and energy transfer.

2.5.3). Dexter Electron Transfer:

This is where there is an exchange of electrons between the donor and the acceptor which leaves the donor in the ground state. This is a short range interaction [40] which depends exponentially on the separation between the donor and acceptor as well as the spectral overlap. This necessitates close contact between the donor and acceptor in order to compete with other methods of energy transfer. The rate constant [25] for Dexter Electron Transfer, k_{DET}, is given by Equation 2.9:

$$k_{DET} = k_0 e^{-\frac{2R_{DA}}{L}} \quad (2.9)$$

Where k_0 is the overlap integral, R_{DA} is the distance between the donor and acceptor and L is the sum of their van der Waals radii.

As well as close contact being required for electron transfer to occur, the system must also obey the Wigner Spin Selection Rules [20]. This states that there is correlation between the angular momentum of the electron spin for the reacting donors and acceptors, and the angular momentum of the electron spin for the products. If they are fully correlated then the transition is allowed, if they are partially correlated the transition is spin restricted, and if there is no correlation the transition is spin forbidden.

A good example of this is how excited states can be efficiently quenched by oxygen. O_2 can quench both the triplet and singlet excited states formed by organic molecules [20,

25]. This type of quenching both lowers the intensities produced and decreases the lifetime, and is another example of dynamic quenching. For excited singlets, O_2 converts them into triplets using the reaction ${}^1M + {}^3O_2 \rightarrow {}^3M + {}^1O_2$. This is a spin allowed process. For the triplets, O_2 causes triplet-triplet energy transfer using the reaction ${}^3M + {}^3O_2 \rightarrow {}^1M + {}^1O_2$. This is a spin restricted process and so it occurs less frequently.

2.6). Device Materials and Considerations:

2.6.1). Electrodes:

The materials with which OLED devices are manufactured are vital to their performance. Each of the constituent materials is selected to maximise device performance by meeting certain requirements, as described in 2.1). This process starts with the electrodes, which form the outermost layers of the device.

The work function of the cathode should be matched as closely as possible to that of the emissive layer adjacent to it, so that electron injection is maximised [41]. This means that a low work function is required, so materials such as barium or lithium fluoride are commonly used. Unfortunately a lot of the best cathode materials, such as barium, are highly reactive and need to be capped by a less reactive material to prevent oxidation. Aluminium is the metal which is commonly used as the capping layer, but it cannot directly replace either barium or lithium fluoride as its work function will not be as good a match.

In contrast to the cathode, the anode needs to have a high work function to facilitate the injection of holes into the conductive layer adjacent to the anode [42]. In addition to a high work function, the anode also needs to be transparent so that any light generated by the device can escape. Therefore, a Transparent Conductive Oxide (TCO) is commonly used as an anode. These materials are engineered to have a bandgap which is much higher than the

energy of photons found within the visible spectrum, 380 to 750 nm [43]. This means that the oxide does not absorb the light produced by the OLED as discussed in 2.4.1). The most established of these TCOs is Indium Tin Oxide (ITO), which is both conductive and transparent, but alternatives are highly desired and the subject of current research.

2.6.2). PEDOT:

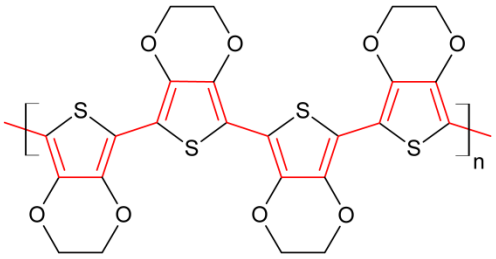

Figure 2.12: *The chemical structure of the conjugated polymer PEDOT. The conjugated backbone of the polymer is highlighted in red.*

Generally, for solution processed OLEDs at least, there is a layer of poly(3,4-ethylenedioxythiophene) (PEDOT) directly on top of the ITO anode; this corresponds to the conductive layer mentioned in 2.1), and is also known as the hole injection layer (HIL). The structure of PEDOT can be seen in Figure 2.12. PEDOT is a conjugated polymer able to transport holes effectively, with a number of other properties that make it suitable for use in OLED devices. These include high transparency and high stability; exposure to temperatures of 100 °C in air for 1000 hours has little effect on the polymer's conductivity [44]. The work function of PEDOT is tuneable, and relatively close to that of ITO, easing the injection of holes into subsequent organic layers by providing an intermediate step in potential barrier. It also planarizes the ITO surface, which prevents large spikes of ITO causing high voltages, or shorts, within the device.

Unfortunately, PEDOT by itself is relatively insoluble, making the solution processing of it difficult. This problem can be rectified by doping PEDOT with poly(styrene sulfonate) (PSS) which renders it water soluble. This is the most popular form of PEDOT

used in OLEDs but it does have an effect on some of the properties. The absorbance of the polymer is increased to 20 % in the visible spectrum, and the conductivity decreased to around 10 S/cm [45]. Fortunately, the conductivity can be improved again by post-treating the PEDOT with various chemicals after depositing. These chemicals include acids, salts, zwitterions and several others. Using post-treatment methods involving sulphuric acid conductivity values of over 3000 S/cm have been reported [46].

Table 2.2: *This table gives the properties of different commercially available PEDOTs, some of which were used to manufacture devices during this project. Properties include resistivity, work function, viscosity, pH, solid content, solvent, composition and potential applications.*

	Application	PEDOT : PSS (by weight)	Solvent	Resistivity (Ohm.cm)	Viscosity at 700 S^{-1} [mPas]	pH	Solid Content [%]	Work Function [eV]
CLEVIOS™ P Al 4083	Buffer Layer (low ohmic)	1:6	Water	500-5000	5-12	~1.7	1.3-1.7	5.0-5.2
CLEVIOS™ P JET	Buffer Layer (by Ink-Jet deposition)	1:6	Water	500-5000	5-11	~1.7	1.2-1.4	5.0-5.2
CLEVIOS™ P CH 8000	Buffer Layer (high ohmic)	1:20	Water	100000-300000	9-20	~1.5	2.5-3.0	5.0-5.2
CLEVIOS™ P HIL 1	Buffer Layer (low ohmic)	Composition not disclosed	Water-Alcohol	10-100	5-15	~2.2	1.2-1.6	5.4-5.9
CLEVIOS™ P HIL 1.3	Buffer Layer (low ohmic)	Composition not disclosed	Water-Alcohol	1000-10000	3-12	~1.6	2.8-3.2	5.4-5.9
CLEVIOS™ P HIL 1.5	Buffer Layer (high ohmic)	Composition not disclosed	Water-Alcohol	100000-1000000	3-12	~1.6	3.2-3.6	5.4-5.9

There are several variations of PEDOT commercially available, the properties of which are detailed in Table 2.2. This table was taken from the primary manufacturer of PEDOT, Heraeus, and highlights the range of different conductivities and work functions available [47, 48]. These properties can have a substantial effect on OLED characteristics such as efficiency, brightness and turn on voltage [49].

2.6.3). Host Materials:

For solution processed OLEDs, on top of the HIL layer of PEDOT is the emissive layer. At its simplest, this takes the form of a polymer that is emissive and conducts both holes and electrons. Polymer based OLED devices are also known as Polymer Light Emitting Devices (PLEDs). There are a large number of PLED polymer hosts currently available, but,

of the commercially available ones, this thesis focuses primarily upon poly(n-vinylcarbazole) (PVK) based devices.

PVK is available in a selection of different molecular weights, commonly ranging from 40,000 to 1,100,000 in atomic units [50]. As can be seen in Figure 2.13, PVK is not conjugated along its backbone; it does, however, still behave as an effective hole transporter. Exciton formation is limited in PVK, as electrons cannot flow along the polymer backbone. Nevertheless, as the carbazole groups are conjugated, they can be stacked to form excimers [51]. The singlet versions of the excimers emit at both 380 nm and 420 nm, due to different stacking configurations available, whilst the 0-0 triple state emits at 431 nm [52, 53].

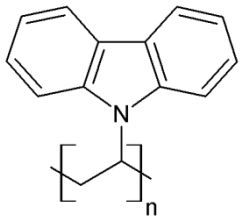

Figure 2.13: *The chemical structure of the polymer PVK. There is no alternating structure of single and double bonds along the polymer backbone so this polymer is non-conjugated.*

Due to the poor electron transporting properties of PVK, it is usually blended with a separate electron transporter; a couple of which will be discussed further in 2.6.4). PVK also acts as an excellent host medium for different heavy metal based dopants, due to its high triplet level of 2.88 eV [53]. This allows the non-emissive triplet states generated to be harvested, increasing device efficiency. Unfortunately, PVK also features dimer triplet state traps, whose energies allow them to quench blue dopants, providing motivation for the discovery of new host materials. Doping with both transporters and emitters can substantially increase OLED efficiency and brightness, in addition to being able to tune the colour emitted. A selection of transport molecules and different colour phosphorescent dopants are discussed further in 2.6.4) and 2.6.5).

2.6.4). Transport Materials:

As mentioned in 2.6.3), it is possible to combine transport molecules with the host polymer in order to improve its carrier mobilities. In addition to modifying the carrier mobilities within the emissive layer, the addition of transport molecules can provide intermediate energy level steps between host and dopant HOMO or LUMO levels, aiding

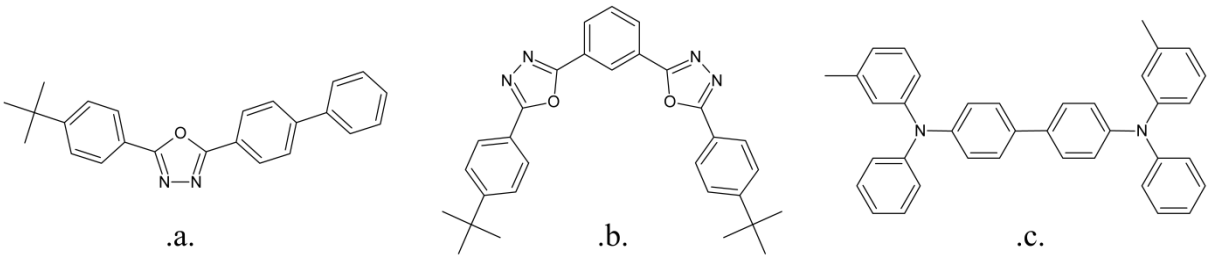

Figure 2.14: *The chemical structures of two electron transporters and one hole transporter used in this thesis. The structure of the electron transporter PBD is shown in .a. The structure of the electron transporter OXD-7 is shown in .b. The structure of the hole transporter TPD is shown in .c.*

charge transfer. Some of the transport molecules used in this thesis, and their properties, will be discussed below.

2-(4-Biphenyl)-5-(4-tert-butylphenyl)-1,2,4-oxadiazole (PBD) is a common electron transporter used in OLED devices [54]. It has an electron mobility of 1.9×10^{-5} $cm^2.V^{-1}.s^{-1}$ [55]. The structure of PBD can be seen in part .a. of Figure 2.14. When paired with the poor electron transporting host PVK, it can result in increased device performance. It is possible for an exciplex to be formed between the oxadiazole group on PBD and the carbazole group on PVK. The resultant emission from this exciplex is red-shifted [56] with respect to the undoped PVK emission. This can cause problems for OLED devices with heavy metal dopants by reducing energy transfer between this exciplex and the dopant by shifting their energy levels.

Another common electron transporting molecule is 1,3,4-oxadiazole,2,2'-(1,3-phenylene)bis[5-[4-(1,1-dimethylethyl)phenyl] (OXD-7), the structure of which can be seen in part .b. of Figure 2.14. It has an electron mobility of 2.1×10^{-5} $cm^2.V^{-1}.s^{-1}$ [55]. This

molecule is similar to PBD but it has different HOMO and LUMO levels, which can make it suitable for a different range of dopant materials, including red and blue dopants.

N,N'-Bis(3-methylphenyl)-N,N'-diphenylbenzidine (TPD) is a hole transporter, the structure of which can be seen in part .c. of Figure 2.14. It has a hole mobility of between 1 $x10^{-4}$ and $1x10^{-3}$ $cm^2.V^{-1}.s^{-1}$ [57]. It can be added to PVK both to help boost hole transportation and to modify the device energy levels, this can again have either a positive or a negative effect as discussed earlier. Once a threshold concentration of TPD in PVK is reached, it has been shown that it is solely responsible for hole transportation [58].

2.6.5). Dopant materials:

As was discussed earlier in in 2.4.4), it is possible for 100% of excitons formed by recombination to decay radiatively when doped by a heavy metal based, phosphorescent material [28]. These dopants mix the character of the singlet and triplet states due to the spin-orbit coupling of the heavy metal centre, allowing intersystem crossing to occur more readily. For these reasons host polymers are often doped with organometallic complexes in order to improve efficiency.

These dopants can be colour tuned depending on the ligands attached to the metal ion, which is usually iridium. By varying the electron withdrawing, or electron donating, properties of the ligands the HOMO and LUMO of the dopants can be changed, altering its absorption and emission profile. The ability to make relatively simple chemical changes to a parent complex, such as tris[2-phenylpyridinato-C2,N] iridium(III) ($Ir(ppy)_3$), in order to yield different emission profiles is important commercially. When these dopants have analogous syntheses it makes their production much more cost and time effective, rather than making each different colour individually. Three different colours of iridium based dopants with different ligands will be discussed further in this section.

$Ir(ppy)_3$ is a green phosphorescent material [33], the structure of which can be seen in part .a. of Figure 2.15, and is commonly used as a dopant in OLED devices. Usually the triplet lifetime is substantially longer than that of the singlet decay, which can form an obstacle in the electrophosphorescent process. Fortunately, $Ir(ppy)_3$ has a relatively short

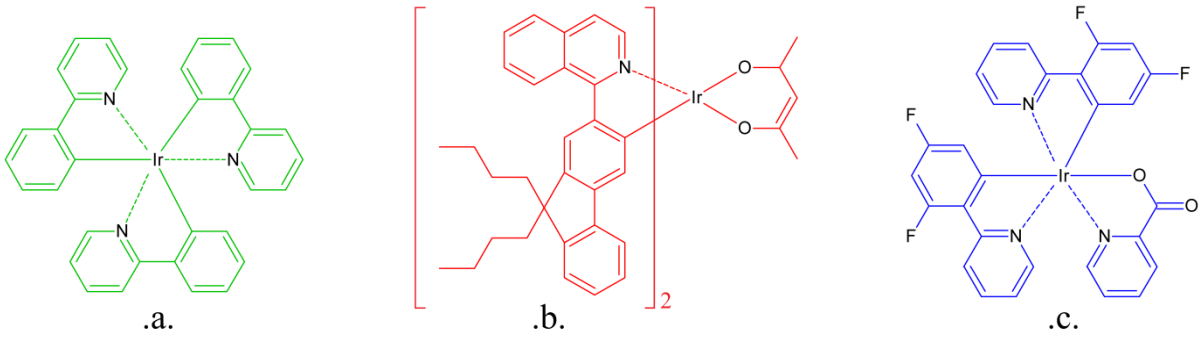

Figure 2.15: *The chemical structures of three different phosphorescent dopants used in this thesis. The structure of the green emitting dopant $Ir(ppy)_3$ is shown in .a. The structure of the red emitting dopant DBFIr is shown in .b. The structure of the blue emitting dopant FIrpic is shown in .c.*

triplet lifetime, at approximately 1 µs, alleviating this problem and making it an excellent choice of dopant material.

Bis(2-(9,9-dibutylfluorenyl)-1-isoquinoline(acetylacetonate)iridium (DBFIr), is a red phosphorescent material [59]. It keeps the same iridium heavy metal centre and octahedral geometry with three bidentate ligands. These ligands are, however, substantially different to those of $Ir(ppy)_3$, resulting in it being a red emitter. The structure of this dopant can be seen in part .b. of Figure 2.15.

Bis(4,6-difluorophenylpyridinato-N,C2)picolinatoiridium (FIrpic) is also a commonly used commercial blue phosphorescent material. This organometallic complex again has an iridium centre and an octahedral geometry with three bidentate ligands. These ligands are relatively similar to those of $Ir(ppy)_3$, and yet produce a blue emitter due to the strong electron withdrawing influence of the fluorine atoms. It also has a phosphorescent lifetime of approximately 1 µs, which is similar to that of $Ir(ppy)_3$ [60]. The structure of this dopant can be seen in part .c. of Figure 2.15.

2.6.6). Device Considerations:

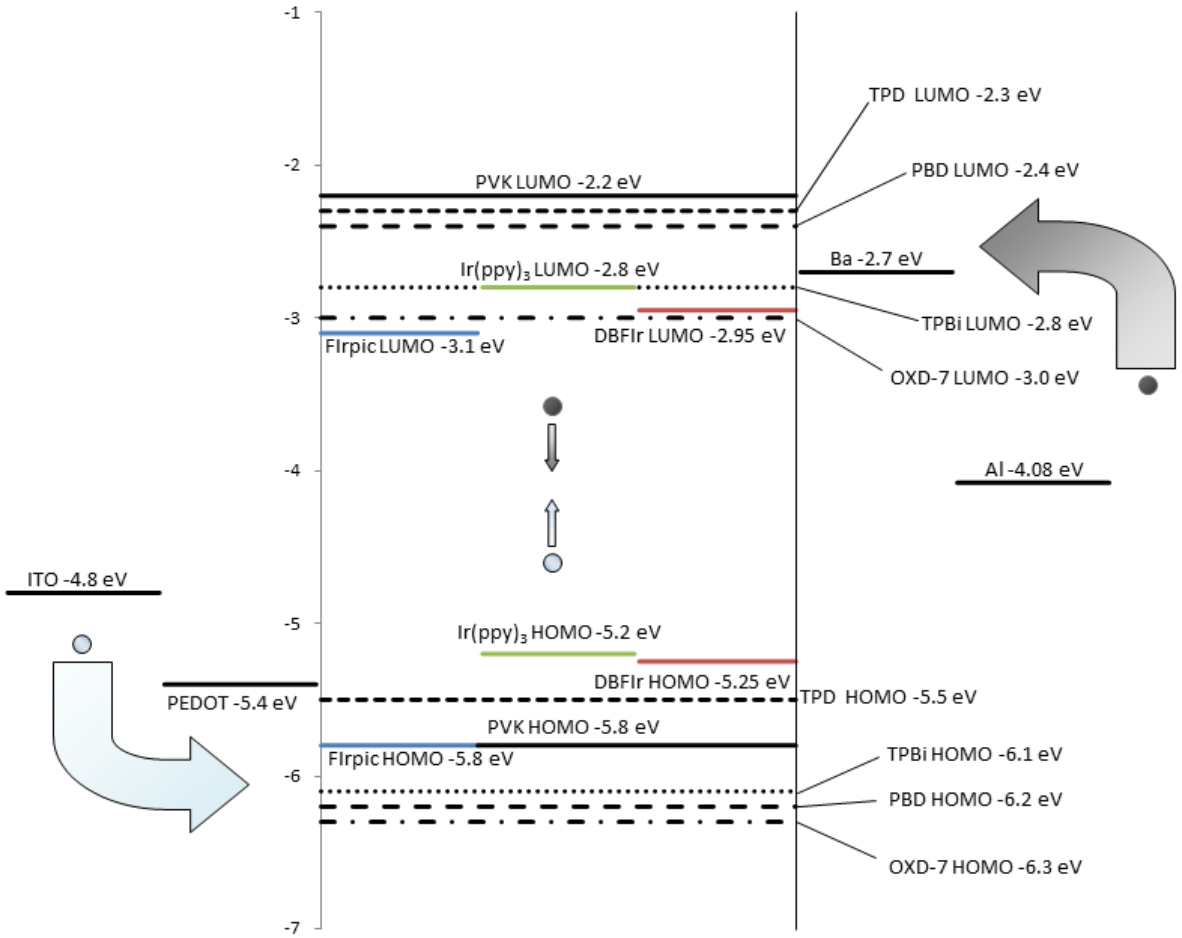

Figure 2.16: *The energy levels of several materials commonly featured in OLED devices. It should be noted how the work functions of barium and PEDOT form intermediate steps for electron and hole injection.*

The individual properties of several common OLED materials have been discussed in detail already in this section. When producing OLED devices it is important to take into account the relative properties of all the materials involved to make sure that they are appropriately matched. Energy levels must be well matched in order to aid both charge transfer between host, transporters and dopants, and charge injection from the electrodes. A visual representation of the different energy levels for all of the compounds detailed earlier can be found in Figure 2.16, and forms a helpful reference when designing OLED devices [48, 61-69]. Another concern is to balance the charge transporting abilities of the constituents to ensure that most of the exciton formation occurs in the emissive layer in order to maximise efficiency.

Holes are injected from the ITO anode on the left side of Figure 2.16, and they remain in the HOMOs of the materials until recombination occurs. Meanwhile, electrons are injected from the cathode and remain in the LUMOs of the materials. It is easy to see in Figure 2.16 that both PEDOT and barium provide intermediate steps in work function between the electrodes and the emissive layer in the middle. Upon reaching the emissive layer, the holes are primarily injected into the PVK HOMO and electrons are primarily injected into the PVK LUMO. From here, the excitations can be transferred from the host, or donor, in this case PVK, to the acceptors via Förster transfer, Dexter transfer and charge trapping [70, 71]. Charge trapping is most accessible when the HOMO of the acceptor is above that of the donor and when the LUMO of the acceptor is below that of the donor.

As mentioned in 2.1), it is possible to use multiple layers in addition to the conductive and emissive layers detailed so far. Blocking layers can be deposited either side of the emissive layers to stop charge carriers from leaving the emissive layer. This can be achieved by using energy levels, conductivities, or both to create an unfavourable barrier preventing its passage. For example in the earlier scheme, an additional layer of undoped PVK between the PEDOT and emissive layer would block electrons due to its poor electron mobility [72]. On the other side, a layer of 1,3,5-tris(N-phenylbenzimidazole-2-yl)benzene (TPBi) could be evaporated between the emissive and the barium layers to block holes and aid electron injection [73]. As TPBi is a poor hole transporter, and its HOMO is below that of PVK, it makes the transfer of holes to it improbable. TPBi will be discussed in more detail in both Chapter 6 and Chapter 7.

When considering candidates for additional layers within solution processed devices, their solubility in different solvents must also be considered. Ideally adjacent layers should be deposited using orthogonal solvents so that the layer underneath is not affected by the new layer being deposited.

References:

1. Z. Li and H. Meng, *Organic Light-Emitting Materials and Devices, 1st Edition*. CRC Press, 2006.
2. A.P. Kulkarni, et al., *Electron transport materials for organic light-emitting diodes.* Chemistry of Materials, 2004. **16**(23): p. 4556-4573.
3. Q.L. Huang, et al., *Covalently bound hole-injecting nanostructures. Systematics of molecular architecture, thickness, saturation, and electron-blocking characteristics on organic light-emitting diode luminance, turn-on voltage, and quantum efficiency.* Journal of the American Chemical Society, 2005. **127**(29): p. 10227-10242.
4. R. Meerheim, B. Lussem, and K. Leo, *Efficiency and Stability of p-i-n Type Organic Light Emitting Diodes for Display and Lighting Applications*. Proceedings of the Ieee, 2009. **97**(9): p. 1606-1626.
5. C.W. Tang and S.A. Vanslyke, *Organic Electroluminescent Diodes.* Applied Physics Letters, 1987. **51**(12): p. 913-915.
6. J.H. Burroughes, et al., *Light-Emitting-Diodes Based on Conjugated Polymers.* Nature, 1990. **347**(6293): p. 539-541.
7. T.R. Hebner, et al., *Ink-jet printing of doped polymers for organic light emitting devices.* Applied Physics Letters, 1998. **72**(5): p. 519-521.
8. C.E. Housecroft and E.C. Constable, *Chemistry, 4th Edition*. Prentice Hall, 2009.
9. I. Fleming, *Molecular Orbitals and Organic Chemical Reactions, Student Edition*. Wiley, 2011.
10. S.C. Roth, D, *One-Dimensional Metals: Conjugated Polymers, Organic Crystals, Carbon Nanotubes, 2nd Edition*. Wiley VCH, 2004.
11. G. Tzamalis, et al., *Doping-dependent studies of the Anderson-Mott localization in polyaniline at the metal-insulator boundary.* Physical Review B, 2002. **66**(8).
12. W. Barford, *Electronic and Optical Properties of Conjugated Polymers, 2nd Edition*. Oxford University Press, 2013.
13. X. Zhu and A. Kahn, *Electronic Structure and Dynamics at Organic Donor/Acceptor Interfaces.* Mrs Bulletin, 2010. **35**(6): p. 443-448.
14. M. Pope and C.E. Swenberg, *Electronic Processes in Organic Crystals and Polymers, 2nd Edition*. Oxford University Press, 1999.
15. J.B. Birks, *Excimers and Exciplexes.* Nature, 1967. **214**(5094): p. 1187-&.
16. J.B. Birks, *Excimers.* Reports on Progress in Physics, 1975. **38**(8): p. 903-974.
17. D. Hertel and H. Baessler, *Photoconduction in amorphous organic solids.* Chemphyschem, 2008. **9**(5): p. 666-688.
18. C. Deibel, et al., *Energetics of excited states in the conjugated polymer poly(3-hexylthiophene).* Physical Review B, 2010. **81**(8).
19. D. Frackowiak, *The Jablonski Diagram.* Journal of Photochemistry and Photobiology B-Biology, 1988. **2**(3): p. 399-408.
20. A. Beeby, *Photochemistry*, 2009.

21. N.J. Turro, *Modern Molecular Photochemistry, New Edition*. University Science Books, 1991.

22. C. Rulliere, *Femtosecond Laser Pulses, 2nd Edition*. Springer, 2004.

23. M. Kasha, *Characterization of Electronic Transitions in Complex Molecules.* Discussions of the Faraday Society, 1950(9): p. 14-19.

24. J.R. Albani, *Structure and dynamics of macromolecules : absorption and fluorescence studies, 1st Edition*. Elsevier, 2004.

25. F. Dias, *Optical Spectroscopy*, 2011.

26. A. Kohler and D. Beljonne, *The singlet-triplet exchange energy in conjugated polymers.* Advanced Functional Materials, 2004. **14**(1): p. 11-18.

27. D.Y. Kondakov, *Characterization of triplet-triplet annihilation in organic light-emitting diodes based on anthracene derivatives.* Journal of Applied Physics, 2007. **102**(11).

28. M.A. Baldo, et al., *Highly efficient phosphorescent emission from organic electroluminescent devices.* Nature, 1998. **395**(6698): p. 151-154.

29. H.A. Al Attar and A.P. Monkman, *Dopant effect on the charge injection, transport, and device efficiency of an electrophosphorescent polymeric light-emitting device.* Advanced Functional Materials, 2006. **16**(17): p. 2231-2242.

30. A.P. Monkman, et al., *The use of substituted iridium complexes in doped polymer electrophosphorescent devices: The influence of triplet transfer and other factors on enhancing device performance.* Advanced Functional Materials, 2006. **16**(8): p. 1043-1050.

31. P. Atkins, et al., *Shriver and Atkins' Inorganic Chemistry, 5th Edition*. Oxford University Press, 2009.

32. C. Adachi, et al., *Nearly 100% internal phosphorescence efficiency in an organic light-emitting device.* Journal of Applied Physics, 2001. **90**(10): p. 5048-5051.

33. M.A. Baldo, et al., *Very high-efficiency green organic light-emitting devices based on electrophosphorescence.* Applied Physics Letters, 1999. **75**(1): p. 4-6.

34. Y.F. Zhang and S.R. Forrest, *Triplets Contribute to Both an Increase and Loss in Fluorescent Yield in Organic Light Emitting Diodes.* Physical Review Letters, 2012. **108**(26).

35. K. Goushi, et al., *Organic light-emitting diodes employing efficient reverse intersystem crossing for triplet-to-singlet state conversion.* Nature Photonics, 2012. **6**(4): p. 253-258.

36. S.Y. Lee, et al., *High-efficiency organic light-emitting diodes utilizing thermally activated delayed fluorescence from triazine-based donor-acceptor hybrid molecules.* Applied Physics Letters, 2012. **101**(9).

37. H. Uoyama, et al., *Highly efficient organic light-emitting diodes from delayed fluorescence.* Nature, 2012. **492**(7428): p. 234-+.

38. V. Jankus, et al., *Highly Efficient TADF OLEDs: How the Emitter-Host Interaction Controls Both the Excited State Species and Electrical Properties of the Devices to Achieve Near 100% Triplet Harvesting and High Efficiency.* Advanced Functional Materials, 2014. **24**(39): p. 6178-6186.

39. T. Forster, *10th Spiers Memorial Lecture - Transfer Mechanisms of Electronic Excitation.* Discussions of the Faraday Society, 1959(27): p. 7-17.

40. D.L. Dexter, *A Theory of Sensitized Luminescence in Solids.* Journal of Chemical Physics, 1953. **21**(5): p. 836-850.

41. R.H. Friend, et al., *Electroluminescence in conjugated polymers.* Nature, 1999. **397**(6715): p. 121-128.

42. J.S. Kim, et al., *Indium-tin oxide treatments for single- and double-layer polymeric light-emitting diodes: The relation between the anode physical, chemical, and morphological properties and the device performance.* Journal of Applied Physics, 1998. **84**(12): p. 6859-6870.

43. J. Maa, G.S. Herman, and A.T. Voutsas, *Solution process for fabricating a textured transparent conductive oxide (TCO)*, Google Patents, 2013.

44. B.L. Groenendaal, et al., *Poly(3,4-ethylenedioxythiophene) and its derivatives: Past, present, and future.* Advanced Materials, 2000. **12**(7): p. 481-494.

45. Y.H. Ha, et al., *Towards a transparent, highly conductive poly(3,4-ethylenedioxythiophene).* Advanced Functional Materials, 2004. **14**(6): p. 615-622.

46. Y.J. Xia, K. Sun, and J.Y. Ouyang, *Solution-Processed Metallic Conducting Polymer Films as Transparent Electrode of Optoelectronic Devices.* Advanced Materials, 2012. **24**(18): p. 2436-2440.

47. Clevios, *Product information*. 2010 [cited 20/06/11]; Available from: http://www.clevios.com/index.php?page_id=995&prod_service_id=443.

48. Clevios, *OLED Applications*. 2010 [cited 20/06/11]; Available from: http://www.clevios.com/index.php?page_id=3430.

49. J.H. Cook, H.A. Al-Attar, and A.P. Monkman, *Effect of PEDOT-PSS resistivity and work function on PLED performance.* Organic Electronics, 2014. **15**(1): p. 245-250.

50. Sigma-Aldrich, *Search Results: PVK*. 2015 [cited 29/01/15]; Available from: http://www.sigmaaldrich.com/catalog/search?term=pvk&interface=All&N=0&mode=match%20partialmax&lang=en&region=GB&focus=product.

51. G.E. Johnson, *Emission Properties of Vinylcarbazole Polymers.* Journal of Chemical Physics, 1975. **62**(12): p. 4697-4709.

52. L. Qian, D. Bera, and P.H. Holloway, *Electrophosphorescence from triplet excimers in poly-(N-vinylcarbazole).* Applied Physics Letters, 2007. **90**(10).

53. V. Jankus and A.P. Monkman, *Is Poly(vinylcarbazole) a Good Host for Blue Phosphorescent Dopants in PLEDs? Dimer Formation and Their Effects on the Triplet Energy Level of Poly(N-vinylcarbazole) and Poly(N-Ethyl-2-Vinylcarbazole).* Advanced Functional Materials, 2011. **21**(17): p. 3350-3356.

54. X. Gong, et al., *High-efficiency polymer-based electrophosphorescent devices.* Advanced Materials, 2002. **14**(8): p. 581-585.

55. T. Yasuda, et al., *Carrier mobilities in organic electron transport materials determined from space charge limited current.* Japanese Journal of Applied Physics Part 1-Regular Papers Short Notes & Review Papers, 2002. **41**(9): p. 5626-5629.

56. X.Z. Jiang, et al., *Effect of carbazole-oxadiazole excited-state complexes on the efficiency of dye-doped light-emitting diodes.* Journal of Applied Physics, 2002. **91**(10): p. 6717-6724.

57. A. Kuwahara, et al., *Carrier mobility of organic thin films using lateral electrode structure with optical slits.* Applied Physics Letters, 2006. **89**(13).

58. D.M. Pai, J.F. Yanus, and M. Stolka, *Trap-Controlled Hopping Transport.* Journal of Physical Chemistry, 1984. **88**(20): p. 4714-4717.

59. H.H. Liao, et al., *Triplet exciton energy transfer in polyfluorene doped with heavy metal complexes studied using photoluminescence and photoinduced absorption.* Physical Review B, 2006. **74**(24): p. 245211.

60. A.M. Gilmore, *Luminescence: The Instrumental Key to the Future of Nanotechnology, 1st Edition*. CRC Press, 2013.

61. L. Hou, et al., *Efficient single layer solution-processed blue-emitting electrophosphorescent devices based on a small-molecule host.* Applied Physics Letters, 2008. **92**(26).

62. S. Sapp, et al., *Work function and implications of doped poly(3,4-ethylenedioxythiophene)-co-poly(ethylene glycol).* Applied Physics Letters, 2006. **88**(15).

63. B.P. Luther, et al., *Investigation of the mechanism for Ohmic contact formation in Al and Ti/Al contacts to n-type GaN.* Applied Physics Letters, 1997. **70**(1): p. 57-59.

64. Sigma-Aldrich, *Poly(9-vinylcarbazole)*. 2014 [cited 04/12/2014]; Available from: http://www.sigmaaldrich.com/catalog/product/aldrich/182605?lang=en&region=GB.

65. B.D. Chin, *Enhancement of efficiency and stability of phosphorescent OLEDs based on heterostructured light-emitting layers.* Journal of Physics D-Applied Physics, 2011. **44**(11).

66. V. Gupta, et al., *Barium: An Efficient Cathode Layer for Bulk-heterojunction Solar Cells.* Scientific Reports, 2013. **3**.

67. Sigma-Aldrich, *2-(4-Biphenylyl)-5-phenyl-1,3,4-oxadiazole (PBD)*. 2015 [cited 29/01/15]; Available from: http://www.sigmaaldrich.com/catalog/product/aldrich/257850?lang=en&region=GB.

68. Sigma-Aldrich, *N,N'-Bis(3-methylphenyl)-N,N'-diphenylbenzidine (TPD)*. 2015 [cited 29/01/15]; Available from: http://www.sigmaaldrich.com/catalog/product/aldrich/443263?lang=en&region=GB.

69. S.H. Kim, J. Jang, and J.Y. Lee, *Relationship between host energy levels and device performances of phosphorescent organic light-emitting diodes with triplet mixed host emitting structure.* Applied Physics Letters, 2007. **91**(8).

70. X. Gong, et al., *Electrophosphorescence from a polymer guest-host system with an iridium complex as guest: Forster energy transfer and charge trapping.* Advanced Functional Materials, 2003. **13**(6): p. 439-444.

71. B. Mi, et al., *Molecular hosts for triplet emitters in organic light-emitting diodes and the corresponding working principle.* Science China-Chemistry, 2010. **53**(8): p. 1679-1694.

72. H.A. Al-Attar and A.P. Monkman, *Solution processed multilayer polymer light-emitting diodes based on different molecular weight host.* Journal of Applied Physics, 2011. **109**(7).

73. J.H. Cook, et al., *Efficient deep blue fluorescent polymer light-emitting diodes (PLEDs).* Journal of Materials Chemistry C, 2014. **2**(28): p. 5587-5592.

Chapter 3 Experimental:

3.1). Substrate Preparation:

The production of OLED devices starts with the preparation of the substrate. The first step of this process is patterning the Indium Tin Oxide (ITO) anode to the required specifications shown in Figure 3.1, where there are three pairs of parallel stripes of ITO running from top to bottom. Once this is complete, the substrates are cut to size and cleaned leaving them ready to use. The individual steps for these processes are detailed below.

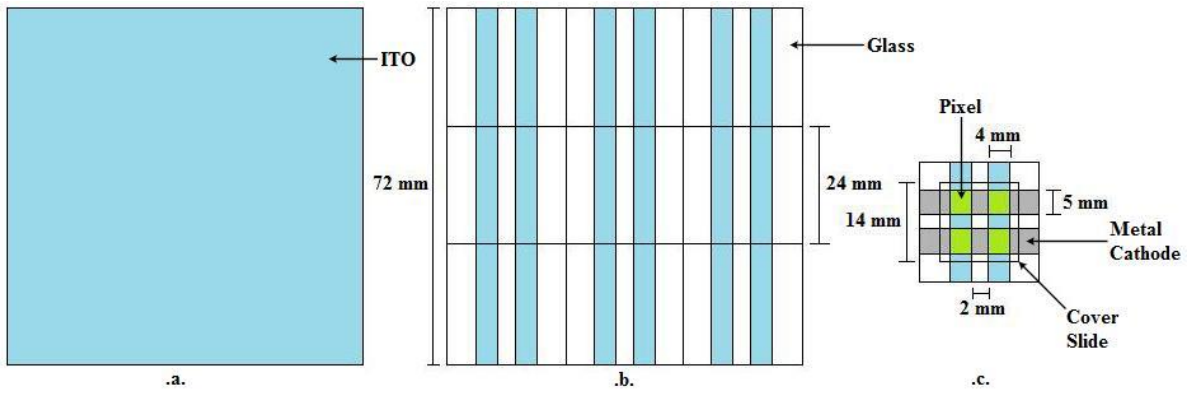

Figure 3.1: *Part .a. of this figure shows the square of ITO covered glass cut down to 7.2 cm by 7.2 cm. Part .b. of this figure shows the patterned square with the parallel strips of ITO running down it. Part .c. of this figure shows the finished device, complete with metal cathode perpendicular to the ITO and the encapsulating cover slide.*

3.1.1). ITO Patterning:

A square sheet of glass (7.2 x 7.2 cm) with a coating of ITO (150 nm, 15 Ω/□) is patterned using photolithography. Photolithography is a fabrication process on the nano, or micro scale, which uses light to transfer a geometric pattern onto a substrate. This is achieved using a photoresist, a chemical that is sensitive to light but resistant to other chemical treatment, and a mask. There are two types of resist; positive, where the exposed resist becomes more soluble; and negative, where the exposed resist becomes less soluble. Exposure to ultraviolet (UV) light breaks bonds in the polymer chain of positive resists converting it into a series of smaller polymer blocks that are more soluble. For negative

resists, exposure to UV light causes crosslinking to occur between polymer chains converting it into a larger polymer that substantially reduces its solubility. Positive resists offer higher resolutions and better process controllability for small geometry features than negative resists. This is because of the solvent induced swelling of the exposed long polymer strands in negative resists when developed, which can impact upon small features. Negative resists are however substantially less expensive and provide superior chemical resistance for use as masks, so the photoresist used depends upon the situation [1]. After exposure, the undesired resist is removed using a developer solution. This leaves areas of the surface unprotected for further processes, like acid etching, to occur. In this case, a positive resist is used to remove ITO from the surface of the glass substrate, the steps of which are detailed below:

1. Spincoat Microposit S1813 on to the ITO side of the square at 500 rpm for five seconds then at 3700 rpm for thirty seconds.
2. Place on a hotplate heated to 95°C for three minutes in order to bake out any remaining moisture.
3. Place the substrate on to a black surface and position a shadow mask on top of it.
4. Expose to UV light for fifty seconds causing the exposed areas to react.
5. Remove the reacted photoresist by immersion in a solution of Microposit 351 Developer and deionised water (1:2 ratio) for thirty seconds then wash in deionised water.
6. Dry with nitrogen and place on a hotplate heated to 95°C for fifteen minutes.
7. Remove excess resist from edges and corners with an acetone soaked cotton bud. This is especially pertinent between the parallel strips of resist to prevent crosstalk.
8. Submerge in a solution of hydrochloric acid (36%) and nitric acid (70%) (20:1 ratio) for five minutes; this removes the ITO not covered by resist from the surface of the glass substrate.
9. Wash with deionised water and remove the last of the resist with acetone.

3.1.2). Substrate Cleaning:

Before cleaning the patterned square of glass is cut into nine smaller squares of dimensions 2.4 x 2.4 cm, the method of which will not be discussed here. The smaller squares are then cleaned using the following steps:

1. Clean the substrates crudely with a cleanroom wipe and both acetone and isopropanol to remove the marks made by the pen used whilst cutting the glass.
2. Place the substrates in a slotted container with the ITO side all facing the same direction.
3. Clean the substrates sequentially with acetone, isopropanol and acetone again in an Ultrawave U50 sonic bath for nine minutes for each wash.
4. Withdraw the substrates from the container with tweezers and dry with nitrogen.
5. Clean with plasma in an Electronic Diener Femto cleaner for three minutes. The plasma cleaner can be seen at the bottom of Figure 3.2.
6. Finally the substrates are exposed to both UV light and ozone, in a Jelight UVO-cleaner for four minutes. The UVO-cleaner can be seen at the top of Figure 3.2.

Figure 3.2: *A Jelight UVO cleaner on top of a Electronic Diener Femto plasma cleaner, both were used to clean substrates.*

3.2). Solution Processing:

With the substrates having being prepared, the organic layers can be deposited upon them. This can be done via evaporation techniques for small molecules, solution processable techniques for polymers or a combination of the two for hybrid devices. Solution processing is discussed in detail in 3.2.2), whereas evaporation techniques are discussed in detail in section 3.3).

3.2.1). Solution Preparation:

Before spin coating can occur, stock solutions of the OLED materials must be prepared. All the devices in a set which have materials in common are made from the same stock solutions so that the results can be accurately compared. Fresh solutions are prepared for each set of devices in order to avoid the effects of contamination or material degradation on device performance.

1. First, the minimum quantity of material needed to produce the required amount of solution at the right concentration is estimated. Solution processing generally requires a minimum of 0.5 mL of solution per deposition.
2. The species required is transferred to a clean glass vial and weighed roughly on a Mettler AE240 analytical balance. When approximately the right amount has been transferred, a final measurement of the mass is taken to four decimal places.
3. Using the recorded mass, the amount of solvent required to produce a solution of the right concentration is calculated and added using a calibrated pipette. The solvents used were super purity solvents from ROMIL.
4. These stock solutions were then placed on an IKA RCT basic hotplate, with magnetic stirrers, and heated gently to aid solvation.

3.2.2). Spin-Coating:

Spin coating is a relatively simple process that can be used to create highly uniform films upon flat substrates from the nanoscale to the microscale in thickness. The material, in solution form, is placed on to the centre of the substrate, whilst it is either stationary or spinning at low angular velocity, and the substrate is then accelerated to a high angular velocity; this spreads the material over the substrate in a uniform manner leaving a film of solution behind. The initial acceleration removes the majority of the solution on the substrate as it moves radially due to centrifugal forces [2].

The film of remaining solution thins further as it spreads across the substrate's surface. As the spinning process continues the solvent evaporates increasing the viscosity of the film until it hits an equilibrium point [3] between the viscosity, the centrifugal forces and the solvent evaporation. After this point, the spinning process is complete and any excess solvent that might still be present is evaporated by placing the substrate onto a heat source. This baking step has the potential added advantage of increasing the interlinks between polymer chains, reducing their solubility and making them more resistant to additional layers which may be deposited on top of them.

The thickness of the film produce by spin coating depends on several factors including angular velocity, the concentration and viscosity of the solution and the surface tension and volatility of the solvent used. Whilst the thickness of the film is highly uniform over the vast majority of the surface area of the substrate, near the edges the layer is thicker due to the retention of material because of edge effects [4]. Layer thicknesses are determined by ellipsometry, which will be discussed in more detail in 3.5.4). Thickness measurements at different concentrations, or spin speeds, can be used to produce thickness plots for a material. As thickness varies in a linear manner [3] with both concentration and spin speed, these plots

can be used to either identify the thickness of a layer of known spin speed and concentration, or predict the settings needed to produce a layer of a certain thickness, with a relatively high degree of accuracy.

Figure 3.3: *The Laurell WS-650MZ-23NPP spin coater used to spin coat the different organic layers onto the glass substrates.*

Varying the spin speed is a useful technique for producing different layer thicknesses when dealing with commercial solutions, such as PEDOT, that have a predetermined concentration that may be difficult to modify. Its use, however, is limited to the speed range of 1000-3000 rpm, as at speeds under 1000 rpm the film quality tends to decrease, whilst at speeds over 3000 rpm the change in thickness tends to reach a threshold. Varying concentration is the more reliable option if materials permit but this is limited at its upper threshold by the solubility of the material. It is therefore sometimes necessary to vary both to produce films of the desired thickness.

Depending on the material being spun, the spin coating process is slightly different for each. During the course of this thesis a number of different materials were deposited via spin coating. The first layer for solution processed devices was always a PEDOT layer. The next

layer could either be an electron blocking layer or the emissive layer itself. The spin speeds and times of the different spinning stages for the three most common materials can be seen in Table 3.1. Typically, three stages are used in spin coating. The first of these is a low speed spreading stage, which removes the majority of the solution leaving a uniform amount spread across the majority of the sample except at the edges where beading occurs. The next stage is a short, high speed, thinning stage, which reduces the film to the correct thickness. Finally, a long slow spin is performed to allow the majority of the remaining solvent to evaporate, leaving behind a uniform film.

After spinning, the substrates are baked to remove any residual solvent. The temperatures and times used depend on the solvent and materials used. For PEDOT layers a baking temperature of 200 °C and a time of three minutes was used. For chlorobenzene based solutions a baking temperature of 120 °C and a time of ten minutes was used. Finally, for toluene a baking temperature of 100 °C and a time of ten minutes was used. The individual steps for producing a spin coated thin film are detailed below:

1. Secure the substrate using the vacuum system within the Laurell WS-650MZ-23NPP spin coater, shown in Figure 3.3.
2. Spray the substrate with a nitrogen gun to remove any dust that may have accumulated.
3. Add solution to the centre of the substrate with a syringe and a 0.45 µm filter until the substrate is completely covered.
4. Initialise spin procedure using the parameters required to produce a layer of the desired thickness.
5. Place substrate on a hotplate at the predetermined temperature for the time needed to remove any residual solvent.
6. Allow to cool for five minutes before processing further.
7. Repeat for all subsequent layers.

Table 3.1: A table detailing the standard parameters used during this thesis for the three most commonly spin processed layers.

	Step 1		Step 2		Step 3	
Material	**Spin Speed / rpm**	**Spin time / s**	**Spin Speed / rpm**	**Spin time / s**	**Spin Speed / rpm**	**Spin time / s**
Microposit S1813	500	5	3700	30		
PEDOT HIL 1.5	400	6	4000	7.5	400	50
Polymer	400	6	2500	7.5	400	50

3.2.3). Drop Casting:

Drop casting is another technique that can be used to produce films on a substrate using materials dissolved in a solution. Unlike spin coating, it is difficult to consistently control both the thickness and uniformity of films produced using this technique. It is, however, extremely simple and wastes very little material. For the purposes of this thesis drop casting was used to prepare samples for solid state spectroscopy, such as triplet level measurements, where thickness and uniformity are not important. The different types of spectroscopy will be discussed in more detail in 3.6).

As discussed in 2.5.1), triplet states are easily quenched, either by other triplet states or by various contaminants. It is therefore necessary to isolate the triplet states when performing measurements that involve phosphorescence. In order to achieve this, small quantities of the material being measured are suspended in an inert matrix. The inert matrix comprises of a cyclo olefin polymer, known as Zeonex 480, which features a very high transmittance for light in the range of 350-800 nm but is otherwise quite inert [5].

The principle of drop casting is very simple. The materials to be deposited are dissolved in a solution, which is then deposited on the substrate. The solvent evaporates and leaves behind a film of the material. Evaporation can be aided by heating the substrate, but this can affect the film morphology. The thickness of the layer produced is roughly

proportional to the concentration of the solution used. The individual steps for producing a drop cast film are detailed below:

1. Prepare a 1:1 mixture of Zeonex (175 $mg.mL^{-1}$) and of the material measured (0.5 $mg.mL^{-1}$), both dissolved in chlorobenzene.
2. Deposit this mixture on a clean substrate.
3. Allow the solvent to evaporate to leave behind a film of the material suspended in zeonex. This step can be aided by heating the substrate but this is not necessary.

3.3). Thermal Evaporation:

3.3.1). Deposition Techniques:

The spin coating discussed earlier in 3.2.2) is an example of a Liquid Phase Deposition (LPD) method. There are also two other groups of deposition techniques called Physical Vapour Deposition (PVD) and Chemical Vapour Deposition (CVD) [6, 7]. Thin films are produced using CVD processes such as thermal CVD and plasma enhanced CVD, when volatile precursor reagents, often organic compounds, react chemically on the substrate surface to leave behind a stable film and a removable gaseous by-product. PVD deposition techniques include evaporation, sputtering and laser ablation. Thermal evaporation PVD was used throughout this thesis for device manufacture and will be discussed in more detail in section 3.3.2).

3.3.2). Thermal Evaporation PVD:

Thermal evaporation based PVD is a common method of thin film deposition requiring relatively little in terms of equipment whilst producing thin films quickly compared to other PVD methods. Typically, a source material is heated under vacuum conditions until it evaporates and later condenses on the substrate to form a thin film. The evaporated atoms

have an energy distribution determined by the source temperature, so thermal deposition techniques are less damaging to the substrate surface than say sputtering which relies on plasmas. This is an obvious advantage for the production of OLED devices, as the spin coated organic layers underneath are left mostly intact. It is also true that the lower the evaporation/deposition rates the less damage would be caused.

The quality of the deposited film depends on both the purity of the source materials and the quality of the vacuum. If the evaporated material collides with another atom on its path to the substrate, it may react with it introducing impurities; for example aluminium reacting with oxygen to produce aluminium oxide. A higher level of vacuum increases the mean free path of the evaporated material, reducing the number of potential collisions and increasing the quality of deposited film. This method is not suitable for refractory metals or those with a high melting point, and care must be taken with alloys due to the potential variation in composition.

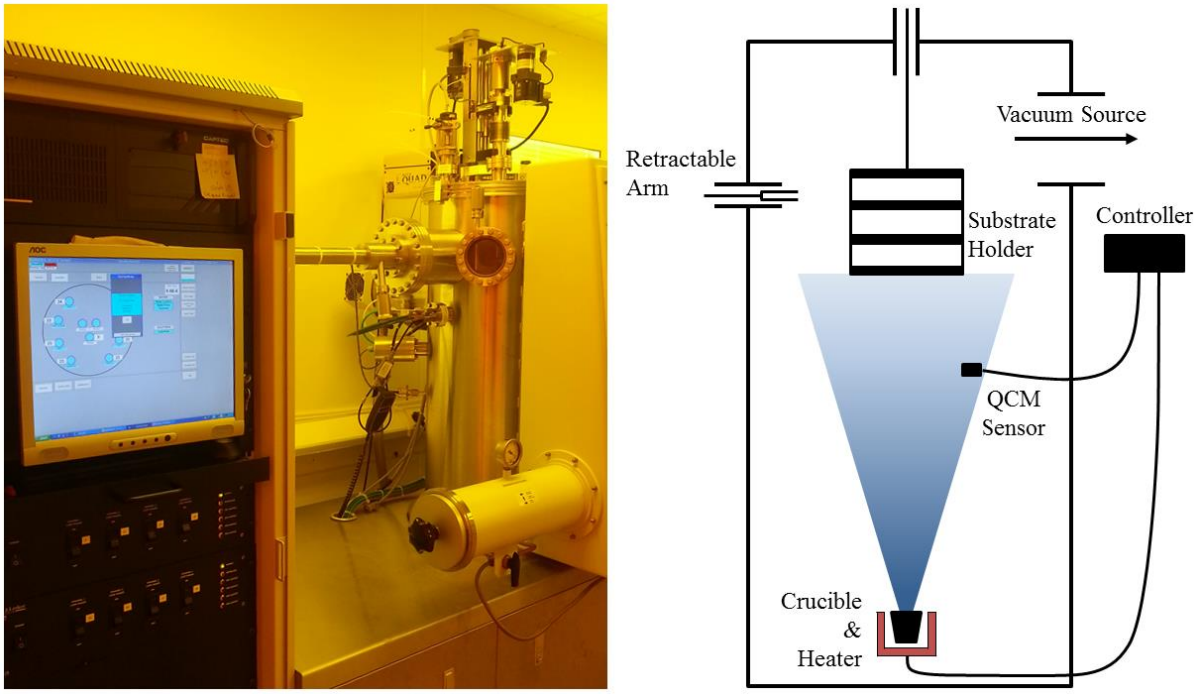

Figure 3.4: *The Kurt J. Lesker Spectros II deposition system on the left of the figure and a schematic view on the right of the figure. Of particular note are the main evaporation chamber, with attached retractable arm, vacuum equipment and rotation/Z-shift motor systems, and the control panel.*

The Durham University Organic Electroactive Materials (OEM) group has a Kurt J. Lesker Spectros II deposition system, which is capable of achieving evaporation pressures of approximately $1x10^{-7}$ mbar and depositing two separate materials at once. As can be seen in Figure 3.4, the system consists of a primary upright cylinder, inside of which there are six available sources for organic materials and another three sources for metals. Attached to the left of the primary cylinder is a retractable arm, which can be used to swap masks, or substrates, whilst still under vacuum with the aid of a rotatable, and z-shiftable, substrate holder. Also to the left of the primary cylinder is the control panel which runs the Sigma Instruments software and controls the system. The film thickness is determined using a Quartz Crystal Microbalance (QCM) system and several deposition parameters which are discussed further in 3.3.3).

3.3.3). QCM and Deposition Parameters:

A QCM system records the change in resonance frequency of a quartz crystal when materials are either added to or removed from it [8]. When a quartz crystal is present in an electronic oscillator circuit, its resonance frequency drives the frequency of the circuit. Therefore, the amount the circuit frequency changes, in response to a change in mass per unit area, can be used to calculate the thickness of film deposited. In order for the thickness to be calculated, however, a couple of the properties of the material being deposited need to be known. These include the density of the material and it's Z-factor, which will be discussed in more detail below.

The Z-factor is the ratio of the acoustic impedances of the quartz crystal (Z_q = 8.83 $Pa.s.m^{-1}$) and the evaporated material (Z_m), where the acoustic impedance is the amount of sound pressure generated by a material at a certain frequency. It is also possible to calculate the Z-factor using the shear moduli of the materials if they are available. Often for new

materials, neither of these values are easily available. Fortunately, the Z-Factor can either be empirically determined, or ignored if the quartz crystal is fresh enough. During the course of this thesis only the well documented materials TPBi, Lithium Fluoride and Aluminium were evaporated.

Also of concern to QCM is the tooling factor, which incorporates the difference in the amount of material deposited on the sensor compared to the amount deposited on the substrate, due to the difference in their relative positions within the evaporation chamber. The tooling factor is given as a percentage value and can be calculated using an estimated value. As with the Z-Factor the tooling factor of the materials and the evaporation chamber were already well known.

3.3.4). Deposition Procedure:

Once spin coating has been successfully completed, it is possible to then evaporate a hole blocking layer if required and the metal cathodes. The individual steps for evaporating a thin film are detailed below:

1. Once the substrates have been prepared they are then transferred, ITO side down, on to a substrate holder and the required masks arranged. The substrates are positioned so that the ITO strips are perpendicular to where the metal cathode strips will be evaporated, corresponding to the gaps in the mask.
2. The substrate holder and masks are then loaded into the evaporation chamber, along with aluminium for one of the crucibles, and the chamber itself pumped down to approximately $1x10^{-7}$ mbar.
3. The substrate holder is then set to rotate at five rpm in order to ensure an even covering of evaporated material.

4. Using the computer interface the recipe of the material to be evaporated is loaded and the heater and shutter for the crucible activated.
5. For lithium fluoride and aluminium the evaporation process is automatic but for miscellaneous organics the voltage to the heaters must be controlled manually to maintain a steady evaporation rate of approximately 1 Å.s^{-1}.
6. When a steady evaporation rate is achieved the substrate shutter is opened, the QCM zeroed and the required thickness of film evaporated.
7. After evaporation the substrate shutter is closed, the crucible heater and shutter deactivated and the rotation stopped.
8. If further layers are to be evaporated the masks can be adjusted using the retractable arm and Z-shift facilities and the above steps repeated from Step 4. onwards.
9. If evaporation is complete the evaporation chamber can be vented back up to ambient pressure and the substrate holder and masks removed.

3.4). Device Encapsulation:

Once the evaporation chamber has returned to the ambient pressure within the MBRAUN MB-200B nitrogen glovebox the substrates can be removed and encapsulated in order to protect them and prolong their lifespan [9, 10]. Encapsulation is necessary in order to reduce contamination of the devices with oxygen and water, which can result in quenching. Device contamination, and the quenching of excited states, have been discussed in more detail in 1.1) and 2.5.1). The individual steps for device encapsulation are detailed below:

1. The devices are removed from the evaporation chamber and transferred to the attached MBRAUN MB-200B nitrogen glovebox.
2. The devices are then removed from the substrate holder with tweezers and placed ITO side up on a Petri dish.

3. A pea sized amount of a UV-curable epoxy resin, Delo-katio bond LP655, is deposited in the centre of each device.
4. A clean glass cover slide (12x12 mm) is placed on top of the epoxy and positioned with tweezers so that the device's four pixels are all covered. The cover slides are cleaned with solvents as described earlier in 3.1.2).
5. The devices are then exposed to UV light for four minutes. This causes the epoxy to set completing both the encapsulation process and the manufacture of the devices.
6. The devices can now be removed from the glove box and characterised. The different characterisation techniques will be discussed in more detail in 3.5).

3.5). Characterisation Techniques:

3.5.1). Steady State Characterisation of Devices:

Steady state electroluminescence characterisation of devices measures the amount of light produced by a device when a steady current is applied to it and is the most common method of assessing OLED devices. Within the Durham OEM group an Agilent 6632B (20 V, 5 A) power supply is used to apply a voltage to the OLED devices and measure the resulting current. A Labsphere LMS-100 integrating sphere is used to collect the photons emitted in all directions by the device, where they can be detected by an Ocean Optics USB4000 fibre optic spectrometer. A NI LabVIEW program is used to control the voltage applied to the OLED. It also collects the data from the power supply and spectrometer where it calculates the device characteristics, such as External Quantum Efficiency (E.Q.E.) and brightness. The LabVIEW program then exports this data both as a .txt file and as a .pdf file. The integrating sphere and a screenshot of the LabVIEW program can be seen in Figure 3.5.

The spectrometer converts the photons it detects into a current; this can be used to calculate the important characteristics of the OLED device. These characteristics include

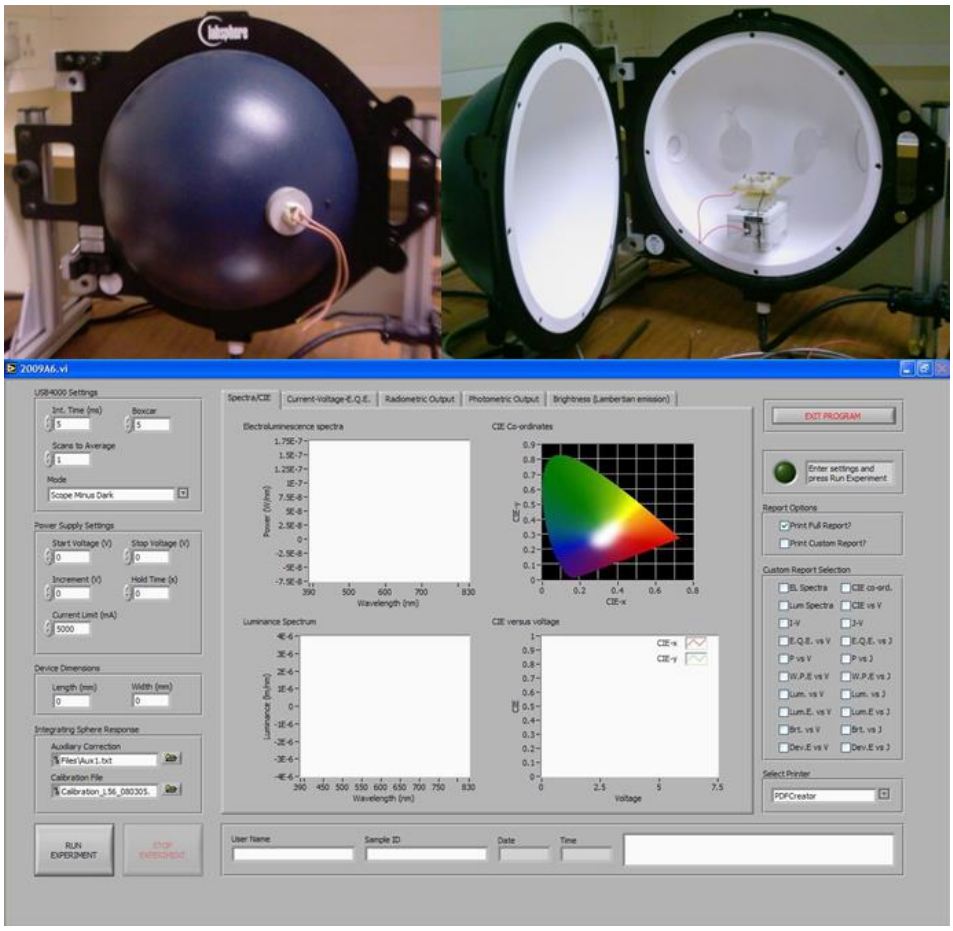

Figure 3.5: *This figure shows the Labsphere LMW-100 integrating sphere used to characterise the devices and the LabVIEW program used to control the system and produce the results.*

different efficiencies such as E.Q.E. (η_{ext}, %), wall plug luminous efficacy (η_{wpe}, $Lm.W^{-1}$) and current efficiency (η_I, $cd.A^{-1}$) and brightnesses such as luminance (L, $cd.m^{-2}$). The rest of this section will focus on calculating these characteristics and a brief explanation of their properties [11].

The E.Q.E. of an OLED is the ratio of the energy put into the OLED in the form of electrons to the energy that comes out in the form of photons. This is a ratio of energies and as such is not affected by the wavelength of light emitted. With current from the spectrometer, the OLED power as a function of wavelength ($P_{OLED}(\lambda)$, W) can be calculated using Equation 3.1:

$$P_{OLED}(\lambda) = \frac{I_{spec}(\lambda)}{f(\lambda)R(\lambda)} \tag{3.1}$$

Where I_{spec} is the current generated in the detector in Amperes, R(λ) is the detector responsivity in Amperes/Watt and f(λ) is the ratio of photons detected to the total number emitted by the OLED. The function f(λ) is obtained by calibrating the integrating sphere, complete with OLED device holder, using a NIST traceable standard lamp.

Using Equation 3.1 and $E = hc/\lambda$, where h is Planck's constant (6.626×10^{-34} J.s) and c is the speed of light (2.998×10^{8} m.s^{-1}), it is possible to determine the total number of photons emitted by the OLED device, forming Equation 3.2:

$$n_{photons} = \frac{\int \lambda I_{spec}(\lambda) d\lambda}{hc \int f(\lambda) R(\lambda) d\lambda} \tag{3.2}$$

Equation 3.2 gives the amount of energy emitted by the OLED in terms of the number of photons. In order to calculate η_{ext} the number of electrons injected into the device must be calculated. This is done using Equation 3.3:

$$n_{electrons} = \frac{I_{OLED}}{e} \tag{3.3}$$

Where I_{OLED} is the current passing through the OLED device in Amperes and e is the charge of an electron (1.602×10^{-19} C). Using the ratio of Equations 3.2 and 3.3 it is possible to calculate the E.Q.E. of the device, this can be seen in Equation 3.4.

$$\eta_{ext} = \frac{n_{photons}}{n_{electrons}} = \frac{e \int \lambda I_{spec}(\lambda) d\lambda}{I_{OLED} hc \int f(\lambda) R(\lambda) d\lambda} \tag{3.4}$$

The human eye, however, is more sensitive to certain wavelengths of light than others, it is therefore necessary to incorporate this into the OLED characteristics. This is done by introducing the photonic luminosity function, $y(\lambda)$, which normalises the detector output to the visual sensitivity of the human eye, peaking at 555 nm. Using this function, the curve of which can be seen in Figure 3.6 in 3.5.2), it is possible to calculate the other characteristics mentioned above. This includes the wall plug luminous efficacy, which is the ratio of the

total luminous flux emitted by the OLED to the total electrical power put into it. This can be calculated using Equation 3.5:

$$\eta_{wpe} = \frac{\phi_0 \int y(\lambda) I_{spec}(\lambda) d\lambda}{I_{OLED} V \int f(\lambda) R(\lambda) d\lambda} \tag{3.5}$$

Where V is the voltage across the OLED device in volts and ϕ_0 is the luminous coefficient (683 $lm.W^{-1}$).

It is easily possible to convert this quantity into luminance and then to current efficiency. Luminance is effectively a measure of how bright the emission from a surface is and is widely used to characterise the brightness of displays and other devices. Current efficiency, like E.Q.E., is a measure of the electrons injected into the device to the number of photons emitted. Unlike E.Q.E., this quantity is again weighted by the photopic luminosity function. Using the relationship between lumens and candela, 1 $lm.sr^{-1}$ is equal to 1 cd, it can be shown that for a full sphere, of solid angle 4.π steradians (sr), 1 candela is approximately equal to 12.57 lumens. In our case, for a Lambertian emission from a half plane, the solid angle is π steradians and so 1 candela is approximately equal to 3.14 lumens. It is therefore possible to calculate L using this relationship and Equation 3.5, which allows η_I to be calculated using Equation 3.6:

$$\eta_I = \frac{AL}{I_{OLED}} \tag{3.6}$$

Where A is the area of the active pixel in m^2.

These calculations are all performed automatically by the LabVIEW program, which controls the characterisation process and converts the current returned by the spectrometer into the important parameters mentioned earlier. The individual steps for steady state device characterisation are detailed below:

1. Load OLED device onto the device holder within the integrating sphere and fasten it in place securely to ensure a good connection to the electrodes.
2. Address the pixel to be tested and manually test the connection by applying a small voltage across the pixel and checking for a resulting current.
3. When satisfied configure the LabVIEW program to test the desired range of voltages (up to 20V), with a suitable voltage step between them (usually 0.5V), hold time (usually 3s) and number of repeats (usually 5). The program is then run and the data exported.

3.5.2). Device Colour and CIE Coordinates:

As mentioned earlier in 3.5.1), the human eye is more sensitive to certain wavelengths of light than others. This can be represented by the luminosity function. In other words, the luminosity function shows the perception of brightness to different wavelengths of light, as observed by the human eye. There are actually two luminosity functions; the most commonly used of these is the photopic luminosity function, $y(\lambda)$, which is most suitable for normal

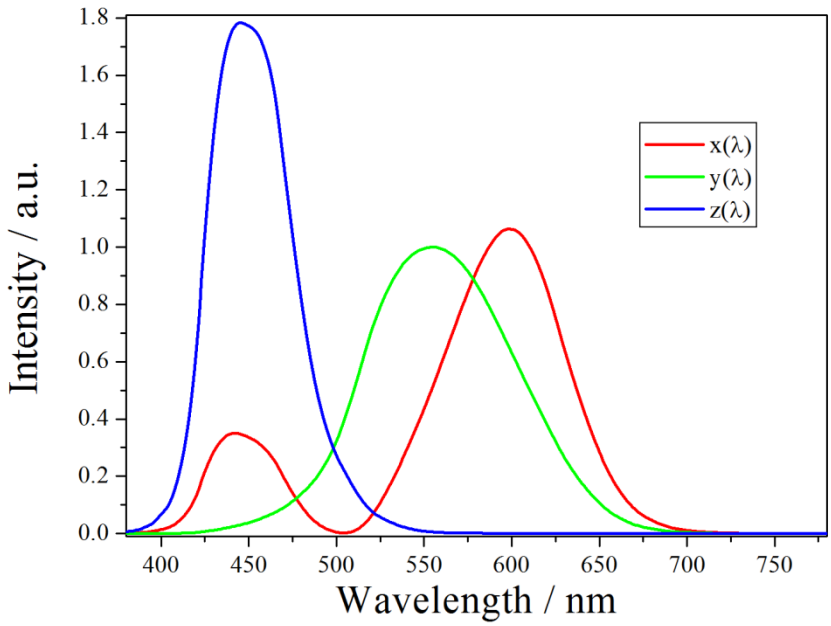

Figure 3.6: *The CIE's three colour matching functions x(λ), y(λ) and z(λ). These are related to the spectral response curves for the three different cone cells present in the human eye and can be used to define the colour of light perceived. The function y(λ) is also known as the photopic luminosity function, which describes the sensitivity of the human eye to the brightness of different wavelengths of light. It peaks at 555 nm, which is within the green, resulting in the sensitivity for blue and red light being reduced in comparison.*

light levels. This is the function by which the OLED emission is normalised, meaning that the blue and red emission is reduced in comparison to the green emission, so more emission is required to achieve the same brightness. A plot of the photopic luminosity function can be seen in Figure 3.6. The second of these functions is the scoptic luminosity curve, which applies only for low light levels, and as such will not be considered in this thesis.

The photopic luminosity function is included as a colour matching function within the Commission Internationale de l'Éclairage's (CIE's) 1931 colour space [12]. The CIE 1931 colour space is used to convert between a spectrum of light and the colour perceived by the human eye. It contains three colour matching functions, each of which is related to one of the three different cone cells present within the human eye. The three functions $x(\lambda)$, $y(\lambda)$ and $z(\lambda)$ [13] can be seen in Figure 3.6 and are used to produce the three CIE tristimulus values X, Y and Z using the OLED power spectrum and Equations 3.7:

$$X = \int_{380}^{780} P_{OLED}(\lambda)x(\lambda)d\lambda$$

$$Y = \int_{380}^{780} P_{OLED}(\lambda)y(\lambda)d\lambda \qquad (3.7)$$

$$Z = \int_{380}^{780} P_{OLED}(\lambda)z(\lambda)d\lambda$$

This gives three values for the response of the eye to a spectrum of light, which would imply that a three dimensional representation of colour is required to describe it. However, as the concept of colour can be divided into two parts, brightness and chromaticity, a two dimensional figure can in fact be used. Here Y is used to describe the brightness of a colour, whilst two extra parameters derived from a normalised combination of X, Y and Z are used to define the chromaticity. Three normalised values, x, y and z, can be calculated but, as

$x + y + z = 1$, only x and y are required to denote the chromaticity. The values for x, y and z are calculated using Equations 3.8:

$$x = \frac{X}{X + Y + Z}$$
$$y = \frac{Y}{X + Y + Z} \qquad (3.8)$$
$$z = \frac{Z}{X + Y + Z}$$

The x and y parameters act as coordinates on the CIE chromaticity diagram. This diagram, a version of which can be seen in Figure 3.7 [14, 15], covers all of the colours perceivable by the human eye, where the locus around the outside corresponds to different wavelengths of monochromatic light. Within the chromaticity diagram different gamuts, or subsets, of colours can be defined. The most common of these is the sRGB gamut, or "standard" RGB, which encompasses the standard colours reproducible by most displays.

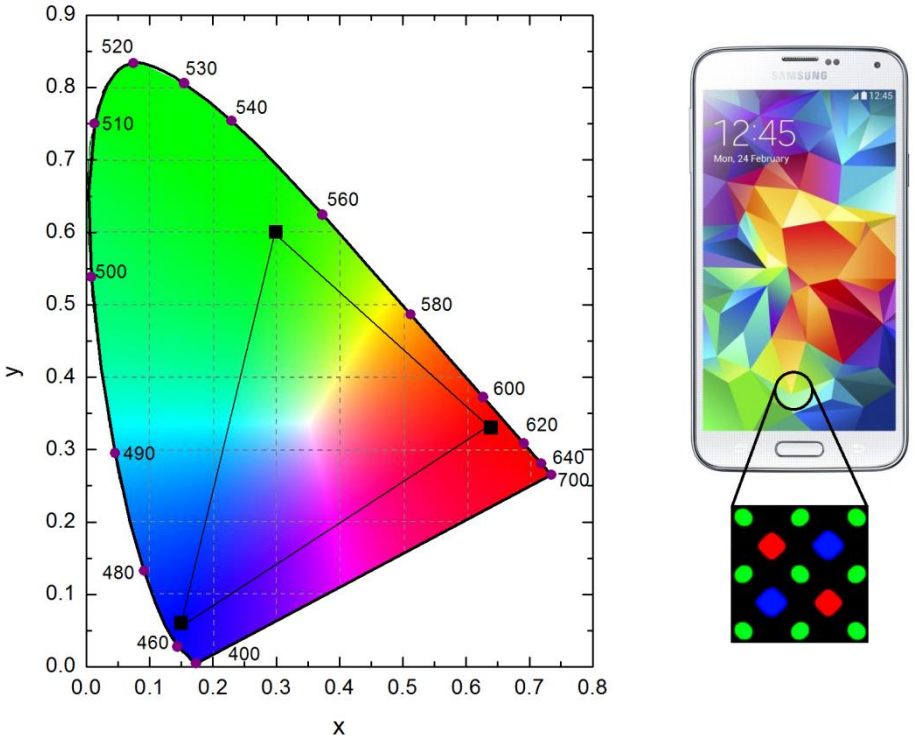

Figure 3.7: *The CIE chromaticity diagram, which contains all of the different colours perceivable by the human eye. Also shown is the sRGB gamut (R = (0.64, 0.33), G = (0.30, 0.60) and B = (0.15, 0.06)), which contains the colours capable of being reproduced by most common displays. These displays utilise RGB pixel systems.*

Displays use clusters of three pixels, one each for red, green and blue, to produce the entire gamut within the triangle bound by the three colours. This does however mean that there is a large range of colours outside of this gamut, which can be perceived by the human eye but not reproduced by most displays. It is therefore important for OLED devices to be able to reproduce these three colours efficiently to replicate the gamut and compete with LCD displays.

3.5.3). Transient Characterisation of Devices:

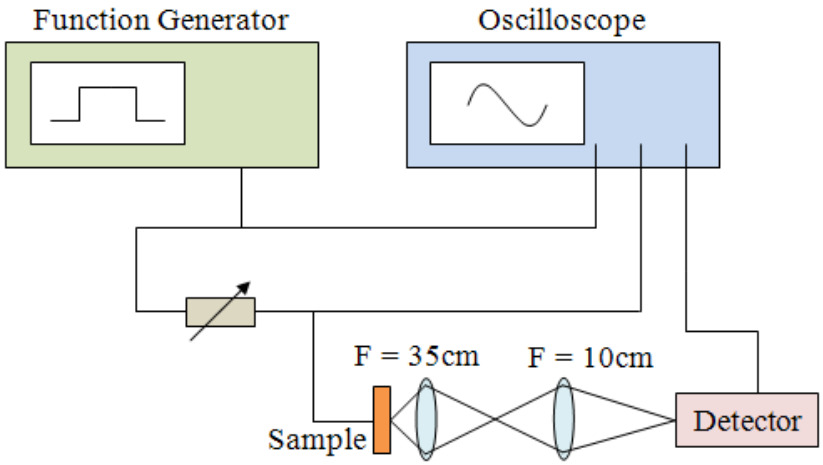

Figure 3.8: *This figure shows the basic experimental setup used to carry out transient electroluminescence on the devices produced for this report.*

Transient electroluminescence characterisation measures the response of an OLED device when voltage pulses are applied to it, and it is a common method of assessing charge carrier mobility [16, 17]. A HP8114A function generator is used to generate square voltage pulses at a regular frequency of 1 kHz and of width 50 μs. An Agilent Infiniium 1 GHz 4 GSa/s oscilloscope is then used to record the pulses before and after passing through the device. A standard Si-PIN-PD detector with an attached DHPCA-100 variable gain high speed current amplifier, which is also connected to the oscilloscope, is used to detect the light response of the OLED. A schematic view of the experimental setup can be seen in Figure 3.8.

The detector converts the light produced into an electric current based on the amount emitted and transmits this measure of intensity to the oscilloscope. Using the oscilloscope it

is possible to observe a delay time (t_d, s) for the OLED device to start emitting light after the voltage pulses are applied. This delay time occurs due to the time taken for the charges induced by the voltage to be transported through the device to the emissive layer, via the methods discussed in 2.5), and for recombination and emission to occur. It is therefore possible to use this delay time to calculate a value for the mobilities of the charge carrier within the OLED device.

For transient EL the mobility of the charge carries (μ, $cm^2.V^{-1}.s^{-1}$) can be expressed using Equation 3.9:

$$\mu = \frac{L}{(t_d F)} = \frac{Ld}{t_d V} \tag{3.9}$$

Where L is the thickness of the emissive layer in meters, F is the electric field in $V.m^{-1}$ and is determined using $F = V/d$, where V is the applied voltage in volts. The value for d corresponds to the field thickness, which can usually be approximated to that of the emissive layer. Outside of the emissive layer the organic layers are usually either primarily hole transporters (PEDOT, PVK) or electron transporters (TPBi), resulting in a large imbalance of charge causing the electric field to drop off.

The values obtained by transient EL characterisation can be used to identify and investigate the different transport mechanisms within an OLED device. The individual steps for transient EL characterisation are detailed below:

1. Load OLED device onto the device holder and fasten it in place securely to ensure a good connection to the electrodes.
2. Address the pixel to be tested and manually test the connection by applying a small voltage pulse across the pixel and checking for a resulting current.

3. The lenses are then used to focus the light from the OLED device on to the Si-PIN-PD detector.
4. Apply square voltage pulses at a regular frequency of 1 kHz and of width 50 μs with increasing magnitudes, from 4V to 20V in 1V intervals.
5. The voltage and light pulses are recorded by the oscilloscope that averages 200 measurements for each of the three signals.
6. The results are saved and exported.

3.5.4). Ellipsometry:

There are a number of different techniques that can be used to measure the thickness of the organic layers deposited by spin coating or evaporation. For the purpose of this thesis, the primary method of thickness determination used was ellipsometry [18-20]. This is a

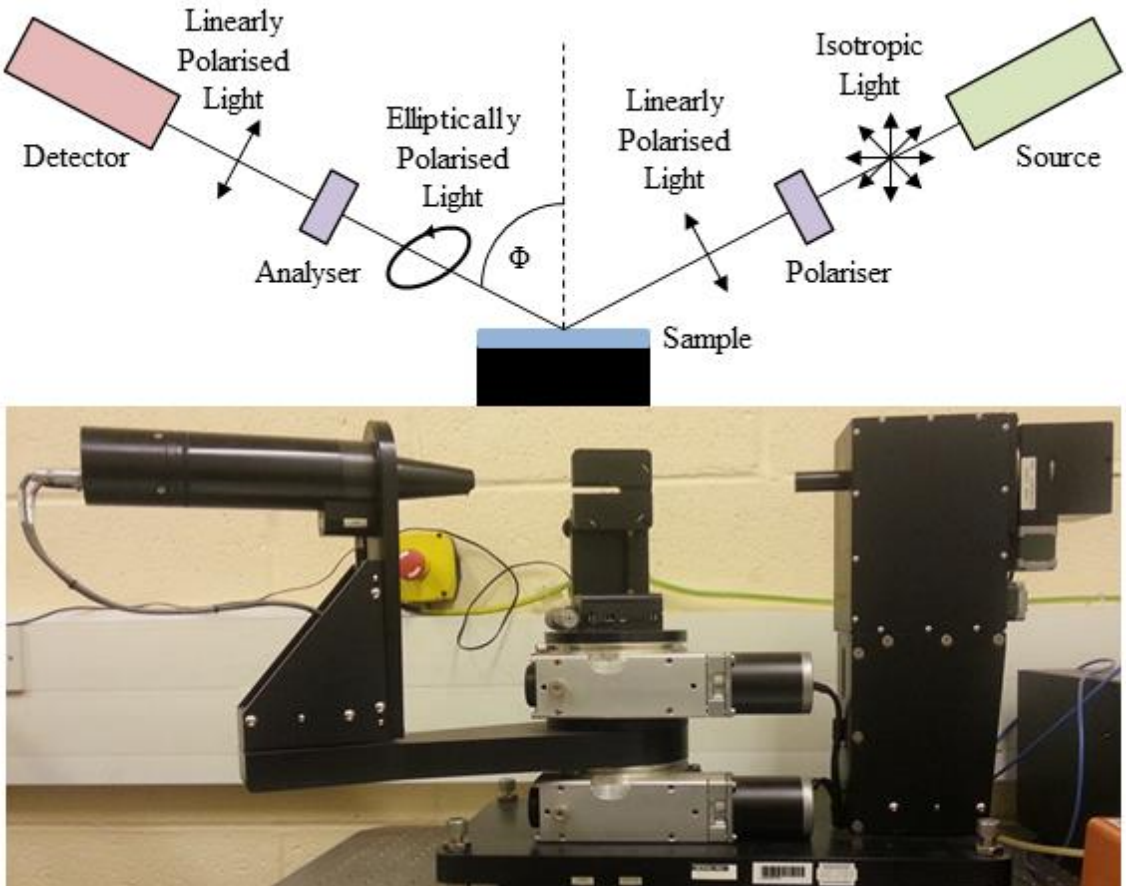

Figure 3.9: A schematic view of the ellipsometer experimental setup and a photograph of a J. A. Woolam VASE Ellipsometer. Note that the angle of incidence is equal to the angle of reflection in this configuration.

powerful optical technique, which makes use of the change in polarisation of the monochromatic light incident upon the sample. The incident light interacts with the sample through various mechanisms, including absorption, transmission, reflection and scattering. The change in polarisation is measured by recording the Stokes Parameters, Δ and Ψ, where Δ is the phase difference and Ψ is the amplitude ratio.

The experimental setup can be seen in Figure 3.9, in both schematic form and a picture of the actual equipment. The ellipsometer used by the OEM group is a J. A. Woolam VASE Ellipsometer. As can be seen in Figure 3.9, the angle of incidence is equal to the angle of reflection (Φ). Light incident on the sample can have its polarisation changed in two different ways, parallel to the plane of incidence (p-polarised) or perpendicular to the plane of incidence (s-polarised). The detector measures the complex reflectance ratio of the sample (ρ) at different angles of incidence. This ratio is related to the Stokes Parameters by Equation 3.10:

$$\rho = \frac{r_p}{r_s} = \tan(\Psi)e^{i\Delta} \tag{3.10}$$

Where r_p and r_s are the amplitudes of the p and s polarisations respectively.

Whilst ellipsometry is a contactless and non-destructive method of obtaining a variety of different film characteristics, including its thickness and refractive index, it is also an indirect method. This means that it is not possible to directly convert the Stokes Parameters into film parameters, and in order to extract physical quantities from them the desired parameters must be modelled and fitted to the measured Δ and Ψ values. Therefore the film thickness is typically found by modelling a thin film, based on a basic organic Cauchy representation [21], and then fitting this to the measured data using an iterative process, such as least-squares minimisation.

Ellipsometry can also be used to test how well multilayers have formed by investigating how the overall film thickness deviates from what would be expected from the sum of the individual layer thicknesses. Typically, if there is a large deviation from the expected total thickness it implies that the base layer has been eroded in some way. This is usually caused by the solvent from the upper layer dissolving the layer upon which it is being spun. The individual steps for ellipsometry are detailed below:

1. Silicon substrates, with a thin coating of silicon dioxide (Si/SiO_2) of known thickness, and of similar size to ordinary device substrates are cleaned using the methods discussed in 3.1.2).
2. After cleaning the thin films are deposited on to the shiny side of the Si/SiO_2, either by spin coating or evaporation, following the procedures outlined in 3.2.2) and 3.3.4).
3. The Si/SiO_2 substrates are loaded on to the ellipsometer and the Stokes Parameters are measured at three different values of Φ over a range of wavelengths, typically 300-1100 nm.
4. A model of the films is constructed in the ellipsometer software. A basic organic Cauchy representation is used for the unknown films and the model is fitted to the experimental data to determine the Stokes Parameters and extract the layer thicknesses.

3.6). Spectroscopy:

3.6.1). Absorption Spectroscopy:

The steady state absorption spectra of thin films and solutions were determined using a Shimadzu UV-3600 UV-VIS-NIR spectrophotometer. This system produces light over a large spectral range using two lamps, a Halogen lamp for the infrared (IR)-visible range and a Deuterium lamp for the UV range. These lamps are coupled with a double monochromator system, which can offer a spectral resolution over these ranges of 0.1 nm. The light produced

by the excitation sources is split into two beams, one of which passes through the sample, the other passes through a reference. The transmitted intensities from the sample and reference are sent on to one of three detectors covering the different spectral ranges. A PbS detector for the IR range, a InGaAs detector for the near-IR range and a photomultiplier tube (PMT) for the visible and UV ranges. The reference transmitted intensities are subtracted from the sample transmitted intensities, and using the Beer-Lambert Law discussed in 2.4.2) the absorbance of the sample is calculated.

For solution based measurements, solutions of the species being investigated were prepared according to the procedures detailed in 3.2.1). A concentration of the order of 50 μg/mL was used and the prepared solution was then transferred to a clean cuvette. Another cuvette containing just the solvent was also prepared to act as a reference. For thin film based measurements solutions of concentrations of the order of 10 mg/mL were prepared according to the procedures detailed in 3.2.1). These solutions were then spun on to clean sapphire discs, of diameter 1 cm, following the method outlined in 3.2.2). Films could also be prepared using the drop casting method outlined in 3.2.3). A sapphire disc was left uncoated to act as a reference. The discs and cuvettes had been cleaned using a sonic bath along with nitric acid (70%), acetone and isopropanol in a similar process to the one detailed in 3.1.2).

3.6.2). Fluorescence Spectroscopy:

The steady state fluorescence spectra of thin films and solutions were determined using a Jobin Yvon FluoroMax-3. A Xe lamp is used to produce an excitation source and coupled with a single monochromator system to provide a good spectral resolution in the range of 250-600 nm. The emission of the sample is collected perpendicularly to the excitation source by a PMT, also coupled with a single monochromator system, covering the range of 250-1000 nm. This setup allows a resolution of 1 nm, or better, to be achieved.

To produce a fluorescence spectrum the excitation wavelength is fixed and the sample emission is scanned. The excitation wavelength is determined from the peak of the first absorption band from the spectra produced in 3.6.1). The solutions and films tested in the FluoroMax were typically the same films tested in 3.6.1) or they were produced to the same specifications. It is also possible to fix the emission wavelength and scan over the excitation range in order to produce an excitation spectrum. This can be used to determine absorption characteristics of the sample, or if there is more than one absorbing species within the absorption curve.

3.6.3). Photoluminescene Quantum Yield Measurements:

The photoluminescence quantum yield (PLQY) of a material is a measure of the ratio of the number of photons emitted by a material to the number of photons it has absorbed [22]. This quantity can give an idea of the photoluminescent efficiency of a material and has a maximum value of 1.0. PLQYs (Φ_{PLQY}) can be expressed in the form of Equation 3.11:

$$\Phi_{PLQY} = \frac{Number\ of\ photons\ emitted}{Number\ of\ photons\ absorbed} \tag{3.11}$$

During the course of this thesis only thin film based PLQY measurements were carried out. These measurements were performed using a small integrating sphere and a Jobin Yvon FluoroMax-3. Emission spectra for both the sample and a reference were taken along with a spectrum of the excitation for both. The excitation spectra were obtained using a neutral density filter (optical density = 2), which reduces the intensity of light of all wavelengths equally. A correction factor was applied to the four resulting spectra to take into account the spectral response of both the integrating sphere and the FluoroMax. The reference emission spectrum was then taken away from the sample emission spectrum in order to remove the background radiation. The PLQY of the film was then calculated using Equation 3.12:

$$\Phi_{PLQY} = \frac{\int F(\lambda)d\lambda}{10^{OD}.\int R(\lambda)d\lambda - \int P(\lambda)d\lambda} \quad (3.12)$$

Where F(λ) is the background removed emission spectrum of the sample, P(λ) is the emission spectrum of the excitation with the sample present, R(λ) is the emission spectrum of the excitation with the reference and OD is the optical density of the filter.

3.6.4). Triplet Levels and Phosphorescence Lifetime Measurements:

The triplet levels and lifetimes of several materials were measured using a Nitrogen laser, emitting at 337 nm, as an excitation source [23, 24]. A pulse frequency of 5 Hz was used to excite a sample mounted within a cryostat under vacuum (<1x10^{-4} mbar) and cooled to approximately 15 K. The emission from the material was collected perpendicularly to the excitement source by a Stanford Computer Optics gated iCCD camera after passing through a dual grating spectrograph. The iCCD camera is synchronised to the laser by using a beamsplitter on the laser pulse to trigger a photodiode connected to the camera. The horizontal pixel direction of the camera corresponds to the different emission wavelengths, whilst the vertical pixels are integrated for intensity.

The lifetime measurements were performed by obtaining a series of spectra at different camera delay and integration times. The spectra were then integrated to obtain overall emission intensities from which the lifetime can be extracted by fitting a logarithmic function to the intensity values. The triplet levels are extracted from the point on the spectra where the first peak of the emission starts to appear and is converted from wavelength into energy using the equation $E = hc/\lambda$.

References:

1. B. Bhushan, *Springer Handbook of Nanotechnology, 3rd Edition*. Springer, 2010.

2. C.J. Lawrence, *THE MECHANICS OF SPIN COATING OF POLYMER-FILMS.* Physics of Fluids, 1988. **31**(10): p. 2786-2795.

3. D.B. Hall, P. Underhill, and J.M. Torkelson, *Spin coating of thin and ultrathin polymer films.* Polymer Engineering and Science, 1998. **38**(12): p. 2039-2045.

4. C.W. Extrand, *SPIN-COATING OF VERY THIN POLYMER-FILMS.* Polymer Engineering and Science, 1994. **34**(5): p. 390-394.

5. ZeonCorporation, *Cyclo Olefin Polymer (COP) Zeonex Datasheet*. 2015 [cited 03/02/15]; Available from: http://www.zeonex.com/lib/pdf/zeonex_e_200809b.pdf.

6. W. Knoll and R. Advincula, *Functional Polymer Films, 1st Edition*. Wiley-VCH, 2013.

7. K. Seshan, *Handbook of Thin Film Deposition 3rd Edition*. Elsevier, 2012.

8. C. Lu and A.W. Czanderna, *Applications of Piezoelectric Quartz Crystal Microbalances 1st Edition*. Elsevier, 2012.

9. A.B. Chwang, et al., *Thin film encapsulated flexible organic electroluminescent displays.* Applied Physics Letters, 2003. **83**(3): p. 413-415.

10. A.P. Ghosh, et al., *Thin-film encapsulation of organic light-emitting devices.* Applied Physics Letters, 2005. **86**(22).

11. S.R. Forrest, D.D.C. Bradley, and M.E. Thompson, *Measuring the efficiency of organic light-emitting devices.* Advanced Materials, 2003. **15**(13): p. 1043-1048.

12. J. Schanda, *Colorimetry: Understanding the CIE System 1st Edition*. Wiley-Blackwell, 2007.

13. InternetArchive, *CIE (1931) 2-deg color matching functions*. 2015 [cited 31/01/2015]; Available from: http://web.archive.org/web/20081228084047/http://www.cvrl.org/database/text/cmfs/ciexyz31.htm.

14. PhoneArena, *Samsung Galaxy S6 (Project Zero) rumor round-up*. 2015 [cited 31/01/15]; Available from: http://www.phonearena.com/news/Samsung-Galaxy-S6-Project-Zero-rumor-round-up-specs-features-price-release-date-and-all-we-know-so-far_id63251.

15. DisplayMate, *Samsung Galaxy S5 Display Technology Shoot-Out*. 2015 [cited 31/01/15]; Available from: http://www.displaymate.com/Galaxy_S5_ShootOut_1.htm.

16. D.J. Pinner, R.H. Friend, and N. Tessler, *Transient electroluminescence of polymer light emitting diodes using electrical pulses.* Journal of Applied Physics, 1999. **86**(9): p. 5116-5130.

17. J.S. Chen and D.G. Ma, *Effect of dye concentration on the charge carrier transport in molecularly doped organic light-emitting diodes.* Journal of Applied Physics, 2004. **95**(10): p. 5778-5781.

18. R.M.A. Azzam and N.M. Bashara, *Ellipsometry and polarized light, New Edition.* Elsevier Science Ltd, 1987.

19. H. Fujiwara, *Spectroscopic Ellipsometry: Principles and Applications, 1st Edition.* John Wiley & Sons, 2007.

20. H.G. Tompkins, *A User's Guide to Ellipsometry*, *1st Edition*. Academic Press Inc, 2012.

21. B.P. Lyons and A.P. Monkman, *A comparison of the optical constants of aligned and unaligned thin polyfluorene films.* Journal of Applied Physics, 2004. **96**(9): p. 4735-4741.

22. J.M. Hollas, *Modern Spectroscopy*, *4th Edition*. Wiley, 2004.

23. V. Jankus, C. Winscom, and A.P. Monkman, *The photophysics of singlet, triplet, and degradation trap states in 4,4-N,N-'-dicarbazolyl-1,1(')-biphenyl.* Journal of Chemical Physics, 2009. **130**(7).

24. C. Rothe and A.P. Monkman, *Triplet exciton migration in a conjugated polyfluorene.* Physical Review B, 2003. **68**(7).

Chapter 4 Analysis of OLED Devices Using SEmiconducting Thin Film Optics Simulation (SETFOS) Software:

Sections of this chapter have been published:

J. H. Cook*, H. A. Al-Attar and A. P. Monkman, *'Effect of PEDOT-PSS resistivity and work function on PLED performance'*, Organic Electronics, **15**, 245, (2014).

4.1). An Introduction to SETFOS:

SEmiconducting Thin Film Optics Simulation (SETFOS) is a software package produced by FLUXiM that simulates the behaviour of OLED devices. It is capable of reproducing both the optical and electrical behaviour of devices using several different models built into the software. Optical models can be used to predict EL emission spectra, the radiating dipole density location and distribution, and also the optimum layer thicknesses for cavity resonance [1, 2]. Electrical models can be used to extract qualitative values for device parameters, such as hole mobility and work function, and reinforce conclusions drawn from experimental work [3]. It is also theoretically possible to use SETFOS to predict device behaviour before making them, potentially saving both time and materials. Optical models are not the focus of this chapter and will not be discussed in more detail. Further details for the principles upon which the electrical models are built, including those discussed below, can be found within the SETFOS 3.2 User Manual [4].

4.1.1). Fundamental Equations:

For electrical drift diffusion simulations there are several governing equations that need to be mentioned. Foremost amongst these equations are the semiconductor continuity equations. These two equations, which define the change in population of holes and electrons within the device, can be seen in equations 4.1 and 4.2:

$$\frac{dn}{dt} = \frac{\vec{\nabla}\overrightarrow{J_n}}{q} - R - \frac{dn_t}{dt} + G_{opt_{np}} g_n \tag{4.1}$$

$$\frac{dp}{dt} = \frac{-\vec{\nabla}\overrightarrow{J_p}}{q} - R - \frac{dp_t}{dt} + G_{opt_{np}} g_p \tag{4.2}$$

Where n is the electron density, p is the hole density, $\vec{E}$ is the electric field, R is the recombination rate, $\frac{dn_t}{dt}$ and $\frac{dp_t}{dt}$ are the rates of charge trapping and $G_{opt_{np}}$ is the optical charge generation efficiency. Trapping will be discussed in more detail in 4.1.3).

These two equations for the different charge transporters can be coupled to form the Poisson equation seen in Equation 4.3:

$$\varepsilon\varepsilon_0 \vec{\nabla}\vec{E} = -q\left(p - n + p_t - n_t + A_{Doping} - D_{Doping}\right) \tag{4.3}$$

Where the A_{Doping} and D_{Doping} are the acceptor and donor doping terms respectively and supplement the local charge density. The local electric field can be obtained using Equation 4.4:

$$\int_0^L \vec{E}\, dx = V_{app} - V_{bi} \tag{4.4}$$

Where V_{app} is the applied voltage and V_{bi} is the built-in voltage, see 4.1.2). The bimolecular process of recombination is described by Equation 4.5:

$$R = \eta np\left(\mu_n + \mu_p\right)\frac{q}{\varepsilon} \tag{4.5}$$

Where η is the Langevin Recombination Efficiency and the recombination process is heavily dependent on the local charge mobilities [5].

SETFOS features two generations of electrical models for simulations. The first generation uses well defined energy states and the classical Einstein relations between diffusion and mobility to model devices, whilst the second generation accounts for disordered

systems with spread energy levels and incorporates a generalised Einstein relationship (GER). For the purposes of this thesis, only second generation models need to be considered as they provide more accurate simulations than the more primitive first generation models. The second generation models incorporate a disordered density of states (DOS) using Equation 4.6:

$$N(E) = \frac{N_0}{\sqrt{2\pi\sigma^2}} exp\left[-\left(\frac{E - E_0}{\sqrt{2}\sigma}\right)^2\right] \tag{4.6}$$

Where N_0 is the density of chargeable sites, σ is the DOS energy width, typically 0.05-0.15 eV, and this equation is linked to the local carrier density by Fermi-Dirac statistics and Equation 4.7:

$$p(x, E_f) = \int_{-\infty}^{\infty} N(x, E) f(x, E, E_f)\, dE \tag{4.7}$$

The disordered DOS bands are filled from the centre and as such $p(x, E_f)$ can be no larger than $N_0/2$ within the OLED device. The models used for carrier mobilities, carrier injection and trapping all follow from this equation and these will be discussed in more detail in 4.1.2) and 4.1.3).

As mentioned earlier, second generation models incorporate a generalised Einstein relationship. This relates the diffusion constant of the charges to their mobility using Equation 4.8:

$$D_{n,p} = \mu_{n,p} \frac{kT}{q} . g_{3_{n,p}}(\{n, p\}, T) \tag{4.8}$$

Where $g_{3_{n,p}}(\{n, p\}, T)$ is the enhancement function of the classical relationship following from the change in the DOS with σ [6]. This function causes $D_{n,p}$ to increase with increasing carrier density and decreasing temperature, and $g_{3_{n,p}}(\{n, p\}, T)$ is found using Equation 4.9:

$$g_{3_{n,p}}(\{n,p\},T) = \frac{1}{kT}\frac{\{n,p\}}{\frac{\partial\{n,p\}}{\partial E_f}} \tag{4.9}$$

4.1.2). The Extended Gaussian Disorder Model (EGDM):

SETFOS has two different models for calculating charge mobilities for second generation simulations. The Extended Gaussian Disorder Model (EGDM), which works best for polymer based devices [7], and the Extended Correlated Disorder Model (ECDM) [8], which works best for small molecule based devices[9, 10]. As this thesis focuses on polymer based devices, EGDM will be discussed in more detail. The EGDM arises from both the GER and the Pasveer mobility law [11] and produces a charge mobility that is not only both field and temperature dependent but also depends on the local carrier concentration. This can be seen in Equations 4.10-4.14:

$$\mu(T,p,E) = \mu_0(T)g_1(T,p)g_2(E) \tag{4.10}$$

$$g_1(T,p) = \begin{cases} exp\left(\frac{1}{2}(\hat{\sigma}^2 - \hat{\sigma})(2p)^{\delta}\right), & \text{for p} \leq 0.1 \\ g_1(T, 0.1), & \text{for p} > 0.1 \end{cases} \tag{4.11}$$

$$\delta = 2\frac{\ln(\hat{\sigma}^2 - \hat{\sigma}) - \ln(\ln(4))}{\hat{\sigma}^2} \tag{4.12}$$

$$\mu_0(T) = \mu_* exp(-c_1\hat{\sigma}^2) \tag{4.13}$$

$$g_2(T,E) = \begin{cases} exp\left(0.44\left(\hat{\sigma}^{\frac{3}{2}} - 2.2\right)\left(\sqrt{1 + 0.8\left(\frac{E.qa}{\sigma}\right)^2} - 1\right)\right), & \text{for E} \leq 2\sigma/qa \\ g_2\left(T, \frac{2\sigma}{qa}\right), & \text{for E} > 2\sigma/qa \end{cases} \tag{4.14}$$

Where c_1 is the molecular orbital overlap integral, which is typically 0.39 for polymer based materials, σ is the Gaussian energy distribution width for the HOMO, or LUMO, levels electronic state DOS and $\hat{\sigma} = \sigma/k_B T$. Equations 4.10-4.14 are given in terms of holes, in order to convert from holes to electrons simple substitute p for n, as they are valid for both.

Ohmic and thermionic injection models work with both of the second generation models mentioned above. Ohmic injection utilises a fixed boundary condition defined by the user. This can be seen in Equation 4.15:

$$n|_{Cathode} = n_{const} \; and/or \; p|_{Anode} = p_{const} \tag{4.15}$$

Whereas the thermionic injection model converts the work function of the electrode into a density boundary condition using a barrier lowering mechanism [12]. This can be seen in Equation 4.16:

$$p(E_f) = \int_{-\infty}^{\infty} N(E) f(E, E_f) dE \tag{4.16}$$

Where E_f is the Fermi energy, which is related to the injection barrier of the electrode by the equations $\Delta \equiv E_{HOMO} - \phi_{Anode}$ and $\Delta \equiv \phi_{Cathode} - E_{LUMO}$.

The method used to calculate V_{bi} depends upon whether the thermionic or the ohmic models are used. For the purposes of this thesis, the thermionic model was selected. This value was mentioned in 4.1.1) and represents the built-in voltage of the device. For a first generation model V_{bi} would be calculated using Equation 4.17:

$$qV_{bi} = \Phi_{le} - \Phi_{re} \tag{4.17}$$

In this equation, Φ_{re} and Φ_{le} represent the work functions of the right and left electrodes respectively. For the thermionic model the user defines the value of Φ_i, whilst for the ohmic model they are determined using Equation 4.18:

$$\Phi_i = \begin{cases} E_{LUMO} - E_f(n_e), & \text{electron injection at Cathode} \\ E_{HOMO} - E_f(p_e), & \text{hole injection at Anode} \end{cases} \quad (4.18)$$

From the above it can be deduced that for the thermionic model the user specifies the work function of the electrode and therefore the Fermi energy, and SETFOS then calculates the boundary charge densities and V_{bi}. For the ohmic model, the user specifies the boundary charge densities and SETFOS calculates the Fermi energy, effective work function and V_{bi}.

The EGDM and ECDM include a system for modelling the processes occurring at the internal organic-organic interfaces [13]. These models incorporate hopping mechanisms, field dependent barrier lowering and the local adaptation of inter-site distances to provide a number of advantages over those used in the first generation models. The primary advantage of these models is that they have a substantially reduced discretisation dependence, increasing the accuracy of the simulation.

4.1.3). Trapping and Excitons:

Like the free charges in 4.1.2), the traps integrated into the second generation models use a distribution function, $N_t(E)$. There are two different variations built-in to SETFOS, the exponential trap distribution and the Gaussian trap distribution. The general trap density is given by Equation 4.19:

$$p_t(E_f) = \int_{-\infty}^{\infty} N_t(E) f(E, E_f) dE \quad (4.19)$$

Where $f(E, E_f)$ is the Fermi-Dirac distribution. For exponential traps the distribution function is given by Equation 4.20:

$$N_{t_{Exp}}(E) = \frac{N_{Trap}}{2kT_0} exp\left[\frac{|E - E_t|}{kT_0}\right] \quad (4.20)$$

Where T_0 is the characteristic temperature, N_{Trap} is the number of available trap states and E_t is the trap depth, usually in the range of 0.05-0.5 eV. For Gaussian traps the distribution function is given by Equation 4.21:

$$N_{t_{Gauss}}(E) = \frac{N_{Trap}}{\sqrt{2\pi\sigma^2}} exp\left[-\left(\frac{E - E_t}{\sqrt{2}\sigma}\right)^2\right] \tag{4.21}$$

Where σ is the width of the Gaussian DOS.

Whilst the equations above focus on electrons and holes in their individual states, SETFOS is also capable of modelling excitons, including their generation, migration and energy transfer characteristics. The exciton current generated in the device is given by Equation 4.22:

$$\vec{J}_{S_i} = D_S \vec{\nabla} S_i \tag{4.22}$$

Where D_s is the exciton diffusion constant and $\vec{\nabla} S_i$ is the exciton population of which there are i different types of exciton. The exciton rate equation is given by Equation 4.23:

$$\begin{aligned} \frac{dS_i(z)}{dt} = G_i R(z) + \overrightarrow{\nabla J_{S_i}}(z) - \left(k_{rad_i}(z) + k_{nonrad_i}(z)\right).S_i(z) - k_{annih_i}.S_i(z)^2 \\ + \sum_{j=1}^{n_{exc}} \left(k_{ji}.S_j(z) - k_{ij}.S_i(z)\right) + G_{opt_i i}\, G(z) - k_{d_i} S_i(z) \end{aligned} \tag{4.23}$$

This equation includes several different generation, migration and decay terms relating to the different individual processes that excitons can undergo. $G_i R(z)$ is the recombination exciton generation factor (where classically, G_i is 0.25 for singlets and 0.75 for triplets), $G_{opt_i i}$ is the optical exciton generation efficiency and $G(z)$ is obtained from the absorption spectra. $k_{rad_i}(z)$, $k_{nonrad_i}(z)$, k_{annih_i} and k_{d_i} are the radiative decay, non-radiative decay, annihilation and dissociation loss terms for the exciton. Finally, $k_{ji}.S_j(z)$ and $k_{ij}.S_i(z)$

represent energy transfer from one excited species to another. This can occur via both the Förster and Dexter mechanisms discussed in 2.5.2) and 2.5.3).

SETFOS can use two exciton dissociation models. The first is the Onsager-Braun model [14, 15] where the mean initial separation distance, a, is the free parameter (typically a ≈ 1 nm). The model is also field and temperature dependent and is calculated using Equations 4.24-4.26:

$$k_d(a,T,E) = \frac{3\mu e}{4\pi\varepsilon\varepsilon_0 a^3} exp\left(-\frac{\Delta\varepsilon(a)}{k_B T}\frac{J_1\left(2\sqrt{-2b(T,E)}\right)}{-2b(T,E)}\right) \quad (4.24)$$

$$b(T,E) = \frac{e^3 E}{8\pi\varepsilon\varepsilon_0 k_B^2 T^2} \quad (4.25)$$

$$\Delta\varepsilon(a) = \frac{e^2}{4\pi\varepsilon\varepsilon_0 a} \quad (4.26)$$

Where J_1 is a Bessel function of the first kind of the first order. The second model is the Koster model [16], which has been modified to also include metastable polarons and positional disorder. SETFOS 3.2 is unable to model the transfer of exciton energy across different layer interfaces and invokes a no-flow condition in order to prevent their migration.

4.2). Introduction:

In order to assess the viability of SETFOS 3.2 as a tool for analysing OLED devices it is necessary to check its ability to replicate device data and its ability to handle changes in device structure. Perhaps the simplest change that could be investigated concerns the type of poly(3,4-ethylenedioxythiophene) (PEDOT) used in devices. The PEDOTs used throughout this thesis come from a commercial source, Heraeus Precious Metals, Germany, and as such

have known properties and are of a high enough quality that allow for reproducible devices. This makes it extremely suitable to be used to test the ability of SETFOS to adapt accurately to carefully controlled changes in device parameters.

To recap 2.6.2), many OLED devices feature a hole-injecting layer (HIL) between an Indium Tin Oxide (ITO) anode and a hole transporting layer (HTL). One of the most commonly used hole-injecting layers is PEDOT. The PEDOT layer acts to smooth the gradient of work functions [17, 18] between the ITO and the HTL, which aids charge injection within the device. As PEDOT possesses a poor solubility it is commonly combined with poly(styrenesulfonate) (PSS) to form a complex; PSS acts as a negative counterion to the positively charged PEDOT and renders the complex soluble. It is possible to tune the properties [19] of PEDOT-PSS, including the work function and resistivity, in order to affect

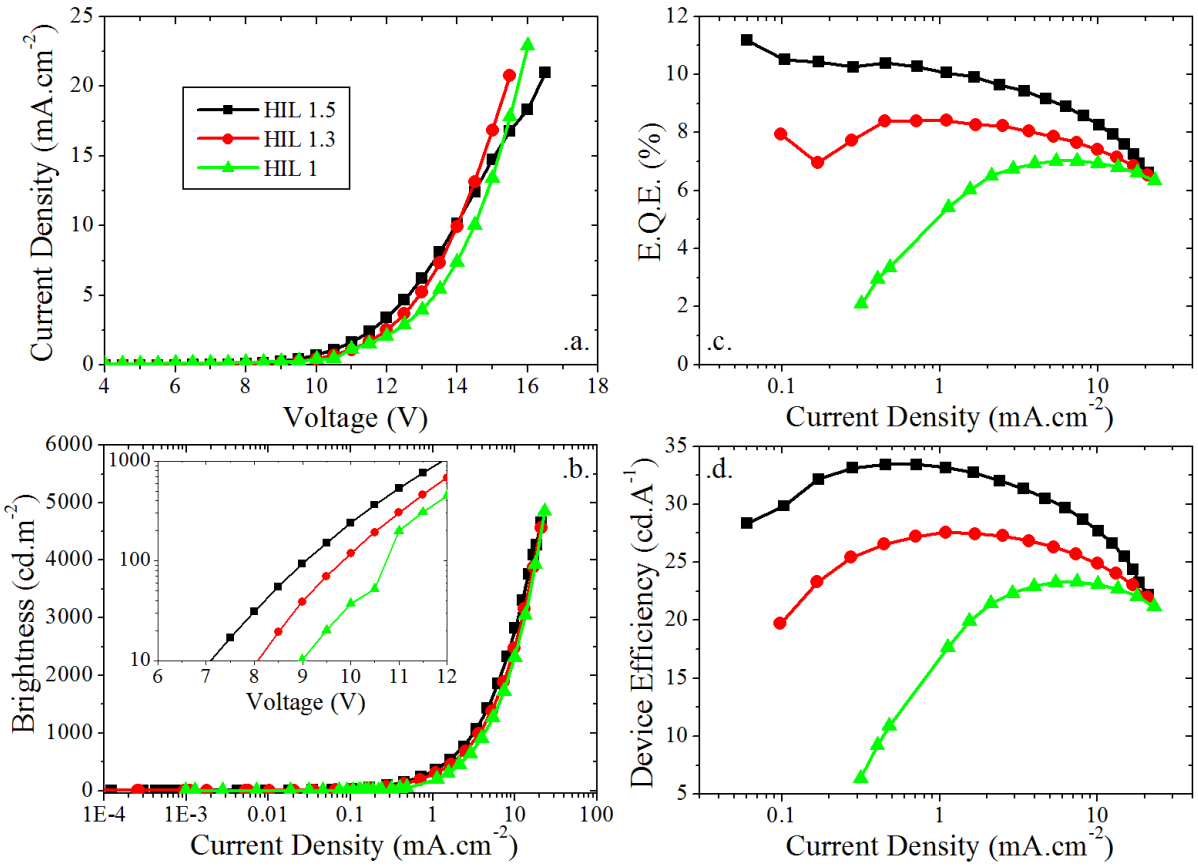

Figure 4.1: *Plots of (a) J-V curves, (b) Luminance vs. J, (c) E.Q.E. vs. J and (d) Device Efficiency vs. J for four devices with PEDOT of different resistivity and work function. Inset to (b) shows the turn on voltages for the three PEDOTs in a plot of Luminance vs. V.*

the overall properties of the device. This can be achieved by changing factors such as the ratio of constituents, impurity density, dopant type and the dispersion solvent [20-22].

A previous investigation [2, 3] into the effect of PEDOT resistivity and work function on device characteristics tested four commercially available variations of PEDOT from Heraeus Precious Metals, Germany [23]. The PEDOTs included CLEVIOS^{TM} HIL 1.1, HIL 1.3 and HIL 1.5, and were used in devices of the same structure to evaluate the effects of the PEDOT resistivity and work function on PLED efficiency and performance. The results of this research can be seen in Figure 4.1. The PEDOT AL4083 also featured in this initial investigation but, as it introduced a change in work function instead of hole mobility, it has not been included here. As only one parameter is varied between the three PEDOTs these results are the ideal subject for testing the viability of SETFOS analysis of OLED devices.

4.3). Experimental:

Three devices were made previously using the PEDOTs HIL 1.5, HIL 1.3 and HIL 1.1 respectively as the HIL. The differing properties[23] of these are detailed in Table 4.1. The devices were manufactured and steady state characterised using the techniques detailed in Chapter 3. The device structure used here was based on the solution processed multilayer

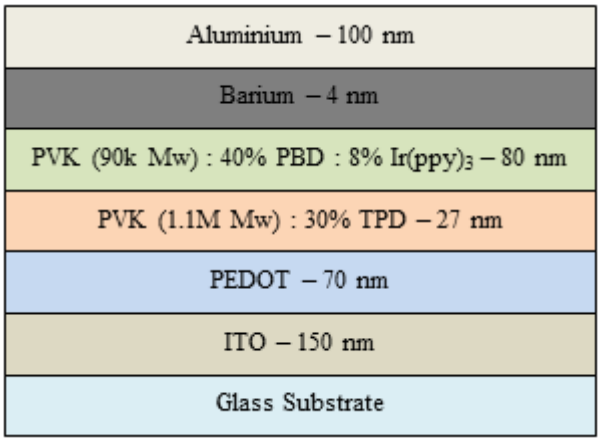

Figure 4.2: *The structure of the devices used to provide the data for SETFOS analysis.*

devices used in previous works [1], where layers of poly(9-vinylcarbazole) (PVK) with different molecular weights (PVKH = 1,100,000 Mw and PVKL = 90,000 Mw) are stacked on top of each other, using their different solubilities in the solvents chlorobenzene and toluene to maintain discrete boundaries between the two. The exact device structure can be seen in Figure 4.2 and these devices provided the results seen previously in Figure 4.1. The data presented is an average over four devices for each different PEDOT and have an error associated with them of approximately 5%.

Table 4.1: *The properties of the different PEDOTs used to manufacture devices for this report.*

PEDOT	Resistivity /Ω.cm	Work Function /eV
HIL 1.1	10-100	5.4-5.9
HIL 1.3	1000-10000	5.4-5.9
HIL 1.5	100000-1000000	5.4-5.9

Using the same solutions, thin films were prepared on Si/SiO_2 substrates. Their thicknesses and refractive indices were then obtained using ellipsometry as detailed in 3.5.4). Both of these material parameters are required by SETFOS and the thicknesses were repeatable to within ±10 nm. These values, along with several others, were entered into SETFOS using the graphical user interface, which can be seen in Figure 4.3. Values not directly obtained by experimental methods were acquired from the literature or estimated using Table 4.9 in the SETFOS 3.2 User Manual.

SETFOS was instructed to sweep over the same voltage range that was used for device characterisation, including the same voltage step size. Three parameters, PEDOT work function, PEDOT resistivity and TPD mobility, were selected to be varied in order to achieve a good fit. The PEDOT parameters were varied in accordance with the ranges given in Table 4.1, whilst the hole mobility of TPD was varied between the literature values of 10^{-4}-10^{-3} $cm^2.Vs^{-1}$[24]. The TPD mobility corresponds in this case to the effective hole mobility of the blocking layer, as the concentration of TPD exceeds the threshold after which transport

occurs without the involvement of the PVKL [25]. Using the three free parameters SETFOS was aiming to fit its values to the device current densities using a built in optimisation algorithm.

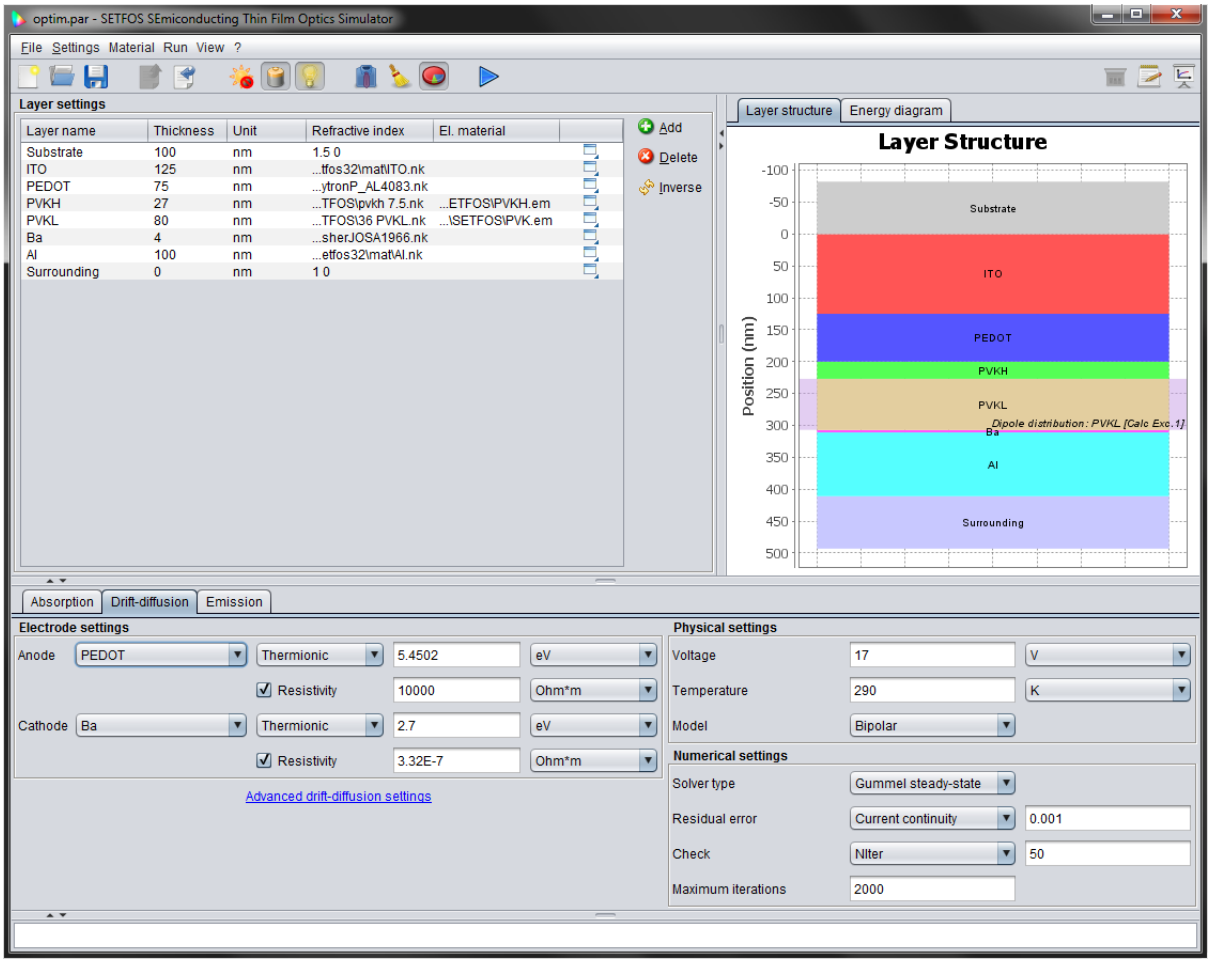

Figure 4.3: *The graphical user interface used to operate SETFOS 3.2. The device parameters have been entered and the simulation is ready to run.*

4.4). Results and Discussion:

Drift-diffusion simulations of the three HIL type PEDOTs were carried out using SETFOS 3.2. The resultant *J-V* curves are in good agreement with the experimentally observed results. These plots are shown in Figure 4.4, along with their experimentally determined counterparts, and allow for the extraction of qualitative values for the PEDOT work function, PEDOT resistivity and the effective hole mobility of the blocking layer. This

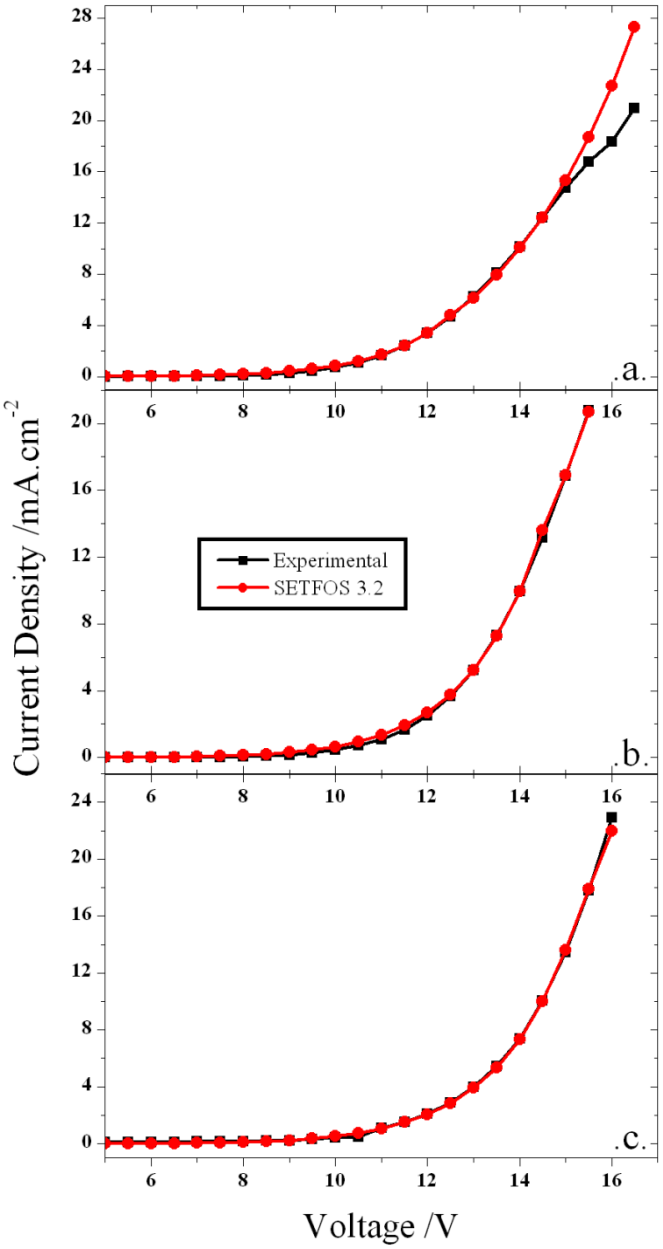

Figure 4.4: *Plots of the simulated J-V curves for (a) PEDOT HIL 1.5, (b) PEDOT HIL 1.3 and (c) PEDOT HIL 1.1, produced using SETFOS 3.2, along with the experimentally determined J-V curves already seen in Figure 4.1.*

is possible due to the fact all the other drift diffusion parameters were kept constant as the type of PEDOT should have no effect on their magnitude.

The parameters used to produce the three different plots are detailed in Table 4.2. From these values, it can be seen that there is indeed an increase in resistivity when going from the HIL 1.1 PEDOT to the HIL 1.5 PEDOT, although these values do not fall within the ranges stated in Table 4.1. This is probably due to the cross-sectional area of the pixels involved not being taken into account by SETFOS; nor does SETFOS consider the

resistivities of the ITO or aluminium layers. There is a slight increase in work function, which is within the prescribed range, but this change is small enough to not be overly significant. Finally, it can also be observed that the effective hole mobility of the blocking layer is dependent on the PEDOT used; there is a decrease in the effective hole mobility as the resistivity of the PEDOT is increased.

Table 4.2: *The parameters used by SETFOS 3.2 to produce the simulated J-V curves seen in Figure 4.4.*

PEDOT	PEDOT Work Function /eV	PEDOT Resistivity / x10^5 Ωm	Effective TPD Hole Mobility / x10^{-4} $cm^2.Vs^{-1}$
HIL 1.1	5.41±0.05	8.90±0.09	3.10±0.03
HIL 1.3	5.42±0.05	9.00±0.09	2.80±0.03
HIL 1.5	5.46±0.05	26.0±0.3	1.30±0.02

The SETFOS simulations yielded values for the hole mobility of TPD from the lower end of the 10^{-4}-10^{-3} $cm^2.Vs^{-1}$ range which, together with the values in Table 4.2, indicates that increasing the resistivity of the PEDOT has the effect of decreasing the effective hole mobility of the TPD. This implies that the resistivity of the PEDOT affects the balance between the charge carriers by changing the holes per unit time entering the blocking layer.

In order to address the discrepancies between the values given in Table 4.1, from the PEDOT manufacturers Heraeus, and the values produced by SETFOS in Table 4.2, more simulations were carried out; the results of which can be seen in Figure 4.5. Initially simulations were performed to try and match the experimental values for HIL 1.5 whilst using the given ranges of resistivity and work function in Table 4.1. This was achieved after modifying several values from the original simulation parameters used to produce Figure 4.4, and produced reasonable, but not as well fitting, results; see plot .a. of Figure 4.5. Unfortunately, when it came to using these parameters to fit the data for HIL 1.3 using the correct resistivity range, it was not possible to create a satisfactory fit; see plot .b. of Figure 4.5.

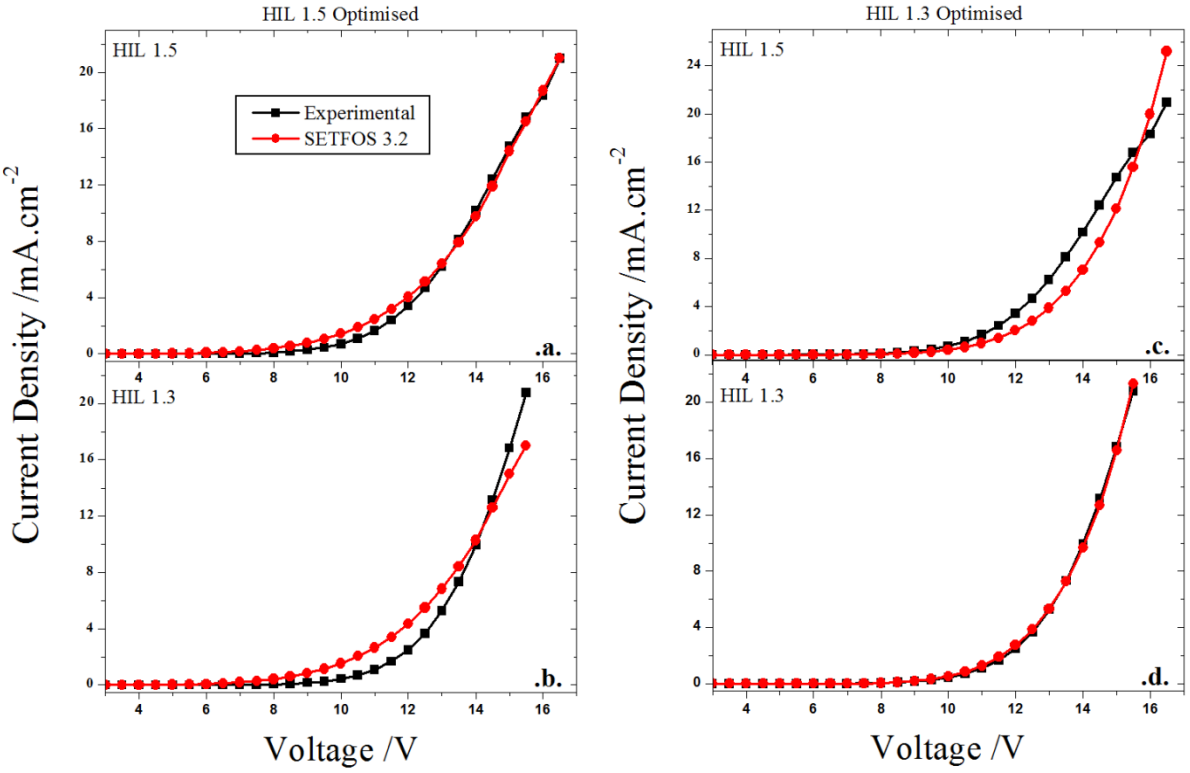

Figure 4.5: *Plots of the simulated J-V curves for (a) PEDOT HIL 1.5 from a simulation optimised for HIL 1.5, (b) PEDOT HIL 1.3 from a simulation optimised for HIL 1.5, (c) PEDOT HIL 1.5 from a simulation optimised for HIL 1.3 and (d) PEDOT HIL 1.3 from a simulation optimised for HIL 1.3, produced using SETFOS 3.2, along with the experimentally determined J-V curves already seen in Figure 4.1.*

This same process was then carried out for HIL1.3 instead, and the original parameters were modified to fit its experimental data. This again produced good, but also not as well fitting, results; see plot d. of Figure 4.5. Unfortunately, as was observed before, when these parameters were used to fit for HIL1.5 it was not possible to achieve a good fit; see plot .c. of Figure 4.5. This serves to highlight that the discrepancies between the given resistivities in Table 4.1 and the simulated ones in Table 4.2 are more than likely due to a problem with the SETFOS model. This is believed to be due to the inability of SETFOS to account for the leakage current that occurs in devices.

Despite these potential problems with the SETFOS model, it is believed that the quantitative trends and values, produced from the simulations, are still valid and can be used to reinforce conclusions drawn from experimental data. The general trends are correct and the difference in magnitudes between the values in Table 4.1 and Table 4.2 are accounted for by

the limitations of the SETFOS model. In this case, the values produced by SETFOS were always intended to be quantitative, and to provide support to conclusions drawn from experimental data, rather than be a direct calculation of qualitative values.

4.5). Conclusions:

In summary, it has been shown that it is indeed possible to reproduce the electronic characteristics of physical device using drift diffusion simulations in SETFOS 3.2. However, this has served to highlight some potential limitations within SETFOS, resulting in an inability to use parameters from within the correct range to produce the best fits. These limitations are thought to be due to a combination of factors, including the cross-sectional area of the pixels involved, the resistivities of the ITO and aluminium layers not being included and SETFOS being unable to account for the leakage current that occurs in devices. Despite this, it has still been possible to extract quantitative values for important device parameters that fit with experimentally observed trends. It is therefore believed that SETFOS analysis can be successfully used to support the conclusions drawn from experimental device data.

References:

1. H.A. Al-Attar and A.P. Monkman, *Solution processed multilayer polymer light-emitting diodes based on different molecular weight host.* Journal of Applied Physics, 2011. **109**(7).
2. J.H. Cook, *Solution processable multilayer Organic Light Emitting Devices, Efficiency*, Durham University, 2010.
3. J.H. Cook, H.A. Al-Attar, and A.P. Monkman, *Effect of PEDOT-PSS resistivity and work function on PLED performance.* Organic Electronics, 2014. **15**(1): p. 245-250.
4. FLUXiM, *User Manual Version 3.2*, 2010.
5. M. Pope and C.E. Swenberg, *Electronic Processes in Organic Crystals and Polymers.* New York: Oxford Univ. Press, 1999.
6. G.A.H. Wetzelaer, L.J.A. Koster, and P.W.M. Blom, *Validity of the Einstein Relation in Disordered Organic Semiconductors.* Physical Review Letters, 2011. **107**(6).

7. R.J. de Vries, et al., *Analysis of hole transport in a polyfluorene-based copolymer-evidence for the absence of correlated disorder.* Applied Physics Letters, 2009. **94**(16).

8. M. Bouhassoune, et al., *Carrier-density and field-dependent charge-carrier mobility in organic semiconductors with correlated Gaussian disorder.* Organic Electronics, 2009. **10**(3): p. 437-445.

9. S.L.M. van Mensfoort, et al., *Electron transport in the organic small-molecule material BAlq - the role of correlated disorder and traps.* Organic Electronics, 2010. **11**(8): p. 1408-1413.

10. S.L.M. van Mensfoort, et al., *Hole transport in the organic small molecule material alpha-NPD: evidence for the presence of correlated disorder.* Journal of Applied Physics, 2010. **107**(11).

11. W.F. Pasveer, et al., *Unified description of charge-carrier mobilities in disordered semiconducting polymers.* Physical Review Letters, 2005. **94**(20).

12. E. Knapp, et al., *Numerical simulation of charge transport in disordered organic semiconductor devices.* Journal of Applied Physics, 2010. **108**(5).

13. R. Coehoorn and S.L.M. van Mensfoort, *Effects of disorder on the current density and recombination profile in organic light-emitting diodes.* Physical Review B, 2009. **80**(8).

14. L. Onsager, *Initial recombination of ions.* Physical Review, 1938. **54**(8): p. 554-557.

15. C.L. Braun, *Electric field assisted dissociation of charge transfer states as a mechanism of photocarrier production.* The Journal of Chemical Physics, 1984. **80**(9): p. 4157-4161.

16. L.J.A. Koster, et al., *Device model for the operation of polymer/fullerene bulk heterojunction solar cells.* Physical Review B, 2005. **72**(8).

17. H. Frohne, et al., *Optimization of organic semiconductor devices by anode modification.* Organic Light-Emitting Materials and Devices Vi, 2002. **4800**: p. 172-181.

18. D. Klotzkin, et al., *A comparative study of electrode effects on the electrical and luminescent characteristics of Alq(3)/TPD OLED: Improvements due to conductive polymer (PEDOT) anode.* Journal of Luminescence, 2007. **126**(1): p. 225-229.

19. M. Petrosino, et al., *Effect of PEDOT : PSS ratio on the electrical and optical properties of OLEDs - art. no. 659310.* Photonic Materials, Devices, and Applications II, 2007. **6593**: p. 59310-59310.

20. P. Anzenbacher, et al., *Efficiency improvement of fluorescent OLEDs by tuning the working function of PEDOT:PSS using UV-ozone exposure.* Organic Electronics, 2010. **11**(5): p. 938-945.

21. W.H. Kim, et al., *Molecular organic light-emitting diodes using highly conducting polymers as anodes.* Applied Physics Letters, 2002. **80**(20): p. 3844-3846.

22. Y.K. Kim, et al., *Improved Efficiency and Adhesion Property between the PEDOT: PSS and ITO in Solution-Processed Organic Light-Emitting Diodes.* Inec: 2010 3rd International Nanoelectronics Conference, Vols 1 and 2, 2010: p. 921-922.

23. Clevios, *OLED Applications*. 2010 [cited 20/06/11]; Available from: http://www.clevios.com/index.php?page_id=3430.

24. A. Kuwahara, et al., *Carrier mobility of organic thin films using lateral electrode structure with optical slits.* Applied Physics Letters, 2006. **89**(13).

25. D.M. Pai, J.F. Yanus, and M. Stolka, *Trap-Controlled Hopping Transport.* Journal of Physical Chemistry, 1984. **88**(20): p. 4714-4717.

Chapter 5 The Effects of Phosphorescent Dopant Colour and Concentration on OLED Device Performance:

Sections of this chapter will be submitted for publication soon:

J. H. Cook* and A. P. Monkman, *'The Effects of Phosphorescent Dopant Colour and Concentration on OLED Device Performance'*, to be submitted.

5.1). Introduction:

The use of phosphorescent dopants to boost performance in OLED and PLED devices has been of substantial interest to the field for a long time now [1-8]. As discussed in 2.4.4), it is possible to use heavy metal phosphorescent dopants to achieve internal quantum efficiencies of 100% by harvesting previously unusable triplet states. Unfortunately, this does not transfer to the device E.Q.E. for a number of reasons including quenching, internal reflection and reabsorption.

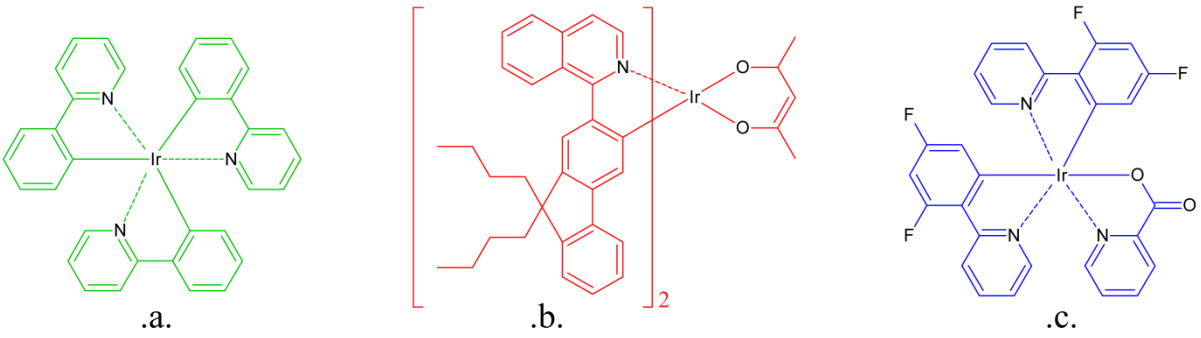

Figure 5.1: *The chemical structures of three different phosphorescent dopants used in this thesis. The structure of the green emitting dopant Ir(ppy)$_3$ is shown in .a. The structure of the red emitting dopant DBFIr is shown in .b. The structure of the blue emitting dopant FIrpic is shown in .c.*

Phosphorescent dopants have been produced in a wide range of colours and the properties of three popular ones have already been discussed in 2.6.5). These three are the dopants of interest to this chapter, the green emitter iridium (III) fac-tris(2-phenylpyridine) (Ir(ppy)$_3$) [9], the red emitter iridium (III) bis[2-(9,9-dibutylfluorenyl)-1-isoquinoline(acetylacetonate)] (DBFIr), and the blue emitter iridium (III) bis[(4,6-

fluorophenyl)-pyridinato-N,C2’]picolinate (FIrpic), the structures of which can be seen in Figure 5.1.

These organometallic compounds feature a heavy metal iridium centre which has a variety of different ligands attached in an octahedral geometry. The different ligands determine the colour of light emitted by the dopant. This is achieved by varying the electron donating or withdrawing properties of the ligands in order to tune the HOMO and LUMO levels of the dopant. The dopants can harvest previously inaccessible triplet states by mixing

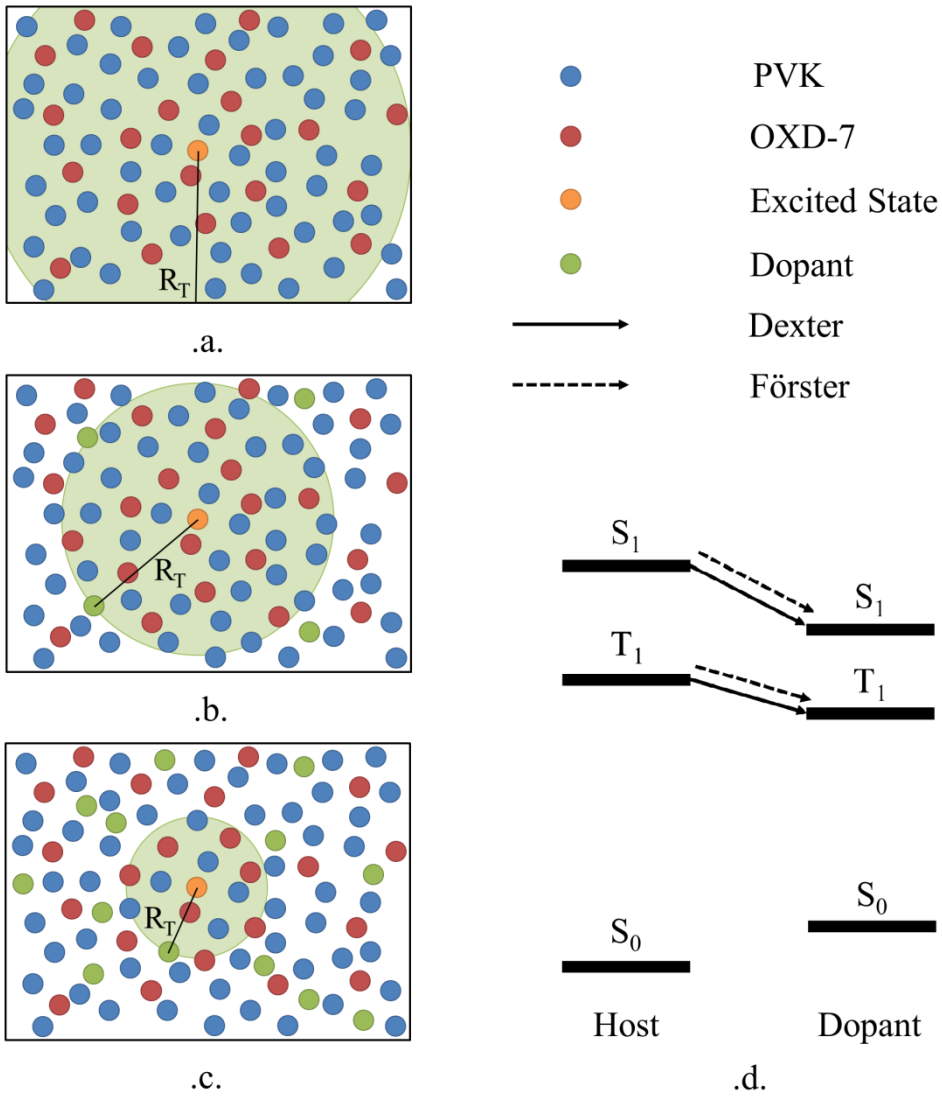

Figure 5.2: *Plots highlighting how the distance between excited species and phosphorescent dopant changes with concentration for .a. <2% dopant concentration, .b. 8% dopant concentration, and .c. 24% dopant concentration, where R_T is the distance between the donor and acceptor. Also shown are the different transfers between the singlet and triplet states of the donor and emissive molecules.*

triplet and singlet state character, allowing spin-orbital coupling to occur [10].

The three phosphorescent dopants mentioned above have been used in devices for a number of years and in this chapter, the effects of both dopant colour and concentration on device properties have been investigated. These properties include the obvious, such as device efficiency and brightness, as well as the more subtle such as carrier mobility, recombination and energy transfer properties. In phosphorescent OLED and phosphorescent PLED devices, dopants primarily harvest energy via three different methods, Förster transfer, Dexter transfer or direct charge trapping. Previous research [11, 12] has investigated the different channels of energy transfer between these dopants and their hosts but the exact degree of each mechanism remains open to speculation.

Energy transmitted via Förster or Dexter transfer depends on a number of factors including the distance between donor and acceptor and the spectral overlap between donor and acceptor, as discussed in more detail in 2.5). Dexter transfer has a range that is typically on the scale of < 10 Å [13, 14] as it involves electron tunnelling and is the transfer of energy from a neutral exciton to another neutral exciton, i.e. singlet to singlet or triplet to triplet transfer. For Förster transfer the process is a dipole-dipole interaction and as such, the range increases to approximately 30-50 Å [13, 14]; this is a transfer of a singlet or triplet excited state from a donor to an acceptor. Therefore, at higher concentrations the distance between donor and acceptors is likely to be reduced, as highlighted in Figure 5.2, resulting in more energy transfer occurring. These methods of energy transfer also require a spectral overlap between the emission spectrum of the donor and the absorption spectrum of the acceptor, rendering the dopant colour of great importance to the energy transfer process.

There is also the possibility that the dopant molecules may acquire charge by sequentially trapping a hole, followed by an electron, on the guest dopant, forming an

emissive complex [13, 14]. This process is heavily dependent on the energy levels of the donor and acceptor molecules, along with the overlap of their molecular orbitals. This pathway is most accessible when the HOMO of the acceptor is above that of the HOMO of the donor and the LUMO of the acceptor is below that of the LUMO of the donor. This is not strictly required; if the HOMO of the acceptor is above that of the donor and a hole is trapped, the cationic complex formed is strongly electron trapping. The energy levels [15-21] of the chemicals pertinent to this chapter feature in Figure 5.3, where it can be seen that all three phosphorescent dopants are possible direct charge trappers.

In order to assess these effects on OLED devices, the well-known and documented device materials poly(n-vinylcarbazole) (PVK) and 1,3,4-oxadiazole,2,2'-(1,3-phenylene)bis[5-[4-(1,1-dimethylethyl) phenyl] (OXD-7) have been used as host and electron transporter respectively. These materials have been used previously and have been shown to

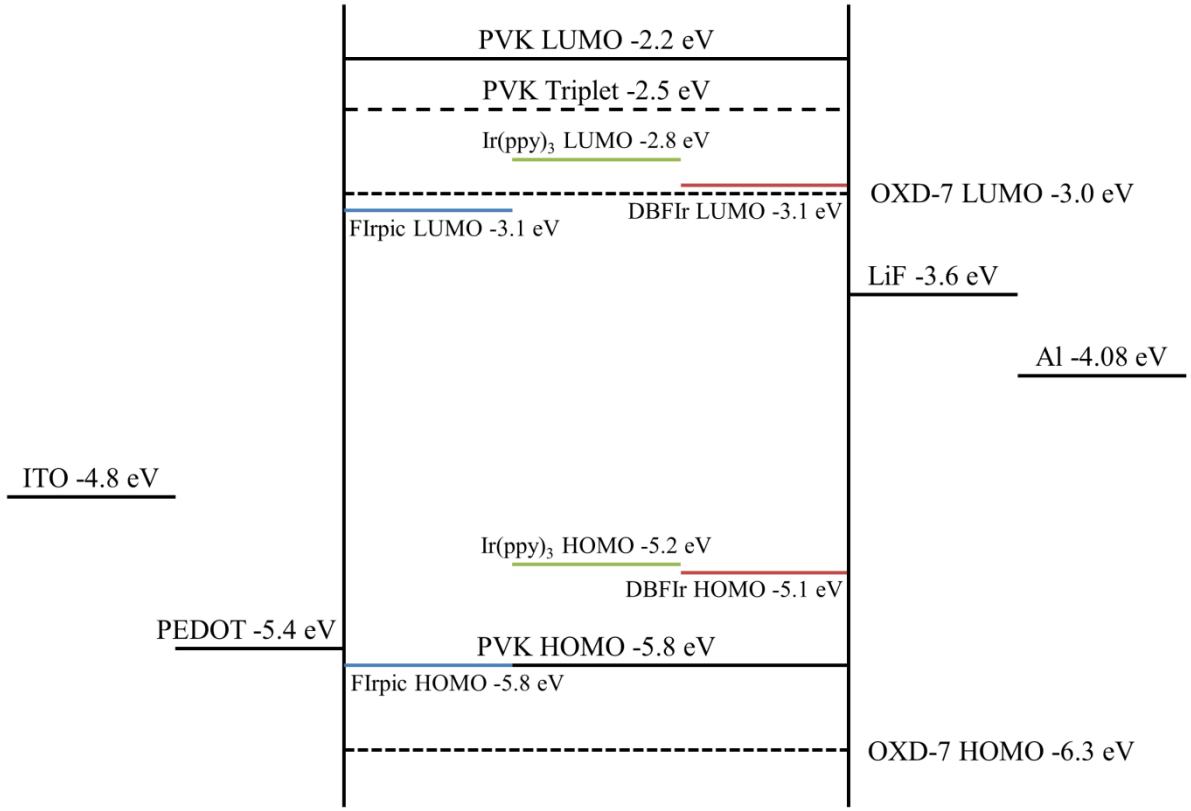

Figure 5.3: *Energy levels for the chemicals pertinent to this chapter. Of particular note is the fact that either both the HOMO and LUMO for FIrpic, or just the HOMO in the cases of DBFIr and Ir(ppy)$_3$, are within the HOMO of PVK and the LUMO of OXD-7, making all three phosphorescent dopants suitable for direct charge trapping.*

be able to host a wide range of different phosphorescent dopants. PVK is a host material with a relatively high triplet energy level [22-24] and is a good hole transporter [25]. This combined with the positions of its HOMO and LUMO levels allows for it to favourably host a wide range of phosphorescent dopants, including blue emitters [11], as a result of the downwards step between the energy levels of donor and acceptor. OXD-7 acts as an electron transporter, and is similar in this respect, in that its energy levels are also well suited for a wide range of phosphorescent dopants [22].

The aim of this investigation was to use these three different phosphorescent dopants to produce OLEDs and assess the effects of colour, or more accurately the dopant energy levels, and concentration on device performance. This has produced OLEDs where the device behaviour when varying dopant concentration is different depending on the dopant used. In addition to this, the device simulation software, SEmiconducting Thin Film Optical Simulation (SETFOS), was used to analyse the device results in an attempt to extract quantitative values for the device properties, such as carrier mobilities. During the previous chapter, SETFOS was introduced as a viable method for analysing device data, despite a couple of limitations. In this chapter these simulations have been continued, and using an updated version, SETFOS 4.0, several device parameters have been extracted from the physical device data.

5.2). Experimental:

5.2.1). Optical Characterisation:

Solid state absorption and emission spectra were obtained, using the methods described in 3.6.1) and 3.6.2). Excitation wavelengths corresponded to the point of maximum absorbance for the material under investigation. Solid state samples were drop-cast films, cast

from a 1:1 mixture of 175 $mg.mL^{-1}$ zeonex and 0.5 $mg.mL^{-1}$ of the polymer, both in chlorobenzene, and had a maximum absorbance of 2.0 OD.

5.2.2). Device Fabrication and Characterisation:

A number of devices were fabricated using the methods outlined in Chapter 3. These devices featured an ITO anode (150 nm, 16 Ω/□) commercially pre-coated on a glass substrate (24 mm x 24 mm), a hole-injection layer (HIL) of the commercial PEDOT HIL 1.5 from Heraeus (70 nm) and an active layer of PVK, OXD-7 and phosphorescent dopant. This was followed by a 1 nm thick electron-injection layer (EIL) of lithium fluoride (LiF) which was thermally evaporated using the method outlined in 3.3.4) and a shadow mask to produce parallel strips perpendicular to the ITO anodes, forming four individually addressable pixels per substrate each of area 5 mm x 4 mm. The LiF was capped with a 100 nm thick layer of aluminium cathode to protect it from oxidation. An evaporation pressure of the order of 10^{-6} mbar and a rate of approximately 0.1 $nm.s^{-1}$ was used for all of the evaporated layers produced. The devices were then encapsulated with DELO UV curable epoxy (Katiobond) and a 12 x 12 mm glass cover slide.

Half of the device pixels were characterised in a calibrated Labsphere LMS-100 integrating sphere, connected to a USB 4000 CCD spectrometer supplied by a 400 µm UV/Vis fibre optic cable, under steady state conditions as detailed in 3.5.1). The other half were characterised using the transient method outlined in 3.5.3) with a HP8114A function generator, an Agilent Infiniium 1 GHz 4 GSa/s oscilloscope and a standard Si-PIN-PD detector, with attached DHPCA-100 variable gain high speed current amplifier. Layer thicknesses were measured using a J. A. Woolam VASE Ellipsometer, as described in 3.5.4). The non-uniformity of the organic layer thicknesses across the samples leads to a 5–10 % error in device efficiencies and all measurements were averages over at least four devices.

5.2.3). SETFOS Simulations:

The material parameters required by SETFOS, such as individual layer thicknesses, were obtained and repeatable to within ±5%. Values not directly obtained by experimental methods were acquired from the literature or estimated using Table 4.9 in the SETFOS 4.0 User Manual. These values were entered into SETFOS using the graphical user interface.

SETFOS was instructed to sweep over the same voltage range that was used for device characterisation, including the same voltage step size. Several parameters, including electron and hole mobility, were selected to be free parameters and varied in order to achieve a good fit. Using the free parameters SETFOS was aiming to fit its values to the device current densities using a built in optimisation algorithm, allowing the extraction of quantitative device data.

5.3). Results and Discussion:

5.3.1). Optical Properties:

Table 5.1: *Photophysical data for the OLED materials.*

Material	λ_{max}^{abs} / nm	λ_{max}^{PL} / nm	CIE (x, y)	J(λ)
PVK	354	403	0.17, 0.06	
OXD-7	294	360	0.20, 0.07	
DBFIr	372	655	0.70, 0.29	84±4
$Ir(ppy)_3$	385	517	0.31, 0.64	103±5
FIrpic	299	470	0.14, 0.31	34±2

The photophysical data for the OLED materials is summarised in Table 5.1. The values for λ_{max}^{abs} and λ_{max}^{PL} for the three phosphorescent dopants, along with the absorption and emission spectra in Figure 5.4 and Figure 5.5, agree well with those on the manufacturer's website [26-28]. The CIE coordinates for the three dopants have been plotted in Figure 5.4, and these can be readily compared to the CIE coordinates for OLED devices in Figure 5.7, Figure 5.9 and Figure 5.11. It is also worth noting here the difference in the colour

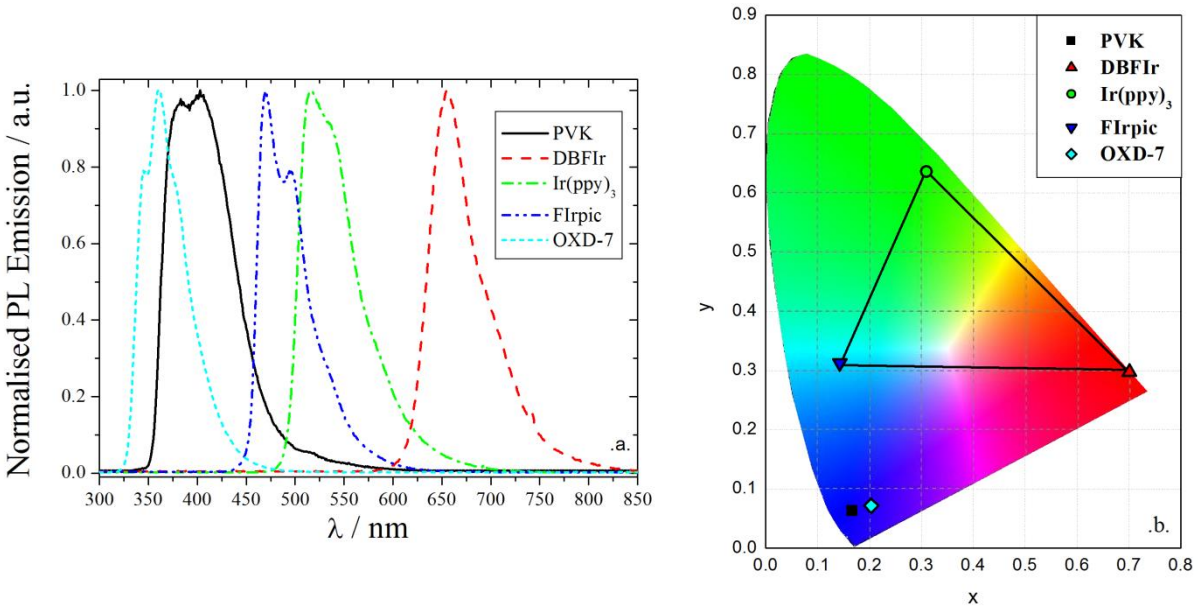

Figure 5.4: *Plots of (a) Normalised thin film based PL emission spectra for the OLED materials, and (b) The CIE coordinates for the emission spectra, where the black triangle highlights the colour gamut produced by the three phosphorescent dopants.*

gamut obtained from the three phosphorescent dopants compared to the sRGB gamut in Figure 3.7 on page 69. Whilst DBFIr and $Ir(ppy)_3$ are close to, if not better, than the sRGB values, the coordinates for FIrpic are very different, it being a sky blue emitter, meaning a large area of CIE space is inaccessible. This highlights the need for OLED devices capable of emitting light in the deep blue region of the visible spectra, which is something that will be discussed in more details in Chapters 6 and 7.

The overlap integrals, J, required for Förster and Dexter transfer have been determined for the three phosphorescent dopants using Figure 5.5. These values have then been given in Table 5.1, where it is possible to see that $Ir(ppy)_3$ has the highest degree of overlap whilst FIrpic has the lowest. From this it could initially be assumed that $Ir(ppy)_3$ and DBFIr will benefit most the from Förster and Dexter transfer, whilst FIrpic will benefit least. However, as the values for λ_{max}^{abs} correspond to the absorption of the ligand centre whilst the smaller peaks at 505 nm and 440 nm for DBFIr, 450 nm and 410 nm for $Ir(ppy)_3$, and 420 nm and 380 nm for FIrpic correspond to the transition from the ground state to the triplet and

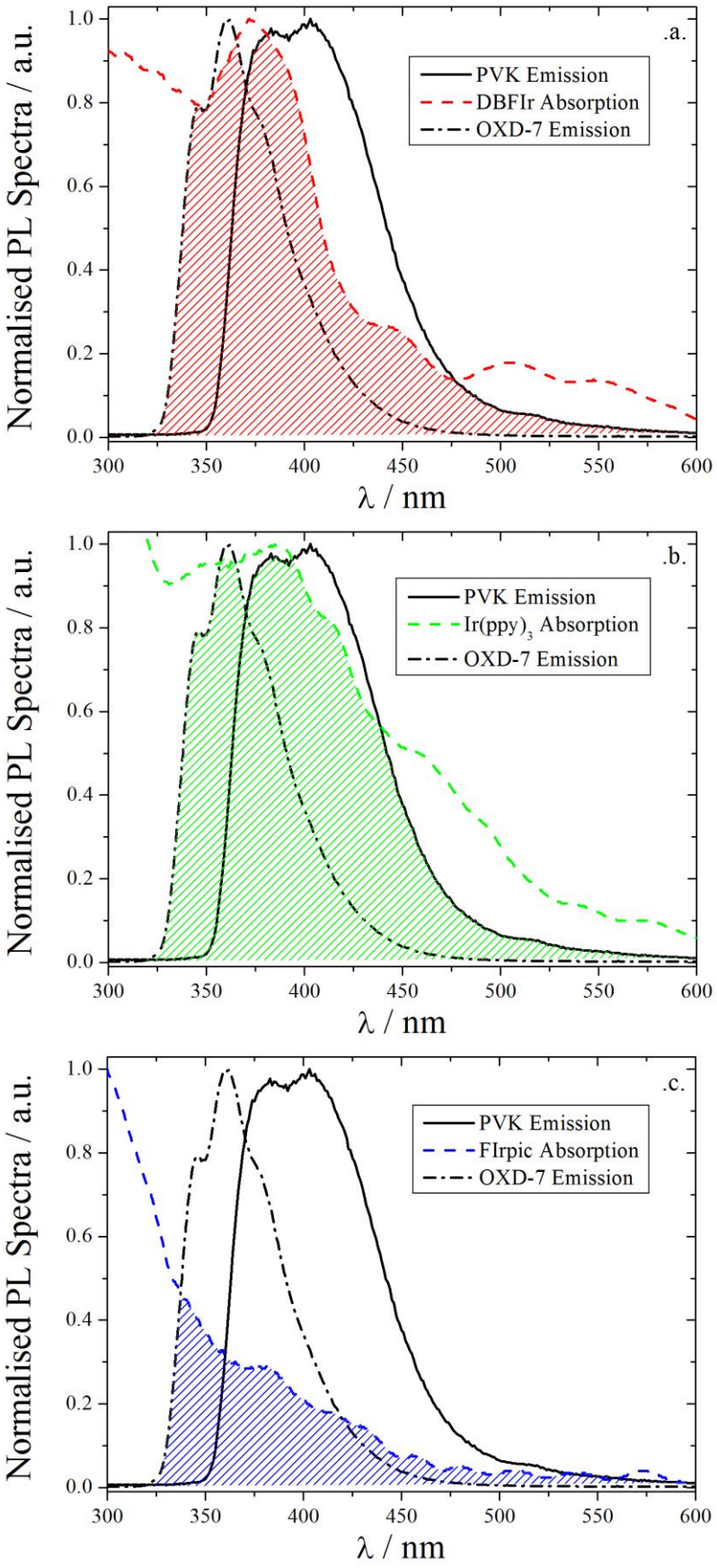

Figure 5.5: *Plots of the absorption spectra for (a) DBFIr, (b) Ir(ppy)$_3$ and (c)FIrpic with the emission spectra of PVK and OXD-7, where the shaded areas under the curves represent the overlap integral, J, for the three phosphorescent dopants, the values of which can be found in Table 5.1.*

singlet MLCT excited states respectively [13], the overlap for these secondary peaks is also important. Therefore, despite FIrpic having the lowest overall overlap, it has potentially the best overlap for MLCT absorption peaks, resulting in efficient energy transfer from the host to some of the dopant's most emissive states.

5.3.2). Red Device Results:

DBFIr was used in nine devices of the structure Glass | ITO (150 nm) | PEDOT HIL 1.5 (70 nm) | PVK : 40% OXD-7 : x% DBFIr (50 nm) | LiF (1 nm) | Al (100 nm), where x was equal to 0.15%, 0.5%, 1%, 2%, 5%, 8%, 12%, 18% and 24%. The results for these devices can be seen in Figure 5.6.

From the results, it can be seen that there is an initial steep increase in the device properties of E.Q.E., brightness and current efficiency. The increase peaks at 5% for the E.Q.E. and current efficiency and at 8% for the device brightness. After this peak, there is a slower decline in E.Q.E. and device efficiency whilst the maximum brightness remains steady between 80-90 $cd.m^{-2}$. This is highlighted in parts .f., .g. and .h. of Figure 5.6, which show the maximum values of the different curves from parts .b., .c. and .d. of the figure. Corresponding to the initial increase in brightness is a decrease in the current density passing through the device at 12 V. This can be attributed to an increase in recombination between carriers increasing the device brightness and reducing the current density passing through the device. This is followed by the current density levelling off between 5-8%, consistent with the lack of change in maximum brightness. This can be seen in part .e. of Figure 5.6.

Also of interest are the emission spectra of the devices. From Figure 5.7 .a. it can be seen that at the concentration of 0.5%, in addition to the expected DBFIr emission in the 600-800 nm range, there is also emission present from PVK in the 400-550 nm range at high voltages. This is revealed to be a phenomenon reserved for low dopant concentrations, as

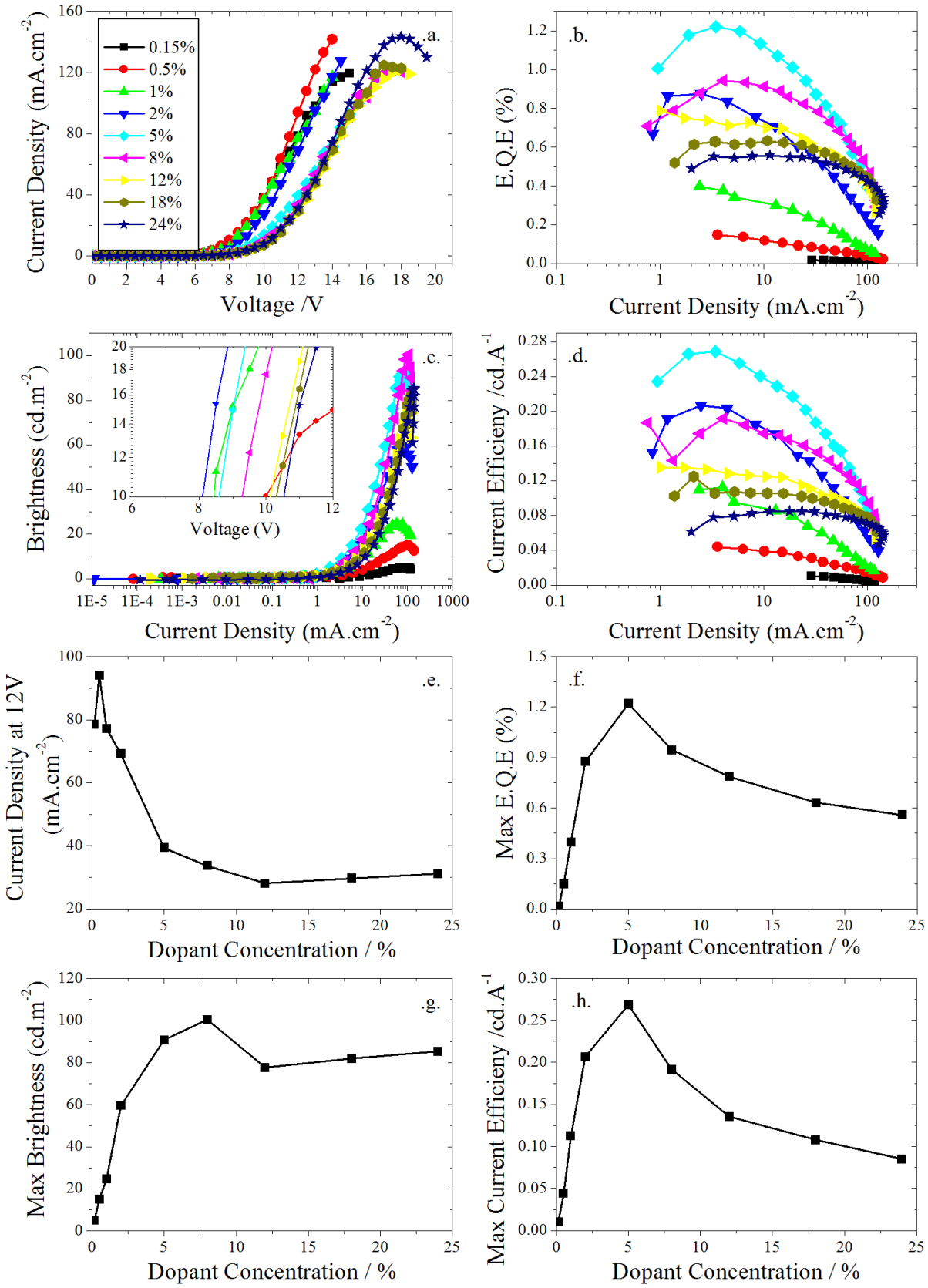

Figure 5.6: *Plots of (a) J-V curves, (b) E.Q.E. vs. J, (c) Luminance vs. J, (d) Device Efficiency vs. J for the polymers (e) J at 12V vs. Concentration, (f) Maximum E.Q.E. vs. Concentration, (g) Max Luminance vs. Concentration and (h) Device Efficiency vs. Concentration for nine different concentrations of the phosphorescent dopant DBFIr. Inset to (c) shows the turn on voltages for the nine devices in a plot of Luminance vs. V.*

Figure 5.7 .b. shows the migration of the CIE coordinates at peak brightness as the concentration of dopant is increased from 0.15% to 24%. It can be seen that at the lowest dopant concentration of 0.15%, due to the extra emission from the PVK host, the CIE coordinates have been skewed towards the blue area of the plot. As the concentration is increased to 5%, the coordinates shift towards the red area, corresponding to a reduction in the emission from PVK. This shift matches the increase in overall maximum brightness and device efficiencies discussed earlier. After 5%, the CIE coordinates stabilise deep in the red region, at a comparable point to that seen for pure DBFIr in Figure 5.4. As the PVK emission is only present at both low concentrations and high voltages, this is an indicator of Förster transfer [13] between the PVK and the DBFIr. At low concentrations the excited states of DBFIr are saturated, the excess carriers and excitons remain on the PVK and recombine there, so some emission comes from the PVK.

From the results shown in Figure 5.6 and Figure 5.7 it is possible to conclude that DBFIr is receiving excitation through a mixture of both Förster energy transfer and direct charge trapping, although it is not possible to identify the dominant mechanism. The evidence

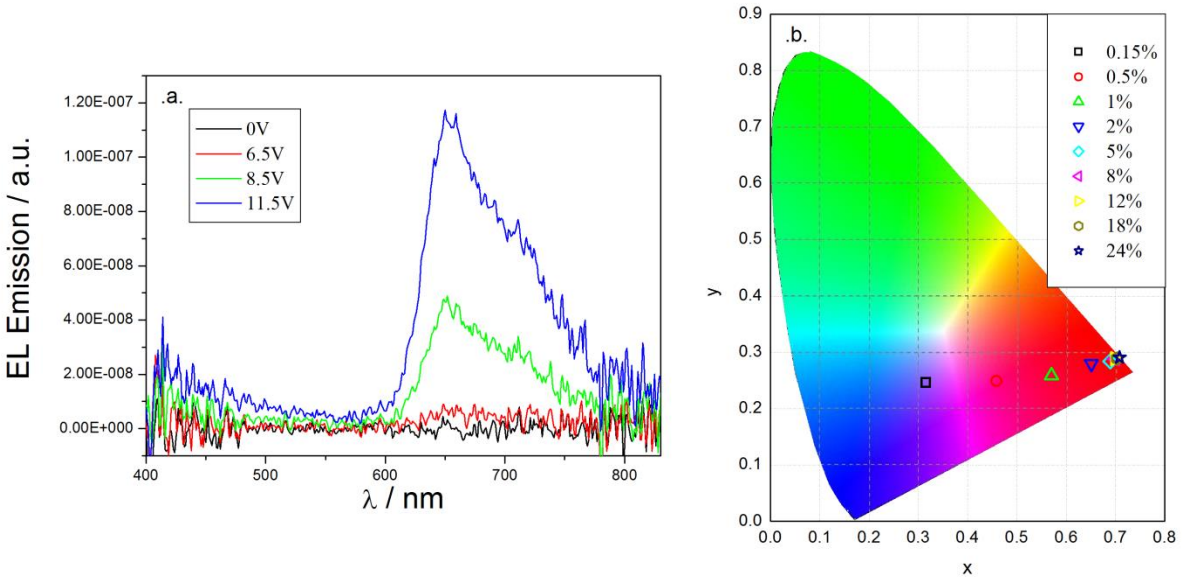

Figure 5.7: *Plots of (a) The EL emission spectra for a device with 0.5% DBFIr at a range of voltages, of particular note is the emission between 400-550 nm that appears at high voltages that is from the PVK host and is a sign of Förster transfer, and (b) A CIE plot showing the migration of CIE coordinates as the concentration of DBFIr is increased from 0.15% to 24% .*

for direct charge trapping is the change in current density with increased dopant concentration [29] observed in Figure 5.6 .e., whilst the evidence for Förster transfer is the prescence of host emission at high voltages and low dopant concentrations in Figure 5.7. If direct charge trapping were the dominant mechanism then there would be no emission observed from the host, whilst if Förster transfer were dominant then there would be no significant concentration dependence for the current density of the devices; this will be discussed further in 5.3.4).

It has previously been shown that it is unlikely for Dexter transfer to occur [12] so this can be ruled out. Once the concentration approaches and exceeds 5% the DBFIr molecules are no longer saturated, resulting in no more emission from the PVK. As the brightness and current density remains constant after 5% it can be assumed that a different limiting factor has been introduced, most likely a limited availability of either holes or electrons. In this case, due to the LUMO of the dopant being slightly above that of the OXD-7 LUMO, the limited charge carrier can be assumed to be the electron; either due to poor charge transfer, or the possibility of thermally activated back transfer, as discussed further in 5.3.4). This is reinforced by the SETFOS simulations discussed in 5.3.6).

5.3.3). Green Device Results:

$Ir(ppy)_3$ was used in nine devices of the structure Glass | ITO (150 nm) | PEDOT HIL 1.5 (70 nm) | PVK : 40% OXD-7 : x% $Ir(ppy)_3$ (50 nm) | LiF (1 nm) | Al (100 nm), where x was equal to 0.15%, 0.5%, 1%, 2%, 5%, 8%, 12%, 18% and 24%. The results for these devices can be seen in Figure 5.8.

Initially the results follow the same pattern as for the red devices, featuring a steep increase in the device properties of E.Q.E., brightness and current efficiency. The increase peaks at 2% for the E.Q.E. and current efficiency and at 5% for the device brightness. After

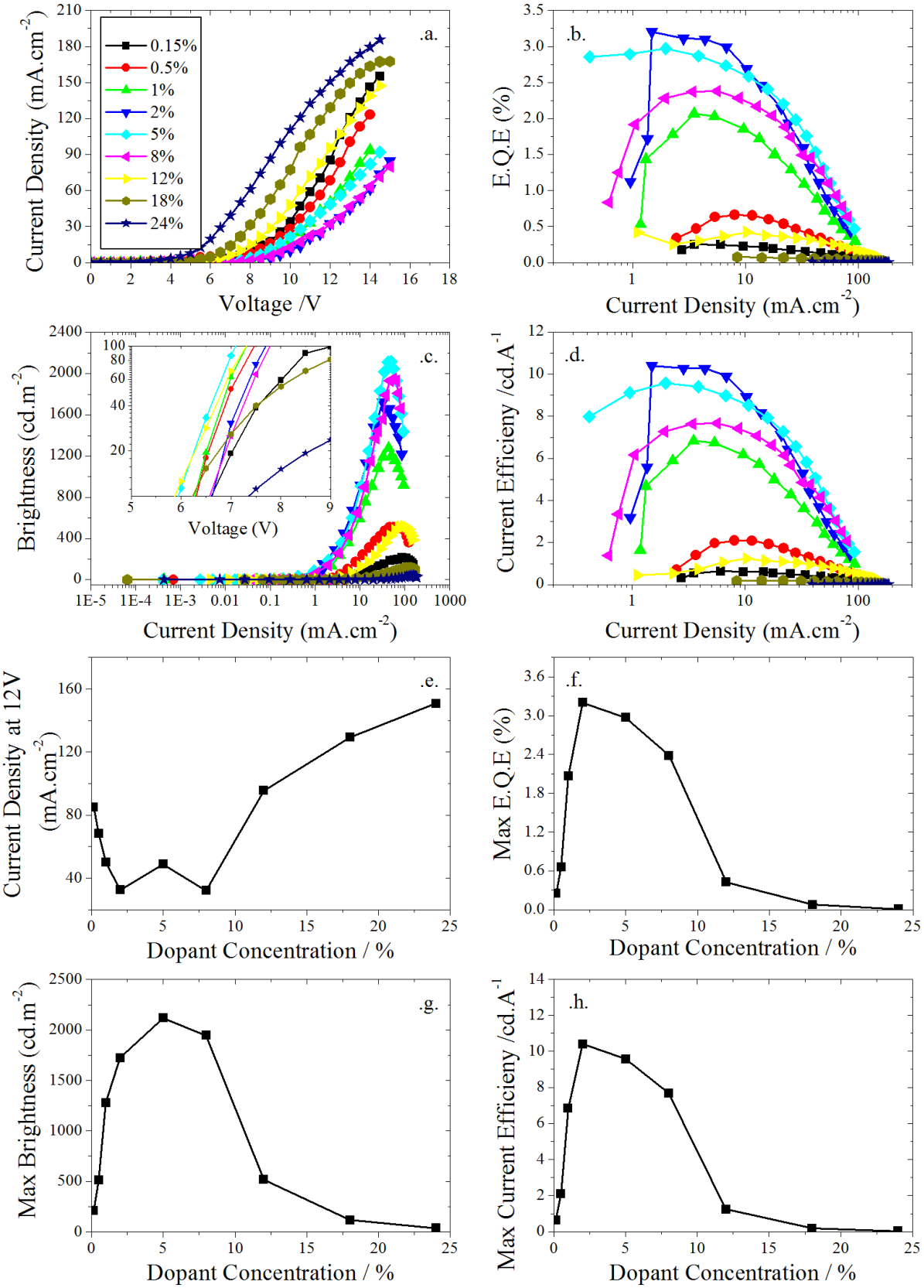

Figure 5.8: *Plots of (a) J-V curves, (b) E.Q.E. vs. J, (c) Luminance vs. J, (d) Device Efficiency vs. J for the polymers (e) J at 12V vs. Concentration, (f) Maximum E.Q.E. vs. Concentration, (g) Max Luminance vs. Concentration and (h) Device Efficiency vs. Concentration for nine different concentrations of the phosphorescent dopant Ir(ppy)$_3$. Inset to (c) shows the turn on voltages for the nine devices in a plot of Luminance vs. V.*

the peak, the results deviate from those of the red devices and there is an almost equally steep decline in E.Q.E., device efficiency and maximum brightness. This is highlighted in parts .f., .g. and .h. of Figure 5.8, which show the maximum values of the different curves from parts .b., .c. and .d. of the figure. As with the red devices, the current density at 12 V varies inversely with brightness and can again be attributed to a change in the degree of recombination between carriers and can be seen in part .e. of Figure 5.8.

As with the device characteristics, there are similarities between the migration of CIE coordinates at peak brightness for the red and green devices, as the concentration of dopant is increased from 0.15% to 24%. From Figure 5.9 .a. it can be seen that at the lowest dopant concentration of 0.15%, there is again emission coming from the PVK host rather than just the dopant, this can be identified by the significantly higher zero y-intercept for the 0.15% concentration devices. This again provides evidence for Förster transfer, as there is emission from the PVK at high voltages and low concentrations that disappears at higher dopant concentrations.

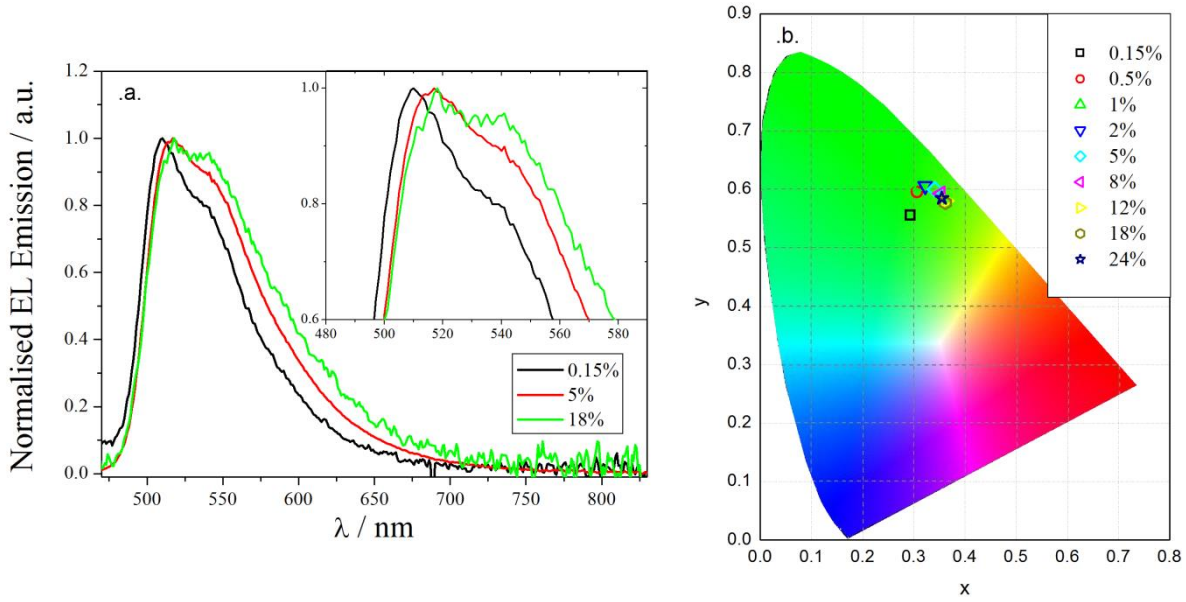

Figure 5.9: *Plots of (a) The EL emission spectra for devices with 0.15%, 5% and 18% Ir(ppy)3 at peak brightnesses, of particular note are the none zero y-intercept for 0.15% dopant due to emission from the PVK host, which is a sign of Förster transfer, and the increasing red-shifting of the spectra with concentration, and (b) A CIE plot showing the migration of CIE coordinates as the concentration of Ir(ppy)3 is increased from 0.15% to 24%.*

From Figure 5.9 .b. it can be seen that the migration of CIE coordinates is less pronounced on this diagram as the spectra are more heavily weighted towards the green in agreement with the luminosity function. As the dopant concentration is increased from 0.15%, the emission from PVK decreases up until around 2-5% where the CIE coordinates are close to those for pure $Ir(ppy)_3$ films, as seen in Figure 5.4. This shift again corresponds to the increase in overall maximum brightness and device efficiencies discussed earlier. After 5% the emission shifts again but this time towards the red. From part .a. it can be seen that the peak emission from the Ir(ppy)3 shifts slightly to the red as concentration increases and the shoulders at around 550 nm and 600 nm increase in size. This is believed to be due to the aggregation of the Ir(ppy)3 at higher concentrations.

It is possible to conclude that $Ir(ppy)_3$ is also acting primarily as a direct charge trap, due to the heavy concentration dependence, and receives some excitation through Förster transfer, due to the CIE shift. However, the LUMO of the $Ir(ppy)_3$ is well above that of the OXD-7, making it unlikely for electrons to be directly trapped. This makes cationic complex formation followed by electron trapping the most likely mechanism for exciton formation in these devices. Unlike DBFIr, it has previously been established that Dexter transfer can occur but the exact degree is unknown [12].

After 5%, the brightness and efficiency of the devices decrease significantly whilst the current density increases again and exceeds its original value for low dopant concentration. This is most likely due to aggregation of the $Ir(ppy)_3$ molecules at higher concentrations which can be identified by an increase in the roughness of the layer morphology with concentration [30]. Aggregation is also believed to open up new long-range non-radiative decay channels, such as triplet-triplet annihilation, as well as short-range non-radiative channels, such as the formation of non-emissive triplet excimers [31]. The degree of aggregation quenching can also assessed by using the red-shifting of the emission spectra in

Figure 5.9 with concentration. The main peak at approximately 510 nm is believed to be due to monomer emission whereas the shoulder at 550 nm is due to excimer formation that occurs when a monomer exciton is transferred to unexcited adjacent $Ir(ppy)_3$ molecules via a thermally activated process [32].

It is also possible that at higher concentrations one of the non-radiative channels is that the $Ir(ppy)_3$ molecules are acting as charge transporters [33]. This is believed to be possible due to the relatively high degree of overlap between the absorption and emission spectra of $Ir(ppy)_3$, which would allow for Förster and Dexter transfer to occur between them [32], and explains why this is not observed for either DBFIr or FIrpic. This would also explain why the current is able to exceed that of the lowest concentration for the three dopants, where the current density would be limited by the properties of the PVK and OXD-7 and relatively unaffected by the dopant molecules.

5.3.4). Blue Device Results:

FIrpic was used in nine devices of the structure Glass | ITO (150 nm) | PEDOT HIL 1.5 (70 nm) | PVK : 40% OXD-7 : x% FIrpic (50 nm) | LiF (1 nm) | Al (100 nm), where x was equal to 0.15%, 0.5%, 1%, 2%, 5%, 8%, 12%, 18% and 24%. The results for these devices can be seen in Figure 5.10.

From the results it can be seen that, unlike for DBFIr and $Ir(ppy)_3$, there is a continual increase in the device properties of E.Q.E., brightness and current efficiency from 0.15% to 24% dopant concentration. This is highlighted in parts .f., .g. and .h. of Figure 5.10. Also differing from the DBFIr and $Ir(ppy)_3$ results are those of the current density. Previously the changes in brightness corresponded inversely to changes in current density. However, for FIrpic the current density remains mostly constant whilst the brightness increases, as can be seen in part .e. of Figure 5.10. This means that the number of carriers passing through the

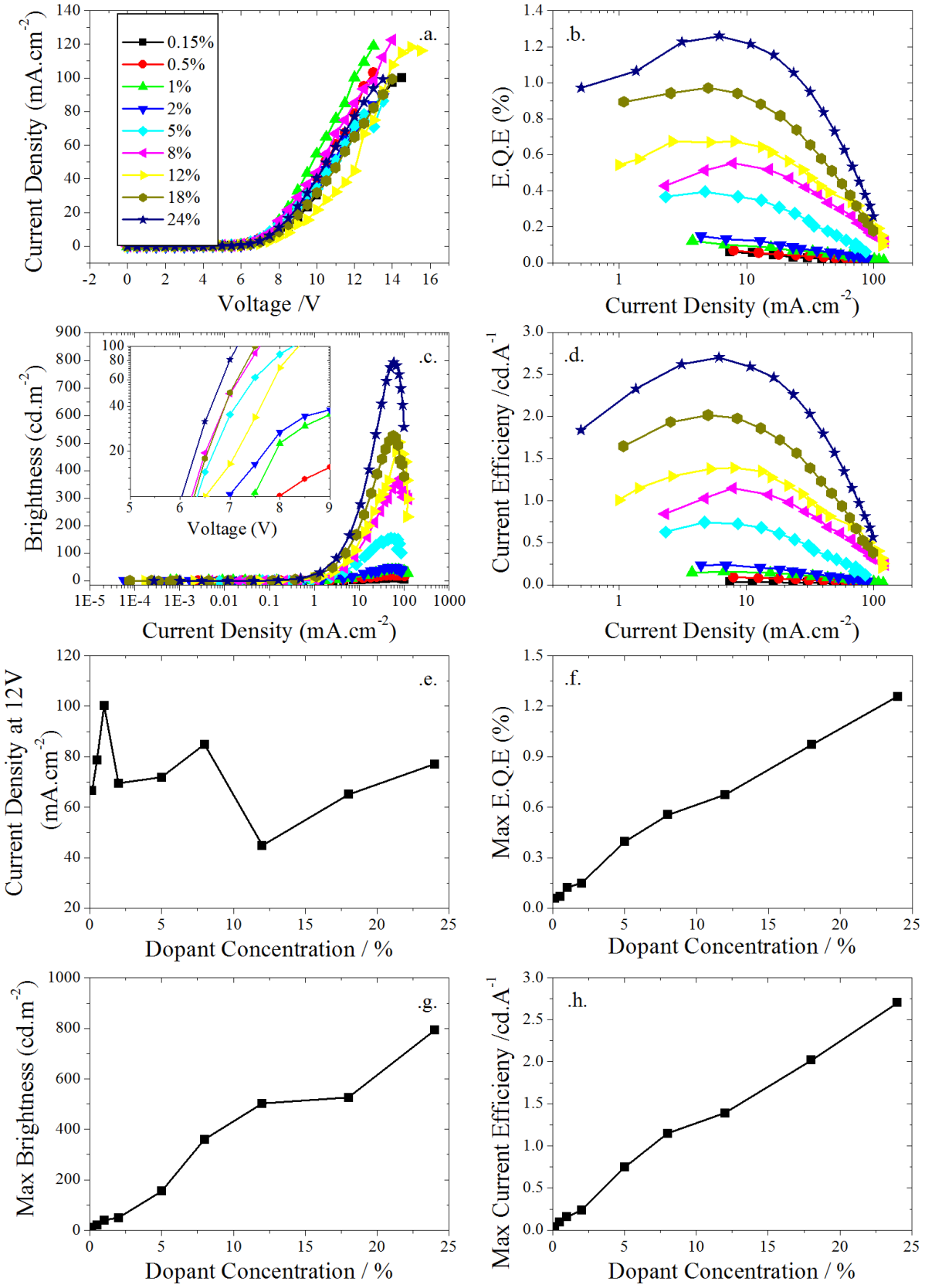

Figure 5.10: *Plots of (a) J-V curves, (b) E.Q.E. vs. J, (c) Luminance vs. J, (d) Device Efficiency vs. J for the polymers (e) J at 12V vs. Concentration, (f) Maximum E.Q.E. vs. Concentration, (g) Max Luminance vs. Concentration and (h) Device Efficiency vs. Concentration for nine different concentrations of the phosphorescent dopant FIrpic. Inset to (c) shows the turn on voltages for the nine devices in a plot of Luminance vs. V.*

device must be increasing with concentration to counteract those lost due to the increased recombination.

This is most likely due to how close the energy levels of FIrpic are to those of the host, meaning that whilst the dopant is able to accept charge it is also able to donate it[14, 23]. This means that, unlike for the other two dopants charges accepted by the FIrpic molecules are not trapped until recombination occurs. In addition, this means that the current density passing through the device is only limited by the ability of the PVK and OXD-7 to transport charge and unaffected by the addition of the dopant, reinforced by the observation that the current density at 12V remains at approximately 80 $mA.cm^{-3}$, the same current density observed at the lowest dopant concentrations when it would have little effect on the transport properties.

Again, similar to the CIE figures for DBFIr and $Ir(ppy)_3$, there is a migration of CIE coordinates from the region of PVK emission to the emission of the dopant as the concentration is increased from 0.15% to 24%. From Figure 5.11 .a. it can be seen that at the concentrations of 0.5% and 2%, emission is again coming from the PVK host as well as the

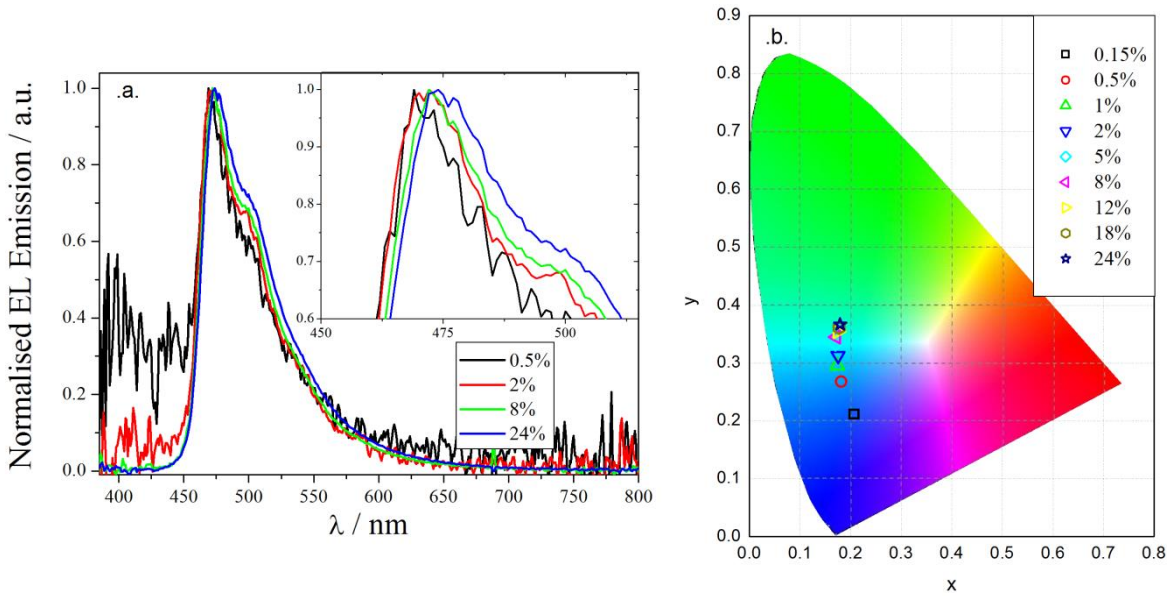

Figure 5.11: *Plots of (a) The EL emission spectra for devices with 0. 5%, 2%, 8% and 24% FIrpic at peak brightnesses, of particular note are the none zero y-intercepts for 0.5% and 2% dopant due to emission from the PVK host, which is a sign of Förster transfer and (b) A CIE plot showing the migration of CIE coordinates as the concentration of FIrpic is increased from 0.15% to 24%.*

dopant, as demonstrated by the emission present in the 400-450 nm region. This is an indicator of Förster transfer between the PVK and the FIrpic, as at low concentrations the FIrpic is saturated at high voltages. From part .b. it can be seen that as the concentration is increased, the emission from PVK can be seen to decrease up until around 8% where the CIE coordinates stabilise in the sky blue region, close to the coordinates seen for a pure FIrpic film in Figure 5.4. From part .a. it can also be seen that there is a small red shift of the primary peak and an increase in the shoulder emission in a similar manner to that seen in the emission spectra for $Ir(ppy)_3$ in Figure 5.9.

From the results shown in Figure 5.10 and Figure 5.11 it is possible to conclude that Förster transfer is now the dominant transfer mechanism and the lack of change in current density with concentration indicates that FIrpic is most likely no longer still acting as a direct charge trap, although this cannot be confirmed. The increase in Förster transfer is due to the high degree of overlap between the emission spectra of PVK and OXD-7, and the MLCT absorption peaks of FIrpic allowing for efficient energy transfer as discussed in 5.3.1).

As the concentration approaches and exceeds 8% the FIrpic molecules are no longer saturated, resulting in no more emission from the PVK. However, as discussed earlier there is likely to be a large degree of thermally activated hole back transfer between dopant and host, due to the proximity of the energy levels. This accounts for the slow and steady continuous increase in device properties and highlights the importance of selecting suitable host materials to match the dopants. In order to investigate at what dopant concentration the continuous increase in device properties ends, a further set of devices with concentrations of 24%, 36% and 48% was produced. The device properties continued to increase and peaked at around 36% and then decreased again at 48%; the decrease is again most likely due to aggregation quenching, similar to that observed for $Ir(ppy)_3$, opening new non-radiative decay channels.

5.3.5). Transient Electroluminescence Results:

The two remaining untested pixels from the red, green and blue devices were tested under transient conditions, as covered in 3.5.3) in more detail. Pulses of frequency 1 kHz and of width 50 μs were applied from 4 V to 20V in 1 V steps. The responses of the devices can be seen in Figure 5.12.

From Figure 5.12, it can be seen that the three different dopants produced similar results in that there is an increasingly quick initial response as the voltage is increased, followed by a second increase several orders of magnitude slower, and finally an exponential decrease once the pulse is complete. The two different increases are thought to be due to the difference in mobility between the two carriers [34]. The red and green devices in Figure 5.12 .a. and .b. are especially similar and the figures are almost identical in their responses. The response for the blue devices, as seen in Figure 5.12 .c., is different to the other two in that after the initial sharp response the second increase, corresponding to the second carrier, is larger than that of the red and green devices, giving it a different shape. This is no doubt due to a change in one of the carrier mobilities; it is not possible to determine which carrier mobility, electron or hole, has changed but given the energy levels concerned it is most likely to be the electrons.

It can also be seen that the time taken for the EL intensity to decay to zero takes substantially longer for the blue devices than for the red and green devices. The natural lifetimes of $Ir(ppy)_3$ and FIrpic are both approximately 1 μs at 300K [35, 36], so there shouldn't be such a large difference between them. This implies that FIrpic's ability to transfer energy back [14, 23] to the host provides a source of delayed emission, and is the most likely cause for the observed differences between the dopants. This has been confirmed in a separate study [37], which ascribes the delayed emission to repopulation of the dopant

from a long lived PVK and OXD-7 exciplex complex. The difference in magnitude for the three dopants is due to the use of different exposures on the detector to maximise detection whilst avoiding saturation of the detector.

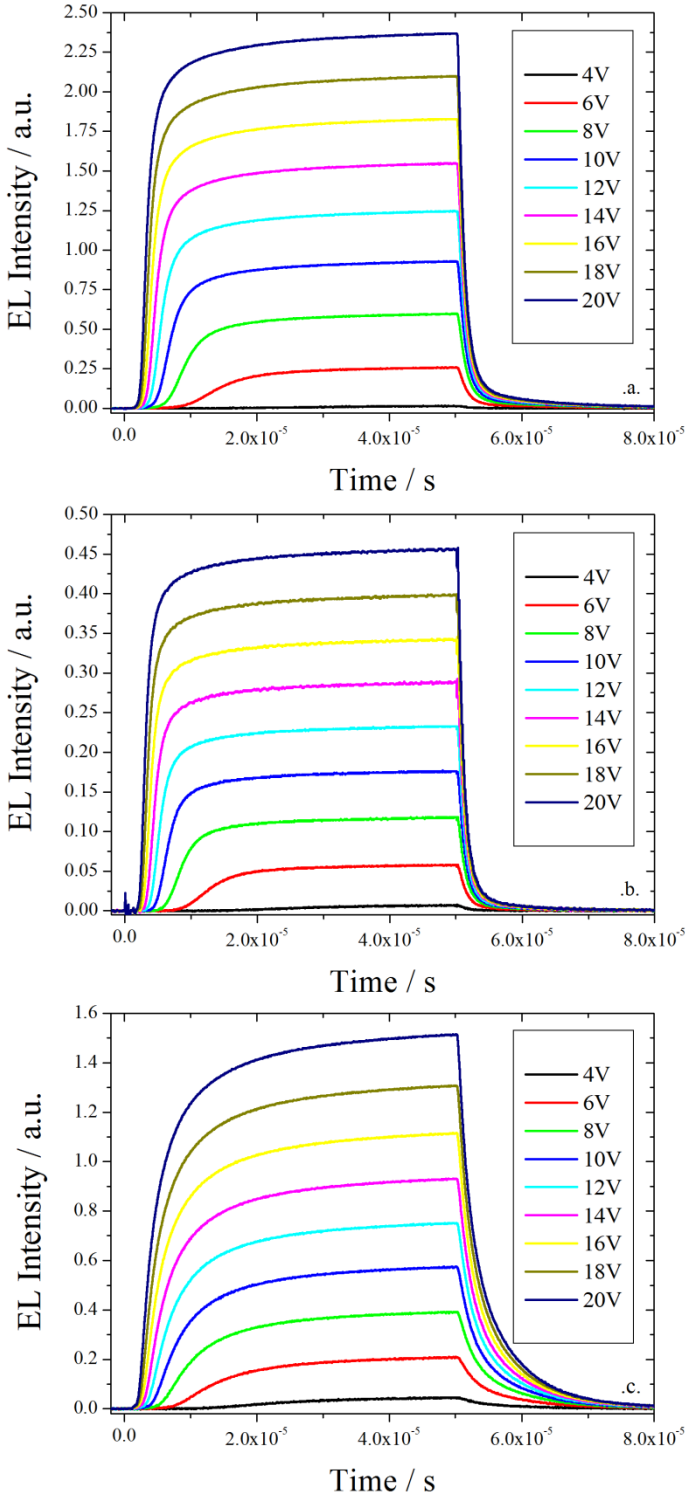

Figure 5.12: *Plots of EL Intensity vs. Time for .a. DBFIr, .b. Ir(ppy)$_3$,and .c. Firpic, showing the different transient responses at different voltages.*

After obtaining the raw transient responses they were then converted into mobilities using Equation 3.9, $\mu = \frac{L}{(t_d F)} = \frac{Ld}{t_d V}$ from page 71. Here L is the thickness of the emissive layer in meters, d corresponds to the field thickness which can be approximated to that of the emissive layer, and F is the electric field in $V.m^{-1}$ which is determined using $F = V/d$, where V is the applied voltage in volts. A value for t_d is extracted from the transient responses in Figure 5.12 by plotting a line of best fit through the initial response to the voltage pulse and recording the x-intercept [29].

The calculated mobilities for the different concentrations of the three dyes can be seen in Figure 5.13, although it is not possible to tell whether they correspond to the hole or electron mobilities. From these results it is possible to see that the carrier mobility increases with concentration for DBFIr and FIrpic but decreases for $Ir(ppy)_3$. The base mobility for the three dopants at their lowest concentration is approximately the same, between $5\text{-}6x10^{-7}$ $cm^2.V^{-1}.s^{-1}$, providing an effective value for the base mobility of PVK and OXD-7 in these devices. Also of interest is how the mobility changes with $F^{1/2}$ for the different concentrations of the different dopants.

From Figure 5.13 .a. and .e. it can be seen that for DBFIr and FIrpic there is typically an increase in mobility at low $F^{1/2}$, corresponding to overcoming low-lying carrier traps, followed by a section where the mobilities stay fairly constant with $F^{1/2}$. This is typical device behaviour [29], and is more pronounced at higher dopant concentrations and for FIrpic. At higher voltages there is a decrease in mobility, which is again more pronounced for FIrpic. The decrease at higher fields is likely due to an increase in the quenching of excited states at high fields. This is unlikely to be Förster or Dexter based, as they are field independent processes, but is instead likely to be polaron exciton quenching [38, 39], as at high field a lot more polarons are present, although the exact mechanism is unknown.

It is possible that the mechanisms of site blocking and carrier scattering are involved [40-44]. Whilst singlet states are short-lived, the triplet states are relatively long-lived and can have an effect on carrier mobility within the device. Triplet states can block a site within a transporting molecule and potentially scatter carriers, reducing the carrier mobility within the layer. At higher fields, and therefore higher triplet populations, there can be an observable decrease in carrier mobility due to the decreased number of available hopping sites, as seen

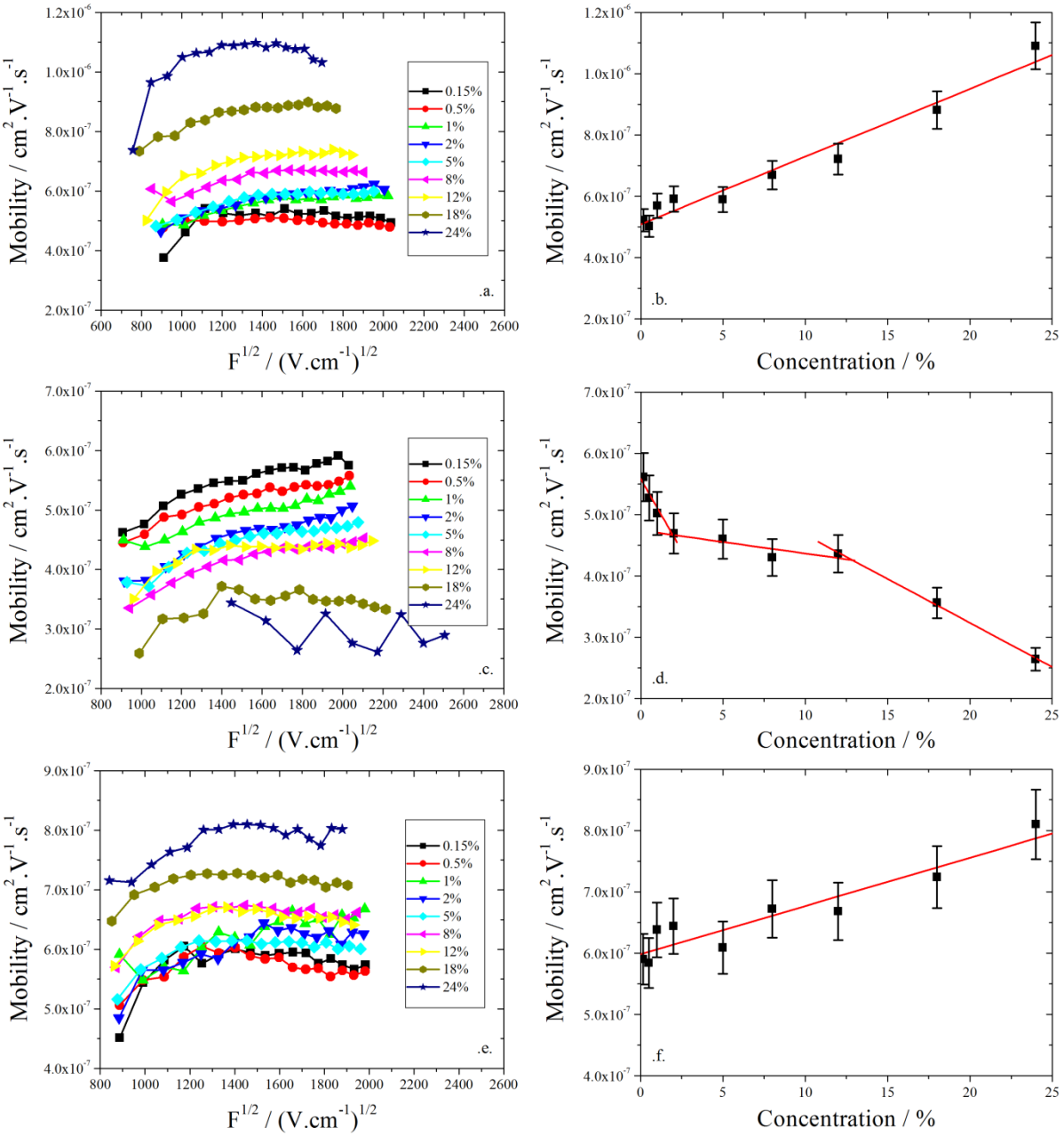

Figure 5.13: *Plots of Mobility vs. $F^{1/2}$ for different concentrations of .a. DBFIr, .c. Ir(ppy)$_3$, and .e. FIrpic. Also featured are plots of Mobility vs. Concentration at 12 V for .b. DBFIr, .d. Ir(ppy)$_3$, and .f. FIrpic. Here 12 V corresponds approximately to a value for $F^{1/2}$ of 1550 $(V.cm^{-1})^{1/2}$.*

for DBFIr and FIrpic in Figure 5.13. Further investigation using magnetic fields [40] may be able to identify the different behaviour of the singlet and triplet states for the different dopants and perhaps highlight if there are concentration dependencies within these devices.

For $Ir(ppy)_3$, as seen in Figure 5.13 .c., there is a linear increase with field for all but the two highest concentrations of dopant. The continuous linear increase in mobility with field for $Ir(ppy)_3$ is typical of devices which feature heavy trapping [45]. Due to the poor solubility of $Ir(ppy)_3$, and its subsequent aggregation, it is highly likely that there are high trapping regions within the emissive layer, this provides additional evidence for the trapping, or non-radiative decay, of charges at high dopant concentration discussed earlier.

Figure 5.13 .b., .d., and .f. show the change in mobility at 12 V for the DBFIr, $Ir(ppy)_3$ and FIrpic devices respectively with dopant concentration. From these figures it is possible to see that there is an increase of approximately $6x10^{-7}$ $cm^2.V^{-1}.s^{-1}$ from $5x10^{-7}$ $cm^2.V^{-1}.s^{-1}$ to $1.1x10^{-6}$ $cm^2.V^{-1}.s^{-1}$ for DBFIr, a decrease of approximately $3x10^{-7}$ $cm^2.V^{-1}.s^{-1}$ from $5.5x10^{-7}$ $cm^2.V^{-1}.s^{-1}$ to $2.5x10^{-7}$ $cm^2.V^{-1}.s^{-1}$ for $Ir(ppy)_3$ and an increase of approximately $2x10^{-7}$ $cm^2.V^{-1}.s^{-1}$ from $6x10^{-7}$ $cm^2.V^{-1}.s^{-1}$ to $8x10^{-7}$ $cm^2.V^{-1}.s^{-1}$ for FIrpic.

The linear increases in mobility for DBFIr and FIrpic is expected due to the increase in the density-of-states (DOS) [29], associated with the increase in dopant concentration, which allows an increase in the density of charge carriers within the emissive layer. The increase in mobility with concentration for FIrpic is not as large as that of DBFIr due to the competition occurring for back transfer with the PVK host. The decrease in mobility for $Ir(ppy)_3$ is likely due to the increase in deep traps associated with the increasing amount of aggregated $Ir(ppy)_3$ present within the emissive layer. This has a large initial effect up to 2%, after which it is less steep until 12% dopant concentration. This is most likely the concentration after which it is possible for the $Ir(ppy)_3$ to transfer charge as well, slowing the

decrease but still competing with the hosts causing an overall decrease. Above 12% the steep decrease resumes again as the increase in aggregation has potentially caused some phase separation [29] to occur within the emissive layer.

5.3.6). SETFOS Analysis:

In order to calculate the less easily measured device properties, such as the density of states, and to verify those already calculated, such as the carrier mobilities, device simulations were carried out with SETFOS 4.0. This is an updated version of the software SETFOS 3.2 that was able to reproduce the effects of different PEDOT on devices with limited success as discussed in Chapter 4.

In total seven parameters were varied between simulations in order to model the effects of the different dopants, and their range of concentrations. These parameters included the hole and electron mobilities, the density of states (otherwise known as the number of chargeable sites), the density of acceptor states, the density of donor states and the density of hole and electron traps. The simulations were fitted to the J-V plots from .a. of Figure 5.6, Figure 5.8 and Figure 5.10. From these figures, it can be seen that not all of the plots are substantially different as concentration changes for the different dopants. For the red devices, the concentrations in the range 0.15%-2% have approximately the same J-V curve whilst the concentrations in the range 5%-24% have approximately the same J-V curve. As such, one concentration from each group, 0.15% and 5%, was chosen to be simulated. For the green devices, instead of the nine J-V curves occupying set regions, they instead followed a pattern. As concentration increases, the J-V curve initially shifts to the right of the 0.15% plot up to the 2% plot and then to the left past the 0.15% plot up to the 24% plot. As such, the initial middle plot, 0.15%, and the two other extreme plots, 2% and 24%, were selected to provide

the full range of values. For the blue devices, the J-V curves all occupy approximately the same region and as such, the 24% device was chosen, as it performed best.

Table 5.2: *The mobility parameters used by SETFOS 4.0 to produce the simulated J-V curves seen in Figure 5.14 for the different concentrations of the different dopants.*

Colour	Conc.	μ_p / $cm^2.V^{-1}.s^{-1}$	μ_n / $cm^2.V^{-1}.s^{-1}$
Red	0.15%	(2.52±0.03)E-4	(3.98±0.04)E-5
	5%	(8.11±0.08)E-5	(2.06±0.02)E-5
Green	0.15%	(3.69±0.04)E-4	(8.71±0.09)E-7
	2%	(4.59±0.05)E-5	(2.01±0.02)E-5
	24%	(8.38±0.08)E-4	(4.37±0.04)E-4
Blue	24%	(2.77±0.03)E-3	(2.05±0.02)E-6

The experimental J-V curves and their corresponding simulated J-V curves for the selected devices can be seen in Figure 5.14 and the parameters that were varied to produce the simulated J-V curves can be seen in Table 5.2 and Table 5.4. From Figure 5.14 it can be seen that fits with a reasonable degree of agreement have been produced for each of the selected devices. However, from the mobility parameters in Table 5.2, it can be seen that not only are the magnitudes of the values wrong, when compared to the experimentally determined values, but the patterns produced are also incorrect. From the red device simulation results it can be seen that a decrease in both hole and electron mobility is predicted. This is in direct contradiction to the results discussed in 5.3.5), where an increase in mobility with concentration was observed for the DBFIr doped devices. For the green devices there is a substantial increase in electron mobility, whilst the hole mobility decreases and then increases again, when an overall decrease was observed experimentally. For the blue devices the mobilities are constant when experimentally an increase is expected.

Whilst the difference in absolute values has been covered and explained in Chapter 4, the differences in the patterns observed for mobility have not. Previously in Chapter 4, although the absolute values were incorrect, the patterns observed fitted with those of the known values. Here, however, they do not; this can be attributed to the change in the amount

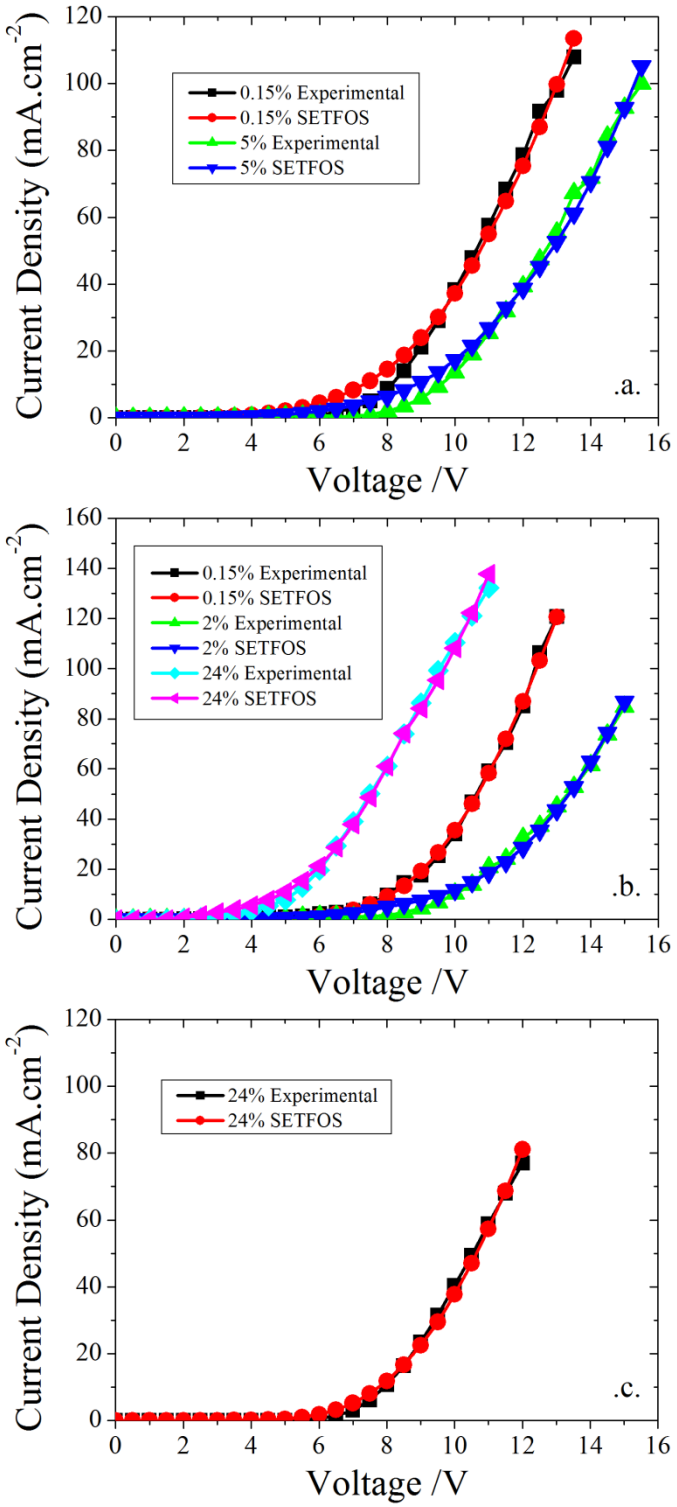

Figure 5.14: *Plots of the simulated J-V curves for (a) DBFIr, (b) Ir(ppy)$_3$ and (c) FIrpic, produced using SETFOS 4.0, along with the experimentally determined J-V curves already seen in Figure 5.6, Figure 5.8 and Figure 5.10.*

of recombination occurring in the devices of increasing dopant concentration. After incorporating the SETFOS parameter for the Langevin Recombination Efficiency, introduced in 4.1.1), into the simulations there was little change observed in the results, indicating that it was not being modelled successfully. However, if the recombination within the devices is

estimated empirically, using the sum of the carrier mobilities introduced in Equation 4.5 and the ratio of the current device brightness to the maximum observed device brightness for a particular dopant, more reasonable results can be produced. The results of this can be seen in Table 5.3.

Table 5.3: *The recombination weighted mobilities, produced using the simulated mobility values from SETFOS 4.0 from Table 5.2 and the ratio of device brightness to maximum device brightness as obtained from Figure 5.6 and Figure 5.8.*

Colour	Conc.	$(\mu_n + \mu_p)$ / $cm^2.V^{-1}.s^{-1}$	Brightness Ratio	Weighted $(\mu_n + \mu_p)$ / $cm^2.V^{-1}.s^{-1}$
Red	0.15%	(2.92±0.03)E-4	0.05	(1.46±0.01)E-5
	5%	(1.02±0.01)E-4	0.90	(9.15±0.08)E-5
Green	0.15%	(3.70±0.04)E-4	0.10	(3.72±0.04)E-5
	2%	(6.60±0.05)E-5	0.81	(5.37±0.04)E-5
	24%	(1.28±0.01)E-3	0.02	(2.25±0.02)E-5

From Table 5.3 it can be seen that with the weighted mobilities there is now the expected increase for the red devices that was observed experimentally. The results for the green devices are not completely correct, however there is now a decrease in mobility between 0.15% and 24% instead of a substantial increase and the three values are of the same order of magnitude. If the same analysis is performed on the simulated blue mobilities and corresponding device mobilities a linear increase is observed, corresponding well to that observed experimentally. This indicates that whilst this crude method of weighting improves upon the results obtained from SETFOS, there are still unknown factors that contribute to the mobility in addition to recombination.

On a more general note, the values obtained from SETFOS highlight an important trend that has been predicted within these devices, lending quantitative credibility to it. In 5.3.2), it was hypothesised that the limiting factor in device brightness after 5% was due to a shortage of electrons. From Table 5.2, it can be seen that the hole mobility is consistently higher than that of the electron mobility in the devices. This is expected due to the larger

energy gap between the work function of LiF and the LUMOs of PVK and OXD-7, when compared to that of the PEDOT work function and the HOMO of PVK.

Table 5.4: *The remaining parameters used by SETFOS 4.0 to produce the simulated J-V curves seen in Figure 5.14 for the different concentrations of the different dopants.*

Colour	Conc.	N_0 / cm^{-3}	Acceptor / cm^{-3}	Donor / cm^{-3}	N_{Tp} / cm^{-3}	N_{Tn} / cm^{-3}
Red	0.15%	(1.41±0.01)E21	(1.51±0.02)E16	(2.55±0.03)E16	(2.02±0.02)E5	(2.02±0.02)E5
	5%	(1.56±0.02)E21	(8.76±0.09)E16	(2.32±0.02)E15	(2.02±0.02)E7	(2.02±0.02)E5
Green	0.15%	(5.46±0.05)E20	(2.43±0.02)E12	(4.87±0.05)E17	(4.17±0.04)E4	(4.17±0.04)E6
	2%	(7.94±0.08)E20	(2.43±0.02)E16	(3.07±0.03)E17	(4.17±0.04)E4	(4.17±0.04)E6
	24%	(6.05±0.06)E20	(3.83±0.04)E14	(3.21±0.03)E17	(4.17±0.04)E2	(4.17±0.04)E6
Blue	24%	(2.60±0.03)E21	(1.51±0.02)E15	(5.92±0.06)E17	(4.17±0.04)E8	(4.17±0.04)E6

Unfortunately, there are no direct experimental measurements of the other five properties that have been changed in order to produce the fits in Figure 5.14. As such it is not possible to verify the validity of the values in Table 5.4, but it is possible to discuss them. It could be expected that as the dopant concentration is increased the acceptor density would also increase, along with the DOS, whilst the donor density stays constant. Whilst this is generally true, to reasonable approximation, the values for 2% $Ir(ppy)_3$ concentration do not fit this trend. This again indicates that there is something unaccounted for in the SETFOS model, related to the anomalous mobility values for the same concentration. The values for the acceptor and donor doping densities are used to directly supplement the local charge density, as shown in Equation 4.3, whilst N_0 is directly related to the carrier mobilities as shown in 4.1.1) and 4.1.2). As such, more investigation is needed to determine the true relationships between these three values and the dopant colour and concentration, and confirm expected changes in the DOS discussed in 5.3.5).

The density of carrier traps have also not been measured directly. From the SETFOS results it can be seen that the density of hole traps increases by a factor of 100 from the 0.15% dopant device to the 5% dopant device for red devices. This makes sense physically, as increasing the concentration of a dopant is likely to increase the amount of traps within the

emissive layer by introducing more defects. For green devices, the density of hole traps decreases by a factor of 100 from the 2% dopant device to the 24% dopant device. Initially, given the explanation above, this does not appear to be correct, especially considering the dramatic decrease in device performance and carrier mobility. However, at high concentrations $Ir(ppy)_3$ molecules are likely to be operating as charge transport molecules in addition to the PVK and OXD-7, which would account for the increase in current density through the devices observed in Figure 5.10 .a., making this decrease appear reasonable within the context of the SETFOS model. The absolute values calculated by SETFOS are again not in agreement with the previously calculated values [46] in the literature.

As in Chapter 4, it has been found that whilst SETFOS is able to model and fit experimental J-V curves, the parameters extracted do not correspond well with experimentally determined ones. The qualitative trends observed appear to be mostly correct and in keeping with the observed experimental ones and can therefore be used to support the conclusions drawn from them, whilst the discrepancies can be accounted for by limitations in the models used by SETFOS. For the parameters with no direct experimental verification, further work is needed in order to assess their validity and check for further limitations within SETFOS.

5.4). Conclusions:

Nine devices have been manufactured for three different phosphorescent dopants to investigate the effects of emission colour and dopant concentration on device performance and different device parameters. Each of the three dopants produced a series of devices that behaved in a different manner. This was due to a number of factors, including their energy levels, their effect on the layer morphology, and carrier availability. The red devices increased in device parameters quickly between concentrations 0.15% and 5% after which a

plateau was reached, most likely due to a shortage in availability of either electrons or holes. The green devices also had a quick initial increase in device properties between 0.15% and 5%. However, after 5% there was a steep decrease in device properties attributed to aggregation of the dopant within the emissive layer and the position of its LUMO above those of PVK and OXD-7. For the blue devices there was a steady increase in device properties from 0.15% to 24% whilst the current density remained unchanged. This was attributed to the proximity in energy levels of the dopant and the hosts allowing back transfer to occur between them.

Each of the three dopants exhibited signs of Förster transfer at low concentrations, highlighted by the migration of their CIE coordinates with voltage. The red dopant DBFIr appears to gain excitation through a combination of Förster transfer and direct charge trapping. In comparison, the green dopant $Ir(ppy)_3$ appeared to operate primarily through direct charge trapping, as evidenced by the high concentration dependency on current density, whilst the blue dopant FIrpic showed signs of acquiring excitation primarily through Förster transfer, as evidenced by the lack of change in J-V characteristics with concentration. This is likely due to the high degree of overlap between the emission spectra of PVK and OXD-7, and the absorption spectrum of FIrpic, allowing for efficient Förster transfer to occur.

Transient electroluminescence characterization was performed on the devices in order to determine their charge mobilities. It was shown that the charge mobility increased with concentration for both the red and blue dopants, whilst decreasing for increased concentrations of the green dopant. The increase in mobility for the red and blue devices is thought to be due to the increase in the DOS associated with an increase in dopant molecules, whilst the decrease for the green devices is thought to be due to the increased presence of deep charge traps caused by increasing amounts of aggregated $Ir(ppy)_3$.

SETFOS simulations were performed to model the J-V characteristics of a selection of the devices. After additional manipulation it was found that the qualitative trends mostly matched those of the experimentally determined mobilities, whilst their absolute values were not in agreement. This mirrored the conclusions drawn in Chapter 4, where SETFOS was found to be able to broadly match the trends but was unable to replicate the actual values due to limitations in the models used. Five parameters were also varied in the simulations that were unable to be verified experimentally and as such, more work is necessary to completely assess the abilities of SETFOS to accurately model device parameters and trends.

In conclusion, it has been shown that both the concentration and the energy levels of a phosphorescent dopant are important when selecting one for devices. The energy levels must be well matched to those of the hosts in order to maximise efficient energy transfer between them, but also avoiding thermally activated back transfer. Concentration is important to device performance as massive differences in efficiency can be observed for relatively small differences in concentration. This is especially pertinent if the dopant concerned aggregates at higher concentrations, which can negatively impact device performance to a significant degree. It has also been shown that despite a number of limitations observed within the SETFOS model, including how it handles recombination, it can be used to extract qualitative values and trends to back up experimentally deduced conclusions.

References:

1. M.A. Baldo, et al., *Highly efficient phosphorescent emission from organic electroluminescent devices.* Nature, 1998. **395**(6698): p. 151-154.
2. K. Brunner, et al., *Carbazole compounds as host materials for triplet emitters in organic light-emitting diodes: Tuning the HOMO level without influencing the triplet energy in small molecules.* Journal of the American Chemical Society, 2004. **126**(19): p. 6035-6042.
3. X.W. Chen, et al., *High-efficiency red-light emission from polyfluorenes grafted with cyclometalated iridium complexes and charge transport moiety.* Journal of the American Chemical Society, 2003. **125**(3): p. 636-637.

4. B.W. D'Andrade, et al., *White light emission using triplet excimers in electrophosphorescent organic light-emitting devices.* Advanced Materials, 2002. **14**(15): p. 1032-+.

5. S. Tokito, et al., *Confinement of triplet energy on phosphorescent molecules for highly-efficient organic blue-light-emitting devices.* Applied Physics Letters, 2003. **83**(3): p. 569-571.

6. A. Tsuboyama, et al., *Homoleptic cyclometalated iridium complexes with highly efficient red phosphorescence and application to organic light-emitting diode.* Journal of the American Chemical Society, 2003. **125**(42): p. 12971-12979.

7. S.J. Yeh, et al., *New dopant and host materials for blue-light-emitting phosphorescent organic electroluminescent devices.* Advanced Materials, 2005. **17**(3): p. 285-+.

8. Y. You and S.Y. Park, *Phosphorescent iridium(III) complexes: toward high phosphorescence quantum efficiency through ligand control.* Dalton Transactions, 2009(8): p. 1267-1282.

9. C.L. Lee, K.B. Lee, and J.J. Kim, *Polymer phosphorescent light-emitting devices doped with tris(2-phenylpyridine) iridium as a triplet emitter.* Applied Physics Letters, 2000. **77**(15): p. 2280-2282.

10. Y.T. Tao, C.L. Yang, and J.G. Qin, *Organic host materials for phosphorescent organic light-emitting diodes.* Chemical Society Reviews, 2011. **40**(5): p. 2943-2970.

11. J. Chang, et al., *Different energy transfer behaviors of poly (9-vinylcabazole) and polyfluorene derivative thin films upon doping with triplet emitters.* Journal of the Korean Physical Society, 2005. **47**(6): p. 1028-1034.

12. H.H. Liao, et al., *Triplet exciton energy transfer in polyfluorene doped with heavy metal complexes studied using photoluminescence and photoinduced absorption.* Physical Review B, 2006. **74**(24): p. 245211.

13. X. Gong, et al., *Electrophosphorescence from a polymer guest-host system with an iridium complex as guest: Forster energy transfer and charge trapping.* Advanced Functional Materials, 2003. **13**(6): p. 439-444.

14. B. Mi, et al., *Molecular hosts for triplet emitters in organic light-emitting diodes and the corresponding working principle.* Science China-Chemistry, 2010. **53**(8): p. 1679-1694.

15. L. Hou, et al., *Efficient single layer solution-processed blue-emitting electrophosphorescent devices based on a small-molecule host.* Applied Physics Letters, 2008. **92**(26).

16. Clevios, *OLED Applications*. 2010 [cited 20/06/11]; Available from: http://www.clevios.com/index.php?page_id=3430.

17. S. Sapp, et al., *Work function and implications of doped poly(3,4-ethylenedioxythiophene)-co-poly(ethylene glycol).* Applied Physics Letters, 2006. **88**(15).

18. S.E. Shaheen, et al., *Bright blue organic light-emitting diode with improved color purity using a LiF/Al cathode.* Journal of Applied Physics, 1998. **84**(4): p. 2324-2327.

19. B.P. Luther, et al., *Investigation of the mechanism for Ohmic contact formation in Al and Ti/Al contacts to n-type GaN.* Applied Physics Letters, 1997. **70**(1): p. 57-59.

20. Sigma-Aldrich, *Poly(9-vinylcarbazole)*. 2014 [cited 04/12/2014]; Available from: http://www.sigmaaldrich.com/catalog/product/aldrich/182605?lang=en&region=GB.

21. B.D. Chin, *Enhancement of efficiency and stability of phosphorescent OLEDs based on heterostructured light-emitting layers.* Journal of Physics D-Applied Physics, 2011. **44**(11).

22. D.H. Lee, et al., *Effect of electron- and hole-transporting materials on the performance of FIrpic-doped PVK phosphorescent devices.* Synthetic Metals, 2009. **159**(15-16): p. 1640-1643.

23. F.C. Chen, et al., *Energy transfer and triplet exciton confinement in polymeric electrophosphorescent devices.* Journal of Polymer Science Part B-Polymer Physics, 2003. **41**(21): p. 2681-2690.

24. V. Jankus and A.P. Monkman, *Is Poly(vinylcarbazole) a Good Host for Blue Phosphorescent Dopants in PLEDs? Dimer Formation and Their Effects on the Triplet Energy Level of Poly(N-vinylcarbazole) and Poly(N-Ethyl-2-Vinylcarbazole).* Advanced Functional Materials, 2011. **21**(17): p. 3350-3356.

25. P. D'Angelo, et al., *Electrical transport properties characterization of PVK (poly N-vinyl carbazole) for electrolumine scent devices applications.* Solid-State Electronics, 2007. **51**(1): p. 123-129.

26. A.D.S. Inc., *ADS077RE*. 2015 [cited 18/07/15]; Available from: http://www.adsdyes.com/products/ADS077RE.html.

27. A.D.S. Inc., *ADS060GE*. 2015 [cited 18/07/15]; Available from: http://www.adsdyes.com/products/ADS060GE.html.

28. A.D.S. Inc., *ADS065BE*. 2015 [cited 18/07/15]; Available from: http://www.adsdyes.com/products/ADS065BE.html.

29. J.S. Chen and D.G. Ma, *Effect of dye concentration on the charge carrier transport in molecularly doped organic light-emitting diodes.* Journal of Applied Physics, 2004. **95**(10): p. 5778-5781.

30. E.B. Namdas, et al., *Photophysics of Fac-tris(2-phenylpyridine) iridium(III) cored electroluminescent dendrimers in solution and films.* Journal of Physical Chemistry B, 2004. **108**(5): p. 1570-1577.

31. Y.Q. Zhang, G.Y. Zhong, and X.A. Cao, *Concentration quenching of electroluminescence in neat Ir(ppy)3 organic light-emitting diodes.* Journal of Applied Physics, 2010. **108**(8): p. 083107.

32. T. Tsuboi and N. Aljaroudi, *Energy transfer between Ir(ppy)3 molecules in neat film and concentration quenching of phosphorescence.* Optical Materials, 2008. **30**(9): p. 1375-1381.

33. M.A. Parshin, J. Ollevier, and M. Van der Auweraer, *Charge carrier mobility in CBP film doped with Ir(ppy)(3) - art. no. 61922A*, in *Organic Optoelectronics and Photonics II*, P.L. Heremans, M. Muccini, and E.A. Meulenkamp, Editors. 2006, Spie-Int Soc Optical Engineering: Bellingham. p. A1922-A1922.

34. D.J. Pinner, R.H. Friend, and N. Tessler, *Transient electroluminescence of polymer light emitting diodes using electrical pulses.* Journal of Applied Physics, 1999. **86**(9): p. 5116-5130.

35. T. Sajoto, et al., *Temperature Dependence of Blue Phosphorescent Cyclometalated Ir(III) Complexes.* Journal of the American Chemical Society, 2009. **131**(28): p. 9813-9822.

36. A.M. Gilmore, *Luminescence: The Instrumental Key to the Future of Nanotechnology, 1st Edition*. CRC Press, 2013.

37. V. Jankus, et al., *The role of exciplex states in phosphorescent OLEDs with poly(vinylcarbazole) (PVK) host.* Organic Electronics, 2015. **20**(0): p. 97-102.

38. N.C. Giebink, et al., *Ideal diode equation for organic heterojunctions. II. The role of polaron pair recombination.* Physical Review B, 2010. **82**(15): p. 155306.

39. N.C. Giebink, et al., *Ideal diode equation for organic heterojunctions. I. Derivation and application.* Physical Review B, 2010. **82**(15): p. 155305.

40. F. Li, et al., *Direct measurement of the magnetic field effects on carrier mobilities and recombination in tri-(8-hydroxyquinoline)-aluminum based light-emitting diodes.* Applied Physics Letters, 2010. **97**(7): p. 073301.

41. J. Kalinowski, et al., *Magnetic field effects on emission and current in Alq3-based electroluminescent diodes.* Chemical Physics Letters, 2003. **380**(5–6): p. 710-715.

42. V. Ern and Merrifie.Re, *MAGNETIC FIELD EFFECT ON TRIPLET EXCITON QUENCHING IN ORGANIC CRYSTALS.* Physical Review Letters, 1968. **21**(9): p. 609-&.

43. A. Kadashchuk, et al., *Triplet dynamics and charge carrier trapping in triplet-emitter doped conjugated polymers.* Chemical Physics, 2009. **358**(1-2): p. 147-155.

44. S. Jingyao, *Charge transport and excited states in organic semiconductors*, in *Department of Physics*2010, Queen Mary, University of London.

45. T. Kreouzis, et al., *Temperature and field dependence of hole mobility in poly(9,9-dioctylfluorene).* Physical Review B, 2006. **73**(23).

46. J. Hirsch, *HOPPING TRANSPORT IN DISORDERED AROMATIC SOLIDS - REINTERPRETATION OF MOBILITY MEASUREMENTS ON PKV AND TNF.* Journal of Physics C-Solid State Physics, 1979. **12**(2): p. 321-335.

Chapter 6 Para and Meta Conjugated Polyfluorene Based Copolymers as High Triplet Hosts in OLED Devices:

Sections of this chapter have been published:

J. H. Cook*, J. Santos, H.Y. Li, H. A. Al-Attar, M.R. Bryce and A. P. Monkman, *'Efficient deep blue fluorescent polymer light-emitting diodes (PLEDs)'*, Journal of Materials Chemistry C, **28**, 5587, (2014).

6.1). Introduction:

As discussed in Chapter 5, phosphorescent dopants have been of substantial interest in the field of OLED and PLED devices for many years [1-8]. Associated with this is the need for new polymer host materials, especially those with high triplet levels, to manufacture even more efficient and brighter devices. High triplet levels and a wide energy gap between HOMO and LUMO are desirable as they allow more charge to be transferred efficiently to, and prevent the quenching of, the dopant [9, 10]. This is especially important for blue dopants, which have naturally high triplet levels and large gaps between the HOMO and LUMO and can cause back triplet energy transfer, negatively impacting the device efficiency [11, 12]. More recently OLEDs which emit from the deep blue through to the violet range of the spectrum have been subject to an influx in investigation [13-20]. Deep blue light is essential to achieve good colour rendering and high colour temperature in white OLEDs for lighting applications, and for greater colour contrast and a wider colour gamut in displays [21]. As such the development of high triplet hosts is extremely important to the field [22].

Earlier works have focused on derivatives of poly(9,9-dialkylfluorene-2,7-diyl)s (pFs) which have long been recognised as promising constituents in electroluminescent devices. They are in possession of many desirable properties, namely blue emission, high charge-carrier mobilities, good thermal and electrochemical stability, high photoluminescence

quantum yields (PLQY), and facile chemical modification [23, 24]. Previously, a wide range of fluorene-based copolymers were produced; these included several featuring various different varieties of dibenzothiophene-S,S-dioxide-3,7-diyl (S) units [25-31], which were observed to have enhanced blue stability and impressive colour tenability by chemical modification. S is an interesting acceptor unit, which is topologically similar to fluorene, and has a number of desirable effects including lowering the Lowest Unoccupied Molecular Orbital (LUMO) energy, thus improving electron injection; increased dihedral angles in the polymer backbone, disrupting the extended π-conjugation which blue-shifts emission; improved solubility for spin coating; and enhanced spectral stability. In particular, pF-S copolymers, with hexyl substituents attached to the S units (S_6), displayed improved solubility and spectrally stable blue-shifted emission resulting from the twisted backbone structure, which disrupted the extended π−conjugation [32].

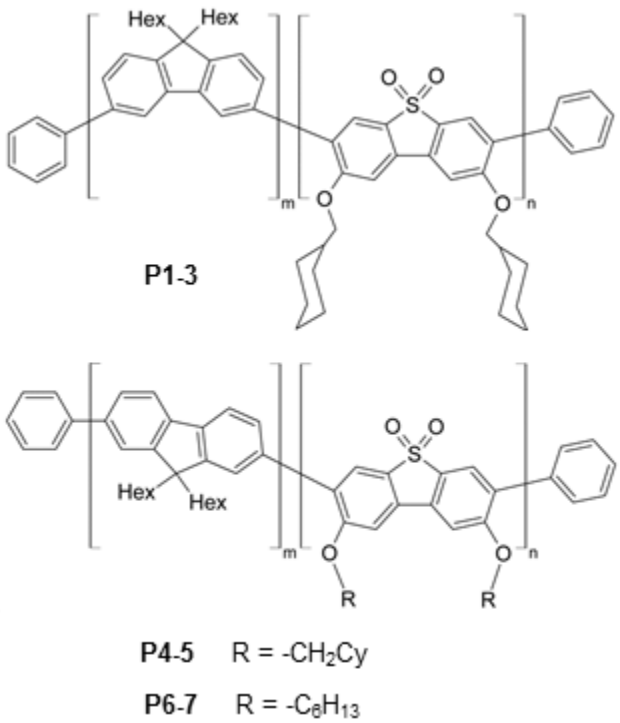

Figure 6.1: *Chemical structures of polymers P**1-7**.*

The aim of this chapter is to build upon this prior work in order to explore novel methods of producing OLEDs with emissions peaking between 410-450 nm. High triplet

polyfluorene based copolymers, with two new S derivatives, were produced and tested in OLEDs. The copolymers were also combined in devices with an electron transporting layer (ETL) of the small molecule 1,3,5-tris(N-phenylbenzimidazole-2-yl)benzene (TPBi) to produce hybrid OLED devices of dramatically improved efficiency, brightness and reduced turn on voltage over their pure polymer device counterparts.

In total seven new polymers were produced by Durham University Chemistry Department where the hexyl units on the S_6 have been substituted for O-hexyl (S_{O6}) or O-methylenecyclohexyl (S_{OCy}) groups. The structure of these polymers, **P1-7**, can be seen in Figure 6.1 and their properties are detailed in Table 6.1. The effect of linkage position within the copolymers on device performance has been considered, i.e. 2,7-para conjugated copolymers, or 3,6-meta broken conjugation copolymers. The feed ratios of the copolymer monomers have also been varied to investigate their effect on device performance.

Table 6.1: *Properties of the polymers **P1-7***

Polymer	m[a]	n[a]	M_w[b]	M_n[b]
P1	50	50	25,700	13,600
P2	70	30	15,200	7,800
P3	85	15	17,500	7,000
P4	50	50	20,900	7,500
P5	70	30	88,900	27,200
P6	50	50	26,800	10,400
P7	70	30	62,000	21,400

[a] Based on monomer feed ratios of F:S_{OCy} or S_{O6} units. [b] Estimated by GPC analysis using polydispersity polystyrene standards obtained from Polymer Laboratories.

6.2). Experimental:

6.2.1). Optical Characterisation:

Solution and solid state absorption and emission spectra were obtained, using the methods described in 3.6.1) and 3.6.2). Solution based measurements were performed in solvents of different polarity, ethyl acetate and cyclohexane, to test for solvatochromism and were kept below 1.0 OD. Solid state photoluminescence quantum yields were measured using

a calibrated Labsphere integrating sphere in a spectrofluorimeter as covered in 3.6.3). Excitation wavelengths corresponded to the point of maximum absorbance for the polymer under investigation. The triplet energy of a film at a temperature of 17 K was calculated from a gated luminescent measurement of the polymer's phosphorescence as described in 3.6.4). Solid state samples were drop-cast films, cast from a 1:1 mixture of 175 $mg.mL^{-1}$ zeonex and 0.5 $mg.mL^{-1}$ of the polymer, both in chlorobenzene, and had a maximum absorbance of 2.0 OD.

6.2.2). Device Fabrication and Characterisation:

A number of devices were manufactured using the methods outlined in Chapter 3. These devices featured an ITO anode (150 nm, 16 Ω/□) commercially pre-coated on a glass substrate (24 mm x 24 mm), a hole-injection layer (HIL) of the commercial PEDOT HIL 1.5 from Heraeus (70 nm) and an active layer of polymers **P1-7** (60 nm). The effect of different emissive dopants in the active layer on device performance was also investigated using the dopants iridium (III) bis[2-(2,4-difluorophenyl)-4-(2,4,6-trimethylphenyl)pyridinato-N,C2′] picolinate (VK-17-B, complex 5 [33], a blue emitter) and tris[2-phenylpyridinato-C2,N] iridium(III) ($Ir(ppy)_3$, a green emitter). Finally, an ETL consisting of TPBi (20 nm) was introduced in an attempt to boost device performance. This layer was thermally evaporated directly on top of the polymer layers using the method outlined in 3.3.4). This was followed by a 1 nm thick electron injection layer (EIL) of lithium fluoride (LiF), or a 4 nm thick layer of barium (Ba), which was thermally evaporated using a shadow mask to produce parallel strips perpendicular to the ITO anodes, forming four individually addressable pixels per substrate each of area 5 mm x 4 mm. The LiF, or Ba, was capped with a 100 nm thick layer of aluminium cathode to protect it from oxidation. Evaporation pressure of the order of 10^{-6} mbar and a rate of approximately 0.1 $nm.s^{-1}$ were used for all of the evaporated layers

produced. The devices were then encapsulated with DELO UV curable epoxy (Katiobond) and a 12 x 12 mm glass cover slide.

The devices were characterised in a calibrated Labsphere LMS-100 integrating sphere, connected to a USB 4000 CCD spectrometer supplied by a 400 µm UV/Vis fibre optic cable, under steady state conditions as detailed in 3.5.1). Layer thicknesses were measured using a J. A. Woolam VASE Ellipsometer, as described in 3.5.4). The non-uniformity of the organic layer thicknesses across the samples leads to a 5–10 % error in device efficiencies and all measurements were averages over at least four devices.

6.3). Results and Discussion:

6.3.1). Optical Properties:

Table 6.2: *Photophysical data for the polymers **P1-7**.*

Polymer	Solvent/Film	λ_{max}^{abs} / nm	λ_{max}^{PL} / nm	PLQY, Φ_{PL}	E_T^{onset} / eV
P1	Ethyl Acetate	345	414		
	Cyclohexane	351	427		
	Film	350	424	0.59±0.06	2.44±0.02
P2	Ethyl Acetate	346	412		
	Cyclohexane	347	413		
	Film	350	420	0.77±0.08	2.49±0.02
P3	Ethyl Acetate	346	412		
	Cyclohexane	346	422		
	Film	350	420	0.75±0.08	2.49±0.02
P4	Ethyl Acetate	379	426		
	Cyclohexane	377	424		
	Film	390	448	0.58±0.06	2.57±0.02
P5	Ethyl Acetate	381	429		
	Cyclohexane	404	442		
	Film	390	450	0.62±0.06	2.55±0.02
P6	Ethyl Acetate	382	425		
	Cyclohexane	394	432		
	Film	395	450	0.58±0.06	2.54±0.02
P7	Ethyl Acetate	384	426		
	Cyclohexane	379	429		
	Film	390	452	0.55±0.06	2.51±0.02

The spectroscopic data produced for all the polymers **P1-7** is summarised in Table 6.2. For polymers **P1-3,** where the S_{O6} units and the capping phenyl groups are bonded through the 3 and 6 positions (*meta* conjugated) with respect to the pF units, the polymer conjugation has been broken. This has resulted in a blue-shifted emission, by approximately 30 nm, with respect to the para analogues, **P4-7**, and the comparable S_6 polymers in the previous results[32].

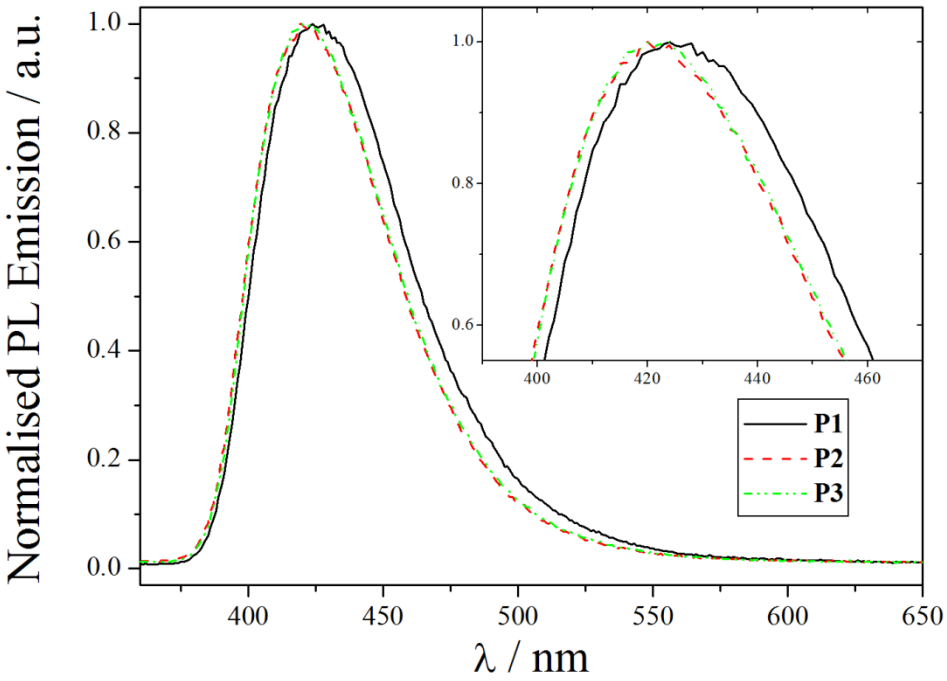

Figure 6.2: *Normalised PL emission spectra for polymers **P1-3** in thin film form. Inset shows a magnification of the λ_{max} region.*

Usually the increased ratio of S derivative compared to pF unit results in a blue shift in both the absorption maxima and the emission spectra observed, due to the increase in dihedral angle breaking the polymer's extended π-conjugation. However, for these meta conjugated polymers there is no significant change in absorption maxima observed, for either solution or thin films, as the ratios of substituents are varied. It can even be seen in Figure 6.2 that the reverse of the usual trend is observed with regard to the thin film emission spectra; increasing the ratio of pF:S_{OCy} to 50:50 actually causes a slight red shift in emission. From this it can be deduced that the effect of meta substitution on reducing the conjugation

dominates that of the S_{OCy}:pF ratio on the absorption and emission maxima. In addition to this it can also be concluded that the introduction of S_{OCy} and S_{O6} side-chains leads to a reduction in the sterically-induced twisting of the polymer backbone, compared with the previous S_6 analogues [32]. This is presumably due to the oxygen atom attached to the S unit, rather than the CH_2 unit previously used.

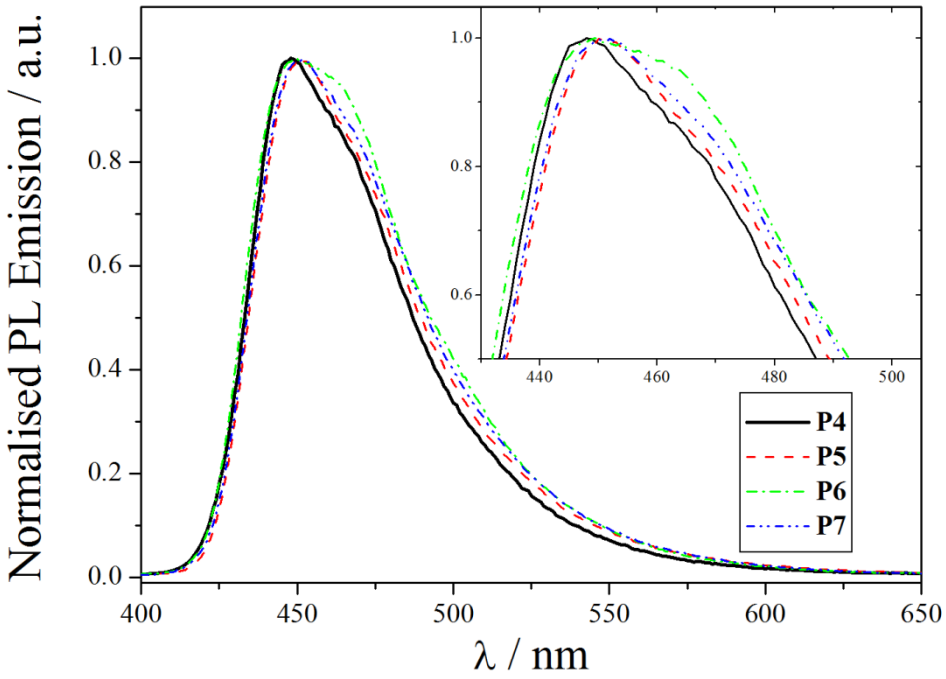

Figure 6.3: *Normalised PL emission spectra for polymers **P4-7** in thin film form. Inset shows a magnification of the λ_{max} region.*

Polymers **P4-7** enable us to investigate the effects of different feed ratios along with two different S derivatives, namely S_{OCy} and S_{O6}, the results of which can be seen in Figure 6.3. As expected the emission spectra for these polymers is strongly red shifted due to the change from meta to para bonding. They also behave more conventionally with respect to feed ratio. The increased ratio of S derivative compared to pF unit for polymers **P4** and **P6** results in a slight blue shift in the observed thin film emission spectra over polymers **P5** and **P7**; there is, however, almost no change in absorption maxima observed as the ratios of substituents are varied. Changing the S_6 derivative from S_{O6} to S_{OCy} has a very slight effect with regards to blue shifting the emission. Increasing the size of group from S_{O6}, **P6** and **P7**,

to S_{OCy}, **P4** and **P5**, has the effect of blue-shifting the emission by 2 nm for each ratio. This is expected due to the increased size of the pendant group increasing the polymer's dihedral angle and reducing the π conjugation. It also has the effect of reducing the size of the shoulder present on the red edge of emission, this results in a narrower emission profile for polymers **P4** and **P5** compared with those of polymers **P6** and **P7**.

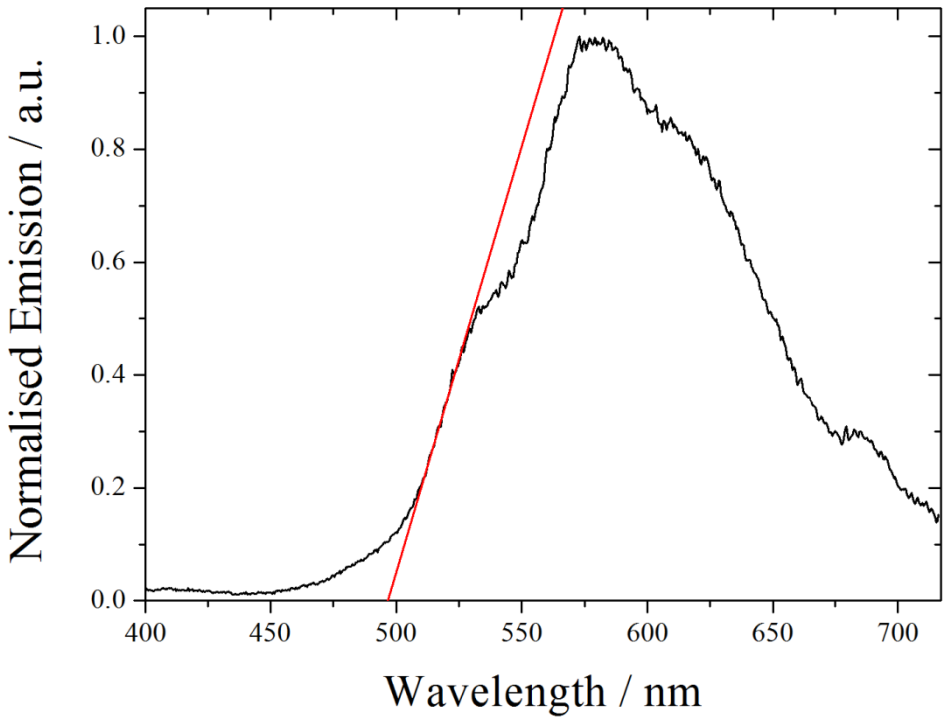

Figure 6.4: *Normalised triplet emission spectra for polymers **P2** in thin film form. The x intercept of the red best fit line gives the onset triplet level, E_T^{onset}, in this case the intercept occurs at 497 nm corresponding to a triplet level of 2.45 eV*

No significant change is observed in the PLQY values for polymers **P1-7** which are all within the range of 0.55-0.77. There is also no significant change in triplet level observed between the seven polymers, all being in the range of 2.44-2.57 eV, and they correspond well to the previously reported values for similar compounds [32]. The triplet emission spectrum of the polymer **P2** is shown in Figure 6.4, the x-intercept of the red line of best fit yields the onset of the triplet level, E_T^{onset}. In this case the x-intercept occurs at 497 nm and can be converted into an energy value of 2.45 eV using the equation $E = hc/\lambda$, where h is Planck's Constant (6.626×10^{-34} $m^2.kg.s^{-1}$) and c is the speed of light (2.998×10^8 $m.s^{-1}$). Polymers **P1-7** also exhibited very little solvatochromism and the differences observed in the λ_{max}^{PL} can be

attributed to a change in refractive index between the two solvents cyclohexane and ethyl acetate. This again agrees well with the previous results for similar compounds.

6.3.2). High Triplet Hosts:

After the optical characterisations were performed upon the seven polymers they were then tested in OLED devices. The aim was to investigate their viability as high triplet hosts for phosphorescent dopants. For this purpose the polymer **P1** was chosen, due to its meta-broken conjugation combined with the high 50:50 ratio of pF:S_{O6}. **P1** was used in two devices of the structure Glass | ITO (150 nm) | PEDOT HIL 1.5 (70 nm) | **P1** : x% $Ir(ppy)_3$ (50 nm) | Ba (4 nm) | Al (100 nm), where x was either 0% or 5%. The results for these devices can be seen in Figure 6.5.

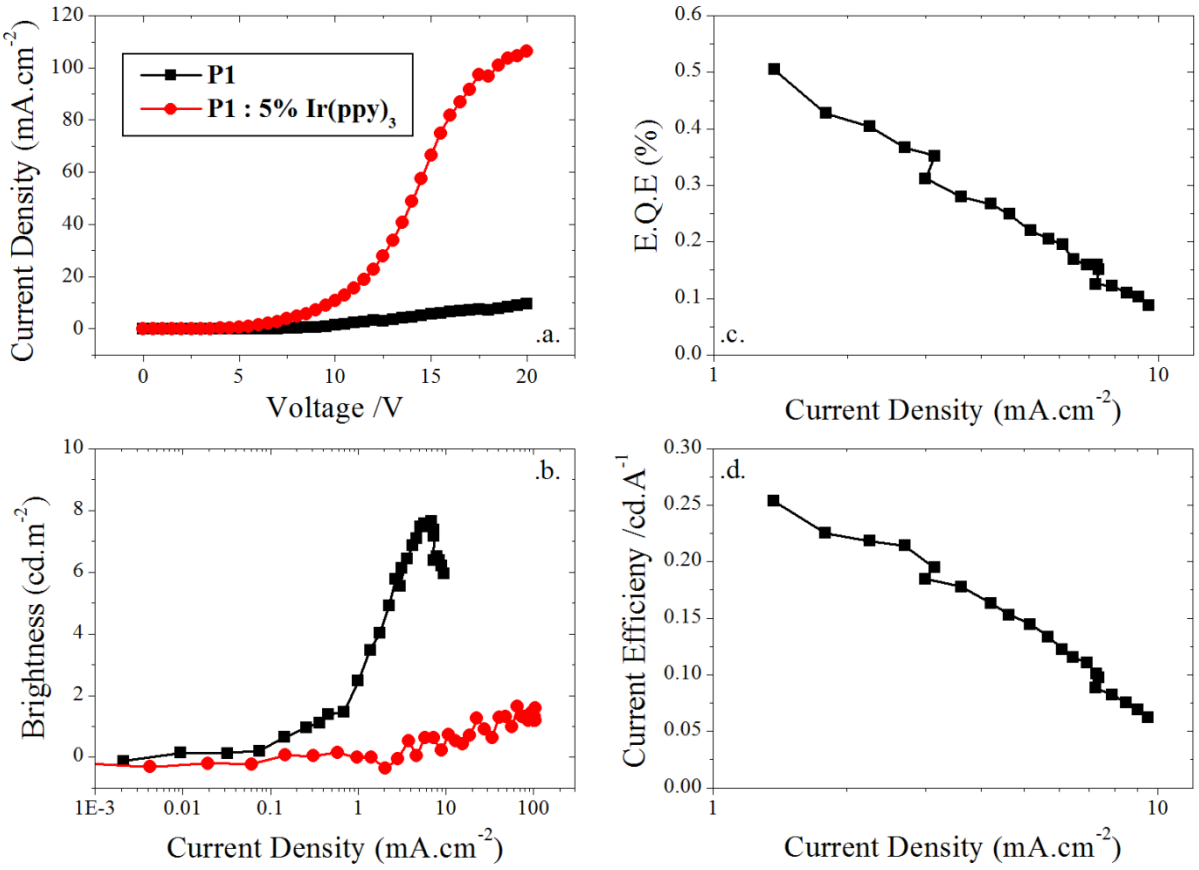

Figure 6.5: *Plots of (a) J-V curves and (b) Luminance vs. J for the polymer **P1** with and without the phosphorescent dopant $Ir(ppy)_3$ and plots of (c) E.Q.E. vs. J and (d) Device Efficiency vs. J for the polymer **P1** without $Ir(ppy)_3$.*

It can be seen that results for this investigation were not particularly encouraging, with the plain polymer device failing to reach turn on (10 $cd.m^{-2}$) and the doped device failing to emit. The undoped device achieves a maximum current density of 9.5 $mA.cm^{-3}$ at 20 V. This is a relatively low value for devices of this architecture, and as such shows that the broken conjugation has negatively affected the carrier transport properties of the polymer. The broken conjugation appears to have led to the formation of isolated domains within the polymer chains that are potentially highly trapping. The addition of the phosphorescent dopant $Ir(ppy)_3$ results in a substantial increase in current density passing through the device. It also, however, results in a complete quenching of all the emission from the device. This is thought to be due to an extreme mismatching between the HOMO and LUMO levels of the polymer, the dopant and the injection layers.

As discussed in Chapter 5, for efficient charge trapping to occur the energy levels of the dopant must lie within those of the host. Here it appears that the HOMO of the host is above the $Ir(ppy)_3$ HOMO, so the direct charge trapping of holes is not possible. However, it should still be possible for the dopant to obtain electrons via direct charge trapping. As discussed in 2.4.3), the LUMO level of a material must be above that of the triplet level. Therefore, as the lowest triplet level for polymers **P1-7** is 2.44 eV, their LUMOs should easily be above 2.8 eV, which is the LUMO of $Ir(ppy)_3$, as stated in Chapter 5. Normally this would result in the formation of an anionic complex which is highly hole trapping. However, due to the lack of emission from the dopant it can be assumed that the holes are already trapped by the polymer host and even such a complex is not sufficiently strong to withdraw them. The dopant is therefore left to act as an electron transporter [34], as observed in Chapter 5, resulting in a high current density but no emission. There also appears to be very little, or no, Förster or Dexter transfer between the host and the dopant. This is no doubt due to poor spectral overlap and a lack of proximity.

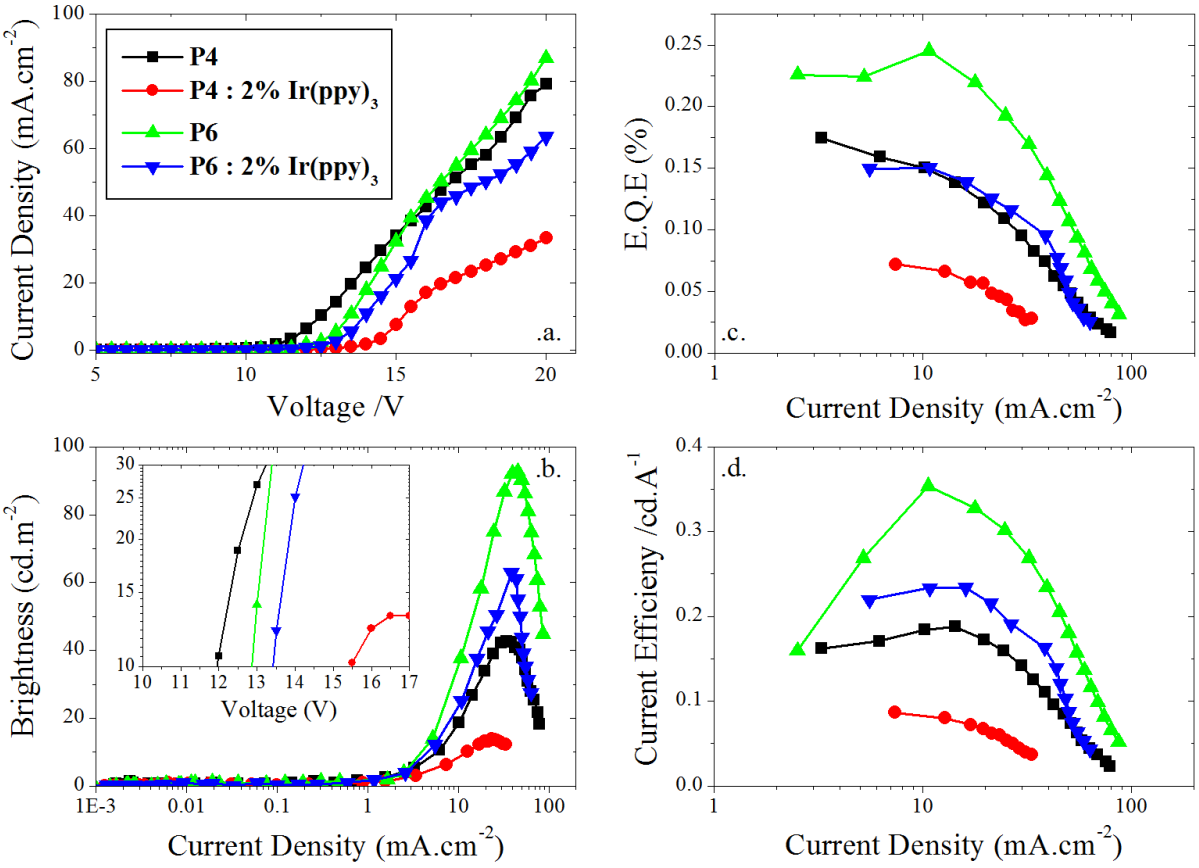

Figure 6.6: *Plots of (a) J-V curves, (b) Luminance vs. J, (c) E.Q.E. vs. J and (d) Device Efficiency vs. J for the polymers **P4** and **P6**, with and without the phosphorescent dopant Ir(ppy)$_3$. Inset to (b) shows the turn on voltages for the four devices in a plot of Luminance vs. V.*

In order to investigate this further the experiment was repeated using the para conjugated 50:50 analogues **P4** and **P6**. The device structure Glass | ITO (150 nm) | PEDOT HIL 1.5 (70 nm) | LEP : x% Ir(ppy)$_3$ (50 nm) | Ba (4 nm) | Al (100 nm), where x was either 0% or 2% was used and the results can be seen in Figure 6.6.

From the results it can be seen that the more conjugated para polymers have a substantially higher current density passing through them, with the undoped devices reaching values between 80-90 mA.cm^{-3}. This shows that the increased conjugation has removed the trapping occurring in **P1**, allowing efficient carrier transport to occur. The addition of the dopant Ir(ppy)$_3$ to the hosts this time results in a decrease in both current density and device brightness, indicating that it is acting as a non-emissive trap state. The change in conjugation is unlikely to have had a large effect on the hosts energy levels, implying that the Ir(ppy)$_3$ is

trapping electrons and is unable to obtain holes from the host, as observed for **P1**. This is reinforced by the results shown in Figure 6.7 where it can be seen that the device emission comes from the polymer and not the dopant.

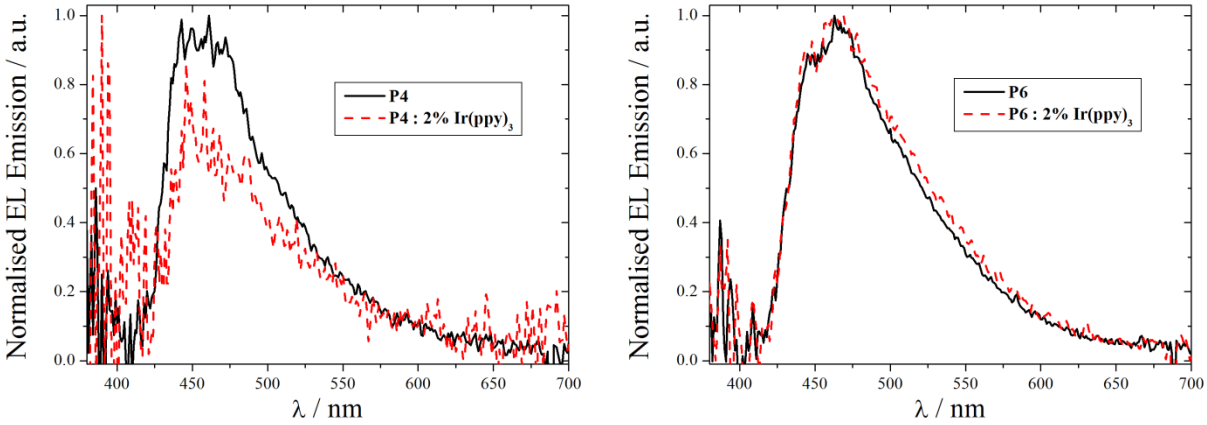

Figure 6.7: *Normalised EL emission spectra for polymers **P4** and **P6**, with and without Ir(ppy)$_3$ at peak device brightness.*

It is also worth noting here the trends appearing between the S_{O6} and S_{OCy} derivatives. It can be seen from Figure 6.6 that the S_{OCy} derivatives are lower in both brightness and efficiency when compared to the S_{O6} derivatives, this is despite having similar current densities when undoped. This is likely due to the relative size difference between the derivatives. The larger S_{OCy} derivatives change the packing arrangement and morphology of the emissive layer compared to the S_{O6} derivative, due to their increased steric bulk. This has the effect of hindering the charge and energy transfer occurring between host polymer strands, potentially introducing more trap states.

Having compared the hosting abilities of the 50:50 ratios for the meta and para analogues and the S_{OCy} and S_{O6} derivatives, it was decided that the next step would be to compare the 50:50 polymers **P1** and **P4** with their 70:30 counterparts **P2** and **P5**. This would see if an intermediate conjugation between the meta and para analogues could be found for **P1** that wouldn't be so strongly trapping. It would also be possible to investigate the effect of increased conjugation on **P4**, the best of the para hosts tested so far, to see if the device performance could be further improved. Device structures of Glass | ITO (150 nm) | PEDOT

HIL 1.5 (70 nm) | LEP : 2% $Ir(ppy)_3$ (50 nm) | Ba (4 nm) | Al (100 nm), were used to investigate this and the results can be seen in Figure 6.8.

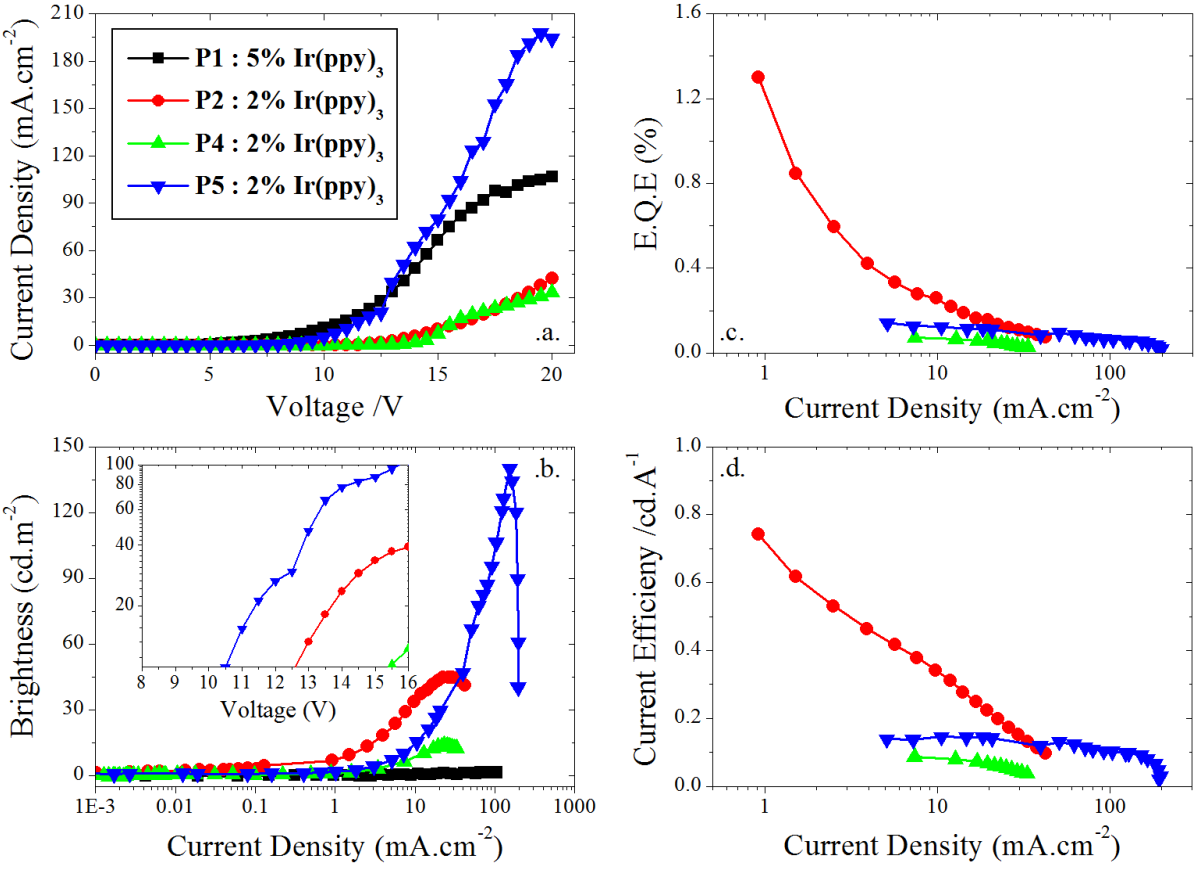

Figure 6.8: *Plots of (a) J-V curves, (b) Luminance vs. J, (c) E.Q.E. vs. J and (d) Device Efficiency vs. J for the polymers **P1**, **P2**, **P3** and **P4**, with the phosphorescent dopant $Ir(ppy)_3$. Inset to (b) shows the turn on voltages for the four devices in a plot of Luminance vs. V.*

From the results in Figure 6.8 it can be seen that the switch from 50:50 to 70:30 has had a drastic effect on the maximum device properties with phosphorescent dopant added. For the meta polymers **P1** and **P2** there is a decrease in current density when changing from 50:50 to 70:30 ratio of $pF:S_{OCy}$. This corresponds to a large increase in emission, going from no emission with dopant for the 50:50 ratio to 45 $cd.m^{-2}$ for the 70:30 ratio, accounting for the decrease in current density through the device with a large increase in carrier recombination. Whilst this is a large increase in brightness, and seems close in maximum brightness to that of the undoped **P4** in Figure 6.6, it has been largely influenced by the luminosity function as discussed in 3.5.1). This shift means that whilst the brightness of the

P2 device is comparatively high, the actual power output by the device is still relatively low, especially when compared to the similarly doped devices in Chapter 5.

As seen in Figure 6.9, the emission is split between the polymer (400-500 nm) and the phosphorescent dopant (500-600 nm), with the peak emission occurring at 400 and 520 nm compared to 460 nm for **P4** and **P5**. This indicates that the holes in **P2** are not trapped as strongly as those in **P1**, due to the increase in conjugation associated with the increased ratio of pF:S_{OCy}. There is therefore, a limited amount of emission from the dopant as it is in direct competition with the host. The dual emission, combined with the unexpectedly high E.Q.E., indicates that whilst this has not been wholly successful it might be possible to produce a viable high triplet host from at least the meta polymers and signifies the first time that these polymers have achieved an efficiency of over 1%.

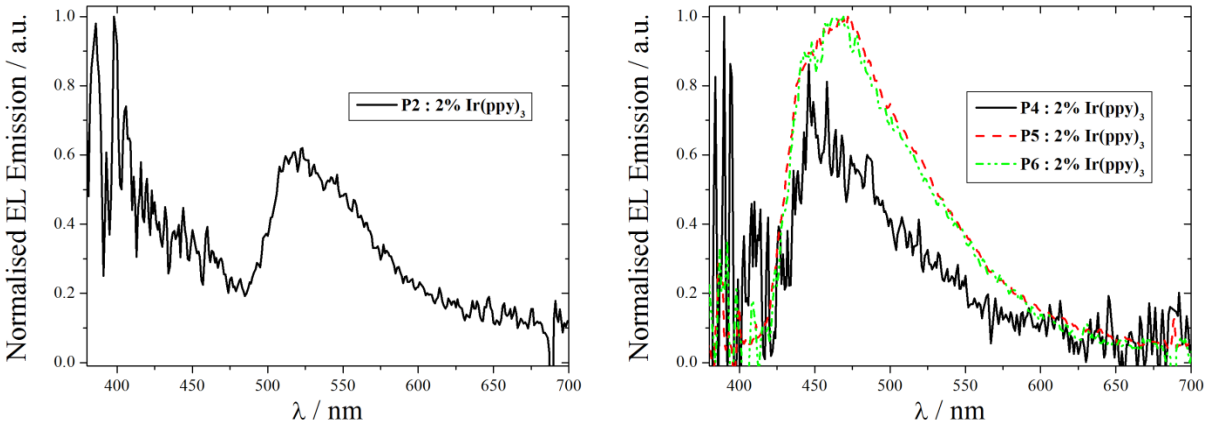

Figure 6.9: *Normalised EL emission spectra for the polymers **P2**, **P4**, **P5** and **P6** with the dopant $Ir(ppy)_3$ at peak device brightness.*

For the para polymers there is a substantial increase in current density passing through the device when changing from the 50:50 to 70:30 ratio; this is accompanied by a corresponding increase in maximum brightness. The increase in conductivity is likely due to the increased conjugation when going from 50:50 to 70:30. There is a small decrease in efficiency, as the magnitude of the increase in brightness does not match up to that of the increase in current density. The emission spectra remain essentially the same despite the

change in pF:S_{OCy} ratio, as can be seen in part .b. of Figure 6.9. From the spectra in Figure 6.7 and Figure 6.9 it can also be seen that there is no change in the emission source, with the $Ir(ppy)_3$ still acting as a non-emissive charge trap unable to harvest the additional carrier needed for emission to occur.

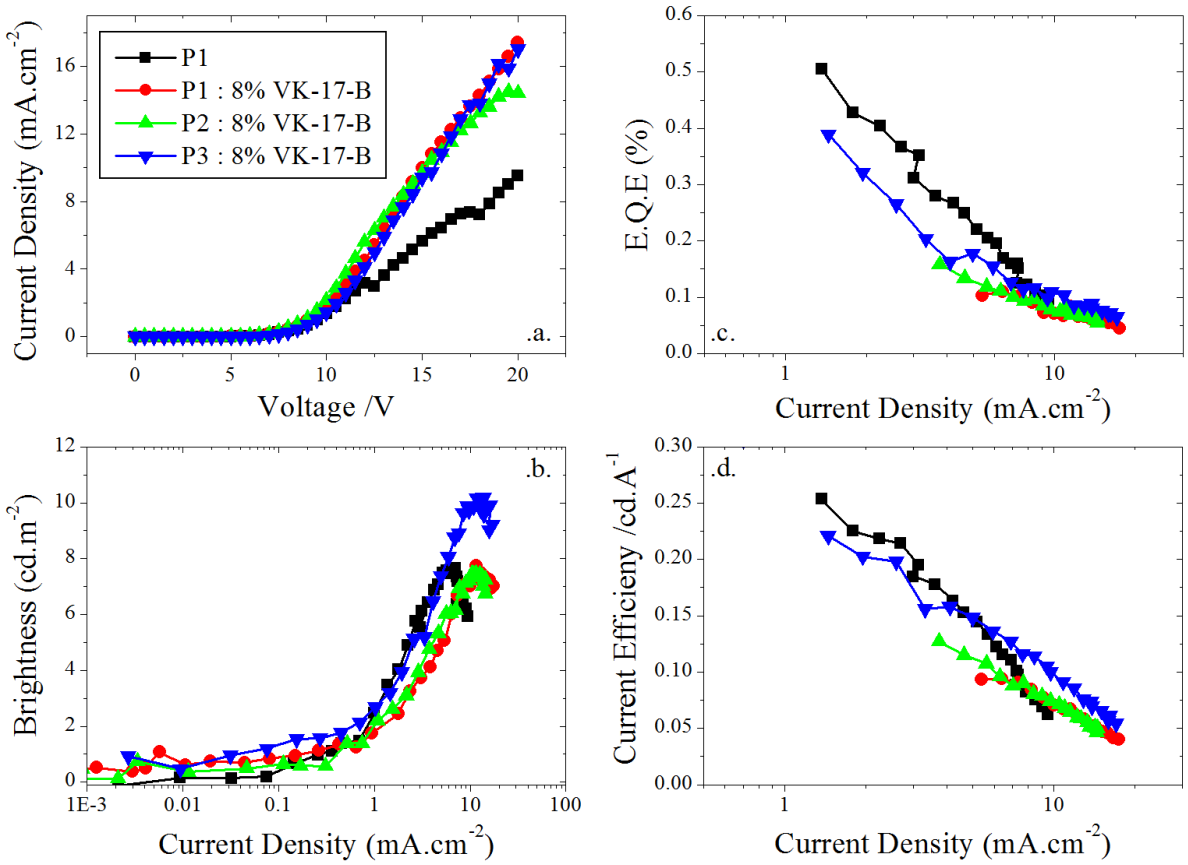

Figure 6.10: *Plots of (a) J-V curves, (b) Luminance vs. J, (c) E.Q.E. vs. J and (d) Device Efficiency vs. J for the polymers **P1-3**, with and without the phosphorescent dopant VK-17-B.*

After the partial success of the **P2** doped device, and in an attempt to better match the energy levels between the meta polymers, the phosphorescent dopant VK-17-B, a blue phosphorescent emitter, has been used in devices instead of the green emitter $Ir(ppy)_3$. A higher dopant concentration of 8% was selected in an attempt to completely quench the host emission and boost the dopant emission. In Chapter 5 it was observed that emission from the host had disappeared at this concentration as the dopant was no longer saturated. In addition, a polymer with the ratio 85:15 has been introduced to investigate the effects of further conjugation. A device structure of Glass | ITO (150 nm) | PEDOT HIL 1.5 (70 nm) | LEP :

x% VK-17-B (50 nm) | Ba (4 nm) | Al (100 nm), where x was either 0% or 8%, was used and the results can be seen in Figure 6.10.

From Figure 6.10 it can be seen that the current density passing through the devices is only slightly above that of the undoped **P1** device. That device was limited by the extremely broken conjugation hindering charge transport. Here it can be seen that the addition of VK-17-B does little to improve the current density through the device. Unlike the previous addition of $Ir(ppy)_3$, it appears that VK-17-B lacks the ability to transport charge and as such the host is trapping one carrier and the dopant another with no recombination occurring between them. This is reinforced by the unchanged current density between the three doped devices, despite the changes in conjugation.

Most of the devices did not reach the turn on brightness, as with the results in Figure 6.5, with the **P3** device being the exception. From these results, it can be assumed that the previous dual emission was the result of direct charge trapping on an anionic complex and not the result of Förster transfer between the host and the dopant. As such, the dual emission was only possible due to the charge transport properties of the $Ir(ppy)_3$ dopant, despite the highly charge trapping properties of the meta polymers. From this it can be concluded that it is unlikely that the meta polymers will make suitable high triplet hosts for the variety of phosphorescent dopants currently available, due to a combination of a relatively high HOMO/LUMO levels compared to the dopants, poor native charge transport capabilities complete with an extremely trapping nature, and an inability to Förster or Dexter transfer energy to the dopants.

After concluding that the meta polymers are unsuitable to be used as high triplet hosts for phosphorescent dopants another investigation was made into the viability of the para polymers as high triplet hosts. The most emissive of the previously tested para polymers was

combined with an increased concentration of $Ir(ppy)_3$ dopant and an ETL of the evaporated small molecule TPBi, forming a hybrid OLED. TPBi was primarily selected due to its hole blocking properties, ensuring that more holes would remain in the emissive layer to recombine with the $Ir(ppy)_3$ dopant.

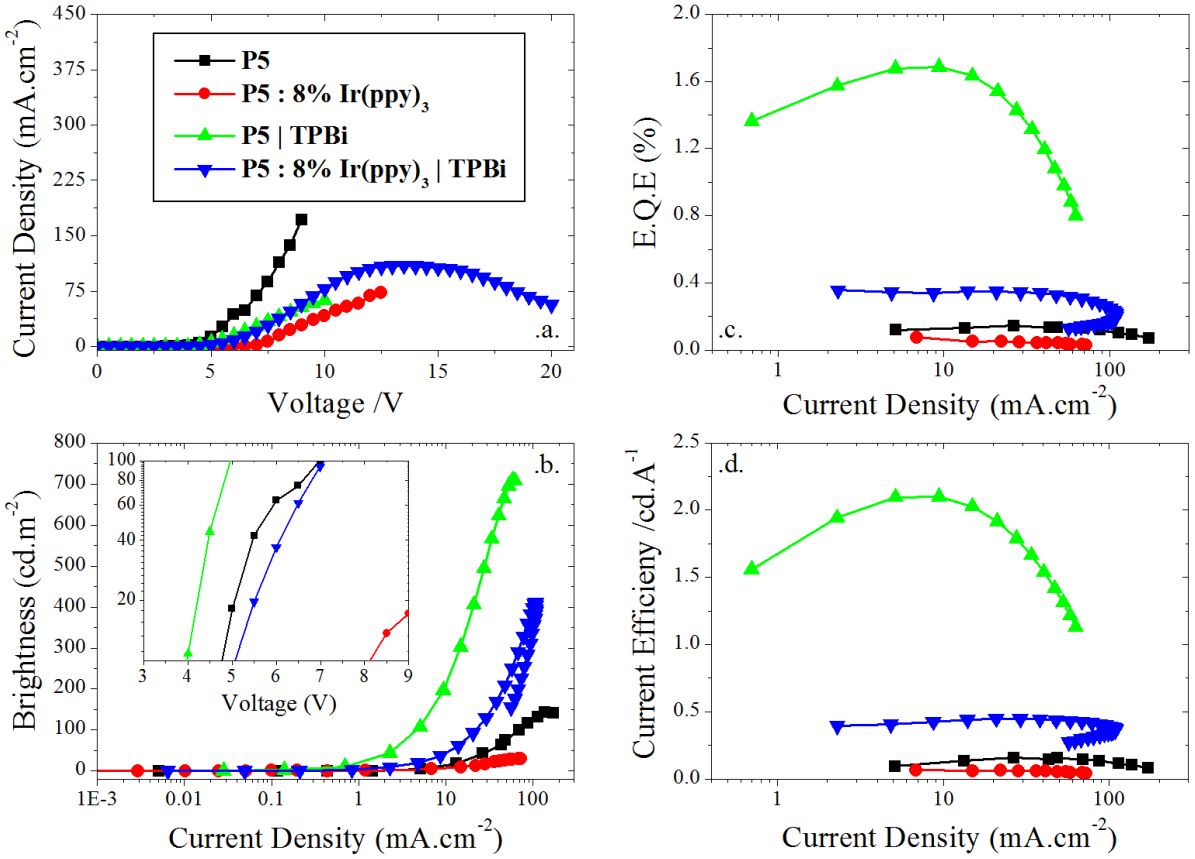

Figure 6.11: *Plots of (a) J-V curves, (b) Luminance vs. J, (c) E.Q.E. vs. J and (d) Device Efficiency vs. J for the polymer **P1** with and without the $Ir(ppy)_3$ or the ETL TPBi.*

To this end a device structure of Glass | ITO (150 nm) | PEDOT HIL 1.5 (70 nm) | **P5** (50 nm) : x% $Ir(ppy)_3$ | TPBi (y nm) | LiF (1 nm) | Al (100 nm) was used, where x was either 0% or 8% and y was either 0 nm or 20 nm. The results for this investigation can be found in Figure 6.11. In order to evaporate the TPBi layer a switch in evaporation chamber was necessary. This also forced a change in EIL from barium to lithium fluoride, which has resulted in a shift in cathode work function from 2.7 eV [35] to around 3.6 eV [36], which is a large enough shift to affect the device results making direct comparison with previous results difficult.

It can be observed from Figure 6.11 that there is a decrease in current density with the addition of the TPBi layer which is likely caused by the confinement of the holes in the emissive layer. It can be seen that, even with the addition of the ETL, there is still a substantial decrease in device properties upon the addition of the phosphorescent dopant. The $Ir(ppy)_3$ is again acting as a non-emissive charge trap, reducing the device brightness as determined previously and negatively impacting the device efficiency. With the addition of TPBi the current density, with and without dopant, remains almost constant whilst the brightness increases significantly.

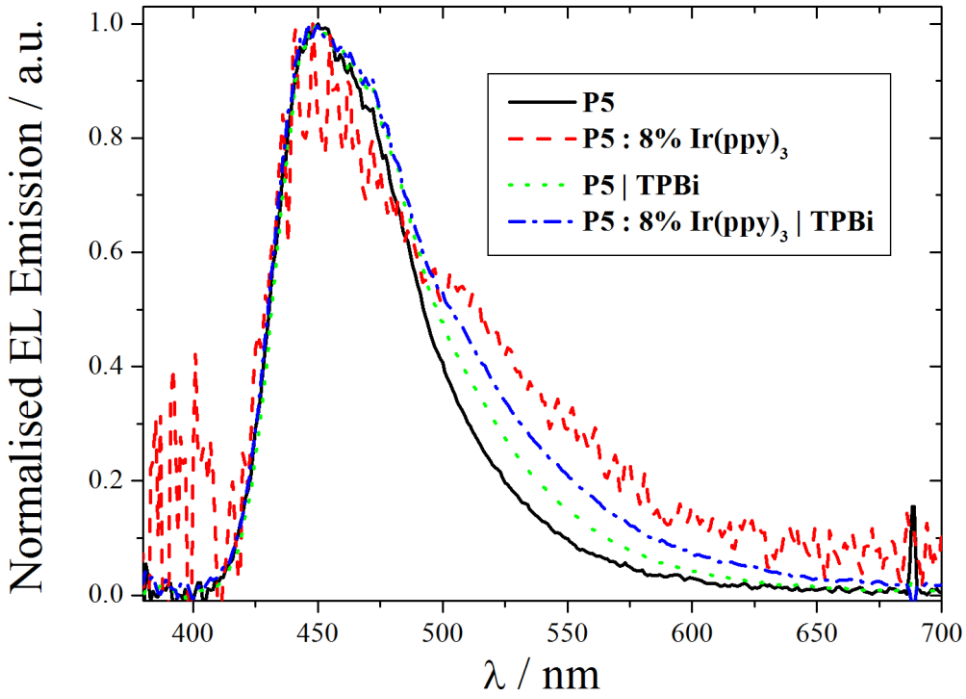

Figure 6.12: *Normalised EL emission spectra for the polymer **P5** with and without TPBi and $Ir(ppy)_3$ at peak device brightness.*

From Figure 6.12, it can be seen that the majority of the emission is coming from the polymer host and not the phosphorescent dopants at peak device brightness. This matches the data observed previously and shows that, despite improved electron injection and hole trapping within the emissive layer, the carriers are still not efficiently being transferred to, or trapped directly by, the $Ir(ppy)_3$ dopant. There is now, however, a noticeable shoulder to the peak emissions at approximately 500 nm, corresponding to emission from the dopant. This is

especially pronounced for the device without the TPBi ETL. This will be discussed in more detail below.

From Figure 6.13 it can be seen that as the voltage through the device is increased the emission shifts from just that of **P5** at low voltages, through emission from both the polymer and the dopant, up to emission primarily from the dopant at high voltages. As the voltage increases the polymer host becomes saturated with holes allowing the remaining ones to be harvested by the $Ir(ppy)_3$, enabling more and more emission to occur from the dopant. Unfortunately, with this shift also comes a substantial decrease in device properties, meaning that this is definitely not a valid method of getting emission from the dopant. It also reinforces how highly trapping these pF based copolymers are and highlights how unlikely it is that they will be suitable for use as high triplet hosts.

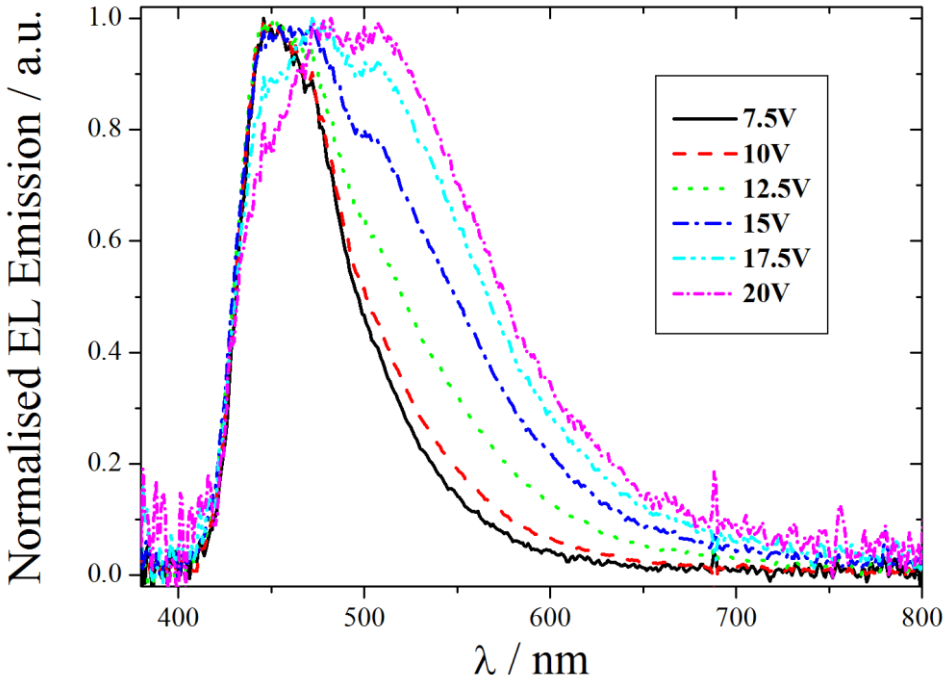

Figure 6.13: *Normalised EL spectra for **P5** doped with $Ir(ppy)_3$ and a TPBi EIL showing the change in emission as the voltage across the device is increased.*

From all of the device results above, it can be safely concluded that the seven polymers are unlikely to make viable high triplet hosts for phosphorescent dopants. However, from the results in Figure 6.11 for the undoped devices, the polymers have displayed great

potential as deep blue fluorescent polymers in Polymer Light Emitting Diodes (PLEDs), being amongst the best in the literature at this time. As such, this will be investigated in more detail in Chapter 7.

6.4). Conclusions:

Devices have been manufactured using seven new polymers synthesised by Durham University Chemistry department. These included three meta conjugated polymers of different pF to S_{OCy} ratios and four para conjugated polymers with 50:50 or 70:30 ratios of polyfluorene to S_{O6} or S_{OCy} groups. The polymers were combined in devices with different phosphorescent dopants in order to assess their potential as new high triplet hosts for deep blue dopants.

It was found that the three meta polymers all had restricted carrier transport capabilities due to the extremely broken conjugation within the polymer backbone, whilst the para polymers were less restricted. It was also concluded that the polymers all had relatively high HOMO/LUMO levels compared to the phosphorescent dopants. This led to the direct charge trapping of electrons on to the phosphorescent dopants, whilst leaving the holes trapped on the host polymers. As a result little, or no, emission was observed from the phosphorescent dopant.

Changing the ratios of pF to S_{O6} or S_{OCy} was investigated in an attempt to promote energy transfer from the polymer host to the phosphorescent dopant and to increase the carrier mobilities within the devices. Increasing the pF:S_{O6}, or pF:S_{OCy}, ratio from 50:50 to 70:30 increased the carrier mobilities within the polymer hosts, allowing for increased current density or brightness from the device, by increasing the conjugation along the polymer backbone. This resulted in emission from both the polymer host and the phosphorescent

dopant simultaneously for the meta polymer **P2**, but it was not possible to isolate the emission from the phosphorescent dopant.

When comparing the S_{O6} and S_{OCy} derivatives directly it was found that the devices with the bulkier S_{OCy} derivative performed worse than the less bulky S_{O6} derivative. This was thought to be due to the bulkier group hindering charge and energy transfer between the host polymer strands, and potentially introducing more trap states.

Using the blue emitting phosphorescent dopant VK-17-B instead of $Ir(ppy)_3$ was not successful , despite the change in energy levels in an attempt to better match those of the host polymer. The introduction of the electron transporting layer, TPBi, in an effort to hold more holes for the phosphorescent dopant within the emissive layer was met with limited success. Emission was observed from the phosphorescent dopant, but only at high voltages and after saturation of the polymer host.

In conclusion, it has been shown that the seven polyfluorene based copolymers are not suitable for use as high triplet hosts. Despite possessing a relatively high triplet level, they are also in possession of relatively high HOMO and LUMO levels which do not match up well with a number of commonly used phosphorescent dopants. This results in the electrons being trapped on the dopant whilst the holes are trapped on the host polymer. There is little or no energy transfer between the two, resulting in very low emission, primarily from the host and not the dopant. In addition to this the meta polymers have severely hindered charge transport abilities and rely on those of the dopant to pass a current density through the device. As such, they are inferior to PVK, or other polyfluorene derivatives.

However, despite their limited abilities as high triplet hosts, the seven polymers have been found to be very good deep blue fluorescent polymers. This is especially true when combined with an evaporated electron transport layer of the small molecule TPBi. As such,

these polymers will be investigated further in this capacity, along with four other analogous polymers, in Chapter 7.

References:

1. M.A. Baldo, et al., *Highly efficient phosphorescent emission from organic electroluminescent devices.* Nature, 1998. **395**(6698): p. 151-154.
2. K. Brunner, et al., *Carbazole compounds as host materials for triplet emitters in organic light-emitting diodes: Tuning the HOMO level without influencing the triplet energy in small molecules.* Journal of the American Chemical Society, 2004. **126**(19): p. 6035-6042.
3. X.W. Chen, et al., *High-efficiency red-light emission from polyfluorenes grafted with cyclometalated iridium complexes and charge transport moiety.* Journal of the American Chemical Society, 2003. **125**(3): p. 636-637.
4. B.W. D'Andrade, et al., *White light emission using triplet excimers in electrophosphorescent organic light-emitting devices.* Advanced Materials, 2002. **14**(15): p. 1032-+.
5. S. Tokito, et al., *Confinement of triplet energy on phosphorescent molecules for highly-efficient organic blue-light-emitting devices.* Applied Physics Letters, 2003. **83**(3): p. 569-571.
6. A. Tsuboyama, et al., *Homoleptic cyclometalated iridium complexes with highly efficient red phosphorescence and application to organic light-emitting diode.* Journal of the American Chemical Society, 2003. **125**(42): p. 12971-12979.
7. S.J. Yeh, et al., *New dopant and host materials for blue-light-emitting phosphorescent organic electroluminescent devices.* Advanced Materials, 2005. **17**(3): p. 285-+.
8. Y. You and S.Y. Park, *Phosphorescent iridium(III) complexes: toward high phosphorescence quantum efficiency through ligand control.* Dalton Transactions, 2009(8): p. 1267-1282.
9. J. Chang, et al., *Different energy transfer behaviors of poly (9-vinylcabazole) and polyfluorene derivative thin films upon doping with triplet emitters.* Journal of the Korean Physical Society, 2005. **47**(6): p. 1028-1034.
10. H.H. Liao, et al., *Triplet exciton energy transfer in polyfluorene doped with heavy metal complexes studied using photoluminescence and photoinduced absorption.* Physical Review B, 2006. **74**(24): p. 245211.
11. F.C. Chen, et al., *Energy transfer and triplet exciton confinement in polymeric electrophosphorescent devices.* Journal of Polymer Science Part B-Polymer Physics, 2003. **41**(21): p. 2681-2690.
12. B. Mi, et al., *Molecular hosts for triplet emitters in organic light-emitting diodes and the corresponding working principle.* Science China-Chemistry, 2010. **53**(8): p. 1679-1694.
13. X.J. Feng, et al., *Fluorene derivatives for highly efficient non-doped single-layer blue organic light-emitting diodes.* Organic Electronics, 2014. **15**(1): p. 57-64.

14. F.B. Dias, et al., *Triplet Harvesting with 100% Efficiency by Way of Thermally Activated Delayed Fluorescence in Charge Transfer OLED Emitters.* Advanced Materials, 2013. **25**(27): p. 3707-3714.

15. S.H. Jeong and J.Y. Lee, *Dibenzothiophene derivatives as host materials for high efficiency in deep blue phosphorescent organic light emitting diodes.* Journal of Materials Chemistry, 2011. **21**(38): p. 14604-14609.

16. S. Nau, et al., *Highly Efficient Color-Stable Deep-Blue Multilayer PLEDs: Preventing PEDOT:PSS-Induced Interface Degradation.* Advanced Materials, 2013. **25**(32): p. 4420-4424.

17. A. Sergent, et al., *Synthesis, characterization, morphological behaviour, and photo- and electroluminescence of highly blue-emitting fluorene-carbazole copolymers with alkyl side-chains of different lengths.* Journal of Materials Chemistry C, 2013. **1**(19): p. 3207-3216.

18. S. Wu, et al., *High-efficiency deep-blue organic light-emitting diodes based on a thermally activated delayed fluorescence emitter.* Journal of Materials Chemistry C, 2014. **2**(3): p. 421-424.

19. Y. Yang, et al., *Blue-Violet Electroluminescence from a Highly Fluorescent Purine.* Chemistry of Materials, 2010. **22**(12): p. 3580-3582.

20. J. Ye, et al., *Carbazole/Sulfone Hybrid D-pi-A-Structured Bipolar Fluorophores for High-Efficiency Blue-Violet Electroluminescence.* Chemistry of Materials, 2013. **25**(13): p. 2630-2637.

21. J.R. Koo, et al., *Highly efficient and simplified phosphorescence white organic light-emitting diodes based on synthesized deep-blue host and orange emitter.* Thin Solid Films, 2013. **544**: p. 234-237.

22. Y.T. Tao, C.L. Yang, and J.G. Qin, *Organic host materials for phosphorescent organic light-emitting diodes.* Chemical Society Reviews, 2011. **40**(5): p. 2943-2970.

23. S.-A. Chen, H.-H. Lu, and C.-W. Huang, *Polyfluorenes for device applications*, in *Polyfluorenes*, U. Scherf and D. Neher, Editors. 2008. p. 49-84.

24. U. Scherf and E.J.W. List, *Semiconducting polyfluorenes - Towards reliable structure-property relationships.* Advanced Materials, 2002. **14**(7): p. 477-+.

25. F.B. Dias, et al., *Dipolar stabilization of emissive singlet charge transfer excited states in polyfluorene copolymers.* Journal of Physical Chemistry B, 2008. **112**(21): p. 6557-6566.

26. S.M. King, et al., *Exploiting a Dual-Fluorescence Process in Fluorene-Dibenzothiophene-S,S-dioxide Co-Polymers to Give Efficient Single Polymer LEDs with Broadened Emission.* Advanced Functional Materials, 2009. **19**(4): p. 586-591.

27. F.B. Dias, et al., *Exciton Diffusion in Polyfluorene Copolymer Thin Films: Kinetics, Energy Disorder and Thermally Assisted Hopping.* Chemphyschem, 2009. **10**(12): p. 2096-2104.

28. H. Liu, et al., *Highly efficient and spectrally stable blue-light-emitting polyfluorenes containing a dibenzothiophene-S,S-dioxide unit.* Chemistry of Materials, 2008. **20**(13): p. 4499-4506.

29. Y. Li, et al., *Enhancement of spectral stability and efficiency on blue light-emitters via introducing dibenzothiophene-S,S-dioxide isomers into polyfluorene backbone.* Organic Electronics, 2009. **10**(5): p. 901-909.

30. H. Xiao, et al., *Novel green light-emitting polyfluorenes containing dibenzothiophene-S,S-dioxide-arylamine derivatives.* Polymer, 2012. **53**(14): p. 2873-2883.

31. L. Yu, et al., *Red, Green, and Blue Light-Emitting Polyfluorenes Containing a Dibenzothiophene-S,S-Dioxide Unit and Efficient High-Color-Rendering-Index White-Light-Emitting Diodes Made Therefrom.* Advanced Functional Materials, 2013. **23**(35): p. 4366-4376.

32. K.T. Kamtekar, et al., *Synthesis and Spectroscopy or Poly(9,9-dioctylfluorene-2,7-diyl-co-2,8-dihexyldibenzothiophene-S,S-dio xide-3,7-diyl)s: Solution-Processable, Deep-Blue Emitters with a High Triplet Energy.* Macromolecules, 2010. **43**(10): p. 4481-4488.

33. V.N. Kozhevnikov, et al., *Cyclometalated Ir(III) Complexes for High-Efficiency Solution-Processable Blue PhOLEDs.* Chemistry of Materials, 2013. **25**(11): p. 2352-2358.

34. M.A. Parshin, J. Ollevier, and M. Van der Auweraer, *Charge carrier mobility in CBP film doped with Ir(ppy)(3) - art. no. 61922A*, in *Organic Optoelectronics and Photonics II*, P.L. Heremans, M. Muccini, and E.A. Meulenkamp, Editors. 2006, Spie-Int Soc Optical Engineering: Bellingham. p. A1922-A1922.

35. V. Gupta, et al., *Barium: An Efficient Cathode Layer for Bulk-heterojunction Solar Cells.* Scientific Reports, 2013. **3**.

36. S.E. Shaheen, et al., *Bright blue organic light-emitting diode with improved color purity using a LiF/Al cathode.* Journal of Applied Physics, 1998. **84**(4): p. 2324-2327.

Chapter 7 Novel Conjugated Polyfluorene Based Copolymers for Deep-Blue or Violet Fluorescent PLED Devices:

Sections of this chapter have been accepted, or submitted, for publication:

J. H. Cook*, J. Santos, H.Y. Li, H. A. Al-Attar, M.R. Bryce and A. P. Monkman, *'Efficient deep blue fluorescent polymer light-emitting diodes (PLEDs)'*, Journal of Materials Chemistry C, **28**, 5587, (2014).

J. Santos*, J. H. Cook, H. A. Al-Attar, A. P. Monkman and M. R. Bryce, *'Fluorene Copolymers with High Efficiency Deep-Blue Electroluminescence'*, Journal of Materials Chemistry C, **3**, 2479, (2015).

J. H. Cook*, J. Santos, H. A. Al-Attar, M.R. Bryce and A. P. Monkman, *'High brightness violet fluorescent OLEDs'*, submitted to Journal of Materials Chemistry C.

7.1). Introduction:

The vast majority of OLED research to date has concentrated on the visible spectrum, primarily for display and lighting applications [1-8]. More recently OLEDs which emit from the deep blue, through to the violet, range of the spectrum have been subject to an influx in investigation [9-16]. Deep blue or violet light is essential to achieve good colour rendering and high colour temperature in white OLEDs for lighting applications, and for greater colour contrast and a wider colour gamut in displays [17]. Previously maximum external quantum efficiencies (E.Q.E.s) of 3-6% for emission peaks in the range 400-480 nm have been reported, featuring both small molecule and polymer based devices [18, 19].

In the previous chapter polyfluorene-thiophene derivative based copolymers were investigated in order to assess their abilities as high triplet hosts. Unfortunately, their prospects as high triplet hosts were not good; they were, however, promising deep-blue

emitters in their own right and warranted further investigation. This is largely due to their abilities to function in PLED devices without the addition of any extra transport or emissive dopants. The properties and structures of polymers **P1-7** can be found in Chapter 6, along with further information on previous research into similar compounds[20-29].

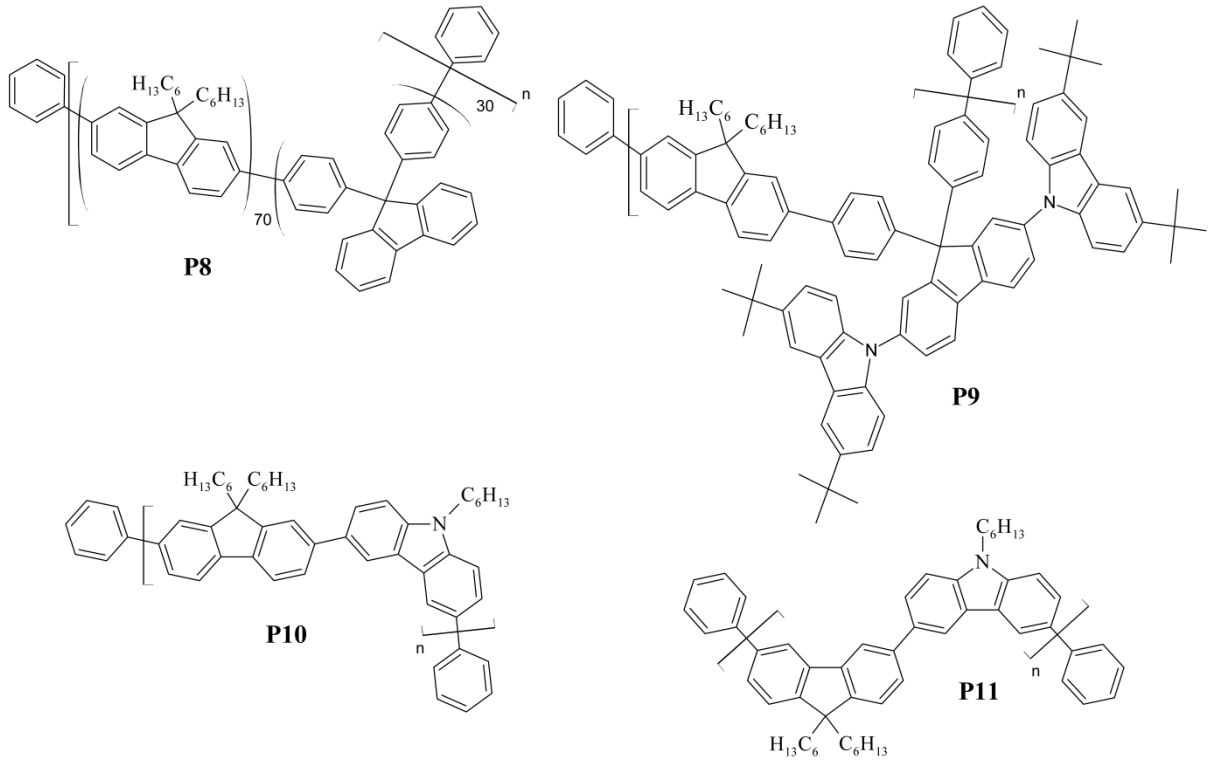

Figure 7.1: *Chemical structures of polymers **P8-11**.*

In addition to the seven polymers from the previous chapter, four new polyfluorene based copolymers, **P8-11**, were produced by Durham University Chemistry Department. The structure of these polymers can be seen in Figure 7.1. The rationale behind this was to attempt to achieve even deeper blue device emission using the lessons learnt from the polymers **P1-7** in Chapter 6. These lessons included the inclusion of bulky side groups into the polymer chain and using meta or para conjugated polymers, which twist the polymer backbone, reducing the conjugation length across the polymer [30], leading to blue shifted emission.

For **P8** two pF units are linked to a 9,9-diphenylfluorene unit via its phenyl rings, this reduces the minimum conjugation length to these three units. For **P9**, the pF units are again linked to a 9,9-diphenylfluorene unit via their phenyl rings, this time however, two *N*-linked 3,6-di-*tert*-butylcarbazole units are attached to the 9,9-diphenylfluorene unit at its 2 and 7 positions to form a large pendant group. This reduces the minimum conjugation length further by removing it from the polymer backbone and it is instead restricted to the attached pendant groups.

Polymers **P10** and **P11** again investigate the effect of meta and para linkage on conjugation lengths and device performance using polyfluorene-carbazole based copolymers. These polymers consist of pF units linked to 9-hexyl-9H-carbazole (pC) units at their 3 and 6 positions. The pC units are linked to the pF units at their 2 and 7 positions for the para copolymer **P10** and at the 3 and 6 positions for the meta copolymer **P11**. Carbazole derivatives have been used in polymers **P9-11** due to their history of deep blue emission, high triplet levels, previous usage in OLED devices and their hole transporting abilities[31-34].

The aim of this investigation was to use polymers to produce PLEDs with emissions peaking between 410-450 nm. In addition to this, there was also a focus on using novel device manufacturing methods in order to boost fluorescent device performance. During the previous chapter, devices were introduced where an electron transporting layer (ETL) consisting of the small molecule 1,3,5-tris(N-phenylbenzimidazole-2-yl)benzene (TPBi) was added, to produce hybrid OLED devices of dramatically improved efficiency, brightness and reduced turn on voltage over their pure polymer device counterparts. In this chapter that idea has been taken to the next level and devices with a solution processed 4,4′-cyclohexylidenebis[N,N-bis(4-methylphenyl) benzenamine] (TAPC) hole transporting layer (HTL) between the PEDOT and LEP layer were trialled. Despite it not being standard practice to spin coat small molecules, this process has resulted in an increase in device

performance for those tested, and shows that multilayer solution processed devices combined with evaporated layers to form hybrid devices are a viable option for fluorescent PLEDs.

7.2). Experimental:

7.2.1). Optical Characterisation:

Solution and solid state absorption and emission spectra were obtained, using the methods described in 3.6.1) and 3.6.2). Solution based measurements were performed in solvents of different polarity, ethyl acetate and cyclohexane, to test for solvatochromism and were kept below 1.0 OD. Solid state photoluminescence quantum yields were taken using a calibrated Labsphere integrating sphere placed within a spectrofluorimeter as covered in 3.6.3). Excitation wavelengths corresponded to the point of maximum absorbance for the polymer under investigation. The triplet energy of a film at a temperature of 17 K was determined from a gated luminescent measurement of the polymer's phosphorescence as described in 3.6.4). Solid state samples were drop-cast films, cast from a 1:1 mixture of 175 $mg.mL^{-1}$ zeonex and 0.5 $mg.mL^{-1}$ of the polymer, both in chlorobenzene, and had a maximum absorbance of 2.0 OD.

7.2.2). Device Fabrication and Characterisation:

A number of devices were manufactured using the methods outlined in Chapter 3. These devices featured an ITO anode (150 nm, 16 Ω/□) commercially pre-coated on a glass substrate (24 mm x 24 mm), a hole-injection layer (HIL) of the commercial PEDOT HIL 1.5 from Heraeus (70 nm) and an active layer of polymers **P1-11**. An ETL consisting of TPBi (20 nm) was introduced in an attempt to boost device performance in accordance with the developments made in the previous chapter. This layer was thermally evaporated directly on top of the polymer layers using the method outlined in 3.3.4). This was followed by a 1 nm

thick layer of lithium fluoride (LiF) cathode which was thermally evaporated using a shadow mask to produce parallel strips perpendicular to the ITO anodes, forming four individually addressable pixels per substrate each of area 5 mm x 4 mm. The LiF was capped with a 100 nm thick layer of aluminium cathode to protect it from oxidation. Evaporation pressure of the order of 10^{-6} mbar and a rate of approximately 0.1 $nm.s^{-1}$ was used for all of the evaporated layers produced. The devices were then encapsulated with DELO UV curable epoxy (Katiobond) and a 12 x 12 mm glass cover slide.

The devices were characterised in a calibrated Labsphere LMS-100 integrating sphere, connected to a USB 4000 CCD spectrometer supplied by a 400 µm UV/Vis fibre optic cable, under steady state conditions as detailed in 3.5.1). Layer thicknesses were measured using a J. A. Woolam VASE Ellipsometer, as described in 3.5.4). The non-uniformity of the organic layer thicknesses across the samples leads to a 5–10 % error in device efficiencies and all measurements were averages over at least four devices.

7.3). Results and Discussion:

7.3.1). Optical Properties:

Table 7.1: *Photophysical data for the polymers **P8-11**.*

Polymer	Solvent/Film	λ_{max}^{abs} / nm	λ_{max}^{PL} / nm	PLQY, Φ_{PL}	E_T^{onset} / eV
P8	Ethyl Acetate	363	412		
	Cyclohexane	360	412		
	Film	375	427	0.44±0.04	2.38±0.02
P9	Ethyl Acetate	344	394		
	Cyclohexane	344	392		
	Film	367	425	0.52±0.05	2.38±0.02
P10	Ethyl Acetate	348	399		
	Cyclohexane	344	394		
	Film	350	421	0.20±0.02	2.34±0.02
P11	Ethyl Acetate	300	400		
	Cyclohexane	304	399		
	Film	287	401	0.17±0.02	2.34±0.02

The spectroscopic data produced for all the polymers **P1-7** is summarised in Chapter 6 in Table 6.2 on page 138. The spectroscopic data for polymers **P8-11** is summarised in Table 7.1and the photoluminescence spectra for the polymers are shown in Figure 7.2. The polymers are all deep blue or violet emitters. They exhibit very little solvatochromism and the small differences observed can be attributed to a change in refractive index between the

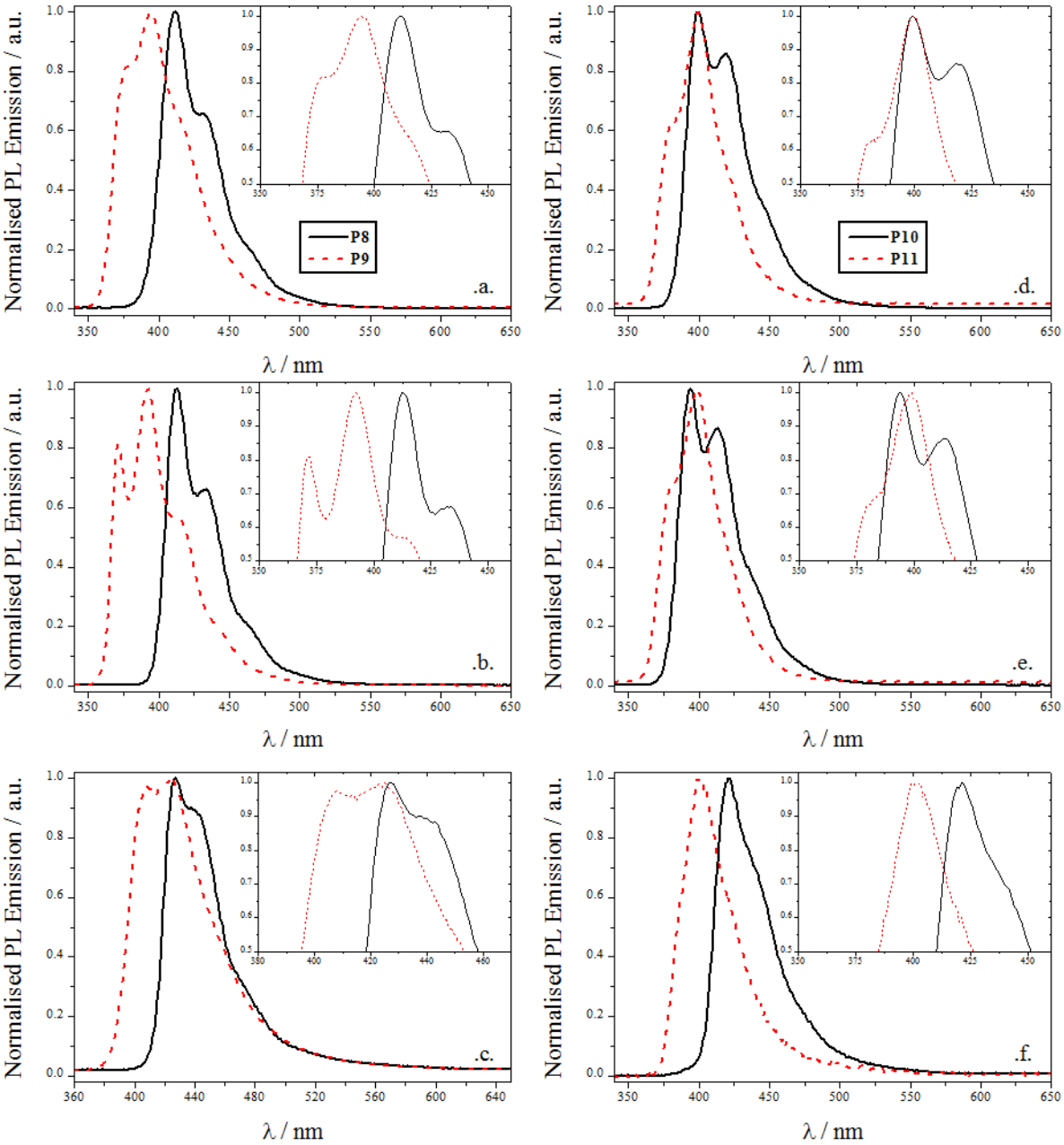

Figure 7.2: *Plots of (a) Normalised solution based PL emission spectra for polymers **P8** and **P9** in Ethyl Acetate, (b) Normalised solution based PL emission spectra for polymers **P8** and **P9** in Cyclohexane, (c) Normalised thin film based PL emission spectra for polymers **P8** and **P9**, (d) Normalised solution based PL emission spectra for polymers **P10** and **P11** in Ethyl Acetate, (e) Normalised solution based PL emission spectra for polymers **P10** and **P11** in Cyclohexane, (f) Normalised thin film based PL emission spectra for polymers **P10** and **P11**. The insets show a magnification of the λ_{max} region.*

solvents. This agrees well with the previous results for analogous materials [29, 30].

We previously showed that a significant blue shift in both the absorption and emission maxima (in both solution and thin film) can be produced by incorporating bulkier groups within the polymer. This blue shift can be ascribed to an increase in the dihedral angle breaking the polymer's extended π conjugation. From the data in Table 7.1 it can be seen that the addition of the two carbazole units to **P9**, and the steric bulk associated with them, causes a substantial blue shift of 15-20 nm over **P8** in solution and a reduced blue shift in thin film form. In this case, it is believed that the blue shift is due to a reduction in conjugation length.

The addition of the carbazole units to the pendant group of **P8** to form **P9** has also introduced a new peak in the solution based PL emission spectra. This is especially easy to observe in part .b. of Figure 7.2 where the spectrum is well resolved in the solvent cyclohexane, showing an additional peak at 371nm. This corresponds well to emission spectra previously documented in the literature for carbazole groups of a similar size [31] to those featured in **P9**.

It was also previously demonstrated that a significant blue shift in both the absorption and emission maxima (in both solution and thin film) can be produced by incorporating a twist within the polymer backbone. This again increases the dihedral angle, breaking the polymer's extended π conjugation. From the data in Table 7.1, and the information in Figure 7.2, it can be seen that the change in bond position between the fluorene and carbazole groups, from para to meta, causes a substantial blue shift of 20 nm from **P10** to **P11** in thin film form and a similar shift in spectra in solution but without the change in λ_{max}^{PL}.

No significant change is observed in the film PLQY values for the polymers **P8** and **P9**, with values of 0.44 and 0.52 respectively. A large decrease is observed in the film PLQY values for the polymers **P8** and **P9**, with values of 0.20 and 0.17 respectively. This is likely

due to the incorporation of the carbazole unit within the polymer chain; as discussed in the literature [31], addition of large groups to carbazole units can result in a decrease in PLQY.

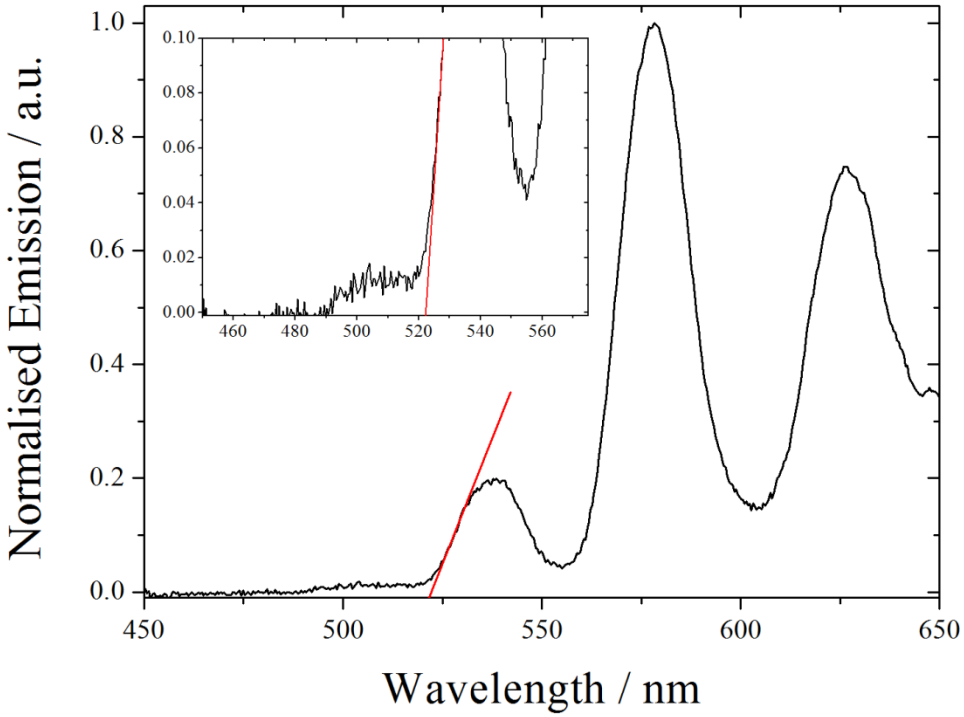

Figure 7.3: *Normalised triplet emission spectra for polymers **P8** in thin film form. The x intercept of the red best fit line gives the onset triplet level, E_T^{onset}, in this case the intercept occurs at 522 nm corresponding to a triplet level of 2.38 eV*

The observed triplet levels for polymers **P8-11** are all in the range of 2.34-2.38 eV, which corresponds well to the reported values for similar polymers which possess restricted backbone π-conjugation [29, 30]. The triplet emission spectrum of polymer **P8** is shown in Figure 7.3, the x-intercept of the red line of best fit yields the onset of the triplet level, E_T^{onset}.

In this case the x-intercept occurs at 522 nm and can be converted into an energy value of 2.38 eV. From the inset to Figure 7.3, it can be seen that there is another area of intensity to the left of the line of best fit. As this feature is above the noise of the system, it is possible that this may be the 0-0 peak instead of the one previously measured. If this were true, the triplet onset would instead occur at 490 nm, giving an energy of 2.53 eV, a shift of 0.15 eV.

A low intensity 0-0 transition peak is observed when there is a large geometric shift between the ground and excited states of a molecule. This implies that the molecule is

relatively flexible and easily distorted upon excitation. This area of intensity is also observed for the other polymers **P8-11** and as such, the values quoted in Table 7.1 may be approximately 0.15 eV lower than they actually are.

7.3.2). pF:S Derivative Based Fluorescent Deep Blue PLEDs:

Table 7.2: *Electroluminescent device data for polymers **P1-7**.*

Polymer	V_{on} / V[a]	Brt_{max} / cd.m^{-2}	E.Q.E.$_{max}$ / %	Dev Eff_{max} /Cd.A^{-1}	Lum_{max} / lm.W^{-1}	CIE_{on} (x, y)[b]	CIE_{max} (x, y)[c]
P1	7.2	28	1.7	0.91	0.47	0.17, 0.11	0.18, 0.13
P2	6.8	37	2.7	1.2	0.70	0.17, 0.10	0.17, 0.11
P3	6.6	81	1.3	0.72	0.34	0.16, 0.09	0.17, 0.12
P4	4.4	740	2.1	2.7	1.7	0.16, 0.15	0.17, 0.17
P5	3.4	2500	3.2	4.4	3.4	0.16, 0.18	0.16, 0.18
P6	4.3	320	2.5	2.1	1.5	0.16, 0.16	0.17, 0.20
P7	3.7	1400	2.8	3.7	2.7	0.16, 0.17	0.16, 0.18

[a]V_{on} is the turn on voltage, the voltage required for a device brightness of 10 cd/m^2 to be reached. [b]CIE coordinates at turn on brightness, 10 cd/m^2 . [c] CIE coordinates at maximum device brightness.

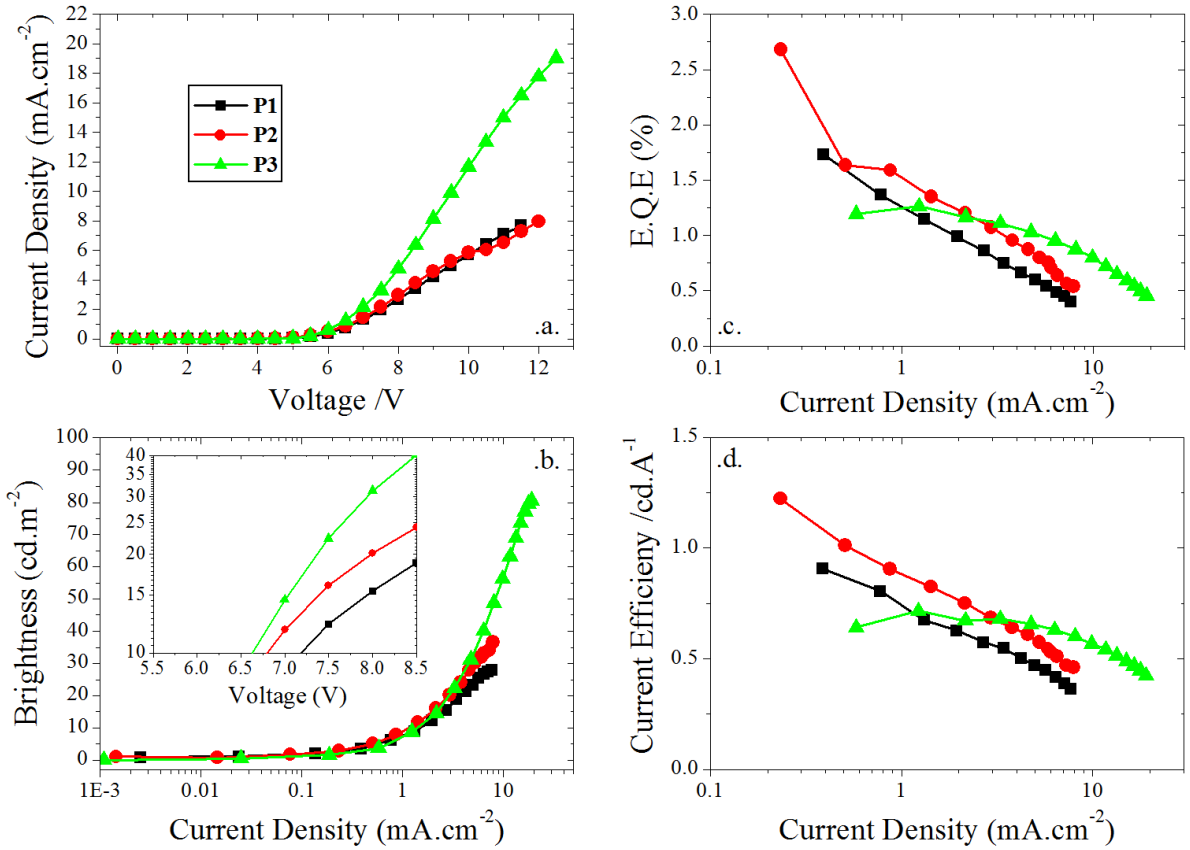

Figure 7.4: *Plots of (a) J-V curves, (b) Luminance vs. J, (c) E.Q.E. vs. J and (d) Device Efficiency vs. J for the polymers **P1-3**. Inset to (b) shows the turn on voltages for the four devices in a plot of Luminance vs. V.*

Devices were made for each of the polymers from Chapter 6, **P1-7**, using the structure: Glass | ITO (150 nm) | PEDOT HIL 1.5 (70 nm) | LEP (60 nm) | TPBi (20 nm) | LiF (1 nm) | Al (100 nm). For all of the devices the LEP layer consisted of just one of the polymers **P1-7** without any other dopants or transporters added. The results for each can be seen in Table 7.2 but initially the results for polymers **P1-3** will be focused on, the results of which can be found in Figure 7.4. It can be seen in Figure 7.5 that each of the three polymers emits in the deep blue, with a peak emission in the range of approximately 415 nm, and have

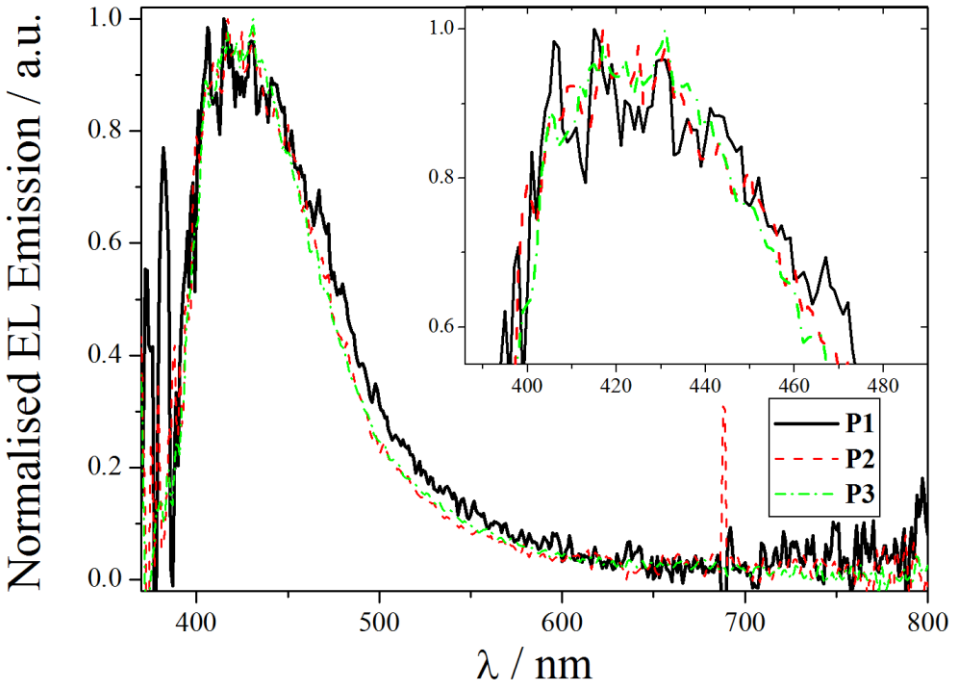

Figure 7.5: *Normalised EL emission spectra for polymers **P1-3**. Inset shows a magnification of the λ_{max} region.*

a reasonable turn on voltage (the voltage required for a device brightness of 10 cd/m^2 to be reached). The exact peak is difficult to identify due to the noise present in the spectra, because of the low relative brightness of the emissive polymers, but the CIE coordinates for the peak emissions are **P1**(0.18, 0.13), **P2**(0.17, 0.11) and **P3**(0.17, 0.12). CIE diagrams for these polymers can be found in Figure 7.13 in 7.3.5).

From Table 7.2 it can be seen that decreasing the ratio of S_{OCy} to pF from 50:50 to 30:70 and again to 15:85 has the effect of increasing the maximum brightness from 28 cd.m^{-2}

to 37 cd.m^{-2} to 81 cd.m^{-2}. The maximum efficiencies initially increase when the ratio decreases from 50:50 to 30:70 but after peaking there, they then decrease again when the ratio is decreased to 15:85. It can also be observed that increasing the amount of S_{OCy} present in the polymer decreases the current density passing through the device. This is consistent

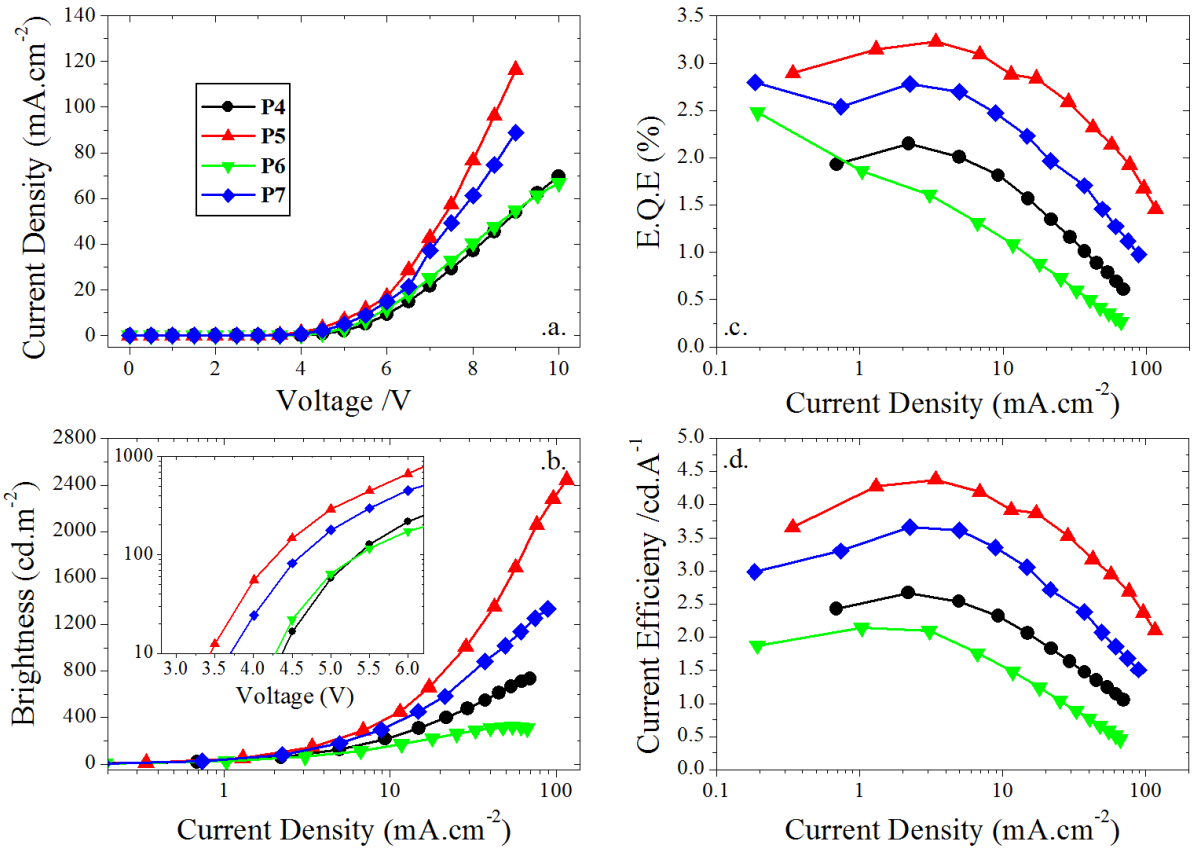

Figure 7.6: *Plots of (a) J-V curves, (b) Luminance vs. J, (c) E.Q.E. vs. J and (d) Device Efficiency vs. J for the polymers **P4-7**. Inset to (b) shows the turn on voltages for the four devices in a plot of Luminance vs. V.*

with the increased proportion of S_{OCy} decreasing the polymers extended π conjugation and thus reducing its carrier transporting properties up to a certain threshold. Once this threshold is reached the current density remains more or less constant, hence the similarity between **P1** and **P2** in Figure 7.4a. It also appears that increasing the concentration of S_{OCy} reduces the amount of emissive species formed accounting for the drop in brightness at comparable current densities and thus the drop in efficiency.

For the para polymers **P4-7**, similar trends to the meta polymers **P1-3** are observed in Figure 7.6. The major differences between the two sets of polymers are the maximum current

densities and the emission spectra. Whilst polymers **P1-3** have a peak emission of approximately 415 nm the other four polymers **P4-7** have EL emission spectra peaking around 450 nm as seen in Figure 7.7. Both this and the change in maximum current density

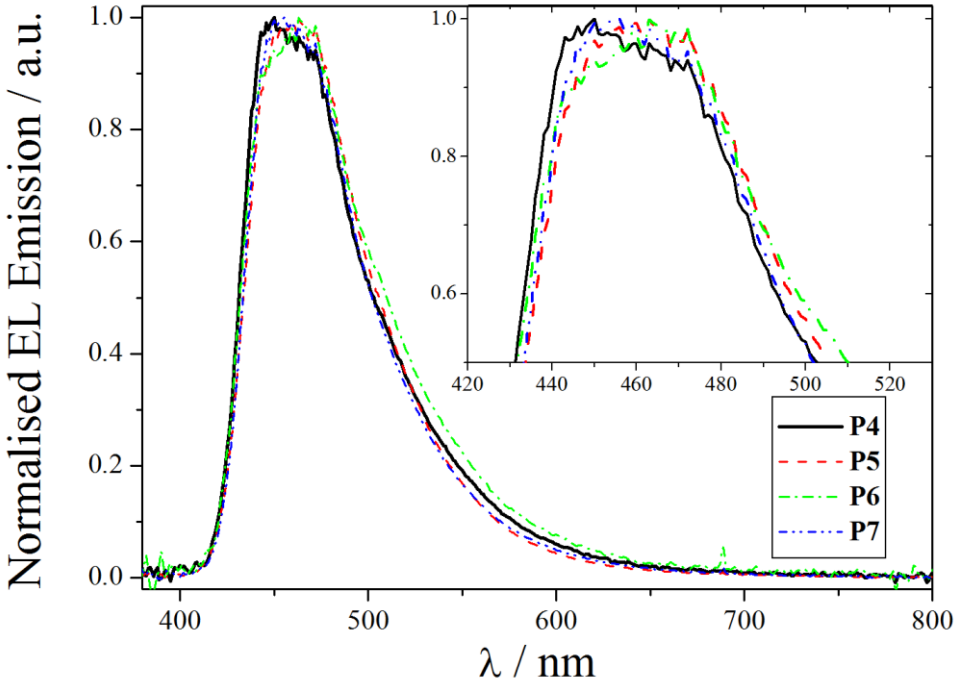

Figure 7.7: Normalised EL emission spectra for polymers **P4-7**. Inset shows a magnification of the λ_{max} region.

can be explained by the conjugation of the polymers being broken for **P1-3** due to the meta-linkage. Similar to polymers **P1-3**, it can be seen that reducing the concentration of S_6 derivative from 50% to 30% increases the maximum brightness and efficiency of the devices as well as substantially decreasing the turn on voltage. The decrease of S_6 derivatives has the effect of increasing the current density through the device, which can be explained by an increase in π conjugation, as well as substantially increasing the quantity of emissive species.

Changing the S_6 derivative from S_{OCy}, to the smaller S_{O6} derivative, results in an overall decrease in device performance. It would be expected that using a larger S_6 derivative within the copolymer would result in a decrease in conjugation, and whilst evidence of this is observed when the EL emission is slightly blue-shifted for **P4** and **P5**, the conductivity of **P5** is higher than that of **P7**. This is unexpected, as ordinarily a polymer with a more broken

conjugation would be expected to conduct less, this indicates that other factors must be taken in to account when considering the effect of substituent size on polymer conjugation and OLED device performance.

7.3.3). pF:Pendant Based Fluorescent Deep Blue PLEDs:

Table 7.3: *Electroluminescent device data for polymers **P8-9**.*

Polymer	V_{on} / V[a]	Brt_{max} / cd.m^{-2}	E.Q.E.$_{max}$ / %	Dev Eff_{max} /Cd.A^{-1}	Lum_{max} / lm.W^{-1}	CIE_{on} (x, y)[b]	CIE_{max} (x, y)[c]
P8	3.75	167	3.3	1.6	1.39	0.16, 0.07	0.17, 0.10
P9	4.25	274	3.9	1.3	0.99	0.16, 0.06	0.17, 0.07

[a]V_{on} is the turn on voltage, the voltage required for a device brightness of 10 cd/m^2 to be reached. [b]CIE coordinates at turn on brightness, 10 cd/m^2 . [c] CIE coordinates at maximum device brightness.

Devices were fabricated for polymers **P8** and **P9** using the structure: glass | ITO (150 nm) | PEDOT:PSS HIL 1.5 (70 nm) | LEP (**P8** 70 nm, **P9** 30 nm) | TPBi (20 nm) | LiF (1 nm) | Al (100 nm). For all of these devices, no other dopants or transporters were added to the LEP layer. The thicknesses of the two LEP layers were determined after prior thickness

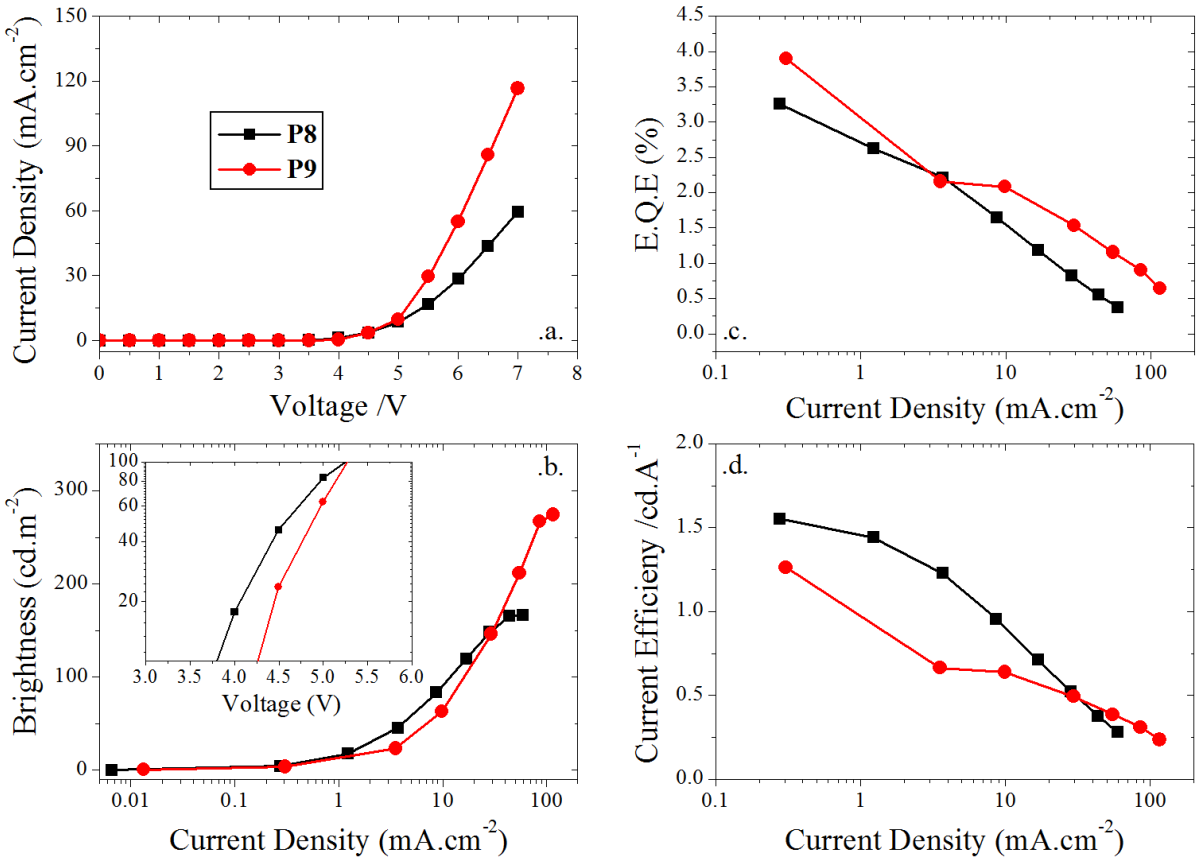

Figure 7.8: *Plots of (a) J-V curves, (b) Luminance vs. J, (c) E.Q.E. vs. J and (d) Device Efficiency vs. J for the polymers **P8-9**. Inset to (b) shows the turn on voltages for the four devices in a plot of Luminance vs. V.*

optimisation for device performance was completed.

The device results can be found in Figure 7.8 and Table 7.3. Devices containing **P8** showed deep blue EL with λ_{max} of 422 nm and maximum E.Q.E. of 3.3% and good CIE_{xy} coordinates (turn on CIE_{xy} (0.16, 0.07) and peak CIE_{xy} (0.17, 0.10)), whereas the carbazole containing material **P9** showed violet emission (λ_{max} of 402 nm) with a higher E.Q.E. of 3.9% and outstanding colour coordinates (turn on CIE_{xy} (0.16, 0.06) and peak CIE_{xy} (0.17, 0.07)). CIE diagrams can be found in Figure 7.13 in section 7.3.5).

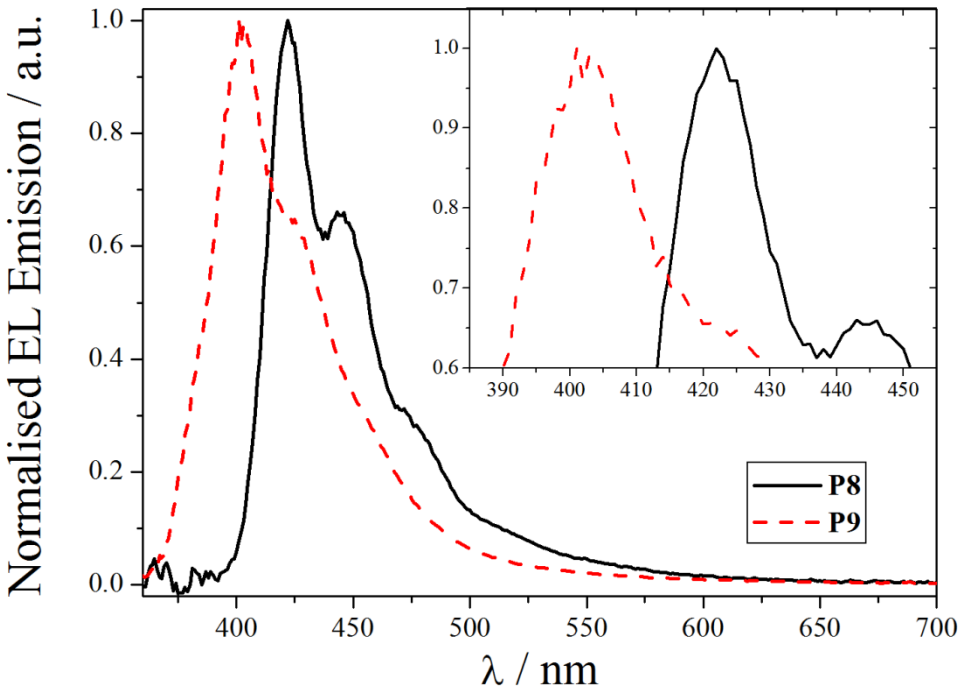

Figure 7.9: *Normalised EL emission spectra for polymers **P8-9**. Inset shows a magnification of the λ_{max} region.*

Both polymers show a remarkably blue shifted emission, below 450 nm, with excellent efficiencies and good brightnesses, when compared to **P1-7**. In the case of **P8** we observe that film EL emission peaks at 422 nm with a small shoulder at 440 nm whilst for **P9** the emission in blue shifted even further, peaking at 401 nm with a small shoulder at 424 nm. The EL spectra can be seen in Figure 7.9. This blue shifting of emission between **P8** and **P9** is expected due to the breaking of **P9**'s extended π conjugation through the addition of the sterically bulky carbazole groups to the pendant group.

The addition of the carbazole groups to the main pendant group also has the effect of increasing the current density passing through the device, the maximum brightness and the maximum E.Q.E. of the device. We have shown in the previous chapter that breaking the conjugation of a polymer typically reduces its conductivity resulting in a limited maximum brightness for the devices. This, however, seems to have been overcome by the intrinsic conduction properties of the carbazole groups incorporated into **P9**, which have caused the current density to double with respect to **P8** and the maximum brightness to almost double too. This is especially impressive when you consider that this measure of brightness is affected by the luminosity function.

The increase in E.Q.E. is most likely due to an increase in hole mobility from the addition of the carbazole groups. This would result in a more balanced proportion of carriers recombining in the LEP layer, reducing the amount of wasted carriers reaching the electrodes. The decrease in current efficiency from **P8** to **P9** is expected, despite the reverse trend in E.Q.E., as this value depends heavily upon the luminosity function and **P9** produces a significantly deeper blue emission than **P8**.

7.3.4). pF:pC Based Fluorescent Deep Blue PLEDs:

Table 7.4: *Electroluminescent device data for polymers **P10-11**.*

Polymer	V_{on} / V[a]	Brt_{max} / cd.m^{-2}	$E.Q.E._{max}$ / %	Dev Eff_{max} /Cd.A^{-1}	Lum_{max} / lm.W^{-1}	CIE_{on} (x, y)[b]	CIE_{max} (x, y)[c]
P10	3.40	565	1.4	0.65	0.63	0.16, 0.07	0.16, 0.07
P11	4.50	16	0.35	0.25	0.99	0.18, 0.12	0.20, 0.15

[a]V_{on} is the turn on voltage, the voltage required for a device brightness of 10 cd/m^2 to be reached. [b]CIE coordinates at turn on brightness, 10 cd/m^2 . [c] CIE coordinates at maximum device brightness.

Devices were fabricated for polymers **P10** and **P11** using the structure: glass | ITO (150 nm) | PEDOT:PSS HIL 1.5 (70 nm) | LEP (20 nm) | TPBi (20 nm) | LiF (1 nm) | Al (100 nm). As before, for all of these devices, no other dopants or transporters were added to the light emitting polymer (LEP) layer. In addition to the ETL of TPBi evaporated on top of the

LEP layer a solution processed HTL of different thicknesses, consisting of the small molecule TAPC, was trialled between the PEDOT and the LEP layers for **P10**.

The device results for **P10** and **P11** can be found in Figure 7.10 and Table 7.4. Devices containing **P10** showed violet/deep blue EL with λ_{max} of 409 nm and maximum

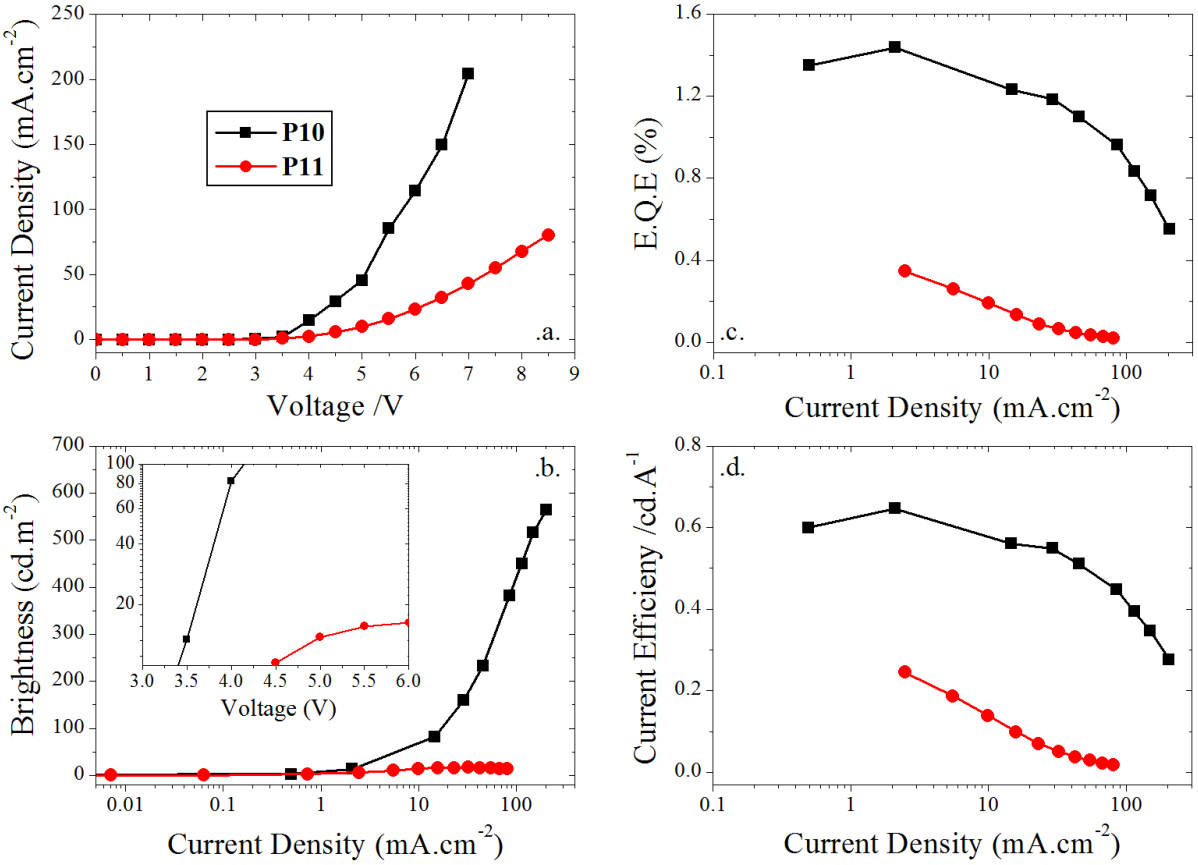

Figure 7.10: *Plots of (a) J-V curves, (b) Luminance vs. J, (c) E.Q.E. vs. J and (d) Device Efficiency vs. J for the polymers **P10-11**. Inset to (b) shows the turn on voltages for the four devices in a plot of Luminance vs. V.*

E.Q.E. of 1.4% and good CIE_{xy} coordinates (turn on CIE_{xy} (0.16, 0.07) and peak CIE_{xy} (0.16, 0.07)), exhibiting excellent photostability under operation. **P11** also showed violet/deep blue emission, again with a λ_{max} of 409 nm but with a substantially reduced E.Q.E. of 0.35% and poorer colour coordinates (turn on CIE_{xy} (0.18, 0.12) and peak CIE_{xy} (0.20, 0.15)) with a much reduced photostability. The EL spectra for **P10** and **P11** can be found in Figure 7.11 and the CIE plots can be seen in Figure 7.13 in 7.3.5).

P10 produced an excellent maximum brightness of 565 $cd.m^{-2}$, for a device of these CIE coordinates. This region is heavily affected by the luminosity function (the eye

sensitivity here is very low) making such a high value notable. Combining this with an extremely low turn on voltage (3.40V), and potential operating voltage, it is easy to see that this polymer is suitable for a wide range of potential uses including display and medical

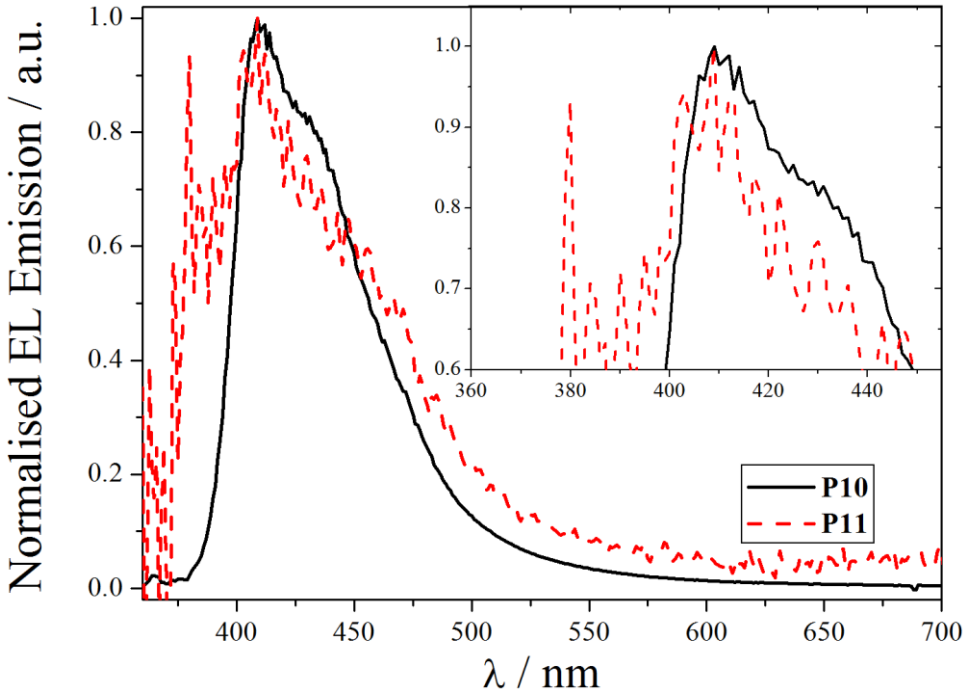

Figure 7.11: *Normalised EL emission spectra for polymers **P10-11**. Inset shows a magnification of the λ_{max} region.*

devices [35]. **P11** has a heavily reduced maximum brightness of 16 cd.m^{-2}, barely achieving the turn on brightness. In addition, despite there being a deeper blue area of spectrum over **P10** and the same λ_{max} of 409 nm, the CIE coordinates are poorer than those of **P10** due to a small tail into the green on the spectrum in Figure 7.11, skewing the coordinates.

As with the polymers **P1-3**, the introduction of the twist in the backbone for **P10** has had the effect of decreasing the current density passing through the device, due to the broken conjugation of the polymer reducing its conductivity. This has lowered both the maximum brightness and the maximum E.Q.E. of the device, whilst causing no substantial blue shift in EL emission.

To further investigate **P10**, devices of the structure glass | ITO (150 nm) | PEDOT:PSS HIL 1.5 (70 nm) | TAPC (60 nm or 90 nm) | LEP (20 nm) | TPBi (20 nm) | LiF

(1 nm) | Al (100 nm) were fabricated. The TAPC layer was solution processed and acted as a hole transport and electron blocking layer. Whilst these TAPC thicknesses are both high relative to the LEP thickness, it was assumed that a portion would be washed away during deposition of the LEP layer leaving a more reasonable thickness behind that could be assessed by ellipsometry. The results of this investigation can be seen in Figure 7.12. Despite the device properties not being as good as those for **P10** in Figure 7.10, due to a bad batch of devices, the general trends observed are still valid. Using the device structure above led to a substantial 55% increase in maximum E.Q.E. over the initial device with no TAPC layer. It did however result in a 25% increase in turn on voltage, due to the increased device thickness, and a 13% decrease in the maximum brightness observed.

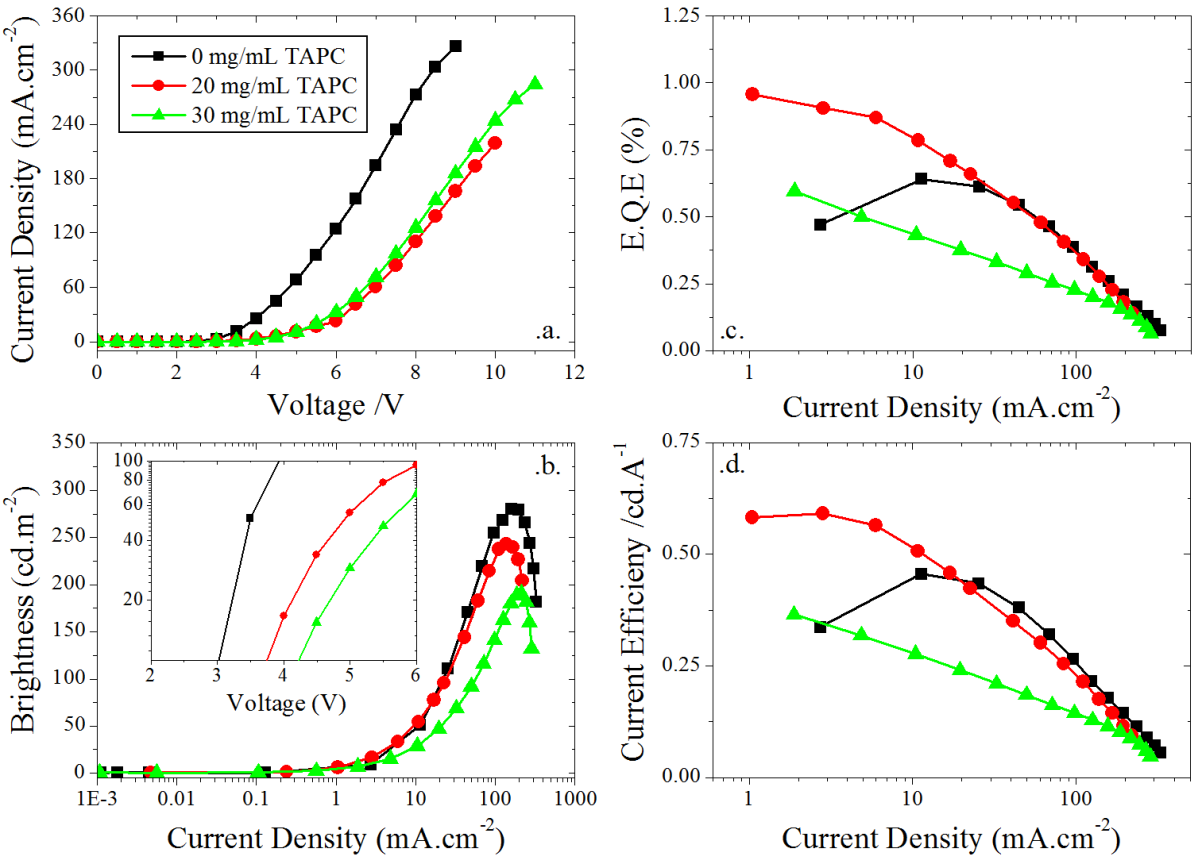

Figure 7.12: *Plots of (a) J-V curves, (b) Luminance vs. J, (c) E.Q.E. vs. J and (d) Device Efficiency vs. J for the polymer **P10** with different thicknesses of the HIL TAPC. Inset to (b) shows the turn on voltages for the four devices in a plot of Luminance vs. V.*

The changes in turn on voltage and brightness were initially believed to be the result of increased device thickness and potential absorption by the TAPC layer respectively. However, ellipsometry of the multilayer structures returns a combined thickness for the two layers between 19-20 nm. This indicates that the majority, if not all, of the TAPC layer has been washed away when the LEP layer is deposited. Despite this, the observed changes in device properties fit with those expected for the addition of an electron blocking layer and so further investigation will be required to fully explain whether either a very thin film of TAPC remains, or whether the two layers have blended.

7.3.5). CIE Plots and General Device Trends:

The CIE plots for the polymers **P1-11** are shown in Figure 7.13. Using this figure it is possible to see the evolution of the electroluminescence spectra with the different techniques used to produce deeper blue emission. From plots a and b it is especially easy to see that a large shift towards the blue can be achieved by changing the polymer from para conjugated to meta conjugated. A shift in y-coordinate of approximately 0.04-0.09 is observed when switching from polymers **P4-7** to polymers **P1-3**. Whilst this is a substantial blue shift, it comes at the cost of a heavily reduced maximum brightness and a reduced efficiency, due to the reduced transport properties of the polymer caused by the more broken conjugation, which makes this technique of limited potential for producing deeper blue PLEDs.

A similar effect is seen when the polymer is switched from para to meta conjugation between the polymers **P10** and **P11** in plots e and f of Figure 7.13. This time, however, the shift is in the opposite direction, despite there being a large area of deeper blue emission. A drastic decrease in device properties is again observed, reinforcing the limited potential of using meta conjugated polymers for fluorescent PLEDs.

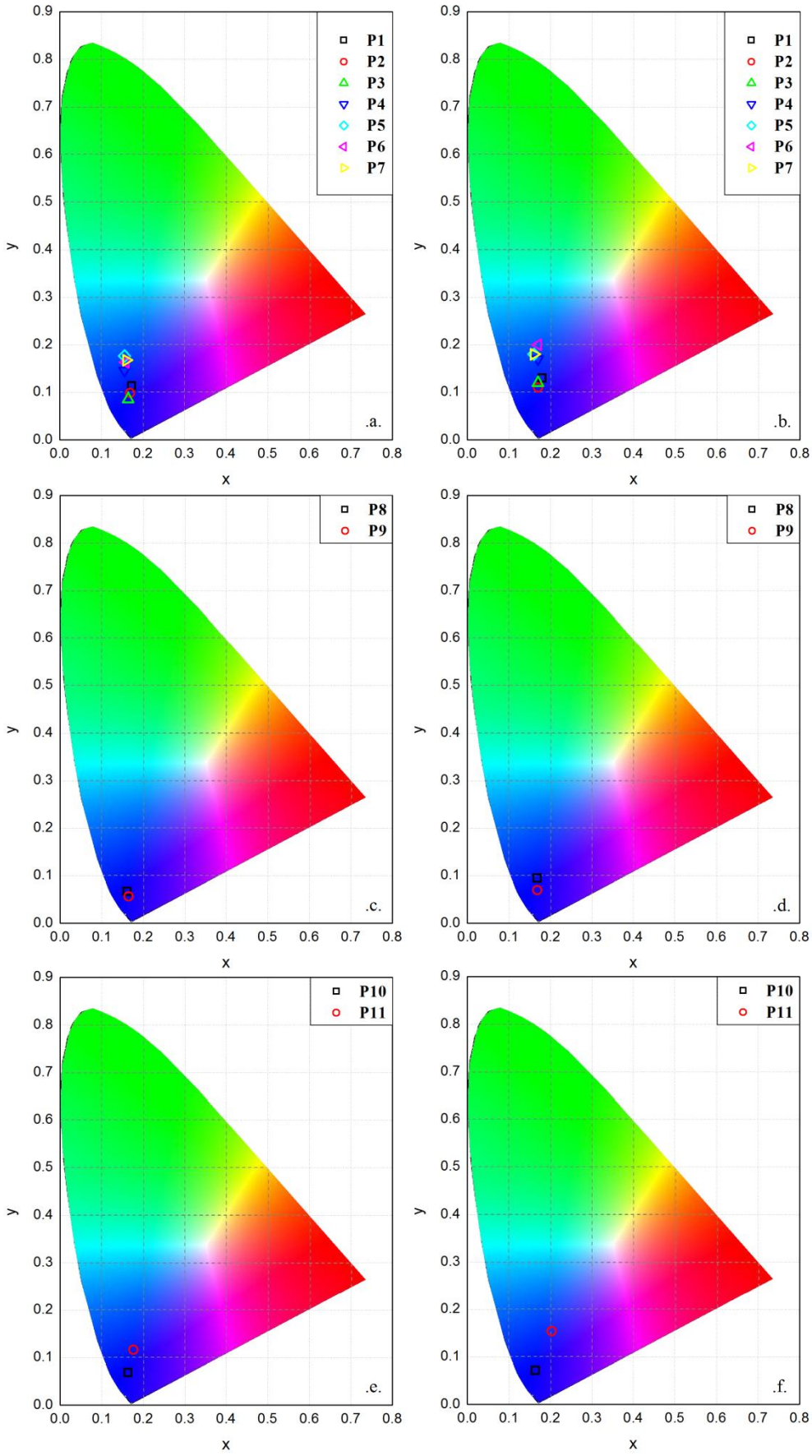

Figure 7.13: *Plots of (a), (c) and (e) turn on CIE coordinates (10 cd.m^{-2}) and (b), (d) and (f) peak brightness CIE coordinates for the polymers* ***P1-11****.*

A more subtle shift in CIE coordinates is caused using feed ratio changes between polymers **P1-3** and polymers **P4-7**. Opposite shifts are observed depending upon whether the polymer is para or meta conjugated and the reasons for this were discussed in 7.3.2) and 6.3.1). This slight blue shift is again accompanied by a decrease in device properties for polymers **P4** and **P6**, when compared to **P5** and **P7**, which again reduces its potential effectiveness for producing deeper blue emitting PLEDs.

A more successful technique for blue shifting emission is shortening the domain length of the polymer by introducing pendant groups of different sizes, and can be seen in plots c and d of Figure 7.13. This and the introduction of carbazole units into the copolymer as seen in e and f, has the effect of blue shifting the EL emission by around 0.04 along the y-axis compared to polymers **P1-3** into the violet/deep blue regions. This shift is combined with either extremely high efficiency devices for **P9**, or high brightness devices for **P10**, making this a viable technique for engineering violet/deep blue polymers for PLED devices.

7.4). Conclusions:

Eleven polyfluorene based copolymers have been synthesised and used in violet/deep blue fluorescent devices. Polymers **P1-7** had previously been tested as high triplet hosts and were produced with varying ratios of two different S_6 derivatives. Also investigated was the effect of meta or para bonding the polymers with respect to the pF unit. For the meta polymers **P1-3** deep blue emission peaking around 415 nm was observed. The ratio of 70:30 pF to S_{OCy} was observed to have the highest maximum efficiency reaching 2.7 % E.Q.E. whilst the ratio of 85:15 had the highest maximum brightness of 81 $cd.m^{-2}$. For the para polymers **P4-7** deep blue emission peaking around 450 nm was observed. The ratio of 70:30 pF to S_{OCy} was consistently observed to produce better devices than the 50:50 polymers. It was also observed that the bulkier S_{OCy} derivative produced more efficient and brighter

devices with polymer **P5** producing results of maximum efficiency 3.2% E.Q.E. and a maximum brightness of 2500 $cd.m^{-2}$.

Polymers **P8-9** were new polyfluorene based co-polymers incorporating 9,9-diphenylfluorene as a conjugation disrupter unit. For **P8** the minimal conjugated domain is in the main chain whereas for **P9** the minimal structure is isolated from the polymer main chain by carbazole pendant groups. For **P8** deep blue emission peaking at ca. 422 nm is observed with a peak E.Q.E. of 3.3% and brightness of 167 $cd.m^{-2}$. For **P9**, the larger conjugation disrupter unit leads to the highest maximum efficiency reaching 3.9% E.Q.E., the highest maximum brightness of 274 $cd.m^{-2}$ and violet emission peaking at ca. 401 nm.

Polymers **P10-11**were new fluorene and carbazole based co-polymers where between **P10** and **P11** the carbazole bonding positon to the fluorene group has been changed to introduce a twist in the polymer main chain. For **P10** violet/deep blue emission peaking at ca. 409 nm is observed with a peak E.Q.E. of 1.4% and brightness of 565 $cd.m^{-2}$. For **P11**, the disrupted meta conjugation leads to a reduced maximum efficiency of 0.35% E.Q.E., a reduced maximum brightness of 16 $cd.m^{-2}$ and a similar emission profile, also peaking at ca. 409 nm. The efficiency of **P10** can be increased by 50%, upon addition of a solution processed hole-injection layer of TAPC, but this also results in a decrease of 13% in the maximum device brightness. This demonstrates that a substantial boost in efficiency can be produced at a slight cost to maximum brightness, whilst still retaining a relatively simple solution processed hybrid device structure; further investigation is required to determine whether either a very thin film of TAPC remains, or whether the two layers have blended.

In conclusion, it has been shown that the polymers **P1-11** are capable of producing extremely bright violet/deep blue emission at low voltages and with exceptional colour stability whilst using a simple PLED architecture. Different chemical engineering techniques

have been used to develop polymers in an attempt to produce deeper blue emitting PLED devices, with varying degrees of success. Switching from para conjugation to meta conjugation has been successfully shown to blue shift emission by approximately 20 nm but this comes at the price of heavily reduced device properties making this a less attractive technique. Incorporating large pendant groups or carbazole units into the polyfluorene copolymer has a higher success rate, producing violet/deep blue devices with high efficiencies and brightnesses.

References:

1. C. Rothe, *Electrical doping is paving the way for the implementation of OLEDs in consumer electronics.* Laser & Photonics Reviews, 2007. **1**(4): p. 303-306.
2. N.T. Kalyani and S.J. Dhoble, *Organic light emitting diodes: Energy saving lighting technology-A review.* Renewable & Sustainable Energy Reviews, 2012. **16**(5): p. 2696-2723.
3. H. Sasabe and J. Kido, *Multifunctional Materials in High-Performance OLEDs: Challenges for Solid-State Lighting.* Chemistry of Materials, 2011. **23**(3): p. 621-630.
4. P.L. Burn, S.C. Lo, and I.D.W. Samuel, *The development of light-emitting dendrimers for displays.* Advanced Materials, 2007. **19**(13): p. 1675-1688.
5. P.-L.T. Boudreault, S. Beaupre, and M. Leclerc, *Polycarbazoles for plastic electronics.* Polymer Chemistry, 2010. **1**(2): p. 127-136.
6. A.C. Grimsdale, et al., *Synthesis of Light-Emitting Conjugated Polymers for Applications in Electroluminescent Devices.* Chemical Reviews, 2009. **109**(3): p. 897-1091.
7. K.T. Kamtekar, A.P. Monkman, and M.R. Bryce, *Recent Advances in White Organic Light-Emitting Materials and Devices (WOLEDs).* Advanced Materials, 2010. **22**(5): p. 572-582.
8. L. Ying, et al., *White Polymer Light-Emitting Devices for Solid-State Lighting: Materials, Devices, and Recent Progress.* Advanced Materials, 2014. **26**(16): p. 2459-2473.
9. X.J. Feng, et al., *Fluorene derivatives for highly efficient non-doped single-layer blue organic light-emitting diodes.* Organic Electronics, 2014. **15**(1): p. 57-64.
10. F.B. Dias, et al., *Triplet Harvesting with 100% Efficiency by Way of Thermally Activated Delayed Fluorescence in Charge Transfer OLED Emitters.* Advanced Materials, 2013. **25**(27): p. 3707-3714.
11. S.H. Jeong and J.Y. Lee, *Dibenzothiophene derivatives as host materials for high efficiency in deep blue phosphorescent organic light emitting diodes.* Journal of Materials Chemistry, 2011. **21**(38): p. 14604-14609.

12. S. Nau, et al., *Highly Efficient Color-Stable Deep-Blue Multilayer PLEDs: Preventing PEDOT:PSS-Induced Interface Degradation.* Advanced Materials, 2013. **25**(32): p. 4420-4424.

13. A. Sergent, et al., *Synthesis, characterization, morphological behaviour, and photo- and electroluminescence of highly blue-emitting fluorene-carbazole copolymers with alkyl side-chains of different lengths.* Journal of Materials Chemistry C, 2013. **1**(19): p. 3207-3216.

14. S. Wu, et al., *High-efficiency deep-blue organic light-emitting diodes based on a thermally activated delayed fluorescence emitter.* Journal of Materials Chemistry C, 2014. **2**(3): p. 421-424.

15. Y. Yang, et al., *Blue-Violet Electroluminescence from a Highly Fluorescent Purine.* Chemistry of Materials, 2010. **22**(12): p. 3580-3582.

16. J. Ye, et al., *Carbazole/Sulfone Hybrid D-pi-A-Structured Bipolar Fluorophores for High-Efficiency Blue-Violet Electroluminescence.* Chemistry of Materials, 2013. **25**(13): p. 2630-2637.

17. J.R. Koo, et al., *Highly efficient and simplified phosphorescence white organic light-emitting diodes based on synthesized deep-blue host and orange emitter.* Thin Solid Films, 2013. **544**: p. 234-237.

18. Y. Yang, et al., *Ultraviolet-violet electroluminescence from highly fluorescent purines.* Journal of Materials Chemistry C, 2013. **1**(16): p. 2867-2874.

19. U. Giovanella, et al., *Perfluorinated polymer with unexpectedly efficient deep blue electroluminescence for full-colour OLED displays and light therapy applications.* Journal of Materials Chemistry C, 2013. **1**(34): p. 5322-5329.

20. S.-A. Chen, H.-H. Lu, and C.-W. Huang, *Polyfluorenes for device applications*, in *Polyfluorenes*, U. Scherf and D. Neher, Editors. 2008. p. 49-84.

21. U. Scherf and E.J.W. List, *Semiconducting polyfluorenes - Towards reliable structure-property relationships.* Advanced Materials, 2002. **14**(7): p. 477-+.

22. F.B. Dias, et al., *Dipolar stabilization of emissive singlet charge transfer excited states in polyfluorene copolymers.* Journal of Physical Chemistry B, 2008. **112**(21): p. 6557-6566.

23. S.M. King, et al., *Exploiting a Dual-Fluorescence Process in Fluorene-Dibenzothiophene-S,S-dioxide Co-Polymers to Give Efficient Single Polymer LEDs with Broadened Emission.* Advanced Functional Materials, 2009. **19**(4): p. 586-591.

24. F.B. Dias, et al., *Exciton Diffusion in Polyfluorene Copolymer Thin Films: Kinetics, Energy Disorder and Thermally Assisted Hopping.* Chemphyschem, 2009. **10**(12): p. 2096-2104.

25. H. Liu, et al., *Highly efficient and spectrally stable blue-light-emitting polyfluorenes containing a dibenzothiophene-S,S-dioxide unit.* Chemistry of Materials, 2008. **20**(13): p. 4499-4506.

26. Y. Li, et al., *Enhancement of spectral stability and efficiency on blue light-emitters via introducing dibenzothiophene-S,S-dioxide isomers into polyfluorene backbone.* Organic Electronics, 2009. **10**(5): p. 901-909.

27. H. Xiao, et al., *Novel green light-emitting polyfluorenes containing dibenzothiophene-S,S-dioxide-arylamine derivatives.* Polymer, 2012. **53**(14): p. 2873-2883.

28. L. Yu, et al., *Red, Green, and Blue Light-Emitting Polyfluorenes Containing a Dibenzothiophene-S,S-Dioxide Unit and Efficient High-Color-Rendering-Index White-Light-Emitting Diodes Made Therefrom.* Advanced Functional Materials, 2013. **23**(35): p. 4366-4376.

29. K.T. Kamtekar, et al., *Synthesis and Spectroscopy or Poly(9,9-dioctylfluorene-2,7-diyl-co-2,8-dihexyldibenzothiophene-S,S-dio xide-3,7-diyl)s: Solution-Processable, Deep-Blue Emitters with a High Triplet Energy.* Macromolecules, 2010. **43**(10): p. 4481-4488.

30. J.H. Cook, et al., *Efficient deep blue fluorescent polymer light-emitting diodes (PLEDs).* Journal of Materials Chemistry C, 2014. **2**(28): p. 5587-5592.

31. S.C. Dong, Z. Li, and J.G. Qin, *New Carbazole-Based Fluorophores: Synthesis, Characterization, and Aggregation-Induced Emission Enhancement.* Journal of Physical Chemistry B, 2009. **113**(2): p. 434-441.

32. F.C. Chen, et al., *Energy transfer and triplet exciton confinement in polymeric electrophosphorescent devices.* Journal of Polymer Science Part B-Polymer Physics, 2003. **41**(21): p. 2681-2690.

33. H.A. Al-Attar and A.P. Monkman, *Solution processed multilayer polymer light-emitting diodes based on different molecular weight host.* Journal of Applied Physics, 2011. **109**(7).

34. Y.G. Zhang, et al., *Charge carrier injection and transport in PVK: Alq(3) blend films.* Journal of Physics D-Applied Physics, 2003. **36**(16): p. 2006-2009.

35. Y. Zhang, et al., *Antimicrobial Blue Light Therapy for Multidrug-Resistant Acinetobacter baumannii Infection in a Mouse Burn Model: Implications for Prophylaxis and Treatment of Combat-related Wound Infections.* Journal of Infectious Diseases, 2014. **209**(12): p. 1963-1971.

Chapter 8 Conclusions:

This thesis has focused on using novel methods, such as the simulation software SETFOS, to analyse OLED devices and extract important intrinsic parameters that would be difficult to obtain otherwise. After establishing the viability of SETFOS as a modelling tool it was used in conjunction with previously well documented materials to investigate the effects of both phosphorescent dopant colour and concentration on device performance and extract important parameters, such as the density of states and carrier mobilities. The information gathered from this investigation was then used in the characterization of novel high triplet host polymers for OLED applications. When these polymers proved unsuitable hosts for phosphorescent dopants they were instead assessed on their ability to perform as deep blue fluorescent polymers in undoped PLED devices. These devices were found to have some of the highest device characteristics currently detailed in the literature and represent a variety of new ways of achieving efficient deep blue emission using PLED devices.

In Chapter 4 it was shown that it is indeed possible to reproduce the electronic characteristics of physical device using the drift diffusion simulations available in SETFOS 3.2. SETFOS, however, required the use of parameters from outside the correct range to produce the best fits. This highlighted potential limitations within the models used by SETFOS which are thought to include a combination of factors. The cross-sectional area of the pixels involved and the resistivities of the ITO and aluminium layers were not included and SETFOS is believed to be unable to account for the leakage current that occurs in devices. Despite this, quantitative values for important device parameters have been extracted that fit with the experimentally observed trends. It has therefore been concluded that careful SETFOS analysis can be used to successfully support conclusions drawn from experimental

device data. In the future it may be possible with further refinements to predict experimental device behavior or extract qualitative values for important device parameters.

In Chapter 5, nine devices were manufactured for three different colors of phosphorescent dopants to investigate the effects of their concentration on device performance and different device parameters. Each of the three dopants produced a series of devices that behaved in similar, yet individual, manners. Each of the three dopants exhibited signs of Förster transfer at low concentrations. The green dopant appeared to operate primarily through direct charge trapping; the blue dopant showed signs of acquiring charge primarily through Förster, whilst the red dopant appeared to use a combination of the two.

The devices were characterized using transient electroluminescence experiments in order to determine their carrier mobilities. The carrier mobility increased with concentration for both the red and blue dopants, and decreased for increasing concentrations of the green dopant. SETFOS simulations were performed to model the J-V characteristics of a selection of the devices. The qualitative trends mostly matched those of the experimentally determined mobilities whilst their absolute values were not in agreement. This mirrored the conclusions drawn in Chapter 4, where SETFOS was found to be able to broadly match the trends but due to limitations in the models used was unable to replicate the actual values.

Both the concentration and the energy levels of a phosphorescent dopant are important when selecting one for devices. The energy levels must be well matched to those of the hosts in order to maximise efficient energy transfer between them, but also avoid thermally activated back transfer. Concentration is important to device performance as significant changes in efficiency are observed for relatively small differences in concentration. Despite a number of limitations observed within the SETFOS model, it can be used to extract qualitative values and trends to back up experimentally deduced conclusions.

In Chapter 6, seven new polymers synthesized by Durham University Chemistry Department were used in devices to assess their viability as high triplet hosts. These included three meta conjugated polymers, **P1-3**, of different polyfluorene (pF) to O-methylenecyclohexyl (S_{OCy}) ratios and four para conjugated polymers, **P4-7**, with 50:50 or 70:30 ratios of polyfluorene to O-Hexyl (S_{O6}) or S_{OCy} groups. The three meta polymers all had restricted carrier transport capabilities whilst the para polymers were less restricted and achieved much higher current densities. The polymers all had relatively high HOMO/LUMO levels compared to the phosphorescent dopants, leading to direct charge trapping of electrons on to the phosphorescent dopants, leaving the holes trapped on the host polymers. Little, or no, emission was observed from the phosphorescent dopant.

Changing the ratios of pF to S_{O6} or S_{OCy} was investigated in an attempt to promote energy transfer from the polymer host to the phosphorescent dopant and to increase the carrier mobilities within the devices. Increasing the pF:S_{O6}, or pF:S_{OCy}, ratio from 50:50 to 70:30 increased the carrier mobilities within the polymer hosts, allowing for increased current density or brightness from the device. Simultaneous emission from both the polymer host and the phosphorescent dopant was observed for the meta polymer **P2**, but it was not possible to isolate the emission from the phosphorescent dopant.

The S_{O6} and S_{OCy} derivatives were compared directly and it was found that the devices with the bulkier S_{OCy} derivative performed worse than the less bulky S_{O6} derivative. Using the blue emitting phosphorescent dopant VK-17-B instead of $Ir(ppy)_3$ was not successful, and devices failed to achieve the turn on brightness. The introduction of the electron injecting layer TPBi was met with limited success. Emission was observed from the phosphorescent dopant, but only at high voltages and after saturation of the polymer host.

The seven polyfluorene based copolymers were found to be unsuitable for use as high triplet hosts. Despite possessing a relatively high triplet level, they are also in possession of relatively high HOMO and LUMO levels which do not match up well with a number of commonly used phosphorescent dopants. There is little or no energy transfer between the two, resulting in very low emission, primarily from the host. In addition to this the meta polymers have severely hindered charge transport abilities and rely on those of the dopant to pass a current density through the device. As such, they are inferior to PVK, or other polyfluorene derivatives.

In Chapter 7, the seven polyfluorene based copolymers and four new copolymers were characterised and used in violet/deep blue fluorescent devices. For the meta polymers **P1-3** deep blue emission peaking around 415 nm was observed. The ratio of 70:30 pF to S_{OCy} was observed to have the highest maximum efficiency reaching 2.7 % E.Q.E. whilst the ratio of 85:15 had the highest maximum brightness of 81 $cd.m^{-2}$. For the para polymers **P4-7** deep blue emission peaking around 450 nm was observed. The ratio of 70:30 pF to S_{OCy} was consistently observed to produce better devices than the 50:50 polymers. It was also observed that the bulkier S_{OCy} derivative produced more efficient and brighter devices with polymer **P5** producing results of maximum efficiency 3.2% E.Q.E. and a maximum brightness of 2500 $cd.m^{-2}$.

Polymers **P8-9** were new polyfluorene based co-polymers incorporating 9,9-diphenylfluorene as a conjugation disrupter unit. For **P8** deep blue emission peaking at ca. 422 nm is observed with a peak E.Q.E. of 3.3% and brightness of 167 $cd.m^{-2}$. For **P9** the larger conjugation disrupter unit leads to the highest maximum efficiency reaching 3.9% E.Q.E., the highest maximum brightness of 274 $cd.m^{-2}$ and violet emission peaking at ca. 401 nm. Polymers **P10-11**were new fluorene and carbazole based co-polymers. For **P10** violet/deep blue emission peaking at ca. 409 nm is observed with a peak E.Q.E. of 1.4% and

brightness of 565 cd.m^{-2}. For **P11** the disrupted meta conjugation leads to a reduced maximum efficiency of 0.35% E.Q.E., a reduced maximum brightness of 16 cd.m^{-2} and a similar emission, also peaking at ca. 409 nm. The efficiency of **P10** can be increased by 50% upon addition of a solution processed hole-injection layer of TAPC but this also results in a decrease of 13% in the maximum device brightness.

The polymers **P1-11** are capable of producing extremely bright violet/deep blue emission at low voltages and with exceptional colour stability whilst using a simple PLED architecture. Switching from para conjugation to meta conjugation has been successfully shown to blue shift emission by approximately 20 nm but this comes at the price of heavily reduced device properties making this technique less attractive. Incorporating large pendant groups or carbazole units into the polyfluorene copolymer has a higher success rate, producing violet/deep blue devices with high efficiencies and brightnesses.